POR-2015-V1(EX)
(WT-2015-V1)(EX)
EXTRACTED VERSION

AD-A995 425

OPERATION DOMINIC, FISH BOWL SERIES

Project Officer's Report—Project 6.1

Fireball Attenuation and Refraction

R. J. Clawson, Project Officer
S. G. Hoihjelle
C. R. Yalkut
U. S. Army Electronics Research and Development Activity
White Sands Missile Range, NM

D. J. Pearce
C. L. Gardenhire
Physical Science Laboratory
New Mexico State University
University Park, NM

DTIC
ELECTE
JUN 19 1986
S D
D

8 April 1965

NOTICE:
This is an extract of POR-2015 (WT-2015), Operation DOMINIC, Volume 1, Fish Bowl Series, Project 6.1.

Approved for public release;
distribution is unlimited.

Extracted version prepared for
Director
DEFENSE NUCLEAR AGENCY
Washington, DC 20305-1000

1 September 1985

DTIC FILE COPY

86 6 19 01

UNCLASSIFIED
SECURITY CLASSIFICATION OF THIS PAGE

AD-A995 425

REPORT DOCUMENTATION PAGE

1a. REPORT SECURITY CLASSIFICATION UNCLASSIFIED	1b. RESTRICTIVE MARKINGS
2a. SECURITY CLASSIFICATION AUTHORITY	3. DISTRIBUTION/AVAILABILITY OF REPORT Approved for public release; distribution is unlimited.
2b. DECLASSIFICATION/DOWNGRADING SCHEDULE	
4. PERFORMING ORGANIZATION REPORT NUMBER(S)	5. MONITORING ORGANIZATION REPORT NUMBER(S) POR-2015-V1 (EX) (WT-2015-V1) (EX)
6a. NAME OF PERFORMING ORGANIZATION 1-Army Electronics R&D Activity 2-Physical Science Lab,NM Stat Univ.	6b. OFFICE SYMBOL (If applicable)
6c. ADDRESS (City, State, and ZIP Code) 1-White Sands Missile Range, NM 2-University Park, NM	7a. NAME OF MONITORING ORGANIZATION Defense Atomic Support Agency
8a. NAME OF FUNDING/SPONSORING ORGANIZATION	8b. OFFICE SYMBOL (If applicable)
8c. ADDRESS (City, State, and ZIP Code)	7b. ADDRESS (City, State, and ZIP Code) Washington, DC
	9. PROCUREMENT INSTRUMENT IDENTIFICATION NUMBER
	10. SOURCE OF FUNDING NUMBERS PROGRAM ELEMENT NO. / PROJECT NO. / TASK NO. / WORK UNIT ACCESSION NO.

11. TITLE (Include Security Classification) OPERATION DOMINIC, FISH BOWL SERIES, PROJECT OFFICER'S REPORT; PROJECT 6.1 - Fireball Attenuation and Refraction, Extracted Version

12. PERSONAL AUTHOR(S)
R. J. Clawson, S. G. Hoihjelle, C. R. Yalkut, D. G. Pearce, and C. L. Gardenhire

13a. TYPE OF REPORT	13b. TIME COVERED FROM ____ TO ____	14. DATE OF REPORT (Year, Month, Day)	15. PAGE COUNT
		650408	338

16 SUPPLEMENTARY NOTATION This report has had sensitive military information removed in order to provide an unclassified version for unlimited distribution. The work was performed by the Defense Nuclear Agency in support of the DoD Nuclear Test Personnel Review Program.

17. COSATI CODES		
FIELD	GROUP	SUB-GROUP
18	3	
14	3	

18. SUBJECT TERMS (Continue on reverse if necessary and identify by block number)
Dominic, Fish Bowl, Fireball Attenuation, Refraction, Blue Gill, King Fish, Tight Rope

19. ABSTRACT (Continue on reverse if necessary and identify by block number)

A prime objective of the experiment was the quantitative measurement of the attenuation suffered by radar beams passing near or through the fireball of a nuclear detonation. During the test series, measurements were also made of effects produced in regions not directly associated with the fireball proper.

A second prime objective of the experiment was to investigate possible phase differences which were expected to develop in nearly parallel radar rays passing through ionized regions.

Ballistic rockets were used to place CW beacons, radiating at 1-, 5-, and 10-kMc frequencies. Five receiving stations, four on ships and one on Johnston Island, made signal strength measurements. An interferometer on the island made phase-front measurements at 1- and 5-kMc.

20 DISTRIBUTION/AVAILABILITY OF ABSTRACT	21. ABSTRACT SECURITY CLASSIFICATION
☒ UNCLASSIFIED/UNLIMITED ☐ SAME AS RPT. ☐ DTIC USERS	UNCLASSIFIED
22a. NAME OF RESPONSIBLE INDIVIDUAL MARK D. FLOHR	22b. TELEPHONE (Include Area Code) 202-325-7559 / 22c. OFFICE SYMBOL DNA/ISCM

DD FORM 1473, 83 APR

83 APR edition may be used until exhausted
All other editions are obsolete.

SECURITY CLASSIFICATION OF THIS PAGE
UNCLASSIFIED

FOREWORD

Classified material has been removed in order to make the information available on an unclassified, open publication basis, to any interested parties. The effort to declassify this report has been accomplished specifically to support the Department of Defense Nuclear Test Personnel Review (NTPR) Program. The objective is to facilitate studies of the low levels of radiation received by some individuals during the atmospheric nuclear test program by making as much information as possible available to all interested parties.

The material which has been deleted is either currently classified as Restricted Data or Formerly Restricted Data under the provisions of the Atomic Energy Act of 1954 (as amended), or is National Security Information, or has been determined to be critical military information which could reveal system or equipment vulnerabilities and is, therefore, not appropriate for open publication.

The Defense Nuclear Agency (DNA) believes that though all classified material has been deleted, the report accurately portrays the contents of the original. DNA also believes that the deleted material is of little or no significance to studies into the amounts, or types, of radiation received by any individuals during the atmospheric nuclear test program.

Accesion For	
NTIS CRA&I	☑
DTIC TAB	☐
Unannounced	☐
Justification	
By	
Distribution/	
Availability Codes	
Dist	Avail and/or Special
A-1	

UNANNOUNCED

OPERATION DOMINIC

FISH BOWL SERIES

PROJECT OFFICERS REPORT — PROJECT 6.1

FIREBALL ATTENUATION AND REFRACTION

Robert J. Clawson, Project Officer

Sylvia G. Hoihjelle
Carl R. Yalkut

U.S. Army Electronics Research and
Development Activity
White Sands Missile Range, New Mexico

and

David G. Pearce
Charles L. Gardenhire

Physical Science Laboratory
New Mexico State University
University Park, New Mexico

ABSTRACT

This report presents the results of Project 6.1 participation in the Blue Gill, King Fish, and Tight Rope events of the Fish Bowl Series. The project was undertaken to determine the effects of high-altitude nuclear detonations on ABM radar frequencies. Primary measurements included time functions of (1) attenuation through the fireball and associated ionized regions, and (2) refractive effects produced by the detonation.

Ballistic rockets were used to place CW beacons, radiating at 1-, 5-, and 10-kMc frequencies. Five receiving stations, four on ships and one on Johnston Island, made signal strength measurements. An interferometer on the island made phase-front measurements at 1 and 5 kMc.

PREFACE

The functions of Project 6.1 activities in the Fish Bowl Series were designed primarily to support the Blue Gill experiment. As the parameters of other Dominic tests became known, the possibility of using 6.1 instrumentation to retrieve useful data became evident. With some operational modifications, successful participations in the King Fish and Tight Rope events were accomplished.

Because of the individualistic nature of each operation, details pertaining to each of the three operations are separately described in this report. A recapitulation of conclusive results and recommendations follows these presentations. Since several versions of support data have been supplied, the data used to arrive at the solutions in this report have been included in the appendixes.

The Project Officer wishes to acknowledge the technical and administrative assistance afforded this project in both the field operations and in the preparation of this report. From project concept to Blue Gill Double Prime, Mr. George K. Roberts was Project Officer, and Mr. James W. Jones was Technical Director for 6.1a.

Lt. J.D. Garcia of the U.S. Air Force Weapons Laboratory was Project Officer for 6.1c, which provided the phenomenological predictions necessary for experiment design.

Personnel of the U.S. Army Electronics Research and Development Activity, White Sands Missile Range; the Electronic Defense Laboratories, Sylvania, Mountain View, California; and Aerojet General Corporation, Sacramento, California, joined in an effective operating task force for the accomplishment of project objectives.

The Physical Science Laboratory, New Mexico State University, has provided assistance in the task of reducing the project data.

All photographs are from the U.S. Army Electronics Research and Development Activity, White Sands Missile Range, New Mexico.

CONTENTS

ABSTRACT ---- 5

PREFACE ---- 6

CHAPTER 1 INTRODUCTION ---- 15

1.1 Objectives ---- 15
1.2 Phenomenology ---- 16
1.3 General Procedure ---- 22
1.3.1 Fixed Station Measurements ---- 23
1.3.2 Shipboard Measurements ---- 23
1.4 Instrumentation ---- 24
1.4.1 Missileborne CW Signal Package ---- 24
1.4.2 Cubic Corporation Missile Tracking Systems ---- 27
1.4.3 Carrier Vehicles ---- 27
1.4.4 Fixed Station ---- 29
1.4.5 Shipboard Stations ---- 36
1.4.6 Communication System ---- 42
1.5 Calibration ---- 43
1.5.1 Fixed Station, Preshot ---- 43
1.5.2 Fixed Station, Postshot ---- 44
1.5.3 Mobile Stations, Preshot ---- 45
1.5.4 Mobile Stations, Postshot ---- 46
1.5.5 Real-Time Commentary and Operators' Critique ---- 48
1.6 Instrumentation Limitations ---- 49
1.6.1 Missile Beacon Performance ---- 49
1.6.2 Receiving System ---- 51
1.6.3 Tracking Logic ---- 52
1.6.4 Recording Bandwidths ---- 53
1.6.5 Phasemeter Characteristics ---- 53
1.7 Data Interpretation ---- 54
1.7.1 Attenuation ---- 54
1.7.2 Refraction ---- 56

CHAPTER 2 BLUE GILL ---- 96

2.1 Phenomenology ---- 96
2.2 Objectives ---- 97
2.3 Operations ---- 97
2.3.1 Operational Plan ---- 97
2.3.2 Fixed Station Operation ---- 100
2.3.3 Shipboard Station Operation ---- 102
2.3.4 Support Data ---- 102

2.4 Results ---- 104
2.4.1 Attenuation Data ---- 105
2.4.2 Refraction Data ---- 122
2.5 Discussion ---- 128
2.5.1 Data Reliability ---- 128
2.5.2 Attenuation ---- 128
2.5.3 Refraction ---- 130

CHAPTER 3 KING FISH ---- 213

3.1 Phenomenology ---- 213
3.2 Objectives ---- 214
3.3 Operations ---- 214
3.3.1 Operational Plan ---- 214
3.3.2 Fixed Station Operation ---- 218
3.3.3 Shipboard Station Operation ---- 218
3.3.4 Support Data ---- 219
3.4 Results ---- 221
3.4.1 Attenuation Data ---- 221
3.4.2 Refraction Data ---- 225
3.5 Discussion ---- 228
3.5.1 Data Reliability ---- 228
3.5.2 Attenuation ---- 228
3.5.3 Refraction ---- 229

CHAPTER 4 TIGHT ROPE ---- 269

4.1 Phenomenology ---- 269
4.2 Objectives ---- 270
4.3 Operations ---- 270
4.3.1 Operational Plan ---- 270
4.3.2 Fixed Station Operation ---- 271
4.3.3 Shipboard Station Operation ---- 272
4.3.4 Support Data ---- 272
4.4 Results ---- 274
4.4.1 Attenuation Data ---- 274
4.4.2 Refraction Data ---- 282
4.5 Discussion ---- 284
4.5.1 Data Reliability ---- 284
4.5.2 Attenuation ---- 285
4.5.3 Refraction ---- 286

CHAPTER 5 CONCLUSIONS AND RECOMMENDATIONS ---- 334

5.1 Conclusions ---- 334
5.1.1 Attenuation ---- 334
5.1.2 Refraction ---- 335
5.2 Recommendations ---- 335

TABLES

1.1 Missile Package Environmental Characteristics ---------- 58
1.2 Electrical and Mechanical Specifications of the CW Signal Package------ 59
1.3 Fixed Station Antenna Specifications ---------- 60
1.4 Fixed Station Receiver System Specifications ---------- 61
1.5 Shipboard Antenna Specifications ---------- 62
1.6 Shipboard Receiver System Specifications ---------- 63
1.7 Antenna Control System Specifications---------- 64
1.8 Communication System Specifications ---------- 65
1.9 Low-Pass Filtering of Phase Data ---------- 65
2.1 Theoretical Fireball Parameters, Blue Gill---------- 131
2.2 Planned Firing Schedule, Blue Gill---------- 131
2.3 Time Spans of Blue Gill Raw Trajectory Data---------- 132
2.4 Project 6.1 Data Reliability---------- 132
3.1 Firing Schedule, King Fish ---------- 230
4.1 Planned Firing Schedule, Tight Rope---------- 287
4.2 Time Spans of Raw Trajectory Data, Tight Rope---------- 287
4.3 Comparative Characteristic Attenuation for Blue Gill and Tight Rope at H + 40 seconds ---------- 287

FIGURES

1.1 Nike-Cajun prepared for launching ---------- 66
1.2 Missileborne CW signal package---------- 67
1.3 CW signal package radiation patterns ---------- 68
1.4 Nike-Cajun rocket and payload---------- 69
1.5 Missile launcher remote control---------- 70
1.6 Basic interferometer system---------- 71
1.7 X-, C-, and L-band interferometer antennas ---------- 72
1.8 Fixed station antenna array---------- 73
1.9 X-band interferometer azimuth antenna patterns---------- 74
1.10 X-band interferometer elevation antenna patterns ---------- 75
1.11 C- and L-band interferometer azimuth antenna patterns ---------- 76
1.12 C- and L-band interferometer elevation antenna patterns ---------- 77
1.13 X-band interferometer horn antenna pattern, H-plane---------- 78
1.14 X-band interferometer horn antenna pattern, E-plane---------- 79
1.15 Fixed station receiving system---------- 80
1.16 Interferometer Receiver A---------- 81
1.17 Interferometer Receivers B, C, and D---------- 82
1.18 Shipboard tracking station ---------- 83
1.19 X-band tracking antenna patterns, vertical polarization ---------- 84
1.20 X-band tracking antenna patterns, horizontal polarization---------- 85
1.21 C-band tracking antenna patterns, vertical polarization ---------- 86
1.22 C-band tracking antenna patterns, horizontal polarization---------- 87
1.23 L-band tracking antenna patterns, vertical polarization ---------- 88
1.24 L-band tracking antenna patterns, horizontal polarization---------- 89
1.25 Tracking receiver system ---------- 90
1.26 Tracking receiver (all bands)---------- 91
1.27 Shipboard antenna control subsystem---------- 92
1.28 Typical display of phase data ---------- 93

1.29 AGC calibration, Blue Gill, Ship 2, C-band ---------- 94
1.30 Actual and apparent refraction angles ---------- 95
2.1 Blue Gill geometry, Project 6.1---------- 133
2.2 Proposed ship positions at H-hour for Blue Gill ---------- 134
2.3 Blue Gill trajectory, Missile A, Cubic Corporation data---------- 135
2.4 Blue Gill trajectory, Missile C, Cubic Corporation data---------- 136
2.5 X-band relative signal strength, Blue Gill, Missile A, interferometer --- 137
2.6 Relative signal strength, Blue Gill, Missile A, interferometer -------- 138
2.7 C-band relative signal strength, Blue Gill, Missile A, interferometer --- 139
2.8 C-band relative signal strength envelopes, Blue Gill, Missile A, interferometer---------- 140
2.9 L-band relative signal strength, Blue Gill, Missile A, interferometer --- 141
2.10 L-band relative signal strength envelopes, Blue Gill, Missile A, interferometer---------- 142
2.11 Fireball-ray-path parameters, Blue Gill, Missile A, interferometer --- 143
2.12 X-band relative signal strength, Blue Gill, Missile C, interferometer -- 144
2.13 C-band relative signal strength, Blue Gill, Missile C, interferometer -- 145
2.14 L-band relative signal strength, Blue Gill, Missile C, interferometer -- 146
2.15 Fireball-ray-path parameters, Blue Gill, Missile C, Ship 1 --------- 147
2.16 X-band relative signal strength, Blue Gill, Missile C, Ship 1 -------- 148
2.17 C-band relative signal strength, Blue Gill, Missile C, Ship 1 -------- 149
2.18 L-band relative signal strength, Blue Gill, Missile C, Ship 1 -------- 150
2.19 C-band relative signal strength envelopes, Blue Gill, Missile C, Ship 1 - 151
2.20 L-band relative signal strength envelopes, Blue Gill, Missile C, Ship 1 - 152
2.21 Relative signal strength, Blue Gill, Missile C, Ship 2 ---------- 153
2.22 X-band relative signal strength, Blue Gill, Missile C, Ship 2 --------- 154
2.23 Fireball-ray-path parameters, Blue Gill, Missile C, Ship 2 ---------- 155
2.24 Computed power losses due to antenna-pointing errors, Blue Gill, Missile C, Ship 2 ---------- 156
2.25 X-band relative signal strength with corrections for antenna-pointing errors, Blue Gill, Missile C, Ship 2---------- 157
2.26 C-band relative signal strength with corrections for antenna-pointing errors, Blue Gill, Missile C, Ship 2---------- 158
2.27 C-band relative signal strength, Blue Gill, Missile C, Ship 2 -------- 159
2.28 L-band relative signal strength envelopes, Blue Gill, Missile C, Ship 2---------- 160
2.29 L-band relative signal strength, Blue Gill, Missile C, Ship 2 -------- 161
2.30 X-band relative signal strength, Blue Gill, Missile C, Ship 3 -------- 162
2.31 C-band relative signal strength, Blue Gill, Missile C, Ship 3 -------- 163
2.32 L-band relative signal strength, Blue Gill, Missile C, Ship 3 -------- 164
2.33 Fireball-ray-path parameters, Blue Gill, Missile C, Ship 3 ---------- 165
2.34 Computed power losses due to antenna-pointing errors, Blue Gill, Missile C, Ship 3 ---------- 166
2.35 X-band relative signal strength with corrections for antenna-pointing errors, Blue Gill, Missile C, Ship 3---------- 167
2.36 C-band relative signal strength with corrections for antenna-pointing errors, Blue Gill, Missile C, Ship 3---------- 168
2.37 L-band relative signal strength envelopes, Blue Gill, Missile C, Ship 3---------- 169

2.38 X-band relative signal strength, Blue Gill, Missile C, Ship 4 -------- 170
2.39 C-band relative signal strength, Blue Gill, Missile C, Ship 4 -------- 171
2.40 L-band relative signal strength, Blue Gill, Missile C, Ship 4 -------- 172
2.41 Fireball-ray-path parameters, Blue Gill, Missile C, Ship 4 --------- 173
2.42 X-band relative signal strength, Blue Gill, Missile E, interferometer -- 174
2.43 C-band relative signal strength, Blue Gill, Missile E, interferometer -- 175
2.44 L-band relative signal strength, Blue Gill, Missile E, interferometer -- 176
2.45 X-band relative signal strength, Blue Gill, Missile E, Ship 1 -------- 177
2.46 C-band relative signal strength, Blue Gill, Missile E, Ship 1 -------- 178
2.47 L-band relative signal strength, Blue Gill, Missile E, Ship 1 -------- 179
2.48 X-band relative signal strength, Blue Gill, Missile E, Ship 2 -------- 180
2.49 C-band relative signal strength, Blue Gill, Missile E, Ship 2 -------- 181
2.50 L-band relative signal strength, Blue Gill, Missile E, Ship 2 -------- 182
2.51 X-band relative signal strength, Blue Gill, Missile E, Ship 3 -------- 183
2.52 C-band relative signal strength, Blue Gill, Missile E, Ship 3 -------- 184
2.53 L-band relative signal strength, Blue Gill, Missile E, Ship 3 -------- 185
2.54 X-band relative signal strength, Blue Gill, Missile E, Ship 4 -------- 186
2.55 C-band relative signal strength, Blue Gill, Missile E, Ship 4 -------- 187
2.56 L-band relative signal strength, Blue Gill, Missile E, Ship 4 -------- 188
2.57 X-band relative signal strength, Blue Gill, Missile F, interferometer -- 189
2.58 C-band relative signal strength, Blue Gill, Missile F, interferometer -- 190
2.59 L-band relative signal strength, Blue Gill, Missile F, interferometer -- 191
2.60 X-band relative signal strength, Blue Gill, Missile F, Ship 1 -------- 192
2.61 C-band relative signal strength, Blue Gill, Missile F, Ship 1 -------- 193
2.62 L-band relative signal strength, Blue Gill, Missile F, Ship 1 -------- 194
2.63 X-band relative signal strength, Blue Gill, Missile F, Ship 2 -------- 195
2.64 C-band relative signal strength, Blue Gill, Missile F, Ship 2 -------- 196
2.65 L-band relative signal strength, Blue Gill, Missile F, Ship 2 -------- 197
2.66 X-band relative signal strength, Blue Gill, Missile F, Ship 3 -------- 198
2.67 C-band relative signal strength, Blue Gill, Missile F, Ship 3 -------- 199
2.68 L-band relative signal strength, Blue Gill, Missile F, Ship 3 -------- 200
2.69 X-band relative signal strength, Blue Gill, Missile F, Ship 4 -------- 201
2.70 C-band relative signal strength, Blue Gill, Missile F, Ship 4 -------- 202
2.71 L-band relative signal strength, Blue Gill, Missile F, Ship 4 -------- 203
2.72 Interferometer and trajectory angular comparison, Blue Gill, Missile A, interferometer, least-squares combination---------- 204
2.73 Raw phase data at event, interferometer, Blue Gill, C-band --------- 205
2.74 Raw phase data and relative signal strength at event, Blue Gill, Missile A, interferometer, C-band---------- 206
2.75 Phase perturbation at event, Blue Gill, Missile A, interferometer, Leg AB ---------- 207
2.76 Phase perturbation at event, Blue Gill, Missile A, interferometer, Leg BC ---------- 207
2.77 Phase perturbation at event, Blue Gill, Missile A, interferometer, Leg AC ---------- 208
2.78 Phase perturbation at event, Blue Gill, Missile A, interferometer, Leg AD ---------- 208
2.79 Phase perturbation at event, Blue Gill, Missile A, interferometer, Leg BD ---------- 209

2.80 Phase perturbation at event, Blue Gill, Missile A, interferometer, Leg CD ---------- 209
2.81 Perturbation at event, Blue Gill, interferometer, least-squares combination ---------- 210
2.82 Ratio of mean perturbation to dispersion, azimuth plane, Blue Gill ---------- 211
2.83 Characteristic attenuation through the Blue Gill fireball ---------- 212
3.1 King Fish geometry, Project 6.1 ---------- 231
3.2 King Fish simulated trajectory, Missile C ---------- 232
3.3 X-band realtive signal strength, King Fish, Missile C, interferometer ---------- 233
3.4 C-band relative signal strength, King Fish, Missile C, interferometer ---------- 234
3.5 C-band relative signal strength envelopes, King Fish, Missile C, interferometer ---------- 235
3.6 L-band relative signal strength, King Fish, Missile C, interferometer ---------- 236
3.7 L-band relative signal strength envelopes, King Fish, Missile C, interferometer ---------- 237
3.8 X-band relative signal strength, King Fish, Missiles B and C, Ship 1 ---------- 238
3.9 C-band relative signal strength, King Fish, Missiles B and C, Ship 1 ---------- 239
3.10 L-band relative signal strength, King Fish, Missiles B and C, Ship 1 ---------- 240
3.11 X-band relative signal strength, King Fish, Missiles B and C, Ship 2 ---------- 241
3.12 C-band relative signal strength, King Fish, Missiles B and C, Ship 2 ---------- 242
3.13 L-band relative signal strength, King Fish, Missiles B and C, Ship 2 ---------- 243
3.14 X-band relative signal strength, King Fish, Missiles B and C, Ship 3 ---------- 244
3.15 C-band relative signal strength, King Fish, Missiles B and C, Ship 3 ---------- 245
3.16 L-band relative signal strength, King Fish, Missiles B and C, Ship 3 ---------- 246
3.17 X-band relative signal strength, King Fish, Missile B, Ship 4 ---------- 247
3.18 C-band relative signal strength, King Fish, Missile B, Ship 4 ---------- 248
3.19 L-band relative signal strength, King Fish, Missile B, Ship 4 ---------- 249
3.20 Fireball-ray-path parameters, King Fish, Missile B, Ship 1 ---------- 250
3.21 Fireball-ray-path parameters, King Fish, Missile B, Ship 2 ---------- 251
3.22 Fireball-ray-path parameters, King Fish, Missile B, Ship 3 ---------- 252
3.23 Fireball-ray-path parameters, King Fish, Missile B, Ship 4 ---------- 253
3.24 Raw phase data at event, interferometer, King Fish, C-band ---------- 254
3.25 Raw phase data and relative signal strength at event, King Fish, Missile C, interferometer, C-band ---------- 255
3.26 Phase perturbation at event, King Fish, Missile C, interferometer, Leg AB ---------- 256
3.27 Phase perturbation at event, King Fish, Missile C, interferometer, Leg BC ---------- 256
3.28 Phase perturbation at event, King Fish, Missile C, interferometer, Leg AC ---------- 257
3.29 Phase perturbation at event, King Fish, Missile C, interferometer, Leg AD ---------- 257
3.30 Phase perturbation at event, King Fish, Missile C, interferometer, Leg BD ---------- 258
3.31 Phase perturbation at event, King Fish, Missile C, interferometer, Leg CD ---------- 258
3.32 Refraction at event, King Fish, Interferometer Combination AB-AD ---------- 259
3.33 Refraction at event, King Fish, Interferometer Combination AB-BD ---------- 259
3.34 Refraction at event, King Fish, Interferometer Combination AB-BC ---------- 260

3.35 Refraction at event, King Fish, Interferometer Combination AB-AC ---- 260
3.36 Refraction at event, King Fish, Interferometer Combination AC-AD ---- 261
3.37 Refraction at event, King Fish, Interferometer Combination AC-BD ---- 261
3.38 Refraction at event, King Fish, Interferometer Combination AC-CD ---- 262
3.39 Refraction at event, King Fish, Interferometer Combination AD-BD ---- 262
3.40 Refraction at event, King Fish, Interferometer Combination AD-CD ---- 263
3.41 Refraction at event, King Fish, Interferometer Combination BD-CD ---- 263
3.42 Refraction at event, King Fish, Interferometer Combination BC-AC ---- 264
3.43 Refraction at event, King Fish, Interferometer Combination BC-AD ---- 264
3.44 Refraction at event, King Fish, Interferometer Combination BC-BD ---- 265
3.45 Refraction at event, King Fish, Interferometer Combination BC-CD ---- 265
3.46 Refraction at event, King Fish, interferometer, least-squares combination ---- 266
3.47 Ratio of mean perturbation to dispersion, King Fish, azimuth plane ---- 267
3.48 Apparent refraction, elevation and azimuth planes, King Fish ---- 268
4.1 Tight Rope geometry, Project 6.1 ---- 288
4.2 Tight Rope trajectory, Missile A, Cubic Corporation data ---- 289
4.3 Tight Rope trajectory, Missile C, Cubic Corporation data ---- 290
4.4 Relative signal strength, Tight Rope, Missile A, interferometer ---- 291
4.5 Fireball-ray-path parameters, Tight Rope, Missile A, interferometer ---- 292
4.6 X-band relative signal strength, Tight Rope, Missile A, interferometer ---- 293
4.7 X-band relative signal strength envelopes, Tight Rope, Missile A, interferometer ---- 294
4.8 C-band relative signal strength, Tight Rope, Missile A, interferometer ---- 295
4.9 C-band relative signal strength envelopes, Tight Rope, Missile A, interferometer ---- 296
4.10 L-band relative signal strength, Tight Rope, Missile A, interferometer ---- 297
4.11 L-band relative signal strength envelopes, Tight Rope, Missile A, interferometer ---- 298
4.12 Relative signal strength, Tight Rope, Missile A, Ship 1 ---- 299
4.13 Fireball-ray-path parameters, Tight Rope, Missile A, Ship 1 ---- 300
4.14 X-band relative signal strength, Tight Rope, Missile A, Ship 1 ---- 301
4.15 X-band relative signal strength envelopes, Missile A, Ship 1 ---- 302
4.16 C-band relative signal strength, Tight Rope, Missile A, Ship 1 ---- 303
4.17 C-band relative signal strength envelopes, Tight Rope, Missile A, Ship 1 ---- 304
4.18 L-band relative signal strength, Tight Rope, Missile A, Ship 1 ---- 305
4.19 L-band relative signal strength envelopes, Tight Rope, Missile A, Ship 1 ---- 306
4.20 X-band relative signal strength, Tight Rope, Missile C, Ship 2 ---- 307
4.21 C-band relative signal strength, Tight Rope, Missile C, Ship 2 ---- 308
4.22 Fireball-ray-path parameters, Tight Rope, Missile C, Ship 2 ---- 309
4.23 L-band relative signal strength, Tight Rope, Missile C, Ship 2 ---- 310
4.24 Relative signal strength, Tight Rope, Missile B, Ship 3 ---- 311
4.25 X-band relative signal strength, Tight Rope, Missile B, Ship 3 ---- 312
4.26 Computed power loss due to antenna-pointing errors, Tight Rope, Missile B, Ship 3 ---- 313
4.27 X-band relative signal strength with correction for antenna-pointing errors, Tight Rope, Missile B, Ship 3 ---- 314

4.28 C-band relative signal strength, Tight Rope, Missile B, Ship 3 ------ 315
4.29 C-band relative signal strength with correction for antenna-pointing errors, Tight Rope, Missile B, Ship 3---------- 316
4.30 L-band relative signal strength, Tight Rope, Missile B, Ship 3 ------ 317
4.31 L-band relative signal strength envelopes, Tight Rope, Missile B, Ship 3---------- 318
4.32 Fireball-ray-path parameters, boresight data, Tight Rope, Missile B, Ship 3---------- 319
4.33 Interferometer and trajectory angular comparison, Tight Rope, Missile A, interferometer, least-squares combination -------- 320
4.34 Raw phase data and relative signal strength at event, Tight Rope, Missile A, interferometer, C-band---------- 321
4.35 Phase perturbation at event, Tight Rope, Missile A, interferometer, Leg AB ---------- 322
4.36 Phase perturbation at event, Tight Rope, Missile A, interferometer, Leg BC ---------- 322
4.37 Phase perturbation at event, Tight Rope, Missile A, interferometer, Leg AC ---------- 323
4.38 Phase perturbation at event, Tight Rope, Missile A, interferometer, Leg AD ---------- 323
4.39 Phase perturbation at event, Tight Rope, Missile A, interferometer, Leg BD ---------- 324
4.40 Phase perturbation at event, Tight Rope, Missile A, interferometer, Leg CD ---------- 324
4.41 Refraction at event, Tight Rope, Interferometer Combination AC-AD -- 325
4.42 Refraction at event, Tight Rope, Interferometer Combination AC-BD -- 325
4.43 Refraction at event, Tight Rope, Interferometer Combination BC-BD -- 326
4.44 Refraction at event, Tight Rope, Interferometer Combination BC-CD -- 326
4.45 Refraction at event, Tight Rope, Interferometer Combination BC-AC -- 327
4.46 Refraction at event, Tight Rope, Interferometer Combination BC-AD -- 327
4.47 Refraction at event, Tight Rope, Interferometer Combination AB-AD -- 328
4.48 Refraction at event, Tight Rope, Interferometer Combination AB-BD -- 328
4.49 Refraction at event, Tight Rope, Interferometer Combination AB-BC -- 329
4.50 Refraction at event, Tight Rope, Interferometer Combination AB-AC -- 329
4.51 Refraction at event, Tight Rope, Interferometer Combination AD-CD -- 330
4.52 Refraction at event, Tight Rope, Interferometer Combination BD-CD -- 330
4.53 Refraction at event, Tight Rope, Interferometer Combination AC-CD -- 331
4.54 Refraction at event, Tight Rope, Interferometer Combination AD-BD -- 331
4.55 Refraction at event, Tight Rope, interferometer, least-squares combination---------- 332
4.56 Characteristic attenuation through the Tight Rope fireball ---------- 333

CHAPTER 1

INTRODUCTION

The Defense Atomic Support Agency conducted the Fish Bowl series of high altitude weapons effects tests in the summer and fall of 1962 at Johnstoh Island. The overall test series was known as Operation Dominic, under Joint Task Force 8. The purpose of the experiment carried out by Project 6.1 was to study the effects of high-altitude nuclear detonations on electromagnetic waves in the X-, C-, and L-band frequency regions. Project 6.1 participated in the Blue Gill, King Fish, and Tight Rope tests.

1.1 OBJECTIVES

A prime objective of the experiment was the quantitative measurement of the attenuation suffered by radar beams passing near or through the fireball of a nuclear detonation. During the test series, measurements were also made of effects produced in regions not directly associated with the fireball proper.

A second prime objective of the experiment was to investigate possible phase differences which were expected to develop in nearly parallel radar rays passing through ionized regions.

1.2 PHENOMENOLOGY

In a relatively few shakes (1 shake = 10^{-8} second) a combination of fission and fusion reactions convert mass into a tremendous amount of energy. Each megaton of weapon yield corresponds to a total energy of 10^{15} calories or 4×10^{22} ergs. Roughly 95 percent of this is released in less than one microsecond.

Most of the energy is immediately absorbed within the weapon itself. The extremely high particle and photon energies which are the outputs of individual fission and fusion nuclear reactions are successively degraded by interaction with other less energetic particles. Within a microsecond, the warhead material itself, and a small volume of surrounding air, reaches temperatures over 1,000,000° Kelvin About 70 percent of the weapon's energy is quickly radiated as X-rays (still within a microsecond), while some 25 percent is contained as kinetic energy of the debris particles. The X-rays are absorbed by the surrounding air, heating it to incandescence. The incandescent air further radiates softer X-rays and ultraviolet rays which are absorbed by a larger, surrounding shell of air, and so forth. This process (radiation diffusion) causes an overall cooling and growth of the heated region. Within a few milliseconds

a region is formed at about 10,000° Kelvin which then radiates less rapidly and principally in the visible and infrared part of the spectrum.

The debris, which contains about 25 percent of the yield as kinetic energy, expands rapidly. Most of this kinetic energy is soon manifested in the form of radial velocity from the burst point. It generates a strong shock wave in the surrounding air, so this air is also given a large radial velocity and is further heated.

The fireball is that region composed of the extremely hot air heated by the direct bomb X-rays and by the shock wave. Within this heated region the air is wholly dissociated into atomic oxygen and nitrogen and is almost completely ionized into electrons and positive ions. The initial size of this region depends on the yield of the weapon and the atmospheric density at the burst altitude. At the end of some tens of milliseconds (for bursts below about 100 km) the fireball size will be on the order of a few kilometers in diameter, at a temperature near 10,000° Kelvin. It now radiates without growing appreciably until the temperature reaches some 6000° Kelvin, which takes about one-half second. Significant hydrodynamic motion now begins to occur; the fireball will rise and expand. The growth and rise depend

greatly upon the burst altitude and the weapon yield. For altitudes below 80 to 90 km, the shape and motion within the disturbed region is largely governed by hydrodynamic action to form a toroidal shape. For bursts above this altitude, its shape eventually is elongated by the action of the earth's magnetic field.

The weapon debris and the surrounding air are ionized by all the energy forms produced by the burst. The following chart shows the energy distribution for a 50-percent fission, 50-percent fusion weapon.

Energy Distribution 50% fission-50% fusion	Percentage of Yield
Immediate (prompt)	
Gamma	0.02
Neutron	0.5
Thermal (X-ray)	≈ 70
Debris kinetic energy	≈ 25
Delayed	
Gamma	1.5
Beta	1.8
Neutron	$< 10^{-3}$

For altitudes below 100 km, the prompt ionization produced by X-rays and debris shock is essentially confined to the fireball proper. For altitudes below about 30 km, the penetrating distance of the gamma rays is small, and the ionization produced is confined to the debris region.

Above 30 km, the gammas can penetrate far from the debris, causing widespread ionization. The neutron-induced ionization is essentially negligible.

The delayed radiation is that emitted by the fission fragments in the debris and is of long-time duration. As before, gamma ionization is confined to the fireball for altitudes below about 30 km. Above this altitude the gammas produce a continuous region of ionization surrounding the fireball proper.

The delayed betas remain localized to the debris region until the debris is above about 50-km altitude. Above 50 km the penetrating distance of the betas becomes large, and the particles spiral along the magnetic field lines to which they are confined. As they strike the denser portions of the atmosphere they can create a spatially limited, but intense, region of ionization centered at about 70 km for high-altitude bursts. The spatial extent of this beta patch is equal to that of the debris region.

Within the fireball, thermal ionization continues until the temperature drops below about 3000° Kelvin.

Other sources of ionization are photodetachment produced by the presence of sunlight and photodetachment produced by thermal radiation from the fireball itself.

The amount of ionization produced by each of these sources, and its duration, is a function of weapon yield and performance characteristics, burst altitude, latitude, and time. The rate at which the ionization decreases is a function of the various reaction rates, attachment rates, recombination rates, collision frequencies, etc. These, in turn, depend upon the ionization density, local air density, temperature, composition, and other factors.

In general, the prompt ionization produced outside of the fireball disappears fairly rapidly. The fireball ionization due to thermal motion, X-rays, and debris kinetic energy decays rather slowly as the region rises, expands, and cools. The delayed radiation continuously produces ionization, but the ionization density decreases as the debris spreads in space.

The presence of ionization changes the propagation characteristics of the atmosphere to electromagnetic waves. This ionization can produce reflection, refraction, and absorption.

The radio-frequency absorption, or attenuation, due to a given electron concentration is approximately given from the Appleton-Hartree theory by the following equation:

$$\text{attenuation } \frac{\text{db}}{\text{km}} = \frac{4.62 \times 10^4 \, N_e \, \nu}{\omega^2 + \nu^2}$$

where

N_e = electron density in electrons/cm^3

ν = collision frequency in sec^{-1}

ω = radio signal frequency in cycles/sec

The collision frequency is a function of the atmospheric properties: temperature, density, composition, etc. Thus, the severity of attenuation along a propagation path depends upon the weapon yield and construction, the altitude, latitude, and time of burst, as well as the time after burst and the proximity of the propagation path to the burst. In addition, the propagation path is modified from that in the normal atmosphere by changes in the refraction index of the region, which are caused by the changes in temperature and in the magnitude and distribution of the electron density. The spatial distribution of the refractive index determines the propagation path. Because of the simultaneous influence of the multitude of parameters, large and rapid fluctuations in the electron density can occur, producing similar variations in the propagation path and in the attenuation.

Another phenomenon is that of reflection when the plasma frequency exceeds the signal frequency. The plasma frequency is given by:

$$\omega_p = 9 \times 10^3 \sqrt{N_e}$$

where

ω_p = plasma frequency in sec^{-1} (Reference 1)

1.3 GENERAL PROCEDURE

Since the effects associated with a radar beam vary with frequency, the effects on signals at three separate frequencies were studied during the experiment.

In this experiment the three frequencies were simultaneously transmitted from a beacon which was carried to high altitudes above the fireball by an unguided sounding rocket. In this manner, geometric lines of sight were achieved from the beacon through and near the fireball to receivers located at a fixed station on Johnston Island and on four mobile ship stations. Simultaneous measurements of the position of the missile and the fireball permitted the calculation of significant fireball ray-path parameters.

The effects that were measured included the variations induced by the fireball in amplitude and phase of the signals emitted by the in-flight transmitter.

1.3.1 Fixed Station Measurements. Two systems operated on Johnston Island. One system, which constituted the phase measurement array and which consisted of receiving stations located at calculated separations, was termed the interferometer station. The interferometer, operating in both L- and C-bands, was used for the study of phase and angle of arrival of signals.

L- and C-band receivers of the interferometer, together with a related X-band receiving station, provided measurements of amplitude variations.

1.3.2 Shipboard Measurements. Four shipboard stations were utilized during each event in the test series. Each ship was located in a theoretically optimum position to gain the maximum length of viewing time through regions of interest. This positioning was determined by the geometry of each shot in which the project participated. Each shipboard installation included three high-gain antenna systems mounted on a single pedestal. Receivers measured amplitude variations of CW signals received at each of the three frequencies (L-, C-, and X-bands) and provided tracking error signals and antenna pedestal pointing direction derived from the antenna system.

1.4 INSTRUMENTATION

A general description of Project 6.1 instrumentation is presented herein. A more detailed description of systems and equipment may be found in Reference 2.

1.4.1 Missileborne CW Signal Package. The CW signal package was designed for installation on Nike-Cajun and Nike-Apache sounding rockets. Figure 1.1 is a package installed on a Nike-Cajun and prepared for launching. The package consisted of two sections: (1) a three-frequency transmitter to provide the signal for attenuation and refraction measurements, and (2) a transponder which was used to track the missile in order to provide a trajectory.

Transmitter Package. The transmitter was a stable, crystal-controlled unit capable of generating three harmonically related CW signals. The signals were in the L-, C-, and X-band regions. Batteries supplied the primary power. A block diagram of the missileborne CW signal package is shown in Figure 1.2. A crystal-controlled VHF

oscillator was used as a stable first element for the system. This oscillator had an output of three watts at 105.5 Mc, which was fed to a varactor multiplier which, in turn, multiplied the frequency by nine to obtain an output of about 400 mw at approximately 1 Gc.

The 1-Gc signal was divided by a 6-db coupler. One part of the signal went to a circulator and voltage-tuned magnetron which supplied an L-band output of about five watts to the L-band antenna. The other part of the signal was fed into a varactor quintupler which supplied a C-band input signal to a traveling wave tube with a three- to five-watt output. This output was delivered to a combined C- and X-band antenna. The second harmonic of the C-band signal produced an X-band signal of one to two watts which was also radiated through the C-band and X-band antenna.

Environmental Characteristics. The approximate environmental conditions for which the missile package was designed are listed in Table 1.1.

Several radiation environmental tests were conducted on both individual components and the complete payload.

Electrical Characteristics. The transmitters were designed so that an inherent offset of approximately 0.05 Mc in L-band, 0.25 Mc in C-band, and 0.5 Mc in X-band existed between each adjacent transmitter manufactured. The packages were designed to meet the specifications given in Table 1.2.

Missile Package Antenna. Since the direction of the ground antennas, as viewed from the missile, were generally less than 30 degrees off-axis, the missile antenna gain was designed to be highest in this region. The missile antennas generated circularly symmetric radiation patterns to minimize variations in received signal strength caused by missile spin. CW signal package radiation patterns are presented in Figure 1.3.

Because the orientation of the missile, as viewed from the ground, changed constantly, the signal source antennas were linearly polarized, while the ground antennas were

circularly polarized to provide a more consistent signal level at the receivers.

The signal source antenna consisted of two separate concentric monopoles at the front of the missile nose cone. The L-band antenna was formed by electrically isolating the forward three inches of the nose and exciting it as a quarter-wave monopole on a cone.

The C- and X-band antenna was formed by isolating the extreme tip of the nose. This tip was essentially a wide band fat monopole which was used at both C- and X-band frequencies.

1.4.2 Cubic Corporation Missile Tracking Systems. Cubic Corporation was given the responsibility of providing all tracking data for the instrumented sounding rockets utilized by Project 6.1 during the Fish Bowl Series. A transponder and three types of ground tracking systems were employed by Cubic to obtain the required data. These systems are described in Appendix B.

1.4.3 Carrier Vehicles. The stringent requirements of each of these events for accurate beacon placement indicated clearly that the use of guided vehicles would have been optimum. However, the extremely short time frame in which Project 6.1 was planned and the excessive cost of such

carriers precluded their use. Therefore, sounding rockets with high-altitude capability were chosen. The sounding rockets chosen for use on Project 6.1 were Nike-Cajun and Nike-Apache rockets. It was felt that both types of rockets met the requirements for performance and reliability, the only difference between them being the higher altitude and longer flight time capability of the Nike-Apache rocket. A dimentional illustration of the Nike-Cajun rocket and payload is given in Figure 1.4. With the 6.1 payload, the Nike-Cajun had an altitude capability of about 120 km with a normal flight time of approximately 320 seconds. The Nike-Apache vehicle, which had the same physical configuration but utilized a different type of propellant, had an altitude capability with the 6.1 payload of about 150 km with a flight time of approximately 360 seconds for a sea level launch.

Both the Nike-Cajun and Nike-Apache utilized the same type of rocket launcher. The launcher provided rail guidance to the rocket for approximately 12 feet. The azimuth and elevation angles for the launcher were set by a remote control system operated from the Wind Computation and Ballistic Center. The remote control system is shown in Figure 1.5. Utilization of the remote control system

permitted final corrections indicated from upper wind data obtained as late as 30 minutes before firing time. The launchers were mechanically restricted to settings of 87-degree elevation, or less, to prevent a booster hazard to Johnston Island.

1.4.4 Fixed Station. The fixed station on Johnston Island was designed to receive signals in the L-, C-, and X-bands. The X-band signals were used to measure attenuation effects only. L- and C-band signals were used to measure attenuation and to study apparent refraction effects. The L- and C-band receiver systems together made up what was known as the interferometer station. A block diagram of the interferometer system is presented in Figure 1.6.

The interferometer station positioned on Johnston Island was designed primarily to investigate the extent of apparent refraction suffered by a set of microwave signals transmitted through the fireball of a nuclear event. The interferometer was also utilized as a quick-look facility to determine satisfactory transmitter operation of missiles immediately after launch.

The purpose for studying refraction and other phase front anomalies stems from the fact that the antenna gain and directional accuracy required in high performance radar

systems is dependent upon the stable, flat characteristics of such a phase front. In phased-array antenna systems, the relationship of antenna operation to phase-front geometry is of obvious importance, but even in the case of the common, paraboloic reflector, amplitude-sensing receiving systems degradation results from phase perturbations. A C-band target tracking radar imposes the most stringent angular requirements (0.1 milliradian), while an L-band acquisition radar with a large aperture (50 to 100 ft) requires phase flatness over large distances to achieve its rated characteristics. The dimensions and direction of the interferometer are shown in Figure 1.6.

The frequency, accuracy, and distance parameters for the interferometer configuration were chosen to provide data distinctly related to anti-missile missile radars. The main, or longer, axis of the interferometer was chosen to approximate the antenna aperture of an AICBM acquisition radar. The secondary axis was made one-quarter that of the main axis in order to provide a coarse measure of the phenomena under study and to facilitate the removal of ambiguities in the data. The distances from the antennas to the hub (i.e., the intersection of the two perpendicular axes) of the interferometer were chosen in a geometric progression. With this

configuration, data was recorded on all diagonal receiver combinations as well as axial combinations in order to provide necessary data for determination of possible wave-front curvature.

Fixed Station Antennas. Eight-by two-element helical arrays were utilized for each of the fixed station antennas. The four L-band antennas associated in the interferometer system were large, uncovered helical arrays, while the four C-band arrays were enclosed in boxes mounted on the Local Oscillator (LO) box behind each L-band array. The single X-band array in the system was enclosed in a smaller box to the right of the one of the C-band arrays. Table 1.3 lists the specifications of the fixed station antennas. Figure 1.7 illustrates one set of the three-frequency antennas. The complete four-element system array is presented in Figure 1.8.

The 3-db beamwidths were approximately six degrees in azimuth and about 35 degrees in elevation; therefore, with the center of the beam set at 65 degrees elevation, the

10-db beamwidth extended from below 40 degrees to above 90 degrees in elevation. The center of the beam was set at 65 degrees elevation for Blue Gill; 85 degrees for King Fish and Tightrope. The antennas were circularly polarized to optimize the gain for incoming signals of changing linear polarization. Antenna patterns for the fixed station antennas used in Project 6.1 experiments are presented in Figures 1.9 to 1.12. The X-band helical receiving elements used during Blue Gill were replaced by high-gain horn antennas for the King Fish and Tightrope events. X-band horn antenna patterns are given in Figures 1.13 and 1.14. This antenna was aligned on an 85-degree elevation angle with the E-plane vertical.

Fixed Station Receiving System. A block diagram of the fixed station receiving system is shown in Figure 1.15. The system consisted of three receiving systems operating in X-, C-, and L-bands, with their associated antennas and recording subsystems.

Except for the physical size of the antenna elements and the frequency of the LO's, the L- and C-band receiving systems were identical in all respects. The L-band receiving system utilized four antennas fed into separate, but identical, front-end units which were mounted on the antenna pedestals. These four front-end units were supplied by a common LO signal in order to maintain the phase relationship of the four received signals. Changing from one beacon frequency to another was accomplished by switching the output frequency of the first LO. The master R-391 receivers for both the L- and C-band interferometers were each equipped with a panoramic display. This facility displayed all beacon signals simultaneously at positions corresponding to their frequencies and amplitudes indicating their strength, and also provided a blinking-pulse marker which indicated the actual frequency to which the receivers were tuned. Figure 1.16 is a block diagram of master Receiver A for both the C- and L-band interferometer systems.

Automatic Frequency Control (AFC) was also provided in the master receiver by controlling the second LO of the R-391 subsystem through a Marker AFC unit. An output signal from the Marker AFC unit was also fed to the recording subsystem. Outputs

from both the second and third LO's were fed to the three slave receivers in order to maintain coherent phase relationships during the two mixing stages. A block diagram representing the slave Receivers B, C, and D for both interferometer systems is shown in Figure 1.17.

The IF output of the third mixer-amplifier stage (455 kc) was detected in the receiver and sent to the recording system for audio communication, while the AGC voltage was fed through an external cathode follower before reaching the recording system.

A fourth amplifier-mixer stage in the four modified R-391 receivers provided the 20-kc outputs to give six different phase measurements (i.e., AB, BC, DC, AC, BD, and AD). These outputs were filtered, integrated, and sent to the recording subsystem.

In X-band, a single antenna was used. The first mixer was fed by the first LO and the signal input from the antenna. The output of the mixer (30 Mc) was fed to the modified R-390A receiver. This receiver, known as the X-band monitor receiver, also utilized a Marker AFC unit to track the receiver frequency.

The X-band system operated in a manner very similar to that of the C- and L-band master receiver systems.

Automatic frequency control, AGC, and audio outputs were sent to the recording subsystem from the modified R-390A receiver. The panoramic display technique, discussed for the C- and L-band receivers, was also utilized in this system. However, since only one antenna was utilized in this system, no phase comparisons were made; therefore, the fourth mixer-amplifier stage with outputs at 20 kc was deleted from the circuitry.

Performance specifications for the Fixed Station Receiver System are given in Table 1.4.

Fixed Station Recording System. All data propagated by Project 6.1 experiments were recorded on magnetic tape in analog form. The recording device utilized was a half-inch, precision instrumentation recorder with four channels of direct-record electronics. Operating at a tape speed of 60 ips, the recorder had a frequency response that was flat from 100 cps to 120 kc.

Each channel of information to be recorded on magnetic tape was initially fed into a separate channel of a Signal Translation Unit (STU). The function of the STU was to adjust the maximum desired range of data fed to it and to translate that span of data as a dc voltage confined to a specific range, i.e., -2 volts to +2 volts. Thus, a desired recording range of AGC from -40 dbm to -125 dbm had its extremes translated as -2 volts and +2 volts, respectively.

The output of each channel of the STU provided a suitable input to a Voltage Controlled Oscillator (VCO). Each VCO generated a unique subcarrier frequency which was frequency modulated, within its bandwidth, by the adjusted dc level from the STU. Several VCO subcarrier outputs, each representing a separate data channel, were combined non-additively into a composite signal or multiplex.

Due to the considerable number of information channels required, four separate multiplexes were formed, each of which was recorded on a separate tape channel. The separation of multiplexes on magnetic tape allowed for the use of identical subcarrier VCOs contributing to separate multiplexes.

A calibrated stable reference frequency (100 kc) for playback tape-speed compensation was recorded on one of the tape channels together with the composite subcarrier signal. Voice commentary from the station's internal intercommunication system and ship-to-shore radio network was also recorded on separate channels.

1.4.5 Shipboard Stations. The purpose of using shipboard receiving systems was to take advantage of their mobility so that their positions could be adjusted to provide the most favorable geometry to yield the desired measurements. To insure that the desired observations would be made, four

identically equipped ships were dispersed in various configurations depending upon the geometry of each event. Generally speaking, each ship station was designed to: (1) acquire the missileborne beacon in location and frequency, (2) track the beacon into a position such that the ray-path passes near or through the fireball region, and (3) detect and record amplitude and arrival angle information.

Amplitude and arrival angle data were recorded for L-, C-, and X-band frequencies.

Figure 1.18 shows the tracking antenna mount and the equipment van on a typical shipboard station utilized during the experiment.

Shipboard Antennas. Due to the test geometry and the limits on transmitter power and frequency stability (which in turn set the minimum receiver bandwidth), three (C-, L-, and X-band) high-gain antennas were utilized. These antennas had narrow beamwidths which were controlled in azimuth and elevation to point toward the missile. The three antennas were mounted on a single pedestal with a common boresight.

All antennas were right-hand circularly polarized. The C- and X-band systems utilized 5- and 3-foot reflector dishes, respectively. Both employed a conical scanning

beam with a scan rate of 30 cps. Antenna half-power beamwidths were approximately 3 degrees for C-band and 2.5 degrees for X-band. The C- and X-band tracking antennas provided tracking gains to signals of linear polarization of approximately 29 db; C- and X-band antenna patterns for both vertical and horizontal signal polarization are presented in Figures 1.19 to 1.22.

The L-band tracker employed a sequential lobing technique. The antenna was a 16-element phased array of helices which formed four beams simultaneously. A solid-state lobing switch connected these beams alternately to the receiver to generate the angle scan. The lobing rate was 30 cps, and each lobe had a half-power beamwidth of approximately 13 degrees. L-band tracking antennas provided tracking gains to incoming signals of linear polarization of about 15 db. L-band antenna patterns are presented in Figures 1.23 and 1.24.

Shipboard antenna specifications are described in Table 1.5.

Tracking Control And Receiver Systems. The block diagram of the tracking receiver system is shown in Figure 1.25; system specifications are given in Table 1.6. Each of the antennas was fed into a front-end from which the

first generated IF was 30 Mc. This IF was fed to a 30-Mc splitter which provided a 30-Mc signal both to the R-390A receiver and to the panoramic display to indicate signal presence. Figure 1.26 shows the block diagram for the shipboard tracking receiver for all bands. The output of each R-390A was fed to an error signal amplifier. The output of the error signal amplifier was applied to the tracking mode selector, which selected the highest frequency channel in which there was a signal large enough to permit automatic tracking. If the signal which was being tracked faded, this selector automatically switched down to the next lower channel containing a trackable signal. Both the azimuth and elevation channels were provided with velocity memories to allow continual track during short signal fades in which all three signals dropped out.

The position of the antenna pedestal was controlled by the stabilization computer which took its information either from the vertical gyro and manual handwheels or from the tracking information derived from the tracking antennas and receivers. When the system tracked automatically, the output error signal which was selected for tracking was fed to the azimuth and elevation servo control which provided tracking control signals to the antenna

pedestal. A manual control with azimuth and elevation control handwheels was also provided. True azimuth and elevation outputs were sent to an azimuth-elevation plotter which indicated antenna pointing direction.

True azimuth and elevation outputs were also sent to the recording subsystem. Other outputs to the recording subsystem included signals from the time code generator, 30-cps error signals from all three frequencies with reference generator outputs, audio, and AGC voltages from all three frequencies, and the tracking mode of the system. The principal data outputs to the recording system are illustrated in Figure 1.25.

The 30-cps error signals recorded for each frequency were intended to provide angular deviation information from which any refractive effects, caused by the fireball, could be measured.

Figure 1.27 is a block diagram of the antenna control subsystem. A lobing switch control generator supplied a driving signal to the L-band lobing switch, and also provided signals to control the nutators for the C- and X-band antennas. A signal received by these antennas was modulated at a 30-cps rate by these nutating, or lobe switching, actions to provide an error signal proportional

to the direction from which the signal was received.

The error signal which was selected for tracking was fed through the phase detector to the azimuth and elevation servo amplifier control units. These units controlled the pedestal motion to null out the signal modulation that was caused by the nutator, or the lobing switch, thereby causing the antenna to track the signal. The stabilization computer provided stabilized outputs from the antenna pedestal when the manual control mode was used. Its input was derived from the vertical gyro and manual handwheel controls. The ship's compass and the compass data converter provided a true north reference. The manual controls provided analog voltages to the azimuth-elevation plotter and were used to follow preplotted information. The azimuth and elevation follow-up servos caused the manual handwheel controls to follow up the antenna motions during auto track.

Performance specifications for the antenna control system are described in Table 1.7.

Shipboard Recording System. The data recording system used within each shipboard tracking station was essentially identical to the system employed at the fixed station. It is described in Section 1.4.4.

Optical Instrumentation. Thirty-five-millimeter boresight cameras were mounted on the tracking pedestals of the shipboard stations. Photographs, ostensibly of the rocket position, were taken with a 14-degree viewing angle at a frame rate of 20/sec. A coded timing reference for the boresight data was additionally recorded.

Alignments of the boresight cameras with their respective tracking antennas were accomplished before the systems were shipped to the Dominic test site. Thereafter, no additional alignments were attempted, although the tracking equipment was dismantled several times before the start of the operational missions.

The precise relationships between available boresight film data and tracking antenna orientation are unknown.

1.4.6 Communication System. The four shipboard stations and the fixed station on Johnston Island were connected by a high-frequency communication network. Table 1.8 gives the communication system specifications.

The network was used to supply a countdown to all stations as well as to distribute operational instructions and transmit states of readiness.

1.5 CALIBRATION

1.5.1 Fixed Station, Preshot.

Receiver System. All receivers used in the system received a sensitivity check prior to operation. A Hewlett-Packard 608 signal generator was used as the signal level reference. All checks were performed at the input to the R-390A or R-391 receivers with the UHF front-end excluded from the circuitry. No signal reference in the microwave regions was available for calibration of the narrowband system utilized on this project. A receiver sensitivity log was maintained in order to determine the reliability of each unit and locate simple malfunctions before they became serious.

Recording System. Recording system standardization was accomplished at the STN so that all expected voltages modulating a VCO were restricted to lie between -2 and +2 volts. Upper and lower bandwidth limits of the VCO's were designed for ±2.5 volts so that an accommodation was left for inaccuracies in setup or definition of limits. Following are the data range limits which were restricted to lie between ±2 volts:

AGC:	-40 dbm to -125 dbm
AFC:	29.5 Mc ± 100 kc
Audio:	maximum line level with BFO and -60-dbm signal
Phase meter:	sawtooth output
Time code:	signal limits (square wave)

Intercommunication and command link voice channels were fed directly through audio filters into the lower frequency end of multiplex mixers. Levels were three volts peak-to-peak.

At the beginning of each tape, a calibration of each VCO was accomplished by providing standard voltages (-2, 0, +2 volts) in sequence to each VCO. A sweep voltage from -2.5 to +2.5 volts was also used momentarily.

1.5.2 Fixed Station, Postshot. Following the completion of a mission, calibrations of AGC and AFC outputs were performed and recorded.

For the AGC calibration, a Hewlett-Packard 608 signal generator was connected to the appropriate receiver, and both were tuned to 29.5 Mc. With the receiver AFC switch in the OFF position, the generator level was set initially at -40 dbm and was then decreased in discrete steps to -125 dbm. This procedure was performed for L- and C-bands utilizing the "A" receivers (R-391) and for X-band utilizing the monitor receiver (R-390A).

For the AFC calibration, the signal generator, set at -60 dbm, was initially tuned to 29.5 Mc. After the appropriate receiver was tuned to the generator frequency, the AFC switch was placed in the ON position. The receiver was then manually tuned, in discrete steps, from 100 kc above to 100 kc below the center frequency (29.5 Mc). The procedure was performed

for L- and C-band "A" receivers and the X-band monitor receiver. Each step of a calibration was concurrently identified on the intercommunication voice channel.

1.5.3 Mobile Stations, Preshot.

Receiver System. All receivers used in the system received a sensitivity check prior to operation. A Hewlett-Packard 608 signal generator was used as the signal level reference. All checks were performed at the input to the R-390A receiver with the UHF front-end excluded from the circuitry. No signal reference in the microwave regions was available for calibration of the narrowband system utilized on this project. A receiver sensitivity log was maintained in order to determine reliability of each unit and locate simple malfunctions before they became serious.

Recording System. Recording system standardization was accomplished at the signal translation unit so that most expected voltages modulating a VCO were restricted to lie between -2 and +2 volts. Upper and lower bandwidth limits of the VCO's were designed for ±2.5 volts so that an accommodation was left for inaccuracies in setup or definition of limits. Following are the data range limits which were restricted to lie between ±2 volts:

AGC: -40 dbm to -125 dbm

AFC: 29.5 Mc ± 100 kc

Audio:	maximum line level with BFO and -60-dbm signal
Azimuth:	predicted missile azimuth trajectory ±20 degrees
Elevation:	0 degrees (horizon) to 90 degrees
Tracking logic:	8-dc step functions
Time code:	signal limits (square wave)
30-cps error signals:	±2 degrees for L-band; ±1.25 degrees for C- and X-band
30-cps phase reference signals:	peak amplitudes for all bands

An elaborate procedure for the calibration of error signals, described in detail in Appendix C, was performed.

Intercommunication and command link voice channels were fed directly through audio filters into the lower frequency end of multiplex mixers. Levels were adjusted to three volts peak-to-peak.

At the beginning of each tape, a calibration of each VCO was accomplished by providing standard voltages (-2, 0, +2 volts) in sequence to each VCO. A sweep voltage from -2.5 to +2.5 volts was also used momentarily.

1.5.4 Mobile Stations, Postshot. Following the completion of a mission, calibrations of data outputs were performed and recorded. These included AGC, AFC, azimuth, elevation, and tracking logic.

For the AGC calibration, a Hewlett-Packard 608 signal generator was connected to the appropriate receiver and both were tuned to 29.5 Mc. With the receiver AFC switch in the OFF position, the generator level was set initially at -40 dbm and decreased in discrete steps to -125 dbm. This procedure was performed for each of the three (X-, C-, and L-band) receivers.

For the AFC calibration, the signal generator, set at -60 dbm, was initially tuned to 29.5 Mc. After the appropriate receiver was tuned to the generator frequency, the AFC switch was placed in the ON position. The receiver was then manually tuned, in discrete steps, from 100 kc above to 100 kc below the center frequency (29.5 Mc). The procedure was performed for each of the three frequency bands.

The azimuth calibration was performed by manually traversing the pedestal, in 5-degree steps, 20 degrees to each side of the sounding rocket flight azimuth.

The elevation calibration was performed by manually elevating the antennas from 0 to 90 degrees in elevation, in 10-degree steps.

The tracking logic calibration consisted of placing the antenna system in each of the following tracking modes in order that the outputs, each of which is a distinct dc level,

could be identified:

Manual track:

Manual + L-band gate

Manual + C-band gate

Manual + X-band gate

Velocity memory:

Auto track + L-band gate

Auto track + C-band gate

Auto track + X-band gate

Each step of a calibration was concurrently identified on the intercommunication voice channel.

1.5.5 Real-Time Commentary and Operators' Critique.

During the progress of each mission, equipment operators at all stations continually reported the current status pertaining to their part of the operation. Their remarks were recorded in real time on the intercommunication voice channel.

Immediately following a mission, with the instrumentation recorders set at 7.5 inches per second, the crew chief of each station related his overall observations of the test. Following this, each equipment operator, in turn, commented on his observations during the mission, noting any unusual incidents that had occurred.

1.6 INSTRUMENTATION LIMITATIONS

Many anomalies have been introduced into the data from sources not directly associated with the event phenomena. Although some problems were caused by operational errors, most anomalies were generated by inherent limitations in equipment.

Major instrumentation limitations are described below.

1.6.1 Missile Beacon Performance. One serious design deficiency was the omission of any means to provide a clear-path monitor of beacon signal levels at all times. Reports of clear-path operators observing panoramic displays are available to indicate only operation or non-operation of the beacons. Consequently, at times when blackout was purported to be caused by fireball attenuation or absorption, it is not certain that missile transmitters were actually functioning at the same level as before the event.

Relative signal strength data, which is affected by missile-beacon radiation patterns presented to receiving elements, is a function of missile attitude. Certain characteristics in the behavior of the sounding rockets employed in Dominic experiments are significantly reflected in most signal strength data. A significant signal deterioration, commonly noted for all missile flights, commenced

between 70 and 90 seconds prior to splash. At this time the vehicle is at an altitude at which it begins maneuvers peculiar to its atmospheric re-entry. The attitude of the missile is drastically altered during this early traverse through the increasingly denser medium. Missile fin stabilization takes effect, and the projectile, which was canted upward during its free-flight stage, undergoes a rotational reorientation; the nose cone is rotated downward until its pointing direction coincides with that of overall missile motion. During this change from its free-flight attitude, the radiating pattern of the missile's transmitting antenna, as seen by the receiving stations, is gradually altered (Figure 1.3, CW Signal Package Radiation Patterns). The presentation to the receiving antennas of the least efficient portion of the transmitted pattern is reflected as a decrease in relative signal power. The extent of this effect depends upon the frequency under consideration. The somewhat superior X-band antenna pattern display at this time accounts for the less perturbed signals in that frequency band. Immediately prior to splash, look angles permit the viewing of a more efficient portion of the antenna pattern. Hence, a brief rally of signal levels is noted for this late period by the shipboard stations.

During the first half of missile flight, the rear portion of the CW beacon antenna pattern is exposed to receiving elements. This most efficient presentation is reflected in generally stronger detected signals. An exception to this generalization is the very deep notch in the antenna pattern directly to the rear of the rocket. The effect of this notch, coupled with the coning motion of the missile, affected signal levels appearing in interferometer data soon after rocket launch. It also appeared in shipboard station data when the ship was located very close to the island.

As no information is available to define missile attitude accurately at any discrete time, the transmitting antenna radiation pattern presented to any of the several tracking stations could, at best, be estimated for the purpose of explaining some signal strength phenomena.

1.6.2 Receiving System. The automatic frequency control (AFC) was responsible for the questionable character of a considerable volume of data. Design and alignment faults were such that a rapid decrease in signal level resulted in an effective open circuit condition which generally produced an AFC shift. Lack of status information makes it impossible to determine whether or not the AFC was being utilized during certain periods or whether it was disabled. In some cases

when the AFC readout varied, there is no certainty that changes may not have been caused by manual operation of the tuning control.

When an open circuit condition existed, a suitable input was denied to the interferometer phasemeters, and portions of data recorded during such periods must be discounted.

Recorded tones from the beat-frequency oscillators (BFO) did not provide any information on the signal status during periods of blackout other than that indicated in AGC data. It was anticipated that recorded BFO data, reproduced through a sensitive tracking filter, would provide a means of recovering signals from below the system noise level. Unfortunately, AFC tuning problems brought about random frequency variations in the range in which the BFO operated and, in turn, caused the data provided by the BFO to be an unreliable indicator in most instances.

1.6.3 Tracking Logic. The tracking logic system (Section 1.4.5) selected the frequency mode by which the system tracked a missile beacon. Ideally, this selection would be accomplished automatically and would be dependent upon the availability of acquirable signal frequencies. However, a station operator had the option of bypassing the logic and retaining a particular

tracking mode by manually placing an override on the system. Unfortunately, tracking logic analog data does not distinguish between automatic or manual override selection. This leads to some uncertainties concerning system tracking capabilities during signal recovery periods.

1.6.4 Recording Bandwidths. As a result of multiplexing, most recorded data was necessarily bandwidth limited. The most serious limitation was placed on interferometer phase data, the channels of which employed low pass filters ranging from 110 to 1050 cps. The filter used for each phase information channel is listed in Table 1.9.

1.6.5 Phasemeter Characteristics. The recorded phasemeter outputs consisted of dc voltages that varied proportionally with the phase difference. The resulting output was in the form of a sawtooth with the rapid passage from 360 degrees maximum reading to zero degrees minimum (see Figure 1.28). As may be noted in the raw data samples shown in the text, the trigger from maximum to minimum was very often oscillatory and possibly introduced errors in the data reduction processes. It has been determined empirically, from pre-event and test firing data, that noise will exist in interferometer phase data if the signal level does not exceed the system noise level by 20 db. As the signal-to-noise ratio decreases, the

phasemeter outputs become random for signal levels as high as 8-12 db above noise. Phasemeter information recorded during such periods is highly suspect and requires careful evaluation.

1.7 DATA INTERPRETATION

1.7.1 Attenuation. The relative signal strength presentations are derived from AGC data. Since this data was manually enveloped on chart records before reading, these records represent envelope readings only. The only exception to the enveloping procedure is the expanded data which is presented for times less than one second. If only one envelope is presented, it is the maximum.

Corrections have been introduced to AGC data to negate the effects of variations in free-space attenuation. Slant range corrections are derived by use of the expression:

$$(\text{AGC} - \text{noise level}) + 20 \log \frac{D}{R}$$

where D = slant range

and R = distance to a reference point from which corrections are made.

The scaling employed to designate signal levels is strictly relative and is used as a convenience for ascertaining changes and making comparisons within a particular plot. It is not possible to read absolute signal levels from these charts.

The times utilized on all associated graphs and trajectory plots are referenced to event time (H = 0). Portions of data in some presentations have been plotted as questionable because of correlating data or circumstances.

Figure 1.29, a typical AGC calibration graph from Blue Gill event, depicts other reduction techniques applied to the AGC data. Definition of the noise level was an evaluation process, since the signal level calibrations were performed on the R-390A and R-391 receivers only and did not include the front end of the receiving system. Five significant portions of the data were examined for each station in order to resolve the noise level; the recorded level of each is presented in Figure 1.29. The "pre-event" noise level is a sample of data acquired just prior to the acquisition of Missile C (H-112). "Event noise" refers to recorded levels during the blackout period following event. Data levels recorded immediately after the splash (impact) of Missiles C, E, and F are also illustrated. Note the discrepancies among the five references. From these, a weighted level was selected which appeared to be the most representative of the unperturbed samples.

The lengthy duration of the Blue Gill operation made it necessary for each station to record data on two magnetic tapes. At the conclusion of the mission, identical calibration

procedures were performed for each tape. The points plotted in Figure 1.29 represent the discrete levels of the step calibrations from each tape. Since the two curves are not the same, it was necessary to select the best curve or the best fit to both curves. This fit was extended linearly to the selected noise level in order to dispense with nonlinearities in AGC calibrations at levels approaching noise. The effect of this procedure was to desensitize readings near noise level, where the data reading process became somewhat arbitrary at times. Values for signal level changes which have one point at noise level are now conservative figures, but, by the same token, the possibility of small reading errors producing gross value errors have virtually been eliminated. Due to nonlinearities and inconsistencies in recorded AGC calibrations, the establishment of noise level is uncertain to within ±2 db. Signals within 2 db of established noise level are recorded as noise in signal strength records.

1.7.2 Refraction. Two systems were employed to collect data for the determination of refraction. Their electrical and environmental characteristics are given in Sections 1.4.4 and 1.4.5. The prime system, located on Johnston Island, consisted of a fixed-oriented interferometer that operated at C- and L-band frequencies. In this system, comparisons

between combinations of receivers measured the phase differences of an incident plane wave at all combinations of two antennas. The intent was to determine apparent refraction as a function of arrival angles.

The other refraction measurement technique involved the collection of X-, C-, and L-band tracking error data generated at the shipboard stations and essential to the operation of the tracking control system. These measurements were intended to provide values of relative apparent refraction as a function of frequency.

Apparent refraction is defined as the angle formed between a straight-line path to the missile beacon and the actual direction of arrival of the transmitted signal (Figure 1.30). The measured angle, ψ, represents the apparent angular refraction referred to in discussions and graphical illustrations of refraction in this report. The actual angle of refraction, θ, may be calculated from the apparent refraction, ψ, and a knowledge of beacon, receiver, and fireball positions, if assumptions are made as to where the refraction occurred with respect to the fireball. It should be noted, however, that the relationship between apparent and absolute refraction angles is not constant. If the missile beacon is moved from Position 1 to Position 2 (Figure 1.30), the absolute refraction, θ, may remain unchanged even though the apparent refraction is increased to δ.

TABLE 1.1 MISSILE PACKAGE ENVIRONMENTAL CHARACTERISTICS

Maximum loading	70 g
Ambient temperature, before firing	120°F
Skin temperature of nose cone	750°F
Nose cone tip temperature	1200°F
Vibration estimate	10 g at 20 to 2000 cps
Shock	120 g for 4 milliseconds
Neutron radiation of individual components	2×10^{11} neutrons/cm^2
Gamma radiation of entire missile package	50 rads, integrated dose

TABLE 1.2 ELECTRICAL AND MECHANICAL SPECIFICATIONS OF THE CW SIGNAL PACKAGE

	L-Band	C-Band	X-Band	Units
Frequency stability	5	5	5	PPM
Frequency settability	20	20	20	PPM
Power	5	3 to 5	1 to 2	watts
Antenna polarization	Linear	Linear	Linear	
Antenna gain[a]	0	0	0	db minimum
VSWR	2:1	2:1	2:1	maximum
Roll eccentricity[a]	3	3	3	db

Payload weight	95 pounds
Payload length	73 inches-including transponder electronics
Dynamic balance	40 inch^2-ounce maximum unbalance
Temperature	150°F for 10 minutes of uncooled operation

[a] 5 to 30 degrees from tail.

TABLE 1.3 FIXED STATION ANTENNA SPECIFICATIONS

Azimuth beamwidth, 3 db	6 degrees ± 1 degree
Elevation beamwidth, 10 db	55 degrees ± 5 degrees
Nose gain for circularly polarized signal	20 db ± 2 db
Nose gain for linearly polarized signal	14 db ± 1 db
Survey of relative position[a]	± 1/8 inch[b]

[a] L- and C-band only.
[b] Vertical and horizontal.

TABLE 1.4 FIXED STATION RECEIVER SYSTEM SPECIFICATIONS

	L-Band	C-Band	X-Band
System NF	8 db ± 1 db	9 db ± 1 db	10 db ± 1 db
Receiver BW, nominal	8 kc or 16 kc	8 kc or 16 kc	8 kc or 16 kc
AFC range	± 100 kc	± 100 kc	± 100 kc
AFC time constant, minimum	0.5 sec	0.5 sec	0.5 sec
Total AGC range	80 db	80 db	80 db
AGC 3-db response, minimum	100 cps	100 cps	100 cps
Pan display coverage	300 kc	1.5 Mc	3 Mc
Maximum auto tuning time	20 sec	20 sec	20 sec
Manual electronic tuning range	+ 100 kc	+100 kc	+ 100 kc

TABLE 1.5 SHIPBOARD ANTENNA SPECIFICATIONS

	L-Band	C-Band	X-Band
Beamwidth, 3 db	$13^{\circ} \pm 2^{\circ}$	$3.0^{\circ} \pm 0.5^{\circ}$	$2.5^{\circ} \pm 0.5^{\circ}$
Gain	22 db ± 2 db	35 db ± 1 db	35 db ± 1 db
Polarization	right circ	right circ	right circ
Tracking technique	lobing	conical scan	conical scan
Tracking crossover	-5 db ± 1 db	-3 db ± 1/2 db	-3 db ± 1/2 db
VSWR	2:1 max	1.5:1 max	1.5:1 max

TABLE 1.6 SHIPBOARD RECEIVER SYSTEM SPECIFICATIONS

	L-Band	C-Band	X-Band
System NF	8 db ± 1 db	9 db ± 1 db	10 db ± 1 db
Receiver BW, nominal	8 kc or 16 kc	8 kc or 16 kc	8 kc or 16 kc
AFC range	± 100 kc	± 100 kc	± 100 kc
AFC time constant, maximum	0.5 sec	0.5 sec	0.5 sec
AGC range, total	80 db	80 db	80 db
AGC 3-db response, minimum	100 cps	100 cps	100 cps
Pan display coverage	300 kc	1.5 Mc	3 Mc

TABLE 1.7 ANTENNA CONTROL SYSTEM SPECIFICATIONS

The values are computed for an elevation angle of 60 degrees or less and average seas.

	L-Band	C-Band	X-Band
Tracking accuracy, RMS	± 1.5 degrees	± 0.5 degrees	± 0.5 degrees
Pointing accuracy	± 1.5 degrees	± 1.5 degrees	± 1.5 degrees
Detectable pointing deviation	0.10 degree	0.05 degree	0.05 degree
Maximum slew rates	25 deg/sec	25 deg/sec	25 deg/sec
Maximum roll, retaining track	± 9 degrees	± 9 degrees	± 9 degrees
Maximum pitch, retaining track	± 3.5 degrees	± 3.5 degrees	± 3.5 degrees

TABLE 1.8 COMMUNICATION SYSTEM SPECIFICATIONS

Call signal	April Weather
Modulation	AM voice
Power	250 watts
Equipment	BC 610/R390
Frequencies	2.5 to 6 Mc
Number of stations	5

TABLE 1.9 LOW-PASS FILTERING OF PHASE DATA

Low-Pass Filter, cps	C-band	L-band
110		AC
160		AB, BC
220		AD, CD
330	AC	BD
450	AB, BC	
600	AD	
790	CD	
1050	BD	

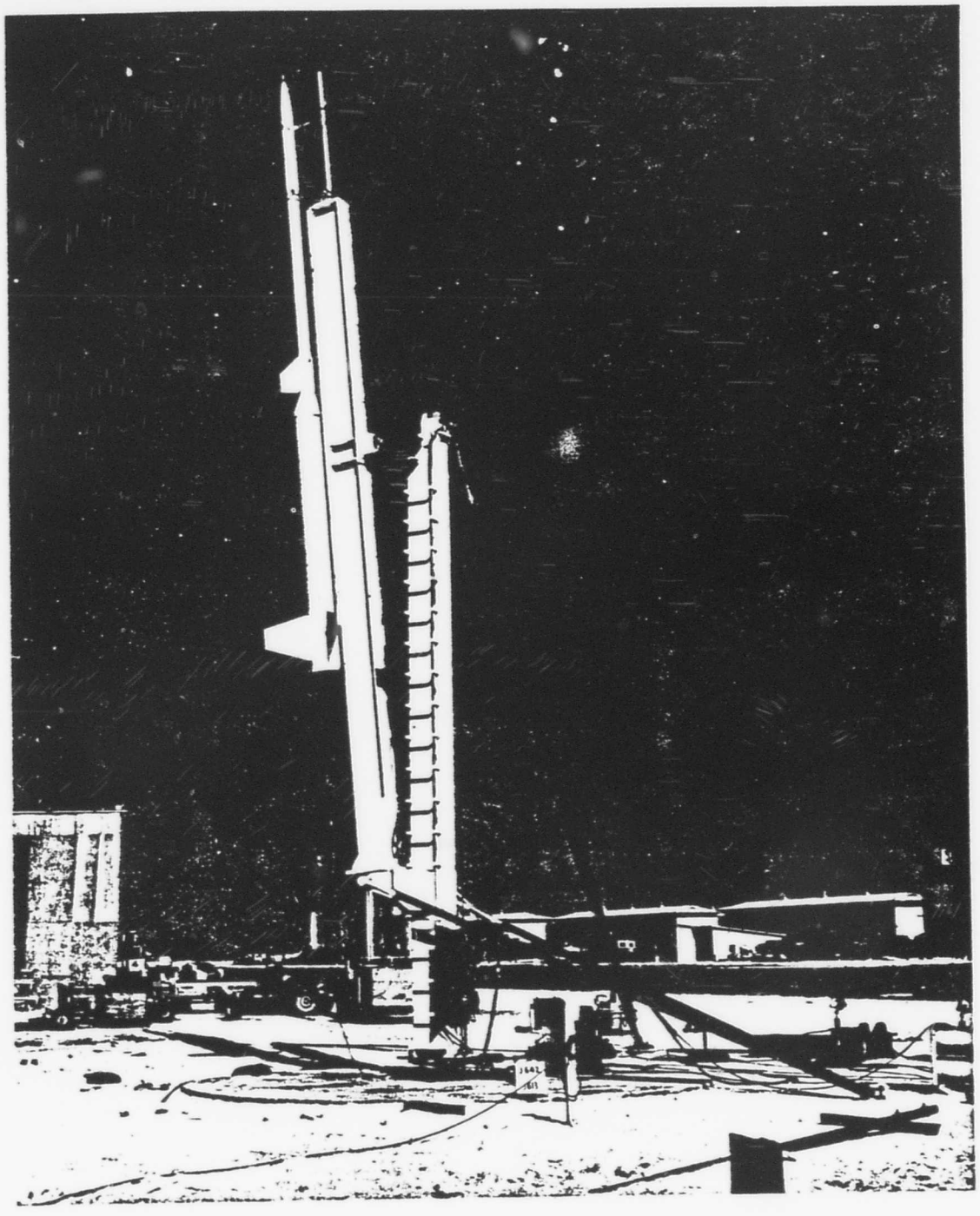

Figure 1.1 Nike-Cajun prepared for launching.

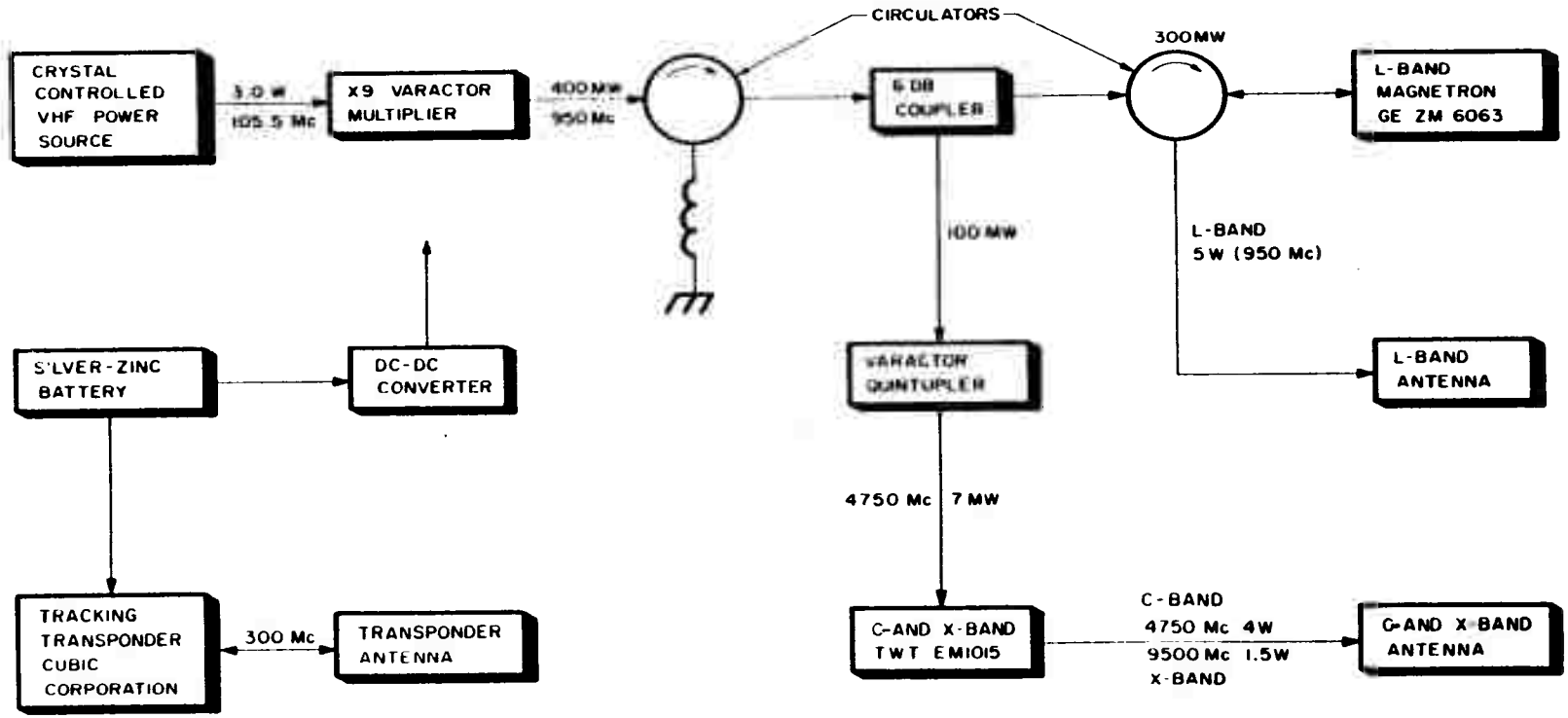

Figure 1.2 Missileborne CW signal package.

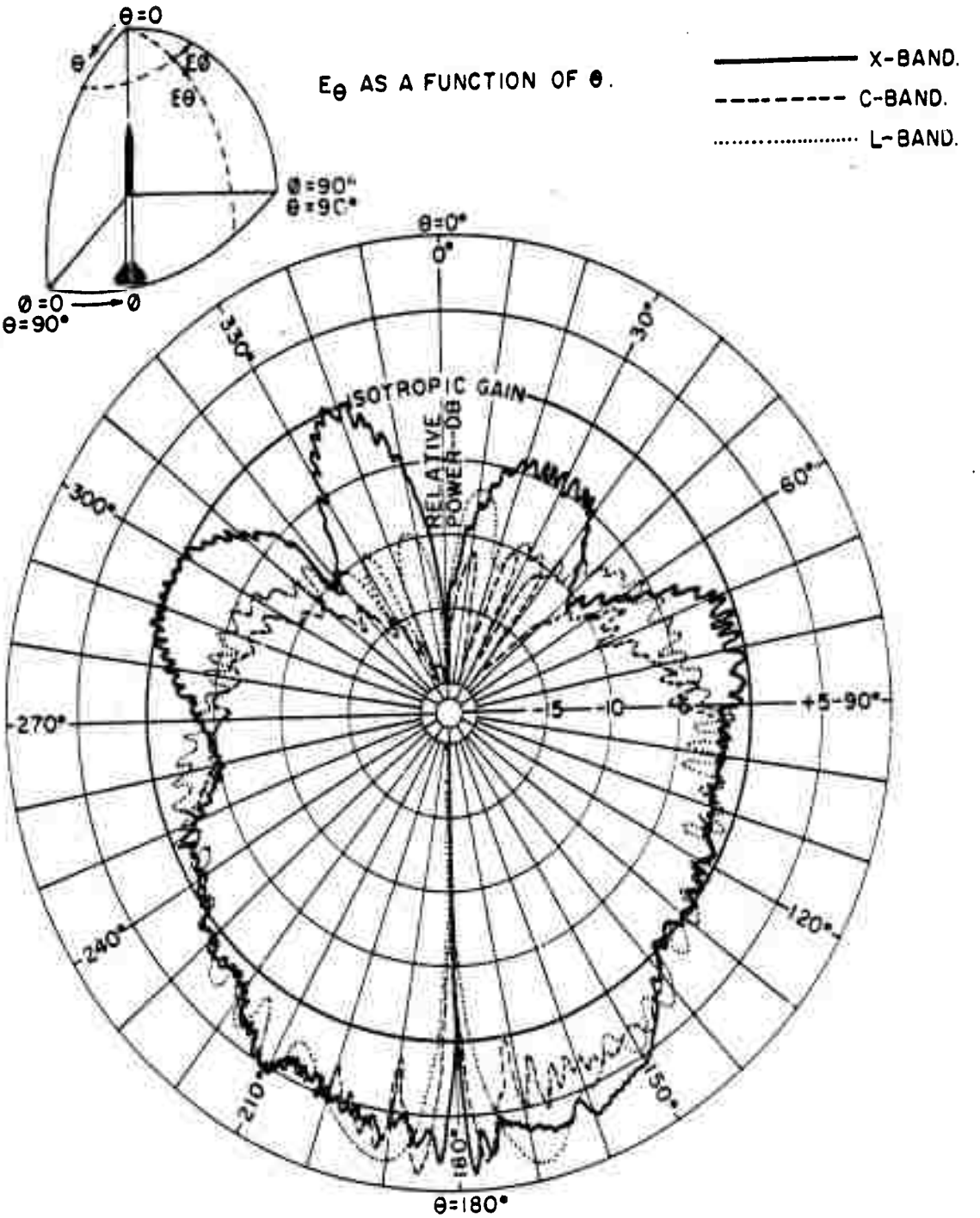

Figure 1.3 CW signal package radiation patterns.

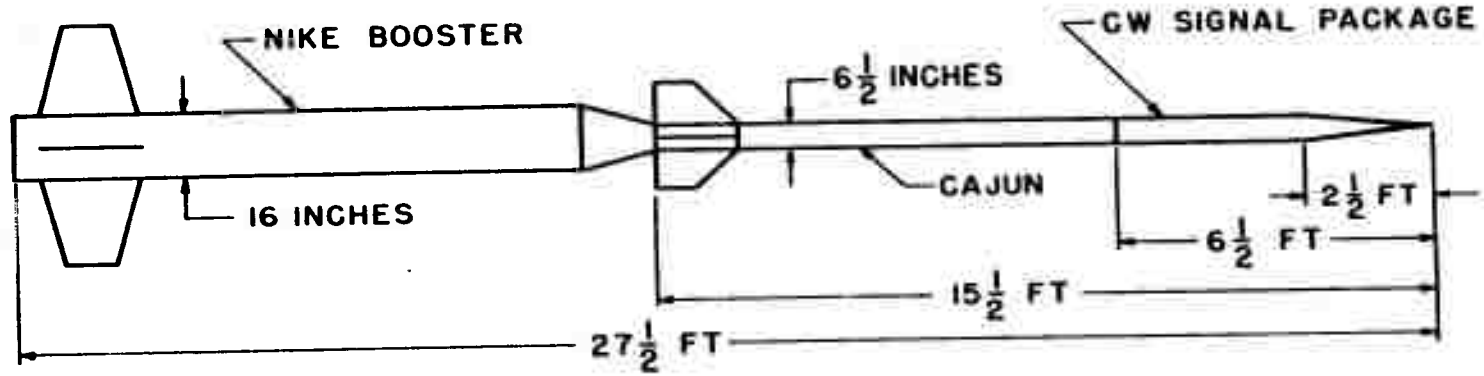

Figure 1.4 Nike-Cajun rocket and payload.

Figure 1.5 Missile launcher remote control.

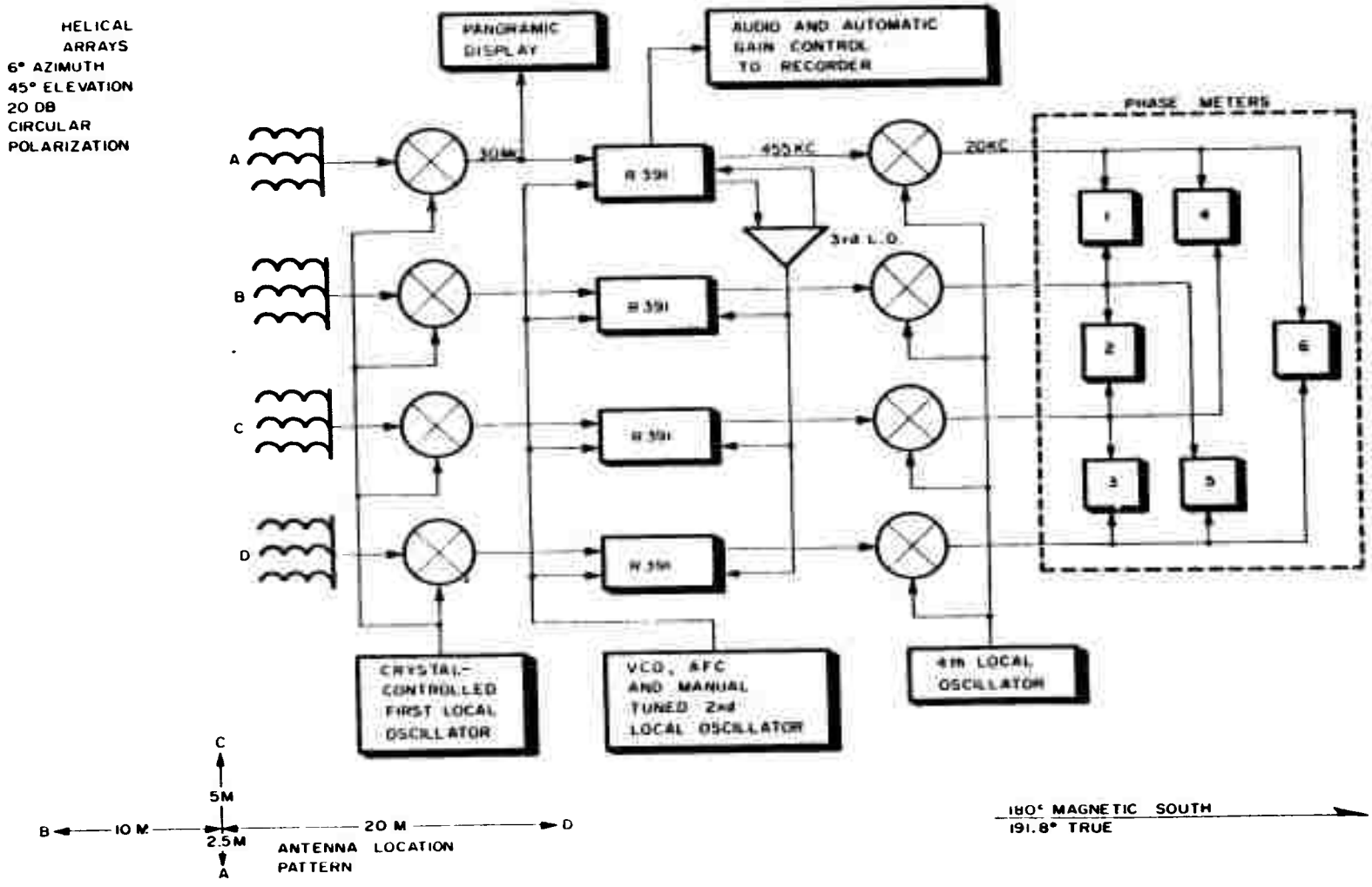

Figure 1.6 Basic interferometer system.

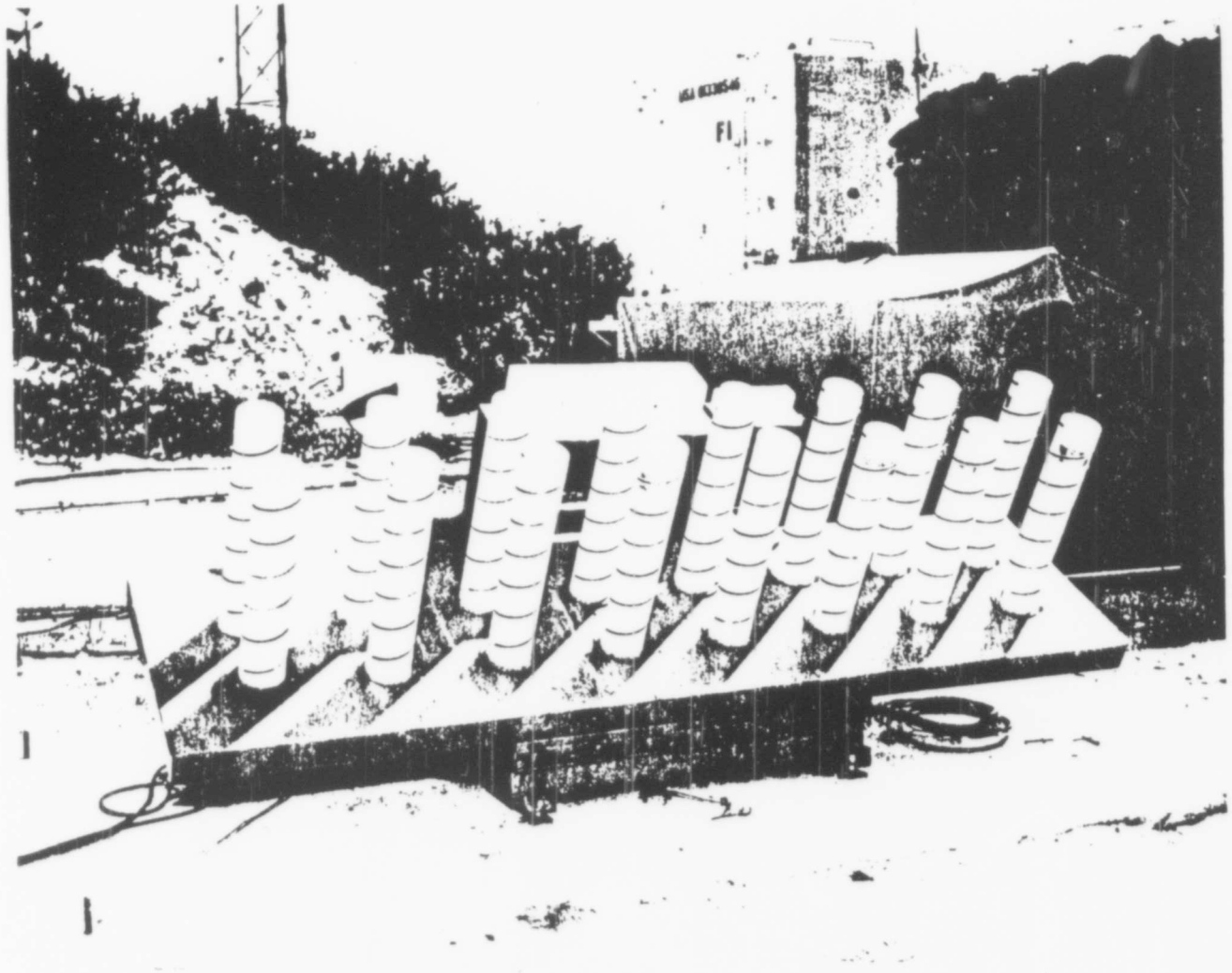

Figure 1.7 X-, C-, and L-band interferometer antennas.

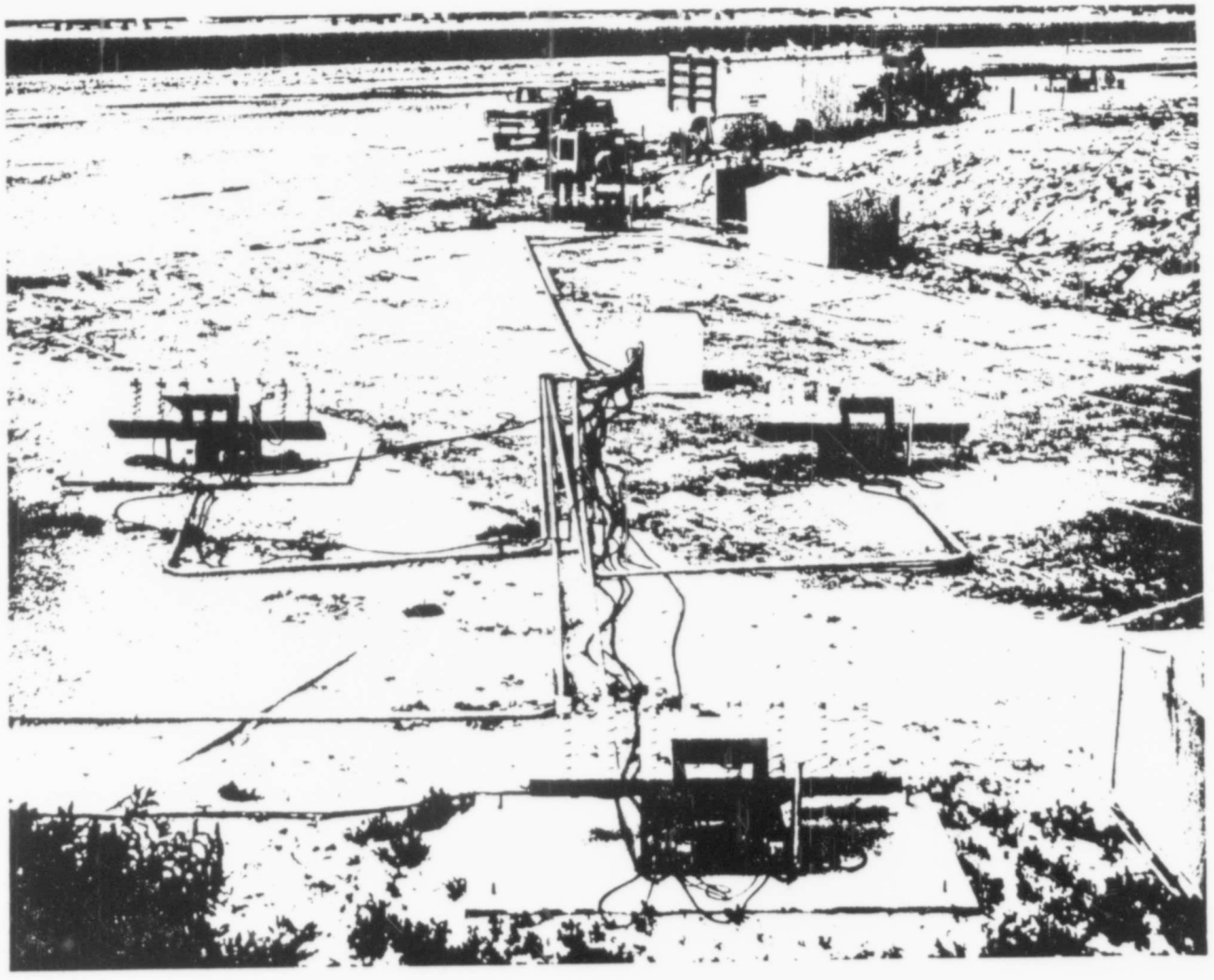

Figure 1.8 Fixed station antenna array.

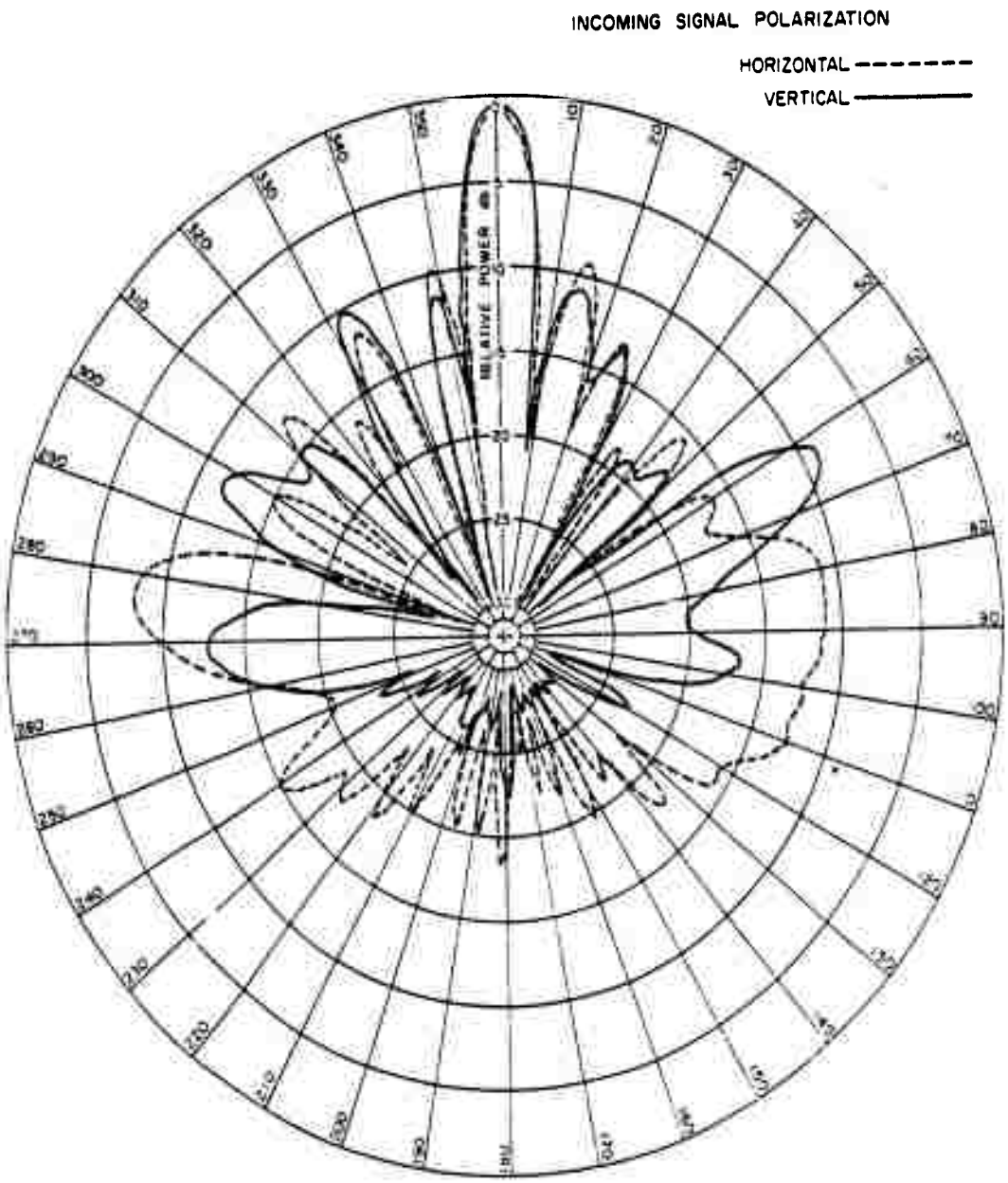

Figure 1.9 X-band interferometer azimuth antenna patterns.

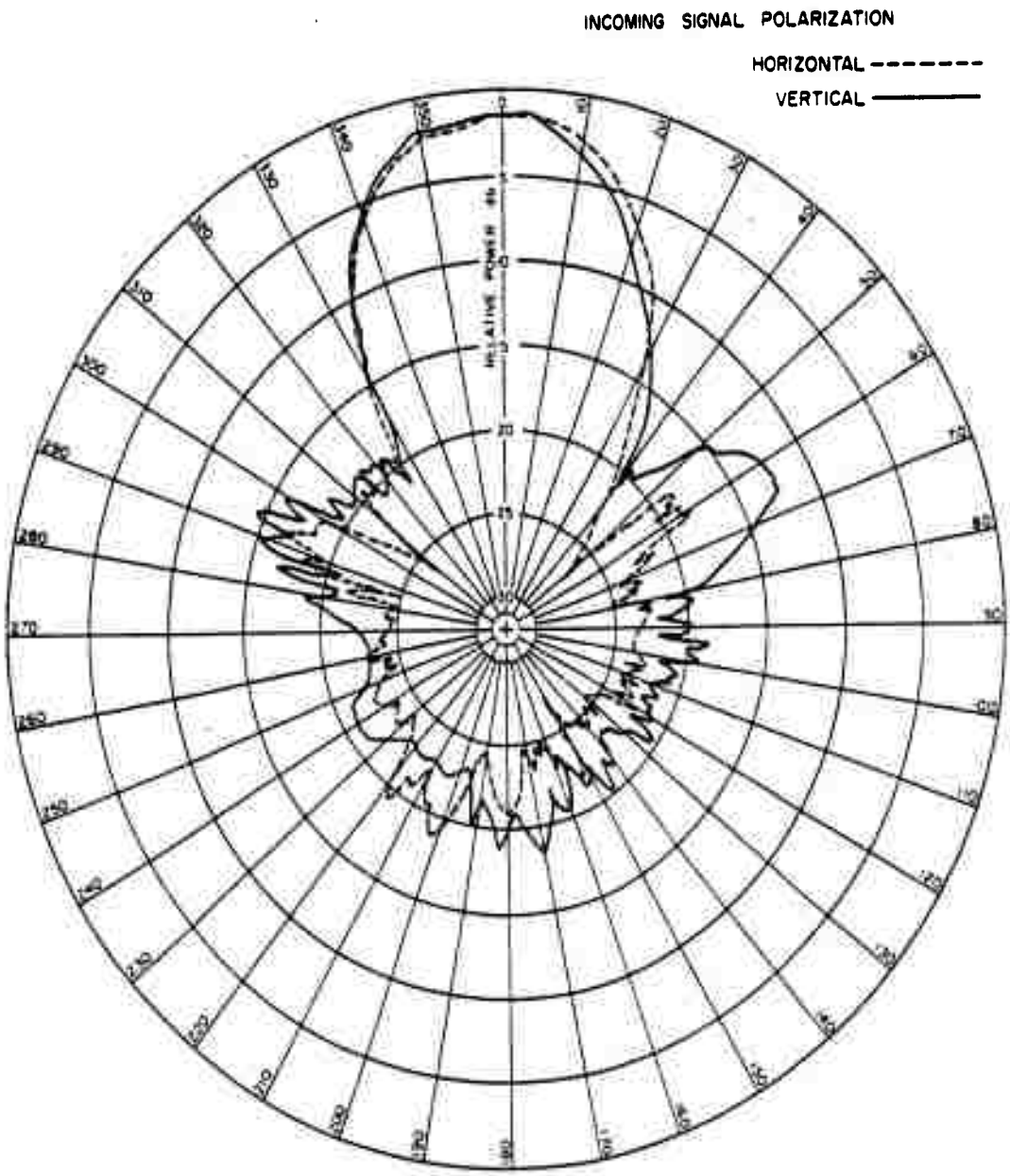

Figure 1.10 X-band interferometer elevation antenna patterns.

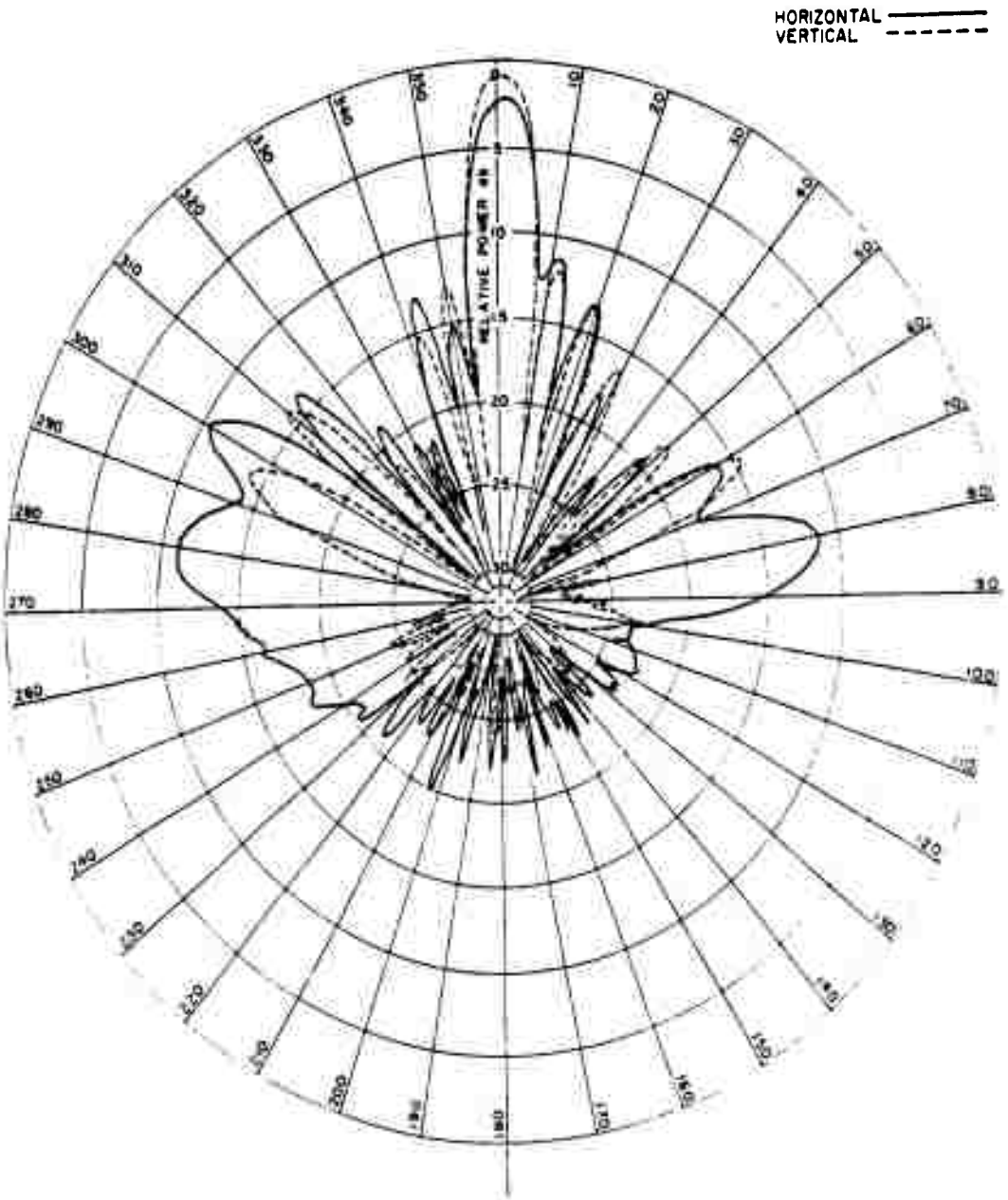

Figure 1.11 C- and L-band interferometer azimuth antenna patterns.

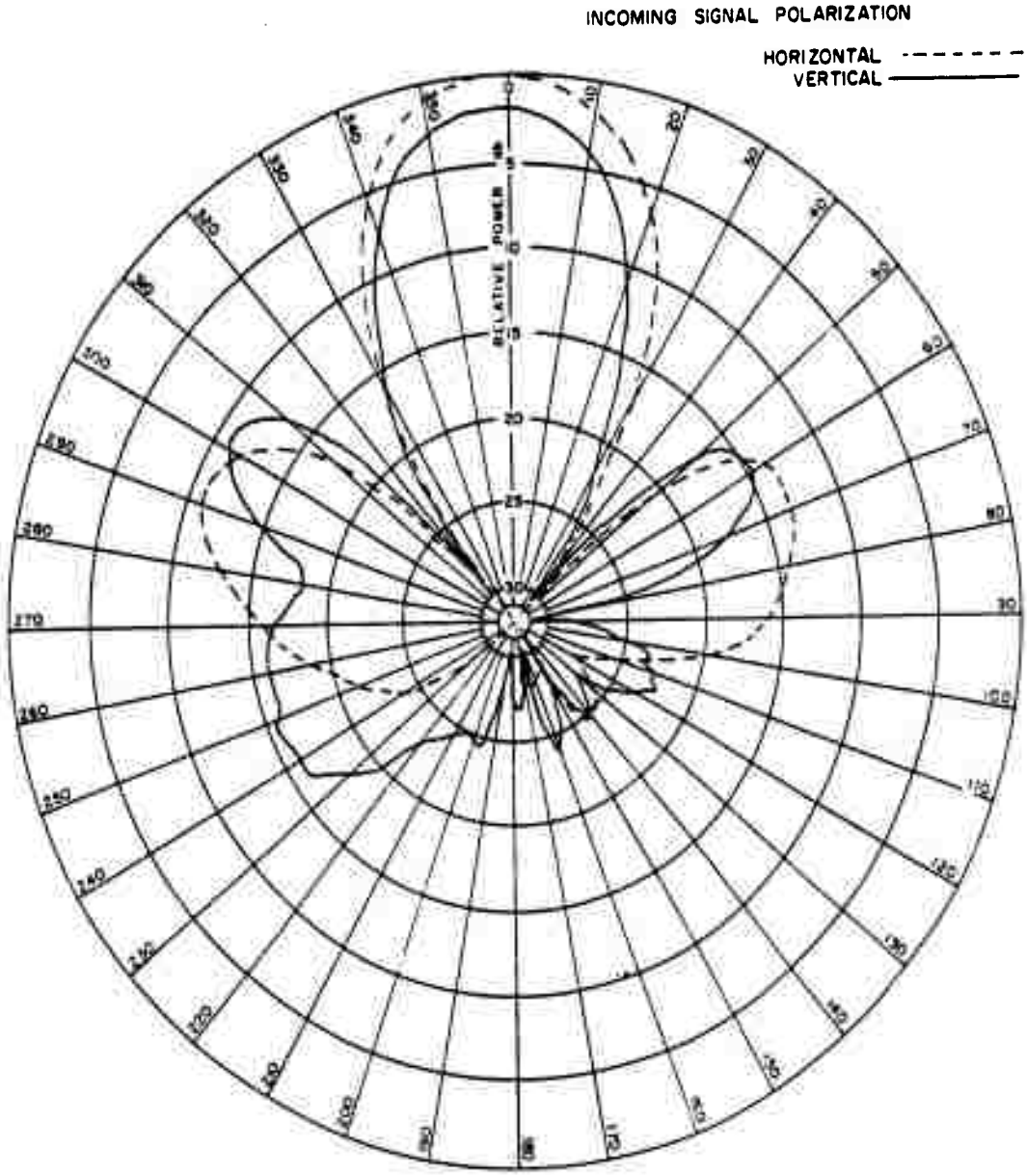

Figure 1.12 C- and L-band interferometer elevation antenna patterns.

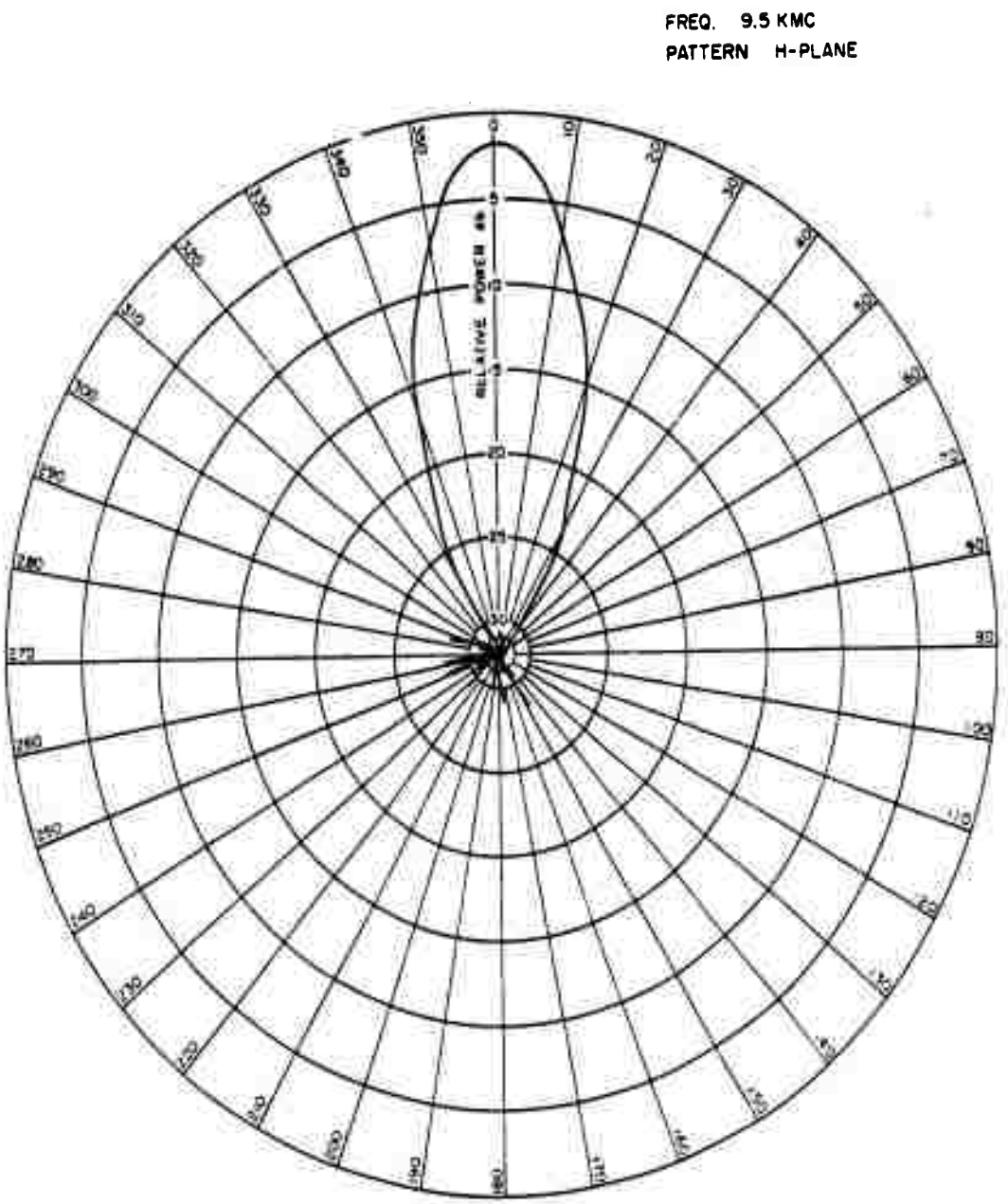

Figure 1.13 X-band interferometer horn antenna pattern, H-plane.

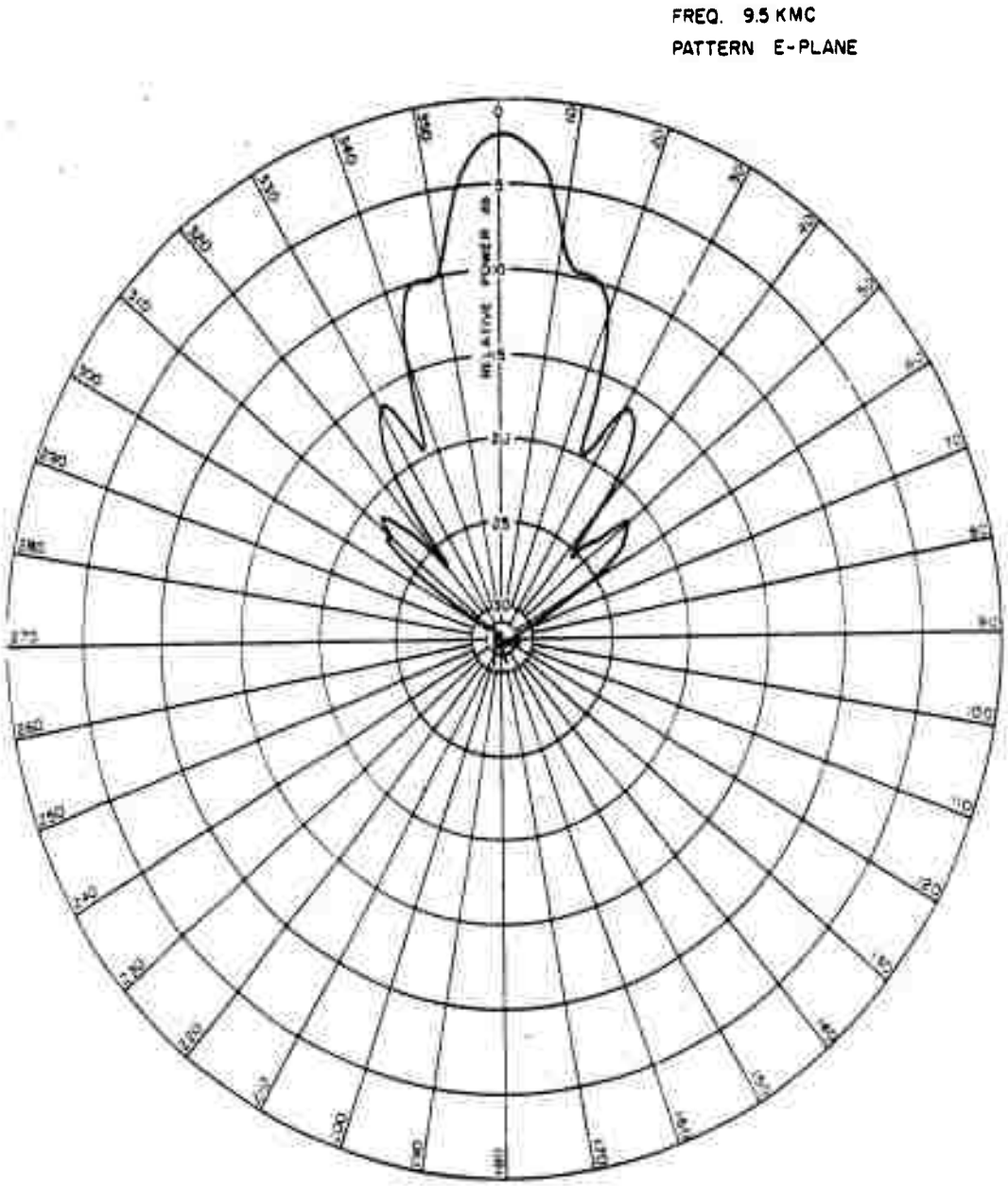

Figure 1.14 X-band interferometer horn antenna pattern, E-plane.

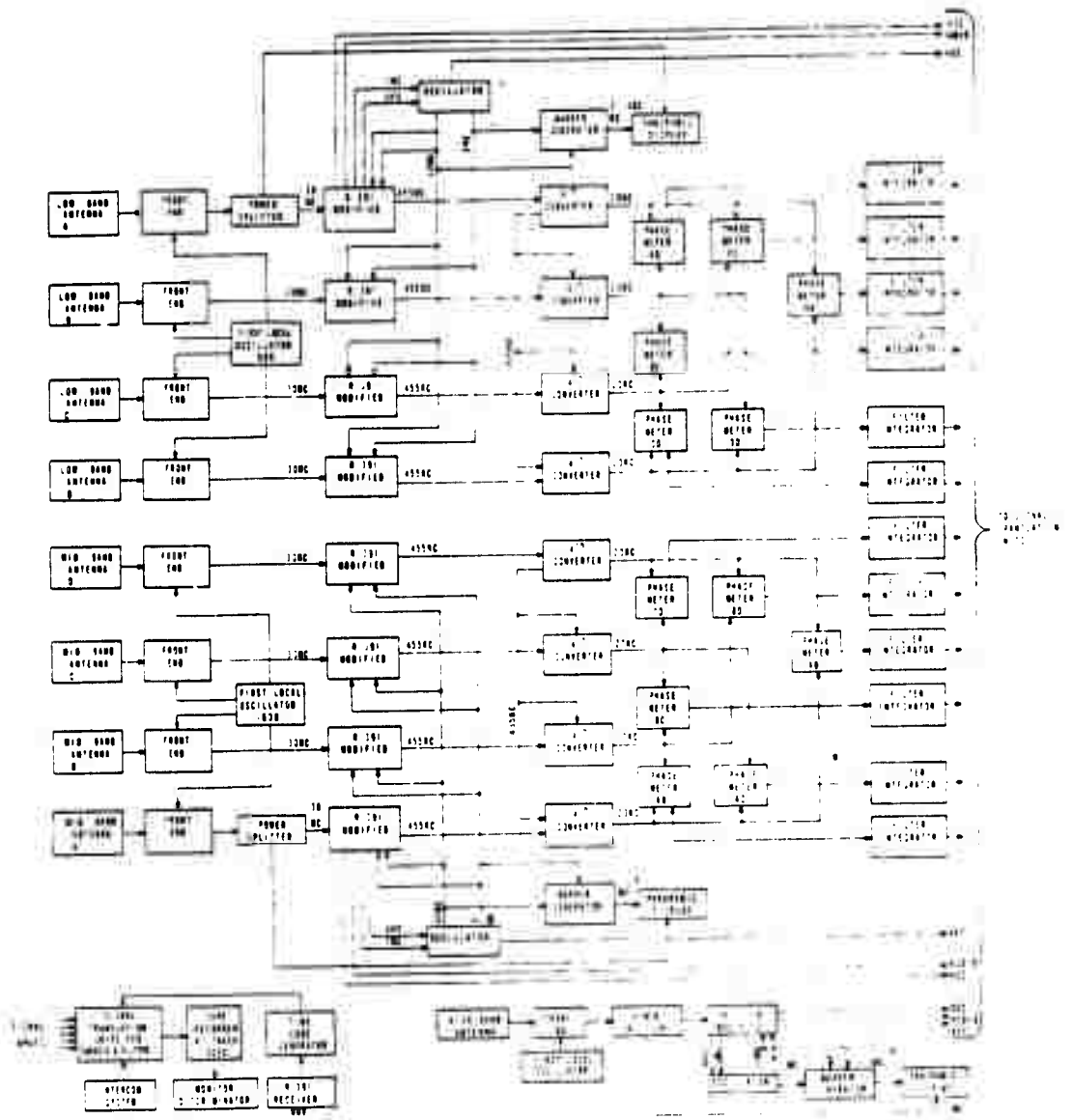

Figure 1.15 Fixed station receiving system.

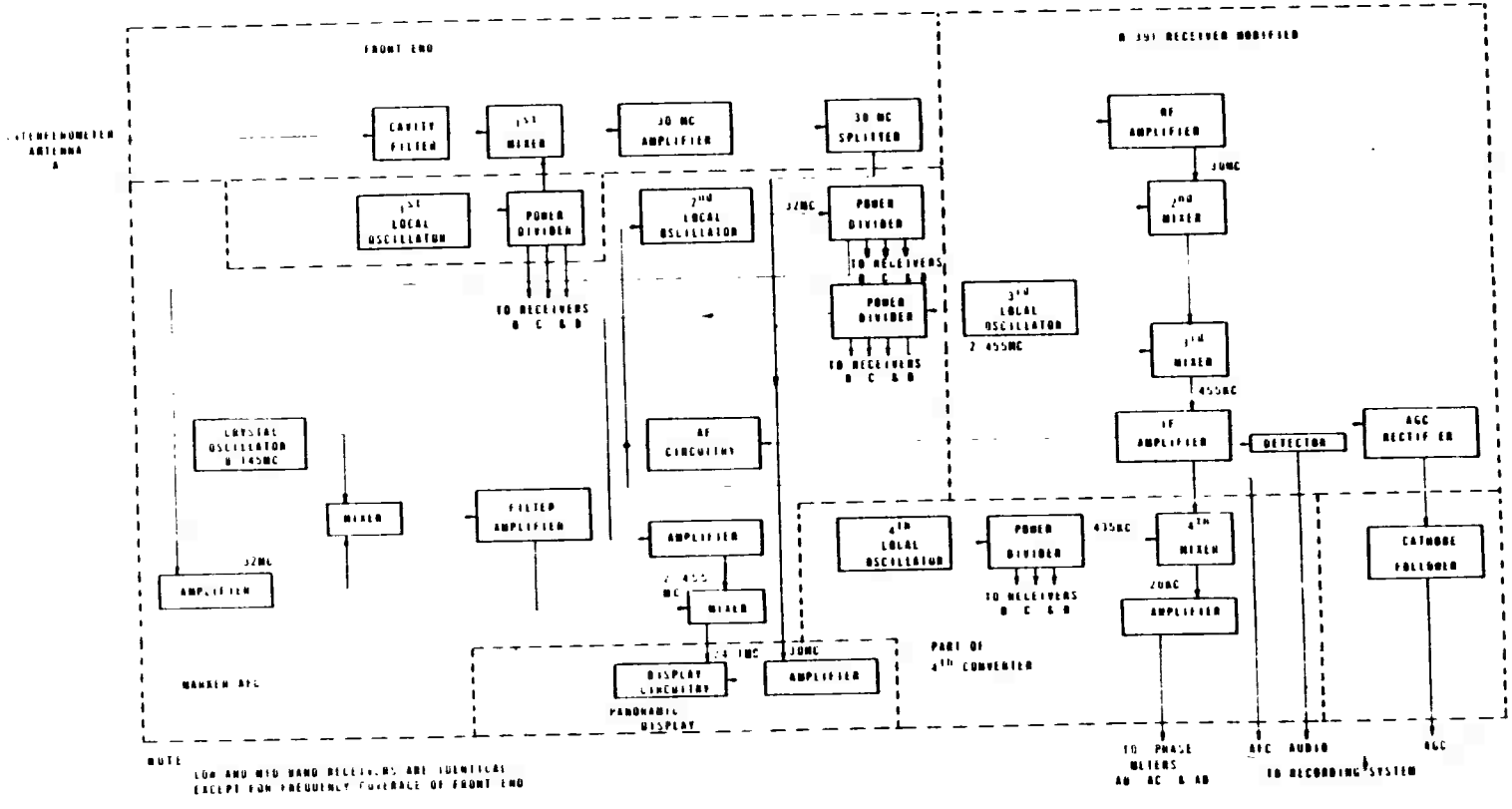

Figure 1.16 Interferometer Receiver A.

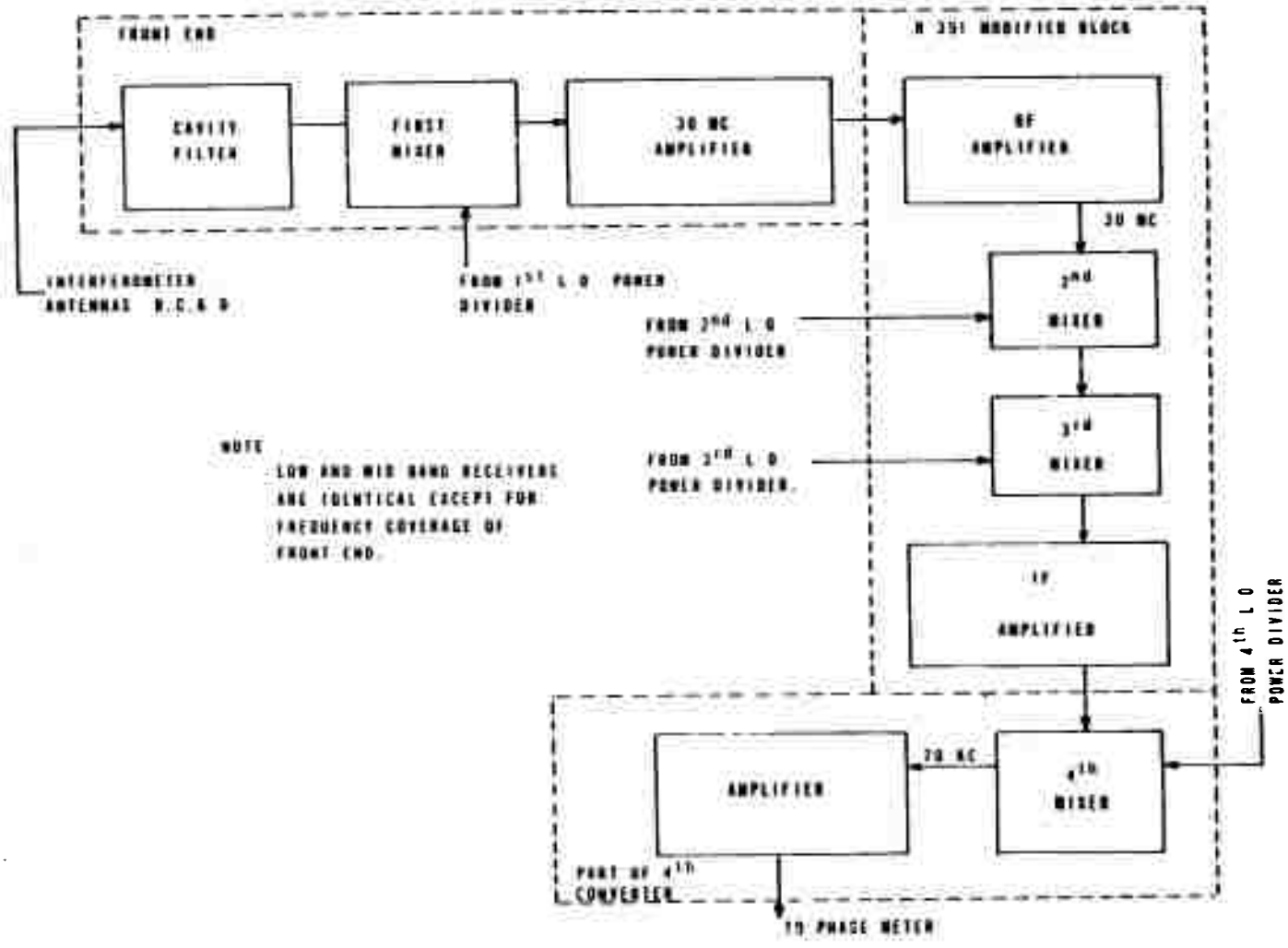

Figure 1.17 Interferometer Receivers B, C, and D.

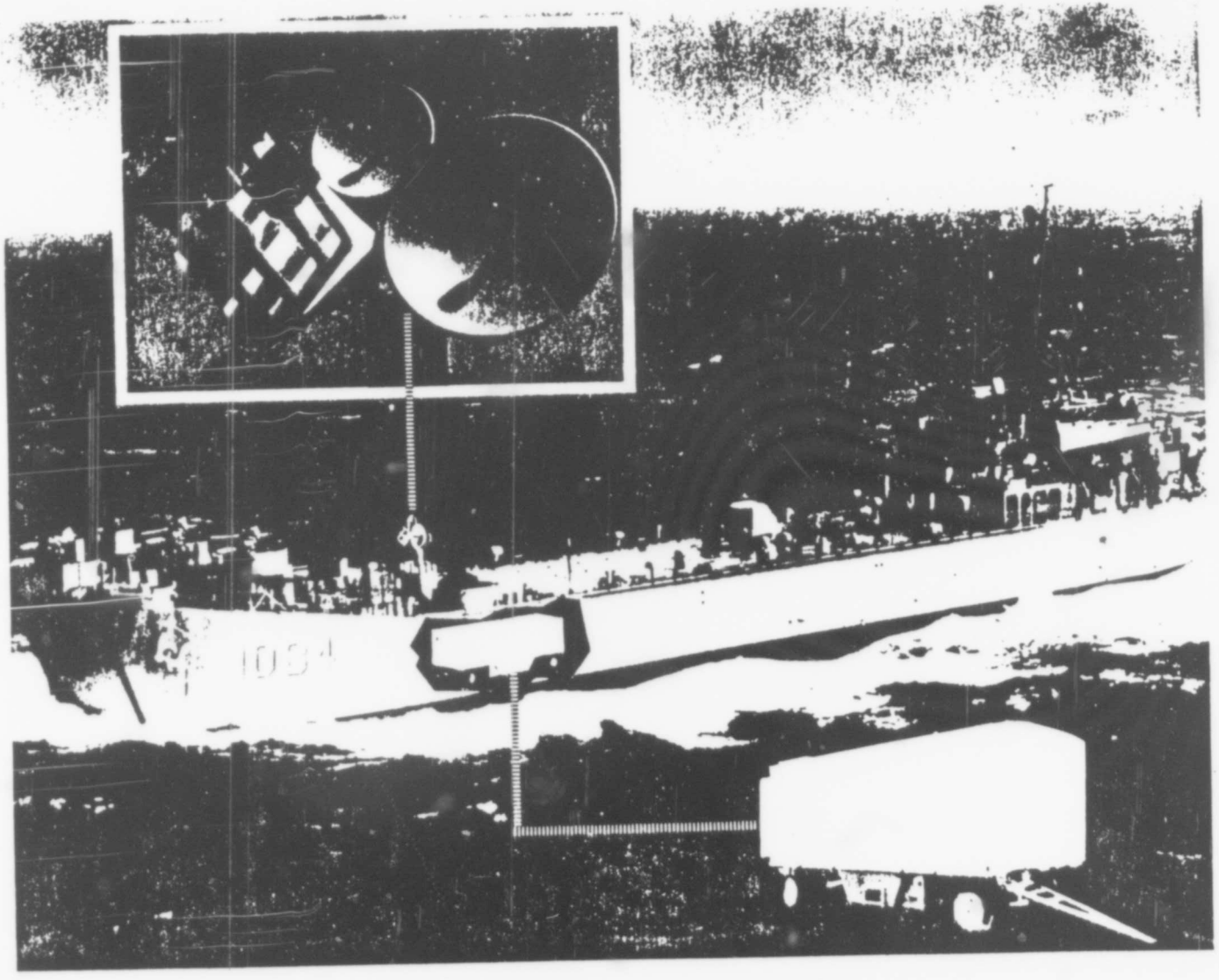

Figure 1.18 Shipboard tracking station.

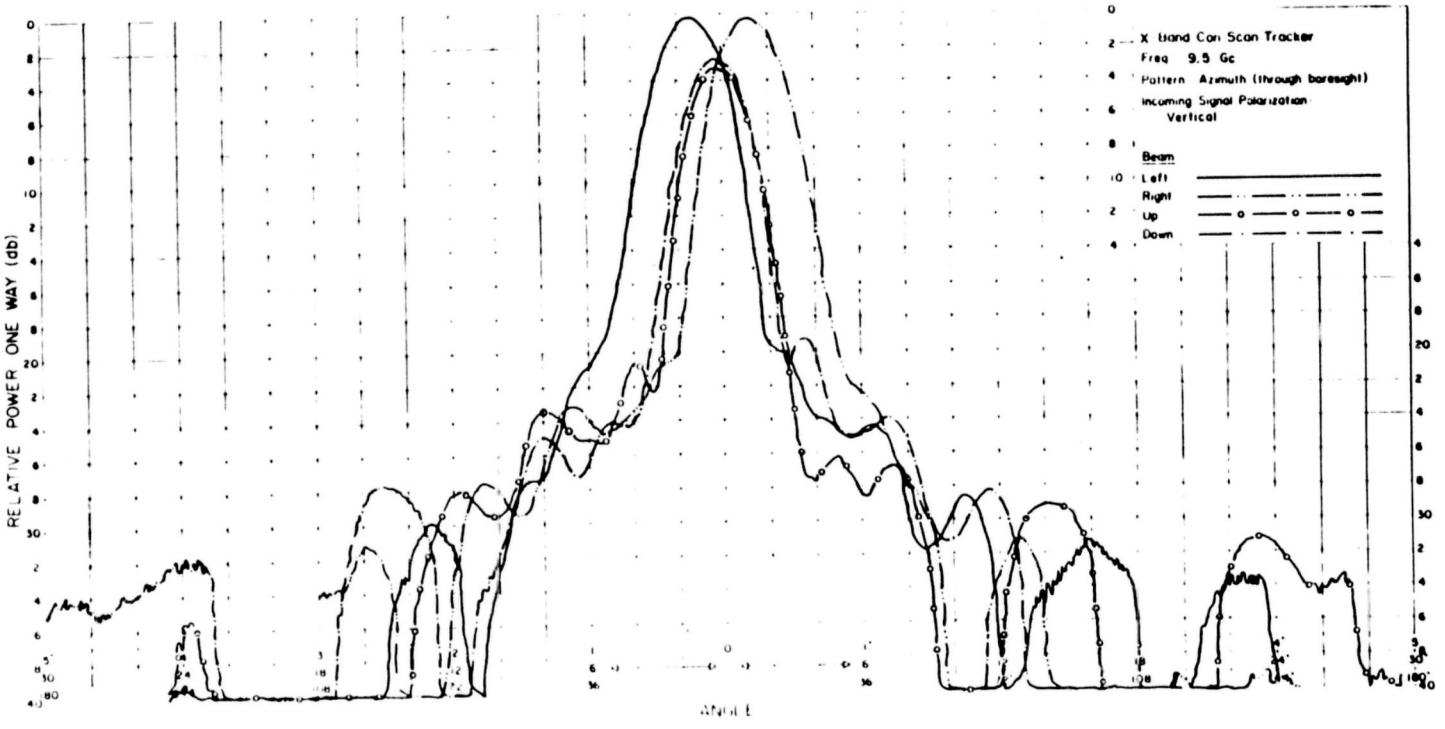

Figure 1.19 X-band tracking antenna patterns, vertical polarization.

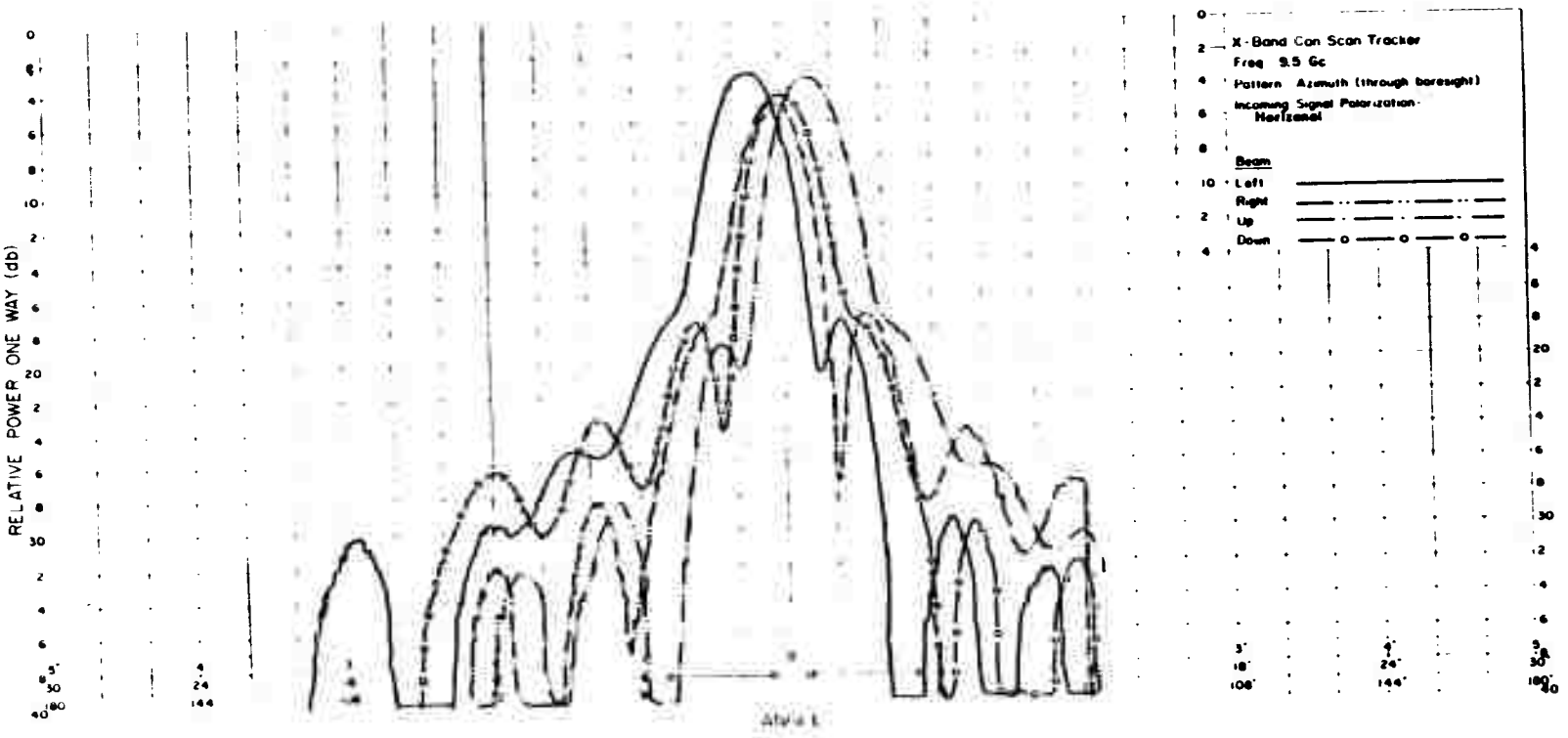

Figure 1.20 X-band tracking antenna patterns, horizontal polarization.

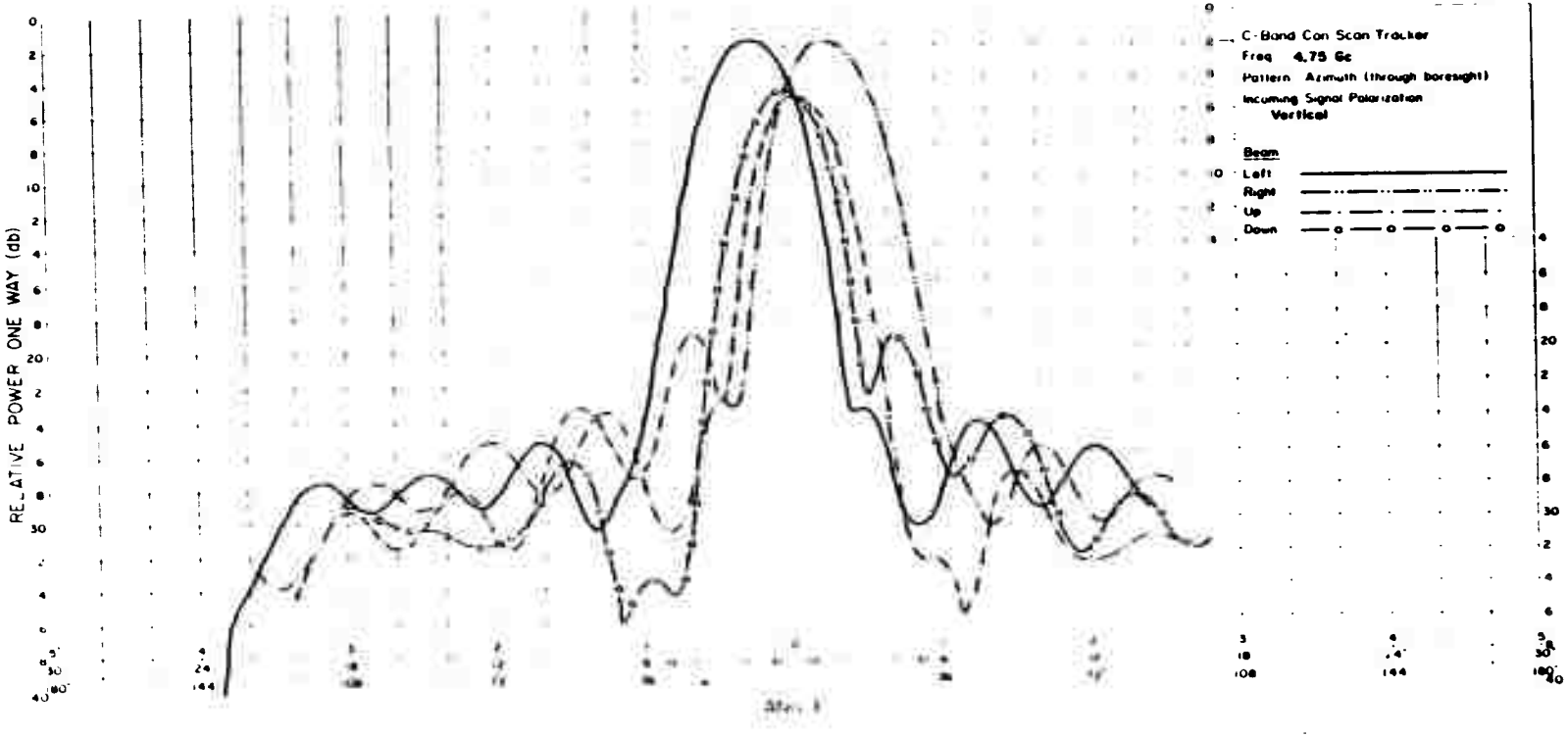

Figure 1.21 C-band tracking antenna patterns, vertical polarization.

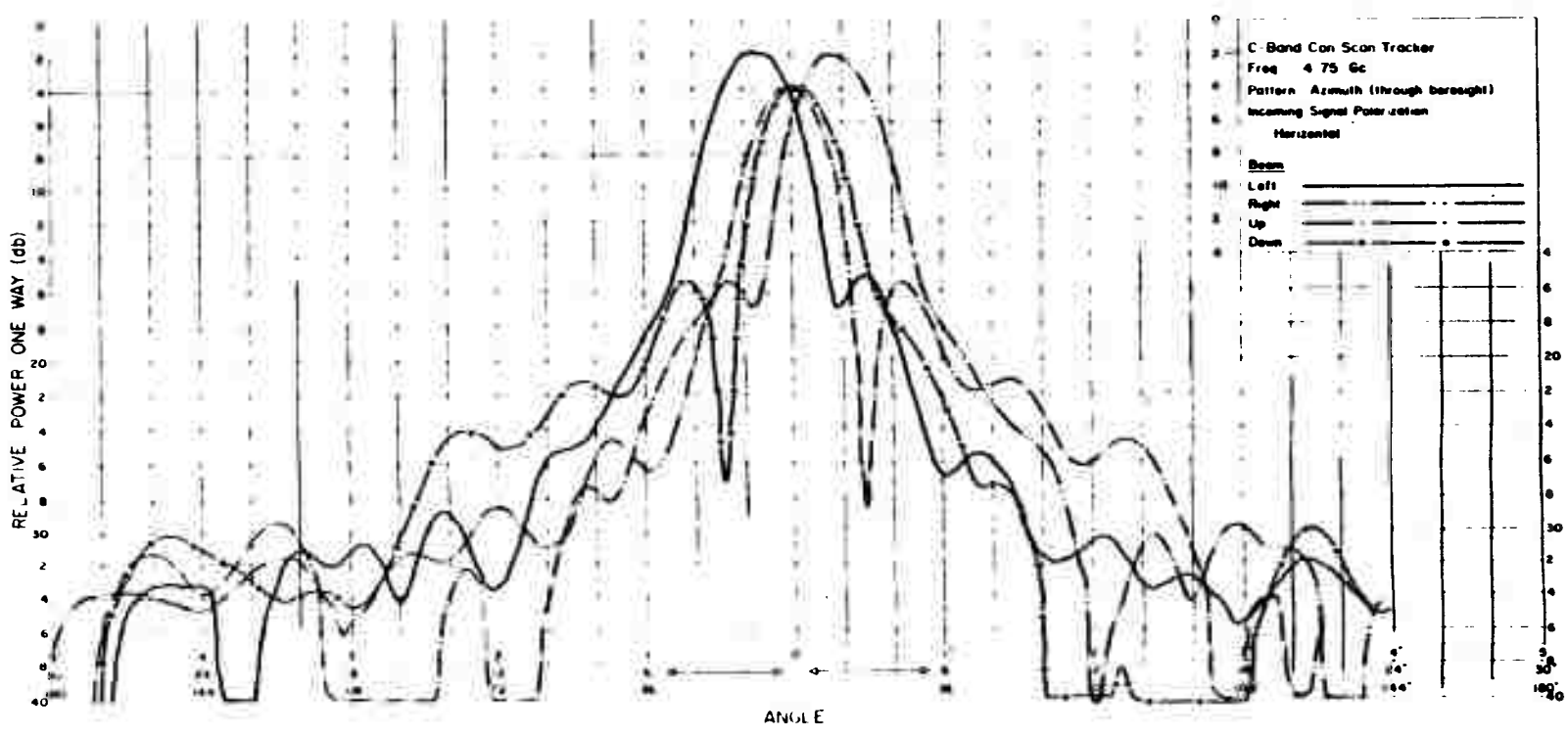

Figure 1.22 C-band tracking antenna patterns, horizontal polarization.

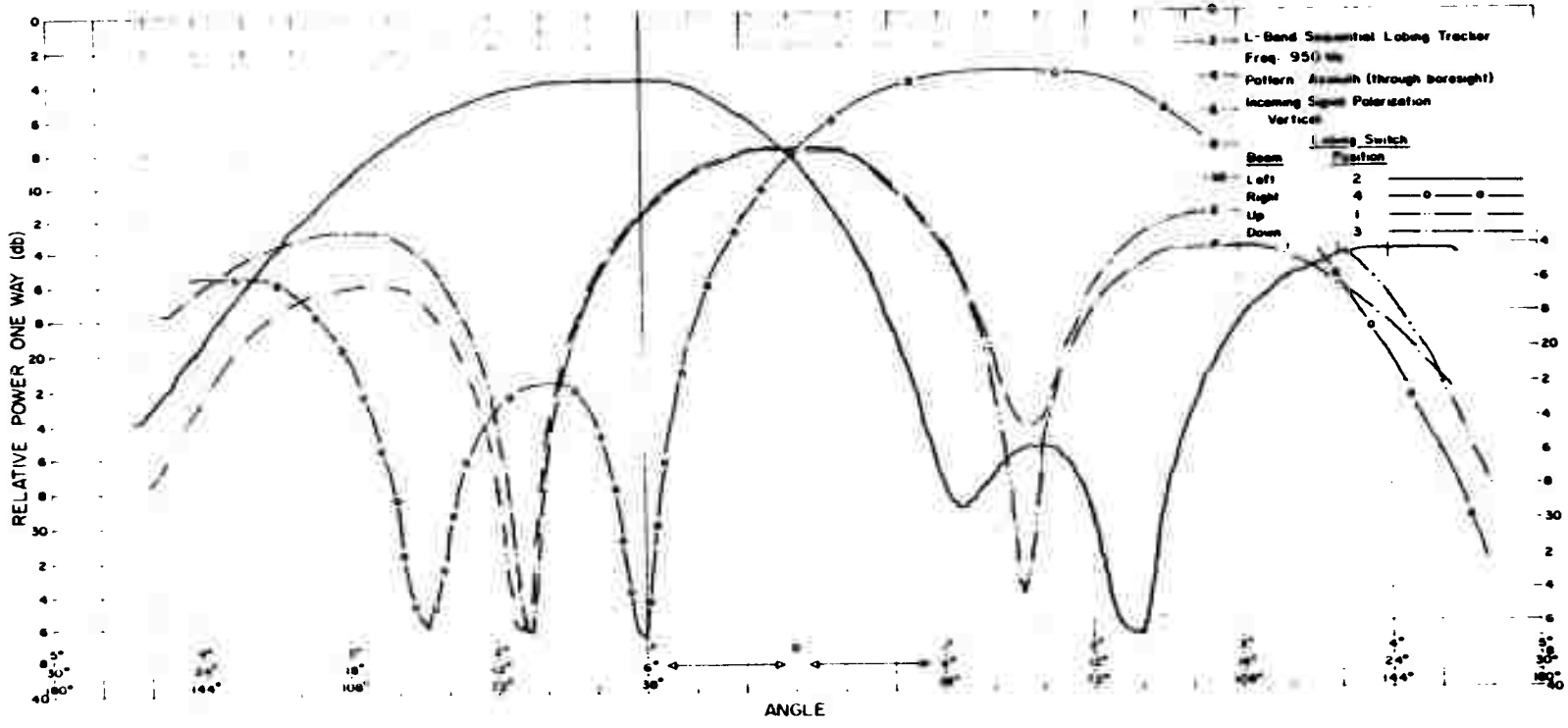

Figure 1.23 L-band tracking antenna patterns, vertical polarization.

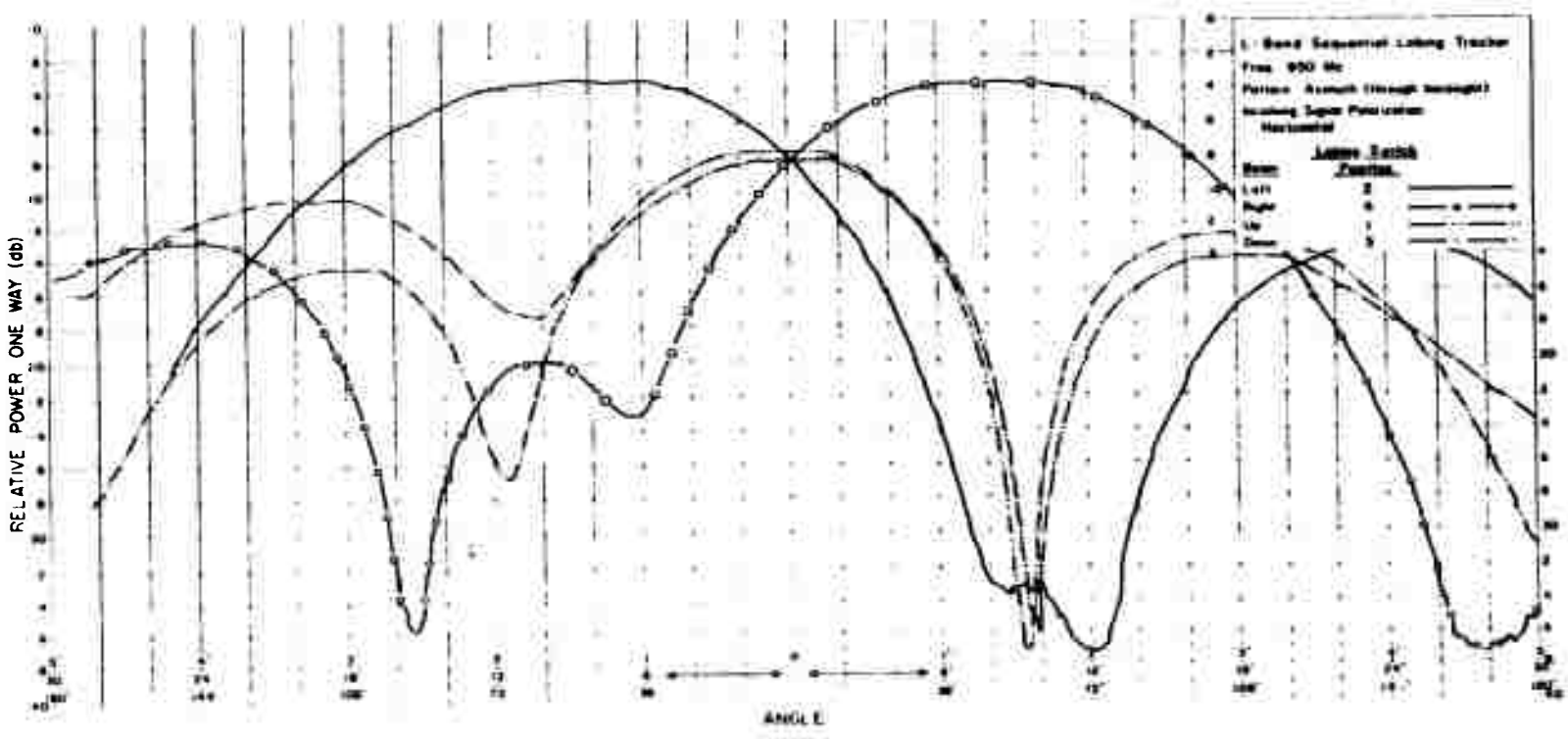

Figure 1.24 L-band tracking antenna patterns, horizontal polarization.

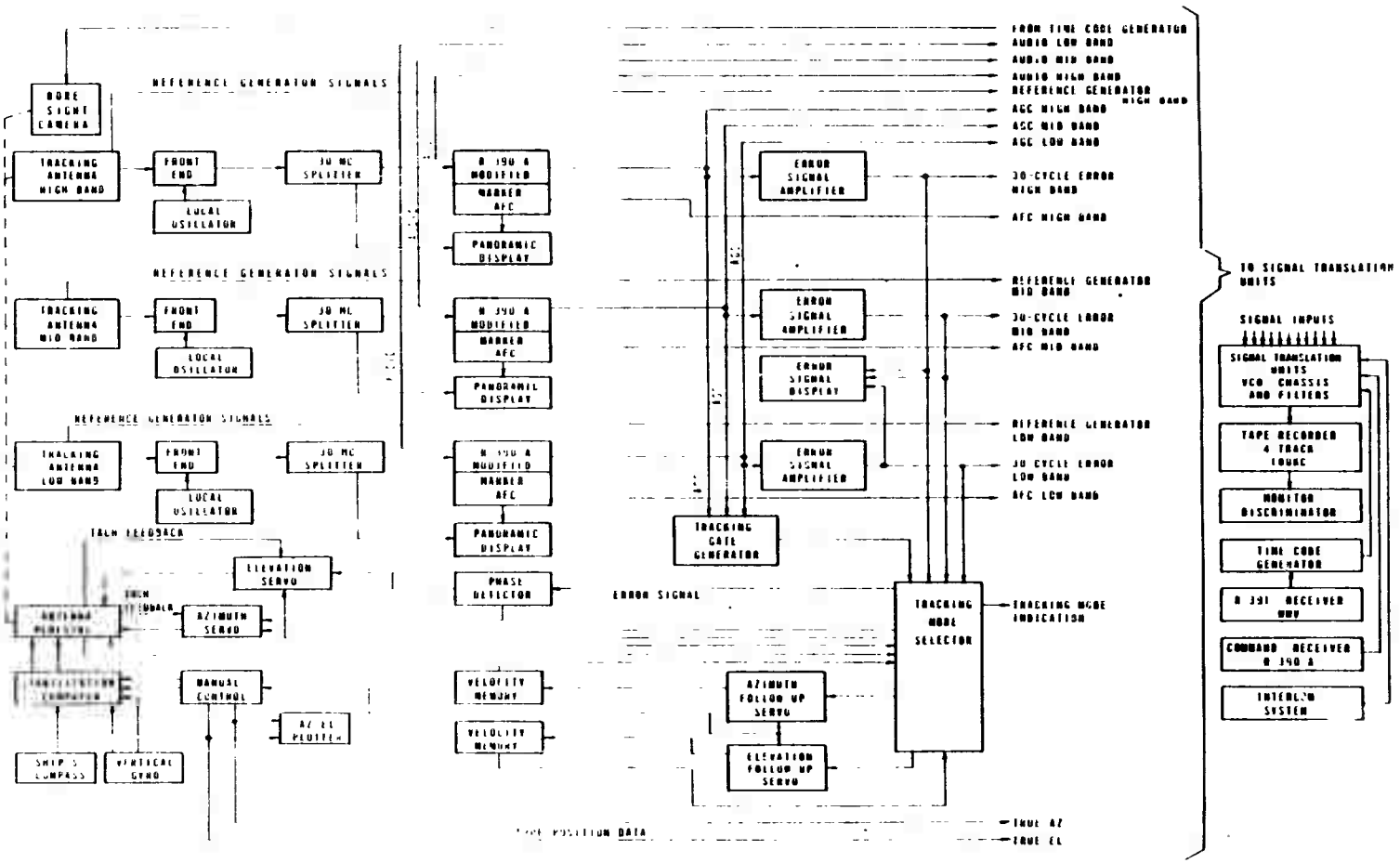

Figure 1.25 Tracking receiver system.

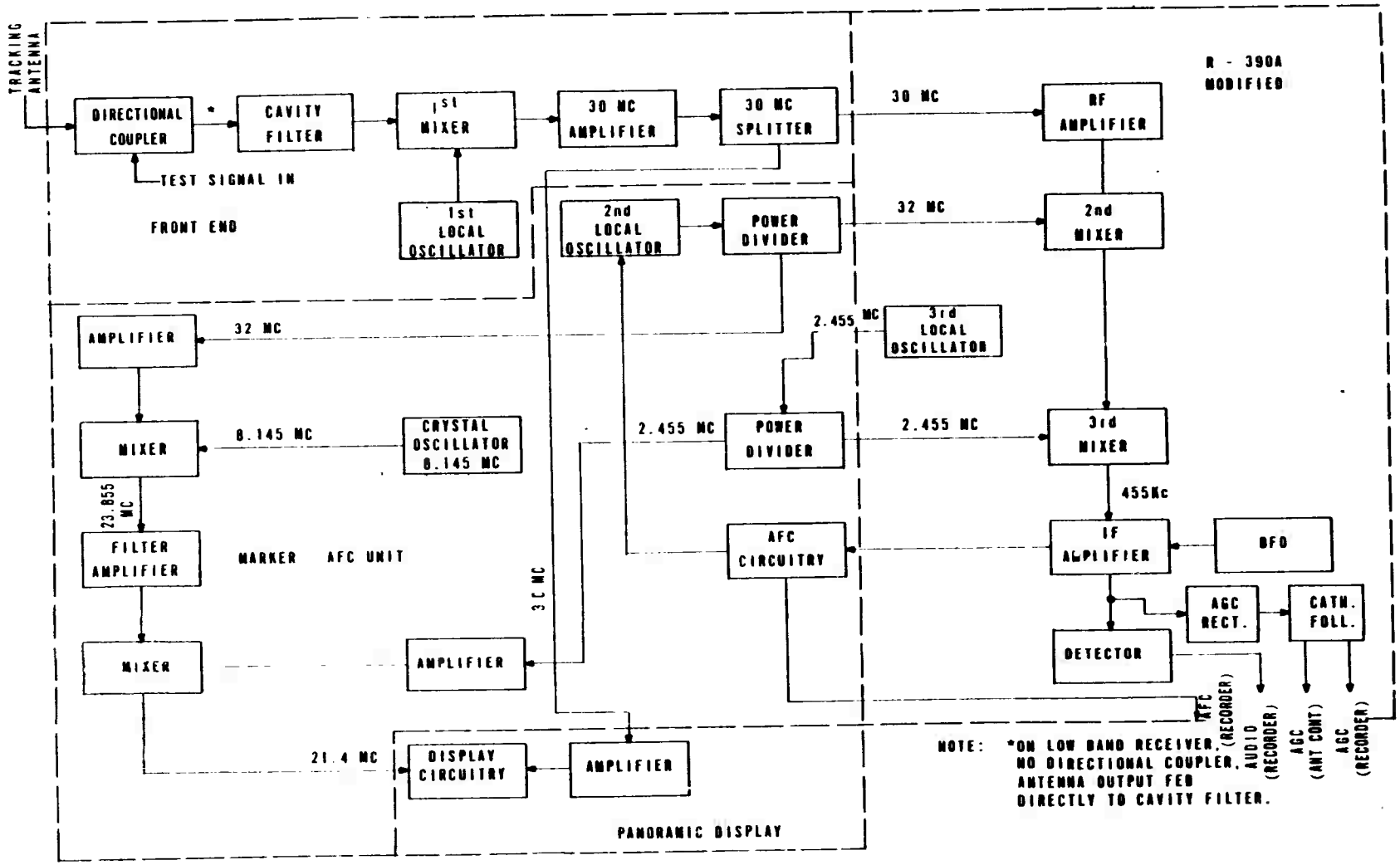

Figure 1.26 Tracking receiver (all bands).

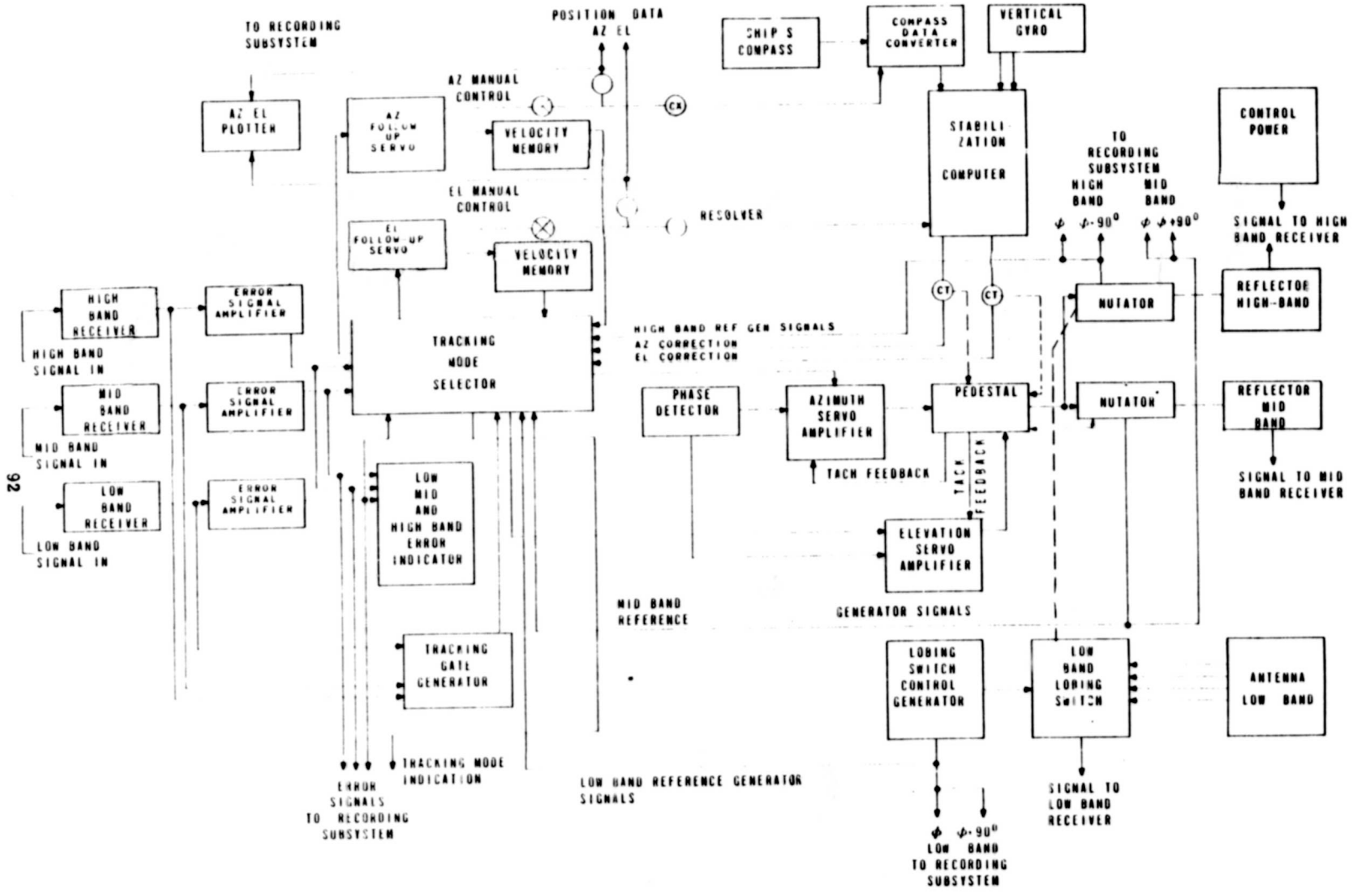

Figure 1.27 Shipboard antenna control subsystem.

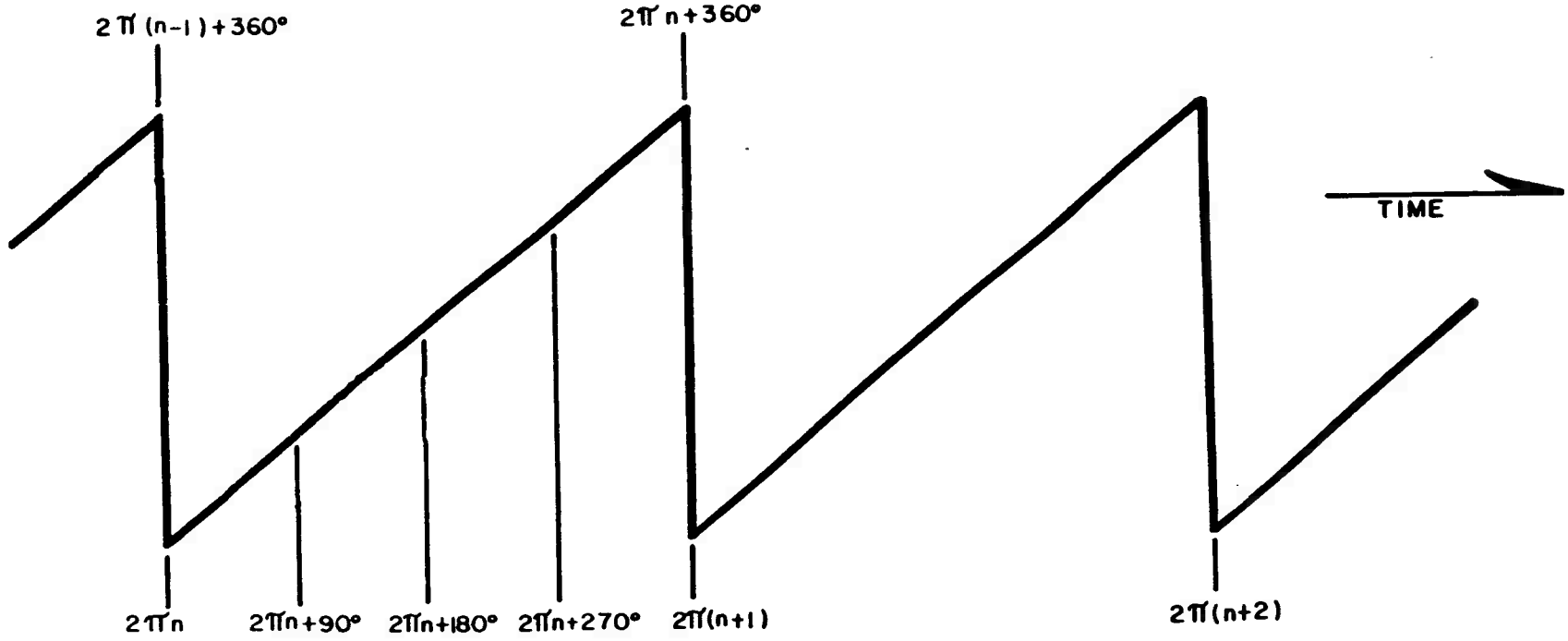

Figure 1.28 Typical display of phase data.

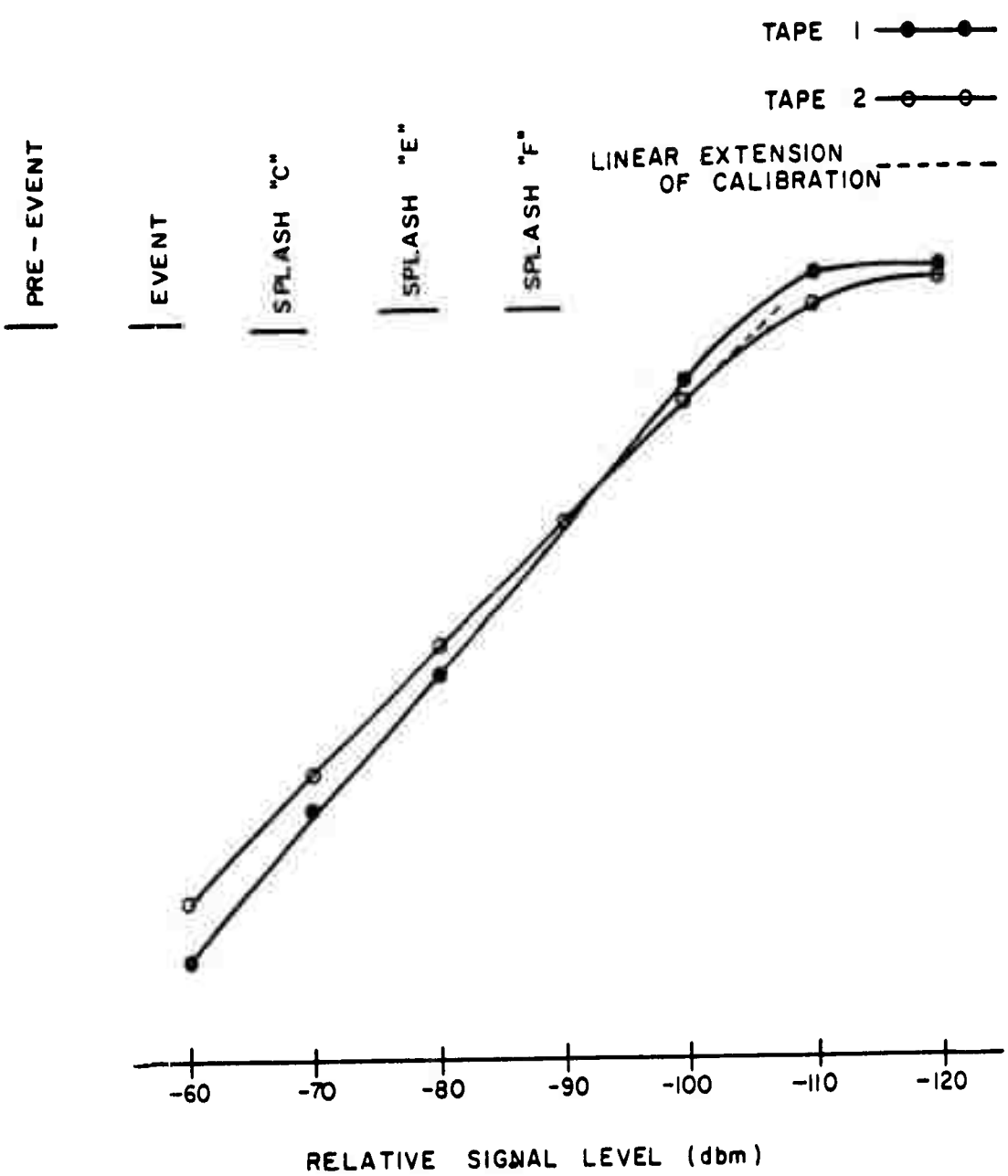

Figure 1.29 AGC calibration, Blue Gill, Ship 2, C-band.

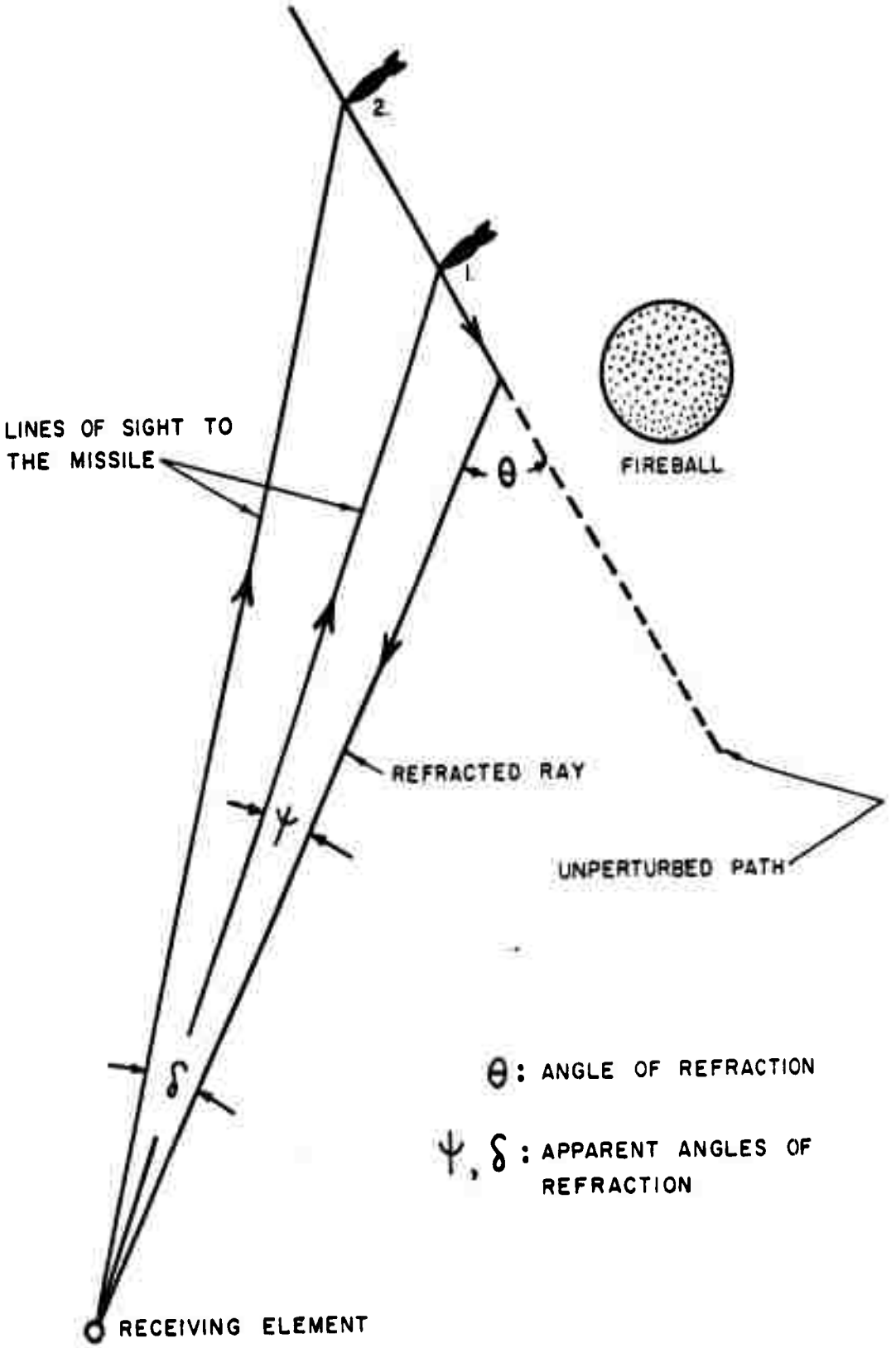

Figure 1.30 Actual and apparent refraction angles.

CHAPTER 2

BLUE GILL

2.1 PHENOMENOLOGY

The Blue Gill shot was a detonation at an altitude of km at 0959:40.4753 Z Greenwich Mean Time on 26 October 1962.

At the detonation altitude, attenuation effects were expected to be due to both the fireball proper and to a gamma-ray aurora in a region closely surrounding the fireball (Reference 3).

2.2 OBJECTIVES

In measuring the effects of the Blue Gill event on X-, C-, and L-band frequencies, two major objectives were proposed. The first objective was the quantitative measurement of the attenuation, as a function of time, which a high-altitude nuclear detonation produces on radar frequency transmissions.

The second objective was the measurement of phase differences which were expected to develop in nearly parallel radar rays passing through the fireball and nearby ionized regions.

2.3 OPERATIONS

2.3.1 Operational Plan. Project 6.1 was originally designed to study the Blue Gill event. Figure 2.1 is an artist's concept of the overall geometry of the experiment. Note that there were two major planned Nike-Cajun rocket trajectories. Each beacon was placed by rocket to provide optimum observation from a given monitoring station.

One trajectory, which provided for the rocket to pass over the event area, was planned so that the beacon would be on the downward portion of the trajectory, above, and

to the south of the event at time of detonation. This position initially allowed a ray path to the interferometer at the fixed station on Johnston Island which was unobscured by the fireball. As the rocket descended and the fireball rose, the distance between the ray path and the fireball became less until the line of sight between the rocket and the ground station was obscured by the fireball. With this geometric arrangement it was possible for the L- and C-band interferometers to measure refraction outside the fireball caused by the initial radiation from the event. It was also hoped to measure longer term refraction as the ray path passed through ionized regions near the fireball and through the fireball itself. Measurement of attenuation of K-, L-, and C-band frequencies was also planned from the fixed station.

The second trajectory, illustrated in Figure 2.1 was planned so that the beacon would remain to the north of the event throughout its flight. Flight parameters were adjusted so that the rocket would be in such a position that the initial fireball at event would obscure the ray path to the four monitoring stations located on Ships S-1, S-2, S-3, and S-4. Plans provided for the ray path between the

beacon and the ships to be obscured by the expanding and rising fireball for more than two minutes so that a time history of attenuation at X-, C-, and L-bands could be recorded. It was also anticipated that relative refraction between the different frequencies could be derived from error signal analysis.

In order to arrive at the optimum geometry for this experiment, it was necessary to have theoretical estimates of the fireball initial size and expansion and rise rates. These parameters were determined by Project 6.1c and are listed in Table 2.1.

Considering the rocket dispersion and possible deviation in the position of the event, it was decided to utilize four ship stations in order to optimize the probability of acquiring the desired data.

The location of the ships downrange and their array configuration was optimized by utilizing the given fireball parameters, computed rocket trajectories, and the following restrictions:

(1) The 3-σ dispersion of the burst point was taken to be one nautical mile (spherical).

(2) No ship was located closer than 10 nautical miles from surface zero (range safety).

(3) The Nike-Cajun was assumed to have a 1-σ dispersion of 11 km at impact. This was assumed to be a linear function of time.

(4) The Nike-Cajun launch angles were restricted to effective settings between 81 and 87 degrees.

(5) No ship was located within the 1-σ circle of Cajun impact points (range safety).

(6) Because of roll motion, tracking from the ships became difficult for look angles greater than 76 degrees; therefore, look angles were restricted to lie below this value.

The proposed ship arrangement was a trapezoidal array stationed 60 km downrange along an azimuth of 191.8 degrees T. Figure 2.2 shows the proposed locations with respect to ground zero.

2.3.2 Fixed Station Operation. Because of the inherent dispersive characteristics of the Nike-Cajun vehicles and the narrow beamwidth of both interferometer antenna systems, it was decided that the possibility of acquiring good data from the fixed station would be vastly enhanced by firing a pair of carriers and choosing the better of the two rockets for tracking throughout the event.

A pair of rockets was launched from the island at H-195 seconds (Missile A) and H-190 seconds (Missile B) to obtain interferometer data. Correlating real-time azimuth estimates from Cubic Corporation with signal strength and beacon stability indications from the fixed station, a quick-look evaluation was made of the two missile trajectories, and the H-195 (Missile A) rocket was chosen to obtain interferometer data. Figure 2.3 shows the plane views of both azimuth and elevation for the H-195 missile upon which fireball data furnished by Edgerton, Germeshausen and Grier, Inc., (EG&G), has been superimposed. The planned firing schedule for these rockets, as well as all other 6.1 rockets, is given in Table 2.2.

Two additional rockets were fired at H+290 seconds (Missile E) and H+905 seconds (Missile F). Each rocket was monitored by the island station to record possible signal attenuation and refraction associated with any residual ionization initially produced by the nuclear detonation. Since study of this region placed no stringent requirements upon the trajectory of the missile to be viewed, only one rocket was fired at each of the two late times.

2.3.3 Shipboard Station Operation. Again, two rockets were fired from the island in order to increase the probability of getting good data and to lessen the possibility of total loss because of rocket or beacon catastrophic failure. As shown in Table 2.2, they were launched at H-112 seconds (Missile C) and H-108 seconds (Missile D). After a quick-look evaluation by the fixed station, Missile C was chosen for ship station tracking, and this decision was relayed through the command communications channel. Figure 2.4 shows the elevation and azimuth plots for Missile C. Also shown are the actual ship positions during the event and fireball size and position data.

The two late-time rockets, fired at H+290 seconds (Missile E) and H+905 seconds (Missile F), were also monitored by the ship stations.

2.3.4 Support Data. The aforementioned Figures 2.3 and 2.4 are azimuth and elevation plots of missile trajectories, ship locations, fireball dimensions, and positions at significant times for the two principal early time missiles tracked during this event. It should be mentioned that the precision of any measurements derived from this data is limited by the relative accuracy of the various parameters.

Due to system operational problems, only partially instrumented trajectory data was available from Cubic Corporation, which provided tracking for the Nike-Cajun rockets. From short-time samples (Table 2.3), it was necessary for Cubic Corporation to extrapolate the trajectories through times of interest before and after event. Tabulations of final Cubic Corporation trajectories are found in Appendix B.

Fireball expansion and rise-rate data available from EG&G is primarily acquired by photographic analysis. At times of interest, especially during and after signal recoveries, the dimensions, positions, and consistency of the debris cloud are rather nebulous. Initial times and configurations of torus formation are uncertain, and estimates had to be made based upon fireball photographs. Fireball data is presented in Appendix B, Figures B.1 to B.5.

Ship locations during the experiment were provided by the Navy and usually were determined by positions noted by three of the ships relative to the position of the fourth ship (Table B.1, Appendix B).

The reference ship, S-1, which fixed its approximate location by radar and other devices, provided a basis for

determining the location of all stations relative to Johnston Island (Table B.2, Appendix B). Positional accuracy submitted by the Navy was limited to 500 radial yards.

During the course of the operation, all ships were under steam and their changing positions were determined by several estimations of heading and speed (Table B.3, Appendix B). The positional relationship of the ships to ground zero at H-hour is given in Table B.4 of Appendix B.

Table B.11, Appendix B, lists the location of the re-entry vehicle at the time of event in the various coordinate systems employed during the Blue Gill operation.

2.4 RESULTS

A discussion of instrumentation limitations and data interpretation is presented in Sections 1.6 and 1.7.

Interferometer data reduction procedures and sources of interferometer system error are described in Appendix D.

2.4.1 Attenuation Data.

Fixed Station. The X-band signal hovered around system noise level for most of its intended track of Missile A(H-195), being in the noise at the time of event. After H+40 seconds, no discernible signal was retrieved (Figure 2.5). A review of data from test firings immediately before and after Blue Gill indicated some prevalent shortcoming in the X-band receiving system. Remedial measures were undertaken prior to subsequent missions.

At H = 0, C-band signal dropped 22.0 db to noise, where it remained for about 10 milliseconds. Following this initial signal loss to noise level, there was a rapid recovery to within 6 db of pre-event level by 60 milliseconds, followed by a more gradual recovery to within 2 db by 350 milliseconds. Figure 2.6 is a time-expanded plot of signal strengths displaying these details near event time. A complete record of maximum signal envelope for C-band is presented in Figure 2.7. After the initial loss (which is believed to have been caused by the prompt radiation from the event) and the subsequent recovery, the signal remained about 2 db below its pre-event level for more than 20 seconds. It is not certain that the 2 db-loss represents any legitimate fireball-associated attenuation. It is more

likely that this loss represents either a change in the transmitter level caused by neutron and gamma radiation or a receiver function deviation caused by the sudden drop at event which was accompanied by an AFC change. In any event, the overall measuring accuracy for any signal strength data is limited to approximately 3 db ($\pm$ 1 1/2 db).

The gradual attenuation, which commenced at approximately 25 seconds, may have to be attributed to the receiver antenna pattern (Figure 1.11). In azimuth, the data was being received on the outside of the main lobe. Although during this period the azimuth of the rocket changes very little (Figure 2.3), the notch in the antenna pattern is very pronounced. By comparison with C-band data, L-band maximum envelope levels were relatively constant until about H+35 seconds, after which a gradual roll-off is noted. A more pronounced decrease in L-band levels for this period would be expected if C-band drop-off was caused by fireball-associated regions.

A sharp drop-out and immediate recovery was noted in C-band at H+31 seconds. No explanation pertaining to ionized regions is offered. The C-band signal loss at H+39.7 seconds

was evidently caused by ray-path entry into the fireball region. There was no subsequent signal recovery because of an uncorrected AFC shift at the time of drop-out. Prior to blackout, small signal amplitude variations resulted from the minor missile instability which caused the viewed portion of the transmitting antenna pattern to change periodically. Figure 2.8 presents the envelope of signal strength data for those times. No unusual scintillations were noted that could be attributed to attenuation caused by a fireball-induced ionized region.

At event, L-band signal level dropped 40 db to system noise. This signal change was accompanied by an AFC shift which was apparently not corrected until almost 20 seconds after event. At that time the receiver operator manually tuned the signal on, off, and then back on again at about H+25 seconds. Figure 2.9 is the complete record of the L-band maximum signal envelope. The failure of the signal to recover completely to pre-event levels may have been caused by radiation damage to the transmitter, or it may be explained by the receiving antenna pattern. No explanation concerning ionized regions is offered for the drop-out at 31 seconds. There were considerable signal amplitude

perturbations between this momentary loss at H+31 seconds and the drop-out as the ray path passed into the fireball region. Figure 2.10 effectively displays the envelopes of these level variations. The possibility exists that these amplitude variations were caused by ionization outside the fireball. However, it should be noted that these fluctuations occurred at the missile spin-rate with an envelope suggestive of rocket instability. Immediately following the H+31-second perturbation, the rate of amplitude variations was drastically altered, suggesting the possibility that the missile experienced a physical shock which would explain both the drop-out at H+31 seconds and the subsequent radical change in signal behavior.

It would appear that the signal losses in both frequency bands at approximately H+40 seconds were caused by the ray path being obscured by the fireball debris. The fireball ray-path parameters illustrated in Figure 2.11 indicate a close approach of the ray path to the fireball for about five seconds but no actual path through this region. It is easily demonstrated, however, that other versions of fireball growth and rise rates will produce closer correlation between ray-path obscuration and attenuation data. Minor changes in rocket trajectories would also be sufficient to produce

fireball-ray-path parameters that would indicate a 16-second passage of ray paths through the fireball.

Following L-band signal recovery from blackout after H+56 seconds, the level varied considerably with the overall maximum level 15 to 20 db below that of pre-event. It is possible that at least a portion of this level change was caused by ionization beneath the fireball; however, at this time, the missile was being reoriented by the increasingly denser atmosphere, and missile antenna patterns presented a diminished signal to the receiver. Differentiation between the two effects is not possible with the available data.

After splash of Missile A(H-195), fixed station receivers were tuned to Missile C(H-112), firmly acquiring its beacon by H+140 seconds. Fireball data at these late times are nebulous, but it would appear that Missile C may have passed through the torus of the fireball at H+140, not completely emerging until approximately H+150 seconds. At this time, the missile was already in the process of being reoriented. Figure 2.4 illustrates rocket location and near-fireball regions after H+140 seconds. Maximum envelopes for each signal frequency are plotted in Figures 2.12, 2.13, and 2.14. The signal levels of C- and L-bands were approximately normal.

X-band receiving system did not operate effectively. Gradual signal roll-off and erratic variations are characteristic of levels received from reorienting rockets. Therefore, it is not possible to state that any anomalies caused by ionization have been observed.

Ship 1. Immediately prior to detonation, X-, C-, and L-band signals were 29.0 db, 43.4 db, and 38.0 db, respectively, above system noise. At event, with all signals lost, the beacon-receiver ray-path distance normal to the point of detonation was about 0.67 km. The signal ray path entered the rapidly expanding fireball by approximately 0.37 second. Figure 2.15 illustrates the fireball-ray-path parameters following event. (Complete records of maximum signal envelope for all frequencies are presented in Figures 2.16, 2.17, and 2.18.)

Tracking logic data indicates the system was tracking in automatic velocity memory mode for most of the time between event and H+56.6 seconds. (Refer to Section 1.4.5.)

As no pedestal elevation information was available from this station, it is impossible to ascertain the extent of pointing errors during this critical period. A record of pedestal information (Figures A.1 and A.2)

indicates no appreciable pointing error in the azimuth plane from event to H+60. Azimuth pointing data indicates some radical slewing commenced at H+60 with the antenna veering 20-25 degrees from the established azimuth track by H+95.

Figures 2.19 and 2.20 indicate the maximum and minimum envelopes of raw C- and L-band signals during the recovery period. It should be noted that a lack of elevation pedestal information prevents the corrective application of computed power losses due to antenna pointing errors.

After event, system tracking modes alternated between automatic and manual antenna control. Non-recovery of signal in K-band, and diminished average levels and fluctuations in C- and L-bands after recovery, can undoubtedly be attributed to gross pointing errors of the tracking antenna. Tracking in side lobes was evidently accomplished in C- and L-bands, with L-band suffering less due to its wider beamwidth and its greater system dynamic range.

Some extent of amplitude scintillations noted after the commencement of signal recoveries can be attributed to side lobe tracking.

Although a number of problems degraded the usefulness of much of the data from this station, information such as event losses and initial recovery times is valuable for corroborating data from other stations.

Ship 2. At event, X-, C-, and L-band signals dropped 28.0 db, 38.8 db, and 44.6 db, respectively, to system noise. X-band recovered shortly to within 10 db of pre-event level and went into noise again at H+430 milliseconds. C-band recovered briefly, detecting a maximum signal level of 12 db above noise at H+125 milliseconds, and was lost again at H+165 milliseconds. No momentary recovery was evidenced in L-band. Figure 2.21 is a time-expanded plot of signal strengths displaying these details near event time. A complete record of maximum X-band signal envelope is presented in Figure 2.22.

Initial loss of signal following event was probably due to the effects of prompt radiation. At event, the normal distance from the beacon-receiver ray path to the point of detonation was about 2.03 km. Trajectory data indicates that the signal ray path intercepted the expanding fireball by approximately 1.42 seconds. Figure 2.23 illustrates the fireball and ray-path parameters for times of interest following event. Momentary recoveries were experienced in X- and C-band before transmissions were subjected to the fields of intense ionization in the expanding fireball. The greater vulnerability of L-band signals accounts for the lack of a brief, immediate recovery in that frequency.

Intermittent low-level indications in X-band, which commenced at H+1S.3 seconds, may, in some cases, be no more than random noise, probably originating from the fireball.

There are other correlating data suggesting the possibility of a momentary signal return at H+25 seconds. This may be an indication of the inhomogeneous nature of the fireball or may simply be an example of multipath reflection from the earth's surface received through an antenna side lobe or reflection from clouds or rain in the vicinity of the ships.

Tracking logic data indicates that the system alternated between velocity memory and C-band automatic tracking modes during the first 12 seconds after event. It then remained in the automatic mode from H+12 to H+39 seconds, after which time the X-band signal had recovered sufficiently to assume automatic track. Periods of automatic tracking in C-band following event may have been the result of a high level of fireball noise detected in that frequency. Regardless of the source of this tracking logic behavior, pedestal data for these periods indicate very little antenna excursion from a calculated optimum trajectory (Figure A.3).

Figure 2.24 illustrates the computed power losses during the blackout period that could be attributed to tracking-antenna-pointing errors regardless of other attenuation criteria. Equivalent power loss is determined by applying pedestal angular pointing deviations to tracking antenna patterns. Periodic indications of minimal pointing errors during the

blackout period tend to substantiate the duration of legitimate signal loss for that time.

The X-band signal, which started to recover at approximately H+38 seconds, had by H+52 seconds reached peak levels equivalent to those of pre-event. However, signal stability was not achieved until after H+75 seconds. X-band signal recovery characteristics are presented in Figure 2.25. Both maximum and minimum data envelopes are indicated, as well as a correction to the maximum envelope for computed power losses due to pointing errors. The signal recovery level was subject to large perturbations (scintillations), and at times, exceeded pre-event amplitudes. Since, at this time, the ray path did pass through the fireball, it may be postulated that the violent level changes and the stronger signal may both be indicative of the inhomogeneity of the fireball and the existence of refraction or diffraction patterns about the hot spots in this region.

It should be noted that a visible torus had formed by H+60 seconds and was undoubtedly in a formative process for some time prior to this. Figure 2.23 illustrates the torus size and the ray-path distance through the fireball. A portion of this distance is through the center of the torus which is assumed to be less densely ionized than the torus proper.

Figure 2.26 presents the maximum and minimum signal envelopes for the C-band recovery period. Also indicated is the maximum envelope with computed corrections for antenna-pointing errors. C-band recovery time and data characteristics for this period are similar to those of X-band. Scintillations were again prominent, and recovery levels occasionally exceeded those of pre-event although not as significantly as was demonstrated in X-band. A complete record of maximum C-band signal envelope is presented in Figure 2.27.

As evident in Figure 2.28, there were no indications of recovery in L-band until 58 seconds after event. Large amplitude scintillations persisted throughout the ensuing recovery period and average pre-event levels were not attained until approximately H+110 seconds. From Project 6.1 data, it is impossible to determine precisely when the ionization scintillations end and the reorientation perturbations begin.

It is possible that reorientation of the missile began as early as H+130 seconds. Late-time fireball data, although nebulous, indicate probable passage of the ray path through some portion of the fireball as late as H+150 seconds. It

is likely that there were combined variations during these periods. A complete record of maximum signal envelope is presented in Figure 2.29.

Ship 3. At H = 0, X-, C-, and L-band signals propagated from Missile C(H-112) dropped 23.2, 43.3, and 42.5 db, respectively, to system noise levels. Complete records of maximum signal envelope are presented in Figures 2.30, 2.31, and 2.32. Coinciding closely with these signal losses were sufficient AFC shifts in all bands to prevent signal recovery. Although X- and C-band tuning problems had been corrected within two seconds, considerable antenna pedestal slewing during this early period produced large pointing errors which were allowed to persist until H+10 seconds. At H+6.6 seconds, the tracking system was removed from the velocity memory mode, and manual acquisition was attempted until H+50.3 seconds. Throughout this period and continuing (while in the C-band automatic tracking mode) until H+59 seconds, antenna slewing was considerable and could have been instrumental in delaying signal recoveries (Figures A.5 and A.6).

The extent of the antenna-pointing errors present some interesting possibilities for the explanation of X- and C-band data. Figure 2.33 indicates that fireball and ray-path parameters

present ray paths through the fireball for times well beyond recovery periods. Figure 2.34 illustrates the computed equivalent power losses attributable to antenna-pointing errors. The periodic indications of minimal pointing errors during the blackout period tend to substantiate the duration of legitimate signal loss for that time.

Signal recovery data for the three frequencies are presented in Figures 2.35, 2.36, and 2.37. These figures present maximum and minimum envelopes for the signal strengths as well as maximum signal data corrected for pointing errors.

Contrary to expectations, recovery commenced in C-band before detection in the higher frequency X-band. It is suspected that the initial recovery of C-band signal was in a side lobe of the receiving antenna, barely beyond the capability of a narrower X-band beam. This would seem to be borne out by the antenna-pointing error existing at the time of C-band acquisition. It is further substantiated by the relatively erratic recovery in X-band which would not ordinarily be expected, because it is less vulnerable to fireball effects. The large, momentary C-band level increase at H+47 seconds is coincidental with a short-duration correction of look angles. Although first indications of

recovery in X-band follow those of C-band within 1.52 seconds, signal amplitude and stability are not sufficient to allow for automatic tracking in the higher frequency until H+64 seconds. Correlating data indicates that a large tracking error signal was generated in C-band at H+46 seconds. The amplitude of these error signals subsequently decreased gradually until normal level and stability was maintained after H+74 seconds. X-band error signals commenced at H+51 seconds with sporadic fluctuations and dropouts and continually decreased in overall amplitude until firm automatic tracking was achieved in that band.

The same data which was utilized to promote a side lobe tracking theory may also be considered to explain the possibility of a refracted C-band signal. This explanation suggests that a highly refracted signal was acquired and tracked until its angle of arrival coincided more nearly with that of a lesser refracted X-band transmission.

An examination of Figure 2.36 reveals that when equivalent pointing error power losses are added to the raw signal strength data in C-band, signal levels exceed pre-event values by 10 to 15 db from H+44 to H+59 seconds. This anomaly suggests that, although C-band antenna pointing is considerably offset from the rocket, it is looking in the general direction of a highly refracted signal. The amplitude of this refracted signal

indicates acquisition in an efficient portion of the main antenna lobe. It is seen that a correction for pointing errors would considerably inflate refracted signal strengths for this period.

A corollary to the side lobe tracking postulation is that an error in selection of the proper antenna side lobe may also produce a correction for pointing errors that would inflate signal amplitudes beyond nominal levels.

The extent of amplitude scintillations, as indicated in Figures 2.35, 2.36, and 2.37, suggests non-homogeneities in the debris region through which ray paths are propagated.

Although there were a number of unfortunate equipment malfunctions and operator errors at this station, a considerable amount of valuable data was retrieved. There were a sufficient number of reliable data intervals during the blackout period to verify the complete loss of signal. Recovery data compares very favorably with information from other stations. Correlation of data collected at this station with that from S-2 has proven valuable verification of data validity.

Ship 4. Signals from Missile C were lost at H = 0, with X-, C-, and L-band levels dropping 25.5, 42.0, and 33.6 db, respectively, into system noise. Complete records of maximum signal envelope for the three frequencies are presented in Figures 2.38, 2.39, and 2.40.

Figure 2.41 illustrates the fireball and ray-path parameters which are of prime interest for the period immediately following the event.

An examination of pedestal data indicates a small oscillatory motion of the antenna tracking the missile prior to event (Figure A.7). At the instant of event, this inherent oscillation was in a generally downward direction distracting, for that moment, from an overall increase in elevation angle for that portion of the missile's trajectory. The loss of all signals at event caused the tracking logic to place the system in the automatic velocity memory mode. (Refer to Section 1.4.5.) The momentary and superfluous downward motion of the antenna was construed by the system's logic to be an actual history of recent overall antenna direction and rate of motion. Unfortunately, the station's antenna control operator permitted the system to remain in the memory mode until H+30.2 seconds, by which time

the antenna had dropped to a position parallel to the ship's deck. A manual attempt to reacquire the missile was ineffectual, due to gross pointing errors, until approximately thirty seconds prior to splash, at which time the L-band signal was detected. Recovery in L-band first is undoubtedly due to the wide beam of its tracking antenna.

The most useful data from this station (for Missile C) were those which described the initial signal dropouts at event. X-band data appears to be reliable, although C- and L-bands displayed AFC shifts that coincided closely with event and which were not rectified until after the antenna had moved through a large angle.

Late-Time Data. Signals from late-time Missiles E(H+290) and F(H+905) did not indicate any attenuation or unusual perturbations that could be attributed to the fireball or residual ionized regions. Complete records of maximum signal envelopes for all stations are presented in Figures 2.42 to 2.71.

Large signal variations observed throughout the flight of Missile F(H+905) undoubtedly can be attributed to an instability of the vehicle. This is corroborated by coincidental fluctuations evident on all bands at all stations.

Although no exact explanation can be submitted, it is fairly certain that a separation of stabilizing hardware took place shortly after launch, resulting in a tumbling, or rotational couple, of the missile. A total flight time, which was about 20 seconds less than nominal for comparable rounds, provides a further indication of shortcomings in the missile's performance.

2.4.2 Refraction Data.

Interferometer. For the Blue Gill experiment, the fixed station was used to sequentially monitor and evaluate each of the four early time missiles. The rockets that eventually were tracked by the ships and the interferometer were selected on the basis of this quick-look analysis. Because of this procedure, the H-195-second rocket was tracked by the interferometer only from launch to H-160 seconds and then not again until H-38 seconds. The discontinuity of phase information for so extensive a period prevented critical matching with early time unextrapolated trajectory data.

In addition to these anticipated data discontinuities, other portions of phase data were lost due to system malfunctions and during times of legitimate fireball-associated attenuation. At event, C-band signal dropped 22.0 db to

noise and recovered 10 db within 45 milliseconds. The signal was subsequently lost at approximately H+40 seconds and was not recovered thereafter. At H = 0, L-band signal was lost to noise and did not significantly recover until H+19.91 seconds. It, too, dropped out at approximately H+40 seconds but recovered from noise after H+56 seconds. (A complete discussion of fixed station signal strength data for Blue Gill is presented in Section 2.4.1.) Figure 2.3 illustrates the trajectory of the H-195-second rocket. Pertinent fireball and ray-path parameters are indicated in Figure 2.11.

Using the Cubic Corporation trajectory, a comparison was made between unit vectors generated by interferometer phase information and vectors to the missile position as computed from trajectory data. For each time considered, a single vector for the six independent phase comparisons was determined by a least-squares averaging solution. Figure 2.72 illustrates the considerable pointing discrepancies between phase and trajectory data.

It should be noted that several trajectories (other than that furnished by Cubic Corporation) were generated by computer simulation programs for comparison with the interferometer data. The phase information could not be matched precisely with any available trajectory; however, the data computed by Cubic

was shown to be most nearly compatible and consequently was selected for use in all final calculations. The inability to match interferometer data closely to trajectory information, even at pre-event times, made it impossible to extract any long-term indications of apparent refraction.

Because a close agreement could not be obtained between the two data sources, no attempts were made to refine the final trajectory by use of the phase data. Since interferometer data may be shown to match any number of trajectories, it is essential to be able to select the correct one with confidence. Lack of confidence in the Cubic trajectory is based upon the erratic nature of the raw trajectory data and anomalies arising from a comparison of attenuation results with purported missile positions. (It should be noted, however, that small variations in fireball size and location could be shown to explain some of the attenuation discrepancies.)

An attempt was made to reduce phase data at times when measurable perturbations were of short duration. Recorded deviations of this type were limited to C-band data at the time immediately following event when signals were subject to the effects of prompt radiation. Figure 2.73 is a photograph of a raw data recording covering the time period of interest. The six channels of C-band phase comparison data

are illustrated. Note the short-duration excursions on all channels at event.

Figure 2.74 is a time-expanded view of this raw phase data at event with a plot of the relative signal strength for that period. At H = 0, the signal started to decrease rapidly to system noise, dropping to that level within seven milliseconds. Since receiver characteristics during periods of rapid signal loss cause an open-circuit condition to exist, excursions recorded during this period must be ignored. It is apparent, from Figure 2.74, that all the major perturbations occur during low signal-to-noise ratios. (Although some channels appear to recover at relatively low signal-to-noise ratios, it should be noted that errors in relative signal strength level are greatest within 8-12 db of noise.) It is believed there was insufficient signal amplitude for proper phasemeter operation during this period.

Although the nature of the data is doubtful, an attempt was made to relate the recorded perturbations to a value for apparent refraction. Figures 2.75 to 2.80 are representations of the recorded phase perturbations indicating the extent of the deviations in electrical degrees. This data has been

reoriented for presentation purposes and enveloped about the major recorded excursions to facilitate comparisons during the period of interest.

All phase readouts were utilized in a least-squares computation of unit vectors. This was compared to a similar solution derived from nondeviated extrapolated data. A time record of these perturbations is presented in Figure 2.81. A more specific examination of the variations in azimuth and elevation components of refraction indicated by the 14 different leg combinations reveals magnitude variations which exceed the total values given in Figure 2.81. The directions were also found to be quite random.

Figure 2.82 presents the ratio of mean perturbation to dispersion in the azimuth plane. (Virtually all deviations appear in azimuth-sensitive phase comparisons.) The preponderance of noise over possible signals precludes the probability that the data plotted in Figure 2.81 was caused by refraction. The development of the differential equations necessary for this computation is given in Section D.1.5.

As a result of the aforementioned conditions, it is concluded that it is not possible to extract refraction information from interferometer data recorded during Blue Gill.

Shipboard Stations. Tracking error signals, recorded by the four shipboard stations, were intended to provide information on relative refractive effects sustained between the three microwave frequencies employed in this experiment. Assuming no functional problems, tracking error data would represent the angle between the pointing direction of an antenna and the arrival direction of a signal. (Error signal instrumentation is discussed in Section 1.4.5.)

When beacon tracking is attempted in an unperturbed region, the characteristics of error signals generated in each of the three tracking systems generally should be constant. When conditions for signal refraction exist, assuming no complete signal absorption, error signals will vary accordingly. Since higher frequency transmissions are less affected by fireball phenomena, X-band error signals were expected to provide a reference for studying the relative effects in the more perturbable C- and L-bands.

In order to extract any meaningful refraction information from error data, it is necessary to be able to calibrate the data accurately. Physical and environmental limitations at the shipboard stations and in the test area made it impossible to calibrate error signals. Hence, no measurable

refraction effects are available from shipboard station data. Two methods, described in Appendix C, were attempted in an effort to calibrate tracking error signals.

2.5 DISCUSSION

2.5.1 Data Reliability. The reliability of Project 6.1 data was determined by the evaluation of test round and event data and experienced estimates of individual equipment reliability. Table 2.4 presents calculated accuracies for Project 6.1 data which include data reading uncertainties and quoted accuracies for support data. These overall confidence figures do not apply equally for all stations or times but represent mean values.

2.5.2 Attenuation. There are three major points of interest in the Blue Gill data. The most important, of course, is the opaqueness of the fireball to X-, C-, and L-band radiation for extended periods of time. For the dynamic range of the 6.1 system, X- and C-band frequencies are obscured for approximately 35 seconds; L-band for 60 seconds. Figure 2.33 is a time history of characteristic attenuation in X-, C-, and L-bands observed through the Blue Gill fireball. Computations from available parameters indicate that most of the late-time observations from the ships were through the center of the fireball torus.

Available data does not reveal whether the debris concentration in the center of the torus is significantly different from concentrations within the torus itself. Although the shapes of the Blue Gill fireball and its torus were not well defined, a spherical fireball was assumed in order to facilitate computations.

A second major point of interest is the large amplitude scintillations during recovery periods. Even though transmissions pass through the fireball at these later times, the effect of the scintillations must be interpreted individually for different systems. In some cases the effect may be to deny information to a tracking system for an additional 30 to 40 seconds. The periods of time during which severe scintillations and absorption are observed are significant when considering ballistic missiles with re-entry velocities of Mach 20.

A third major point of interest indicates the extent of confinement of the attenuation-producing phenomena. Early recovery data from S-2, following the prompt radiation, and fixed station data, immediately prior to the beacon ray-path eclipse, suggest that the region which produces appreciable attenuation near the fireball periphery is relatively small. This indicates that most of the serious attenuation effects are confined closely to the region defined by the visible fireball.

2.5.3 Refraction. A very intensive investigation of Project 6.1 data has failed to produce any success in measuring refraction during the Blue Gill event. It should not be construed that refraction did not exist. Circumstances of project operation, combined with support data problems, prevented such measurements.

Page 131 deleted.

TABLE 2.3 TIME SPANS OF BLUE GILL RAW TRAJECTORY DATA

Missile	Time Span of Unextrapolated Data, seconds
A	H-105 to H-0
C	H-112 to H-52

TABLE 2.4 PROJECT 6.1 DATA RELIABILITY

Data	Accuracy
Relative signal strength	± 1.5 db ± 3.5 db within 10 db of noise
Azimuth and elevation pedestal information	± 1 degree
Refraction:	
Blue Gill, King Fish	± 0.4 milliradian
Tight Rope	± 0.2 milliradian
Ship positions	500 yards
Trajectory angle data[a]	± 2 degrees
Trajectory range data[a]	10 meters relative between targets
Fireball data[a]	Unavailable at this time

[a] Support-supplied information

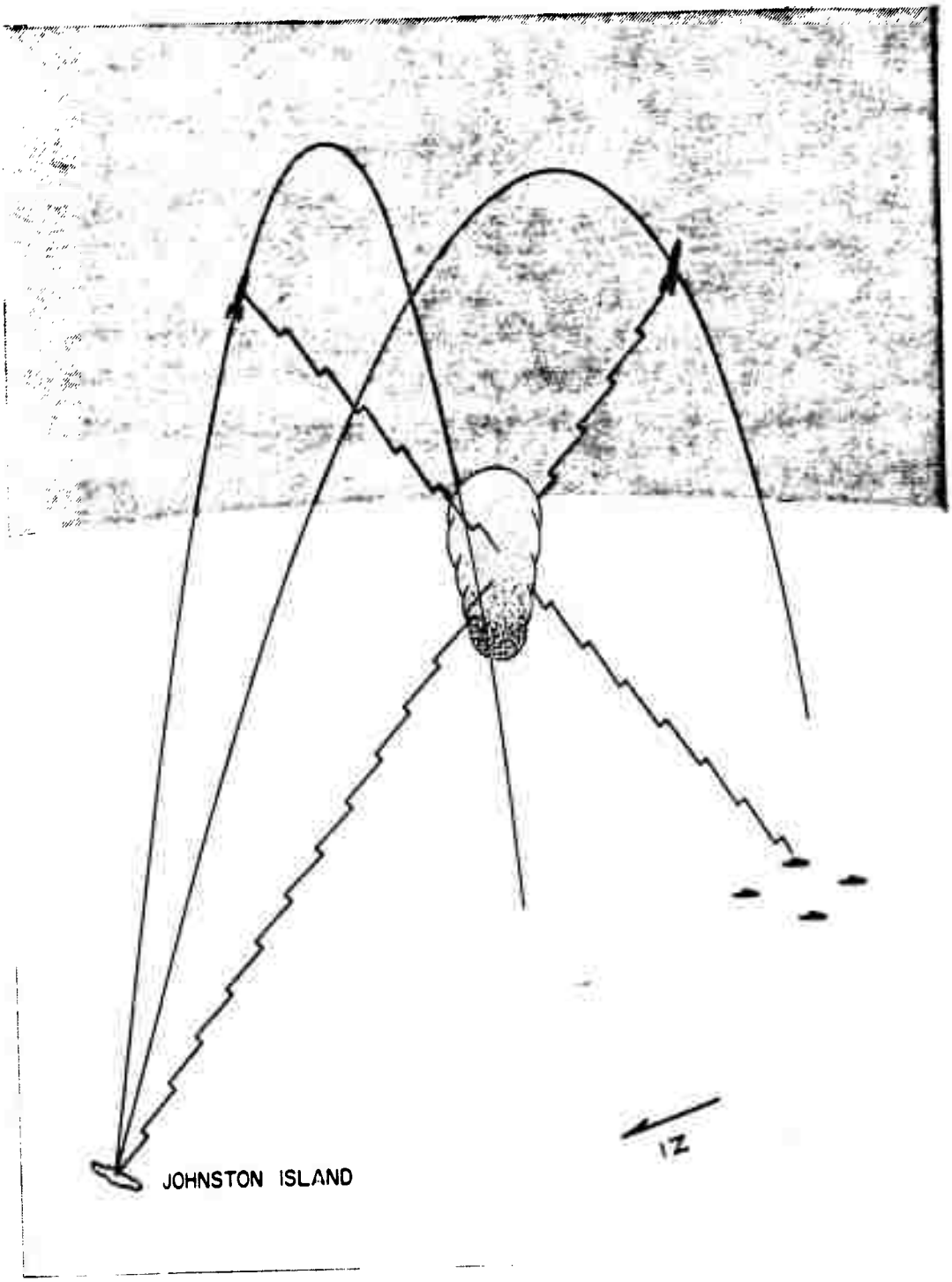

Figure 2.1 Blue Gill geometry, Project 6.1.

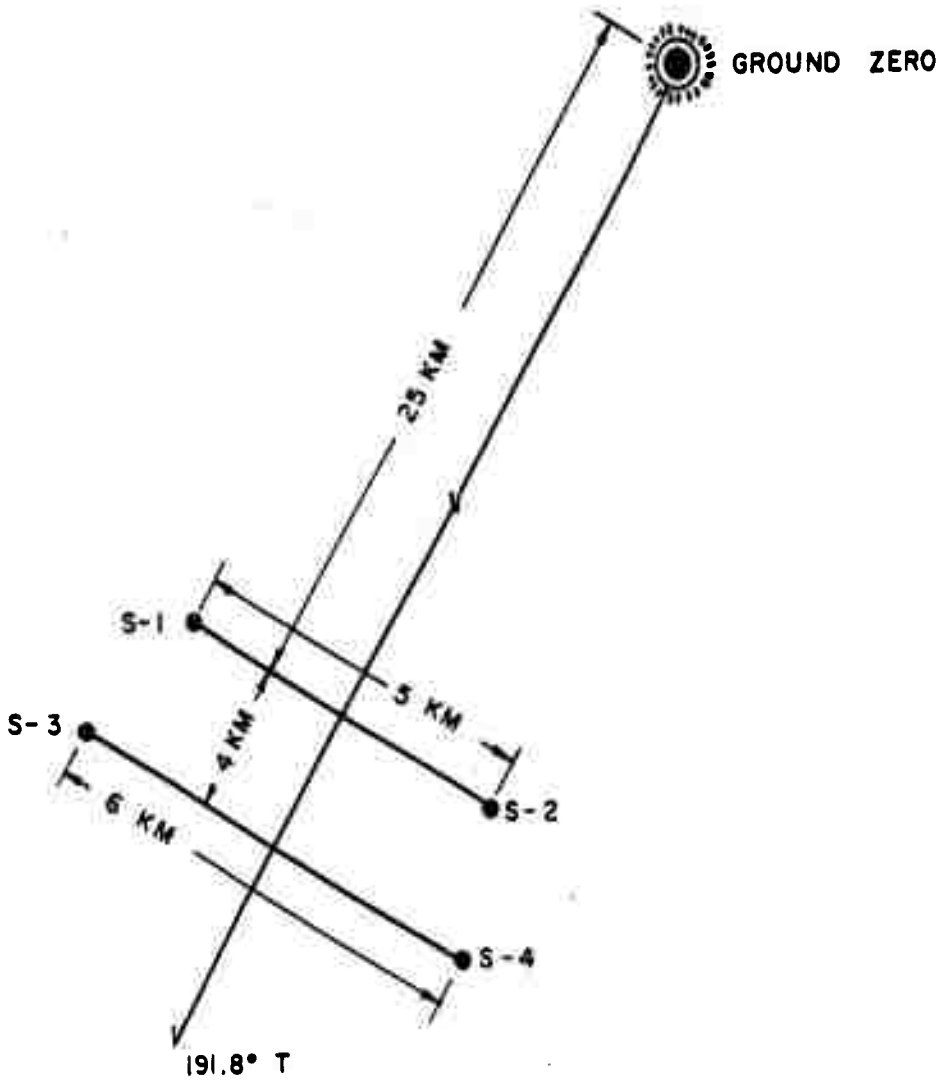

Figure 2.2 Proposed ship positions at H-hour for Blue Gill.

Pages 135 and 136 deleted.

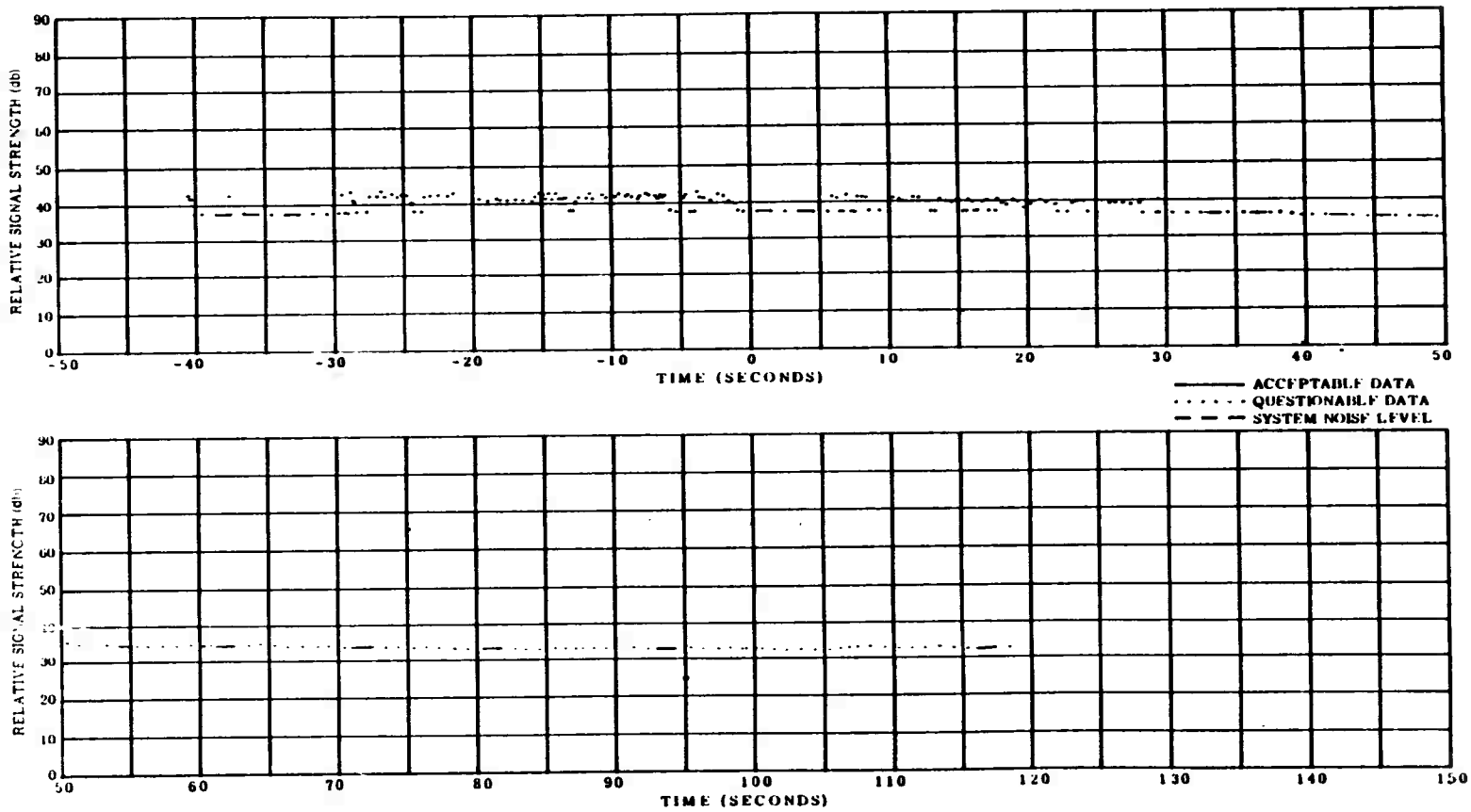

Figure 2.5 X band relative signal strength, Blue Gill, Missile A, interferometer.

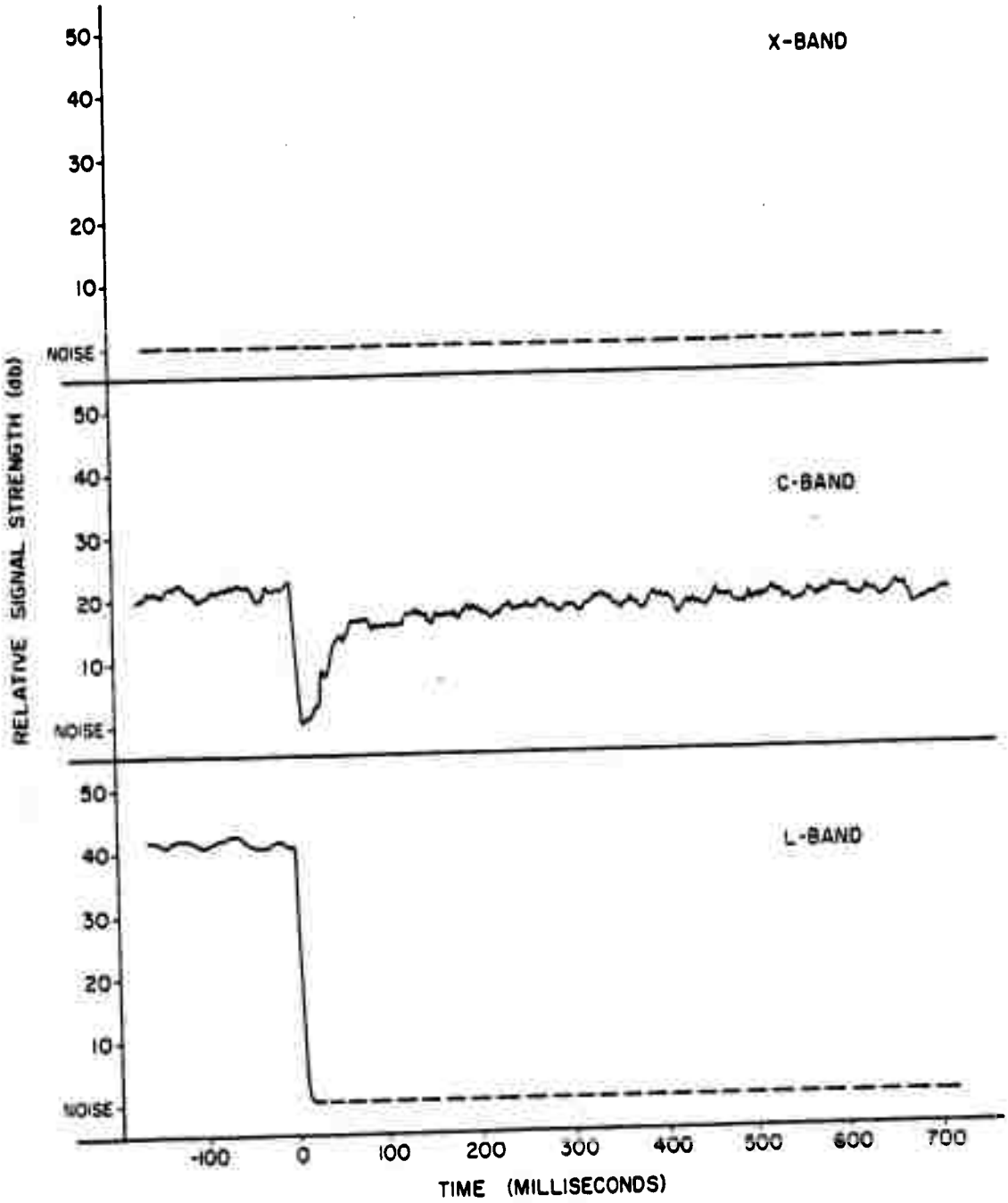

Figure 2.6 Relative signal strength, Blue Gill, Missile A, interferometer.

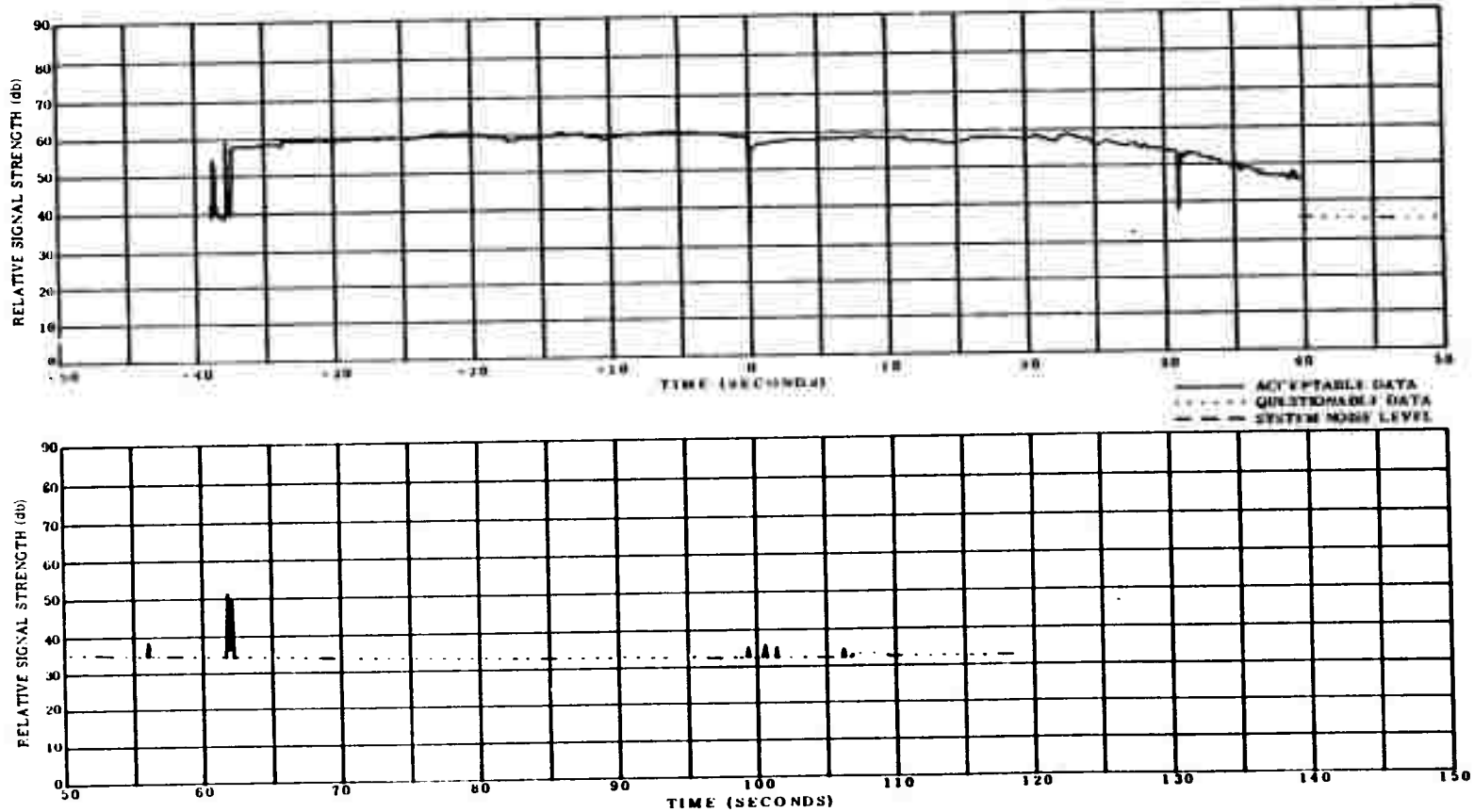

Figure 2-7 C-band relative signal strength, Blue Gill, Missile A, interferometer.

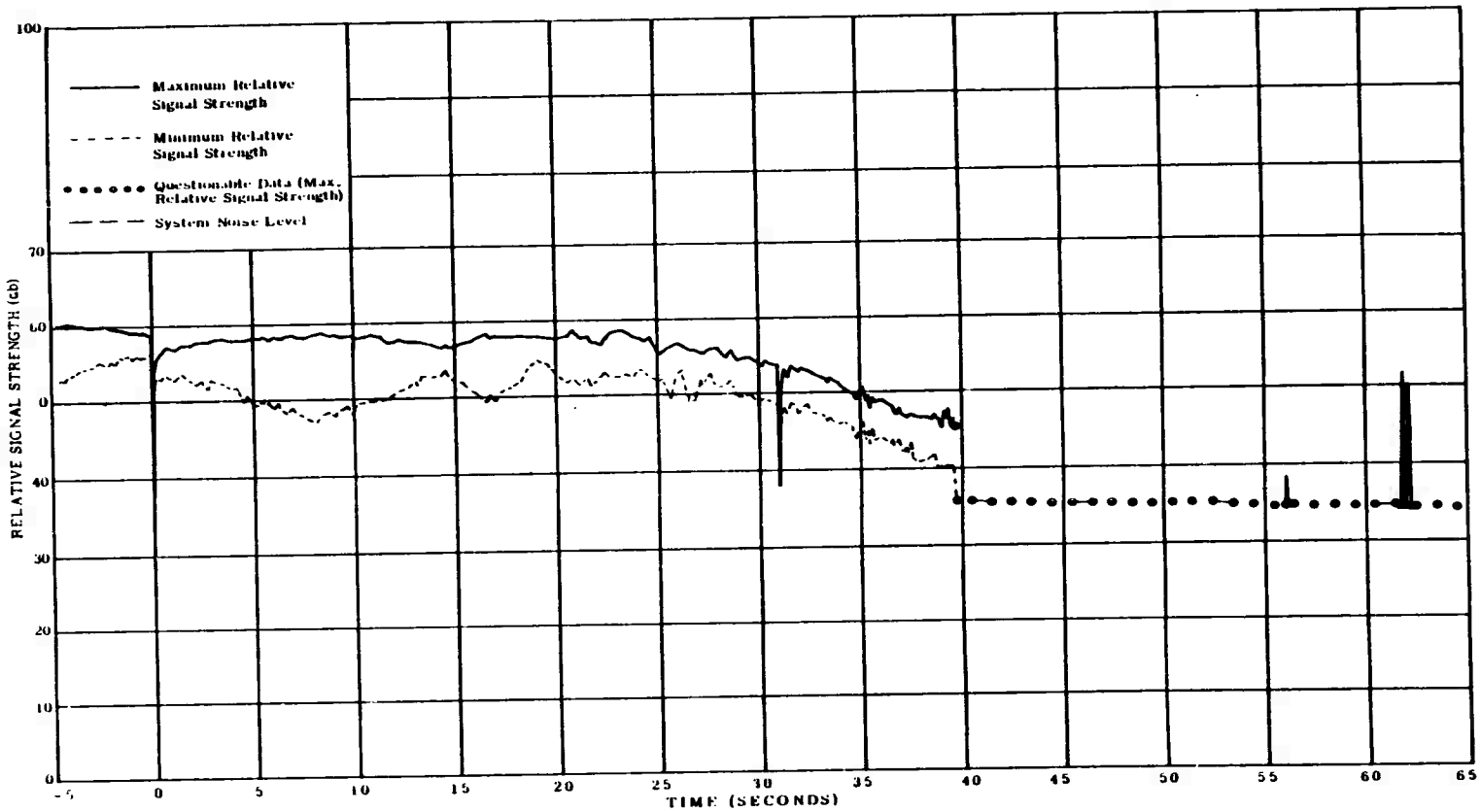

Figure 2 8 C band relative signal strength envelopes, Blue Gill, Missile A, interferometer.

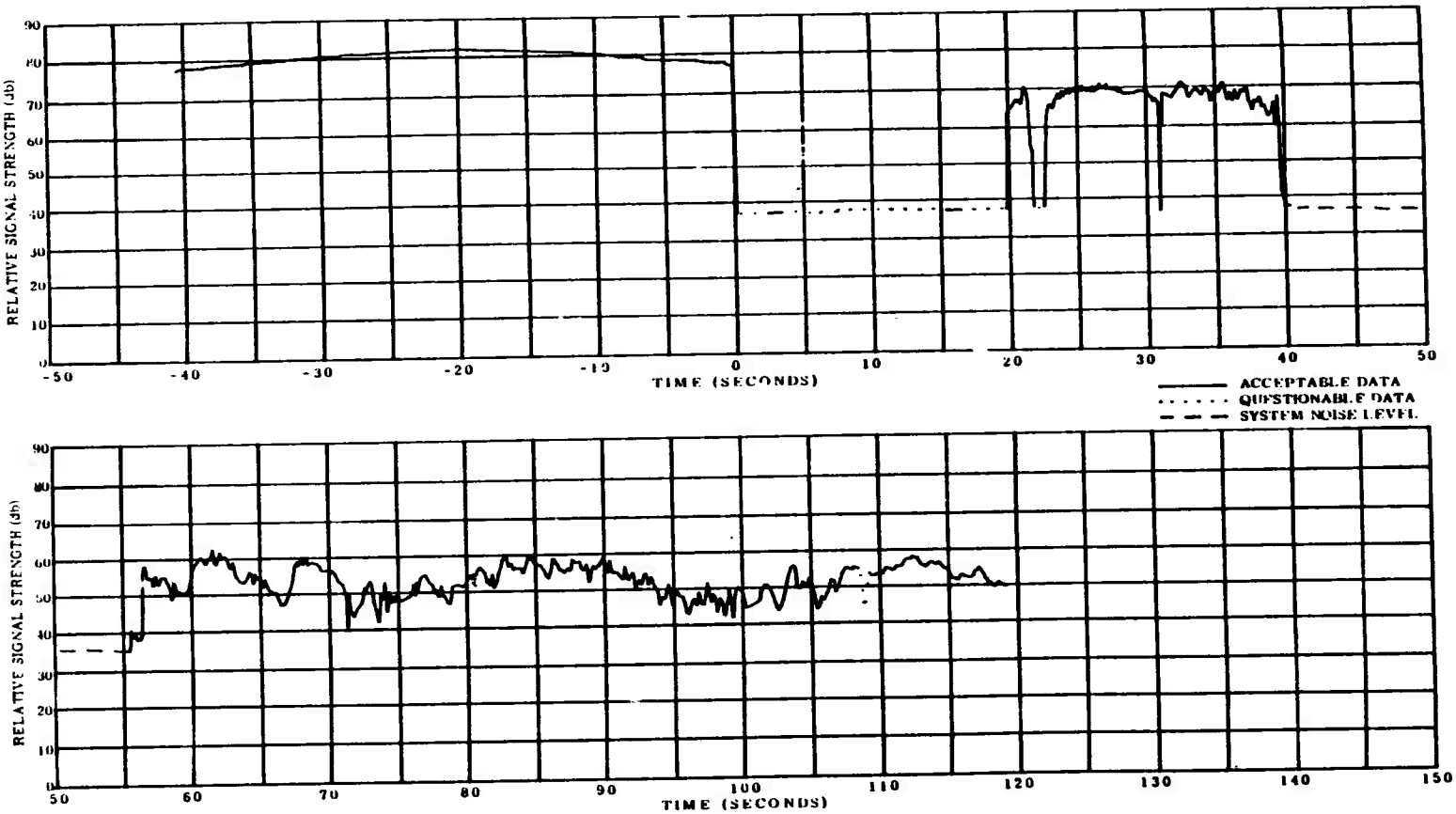

Figure 2.9 L-band relative signal strength, Blue Gill, Missile A, interferometer.

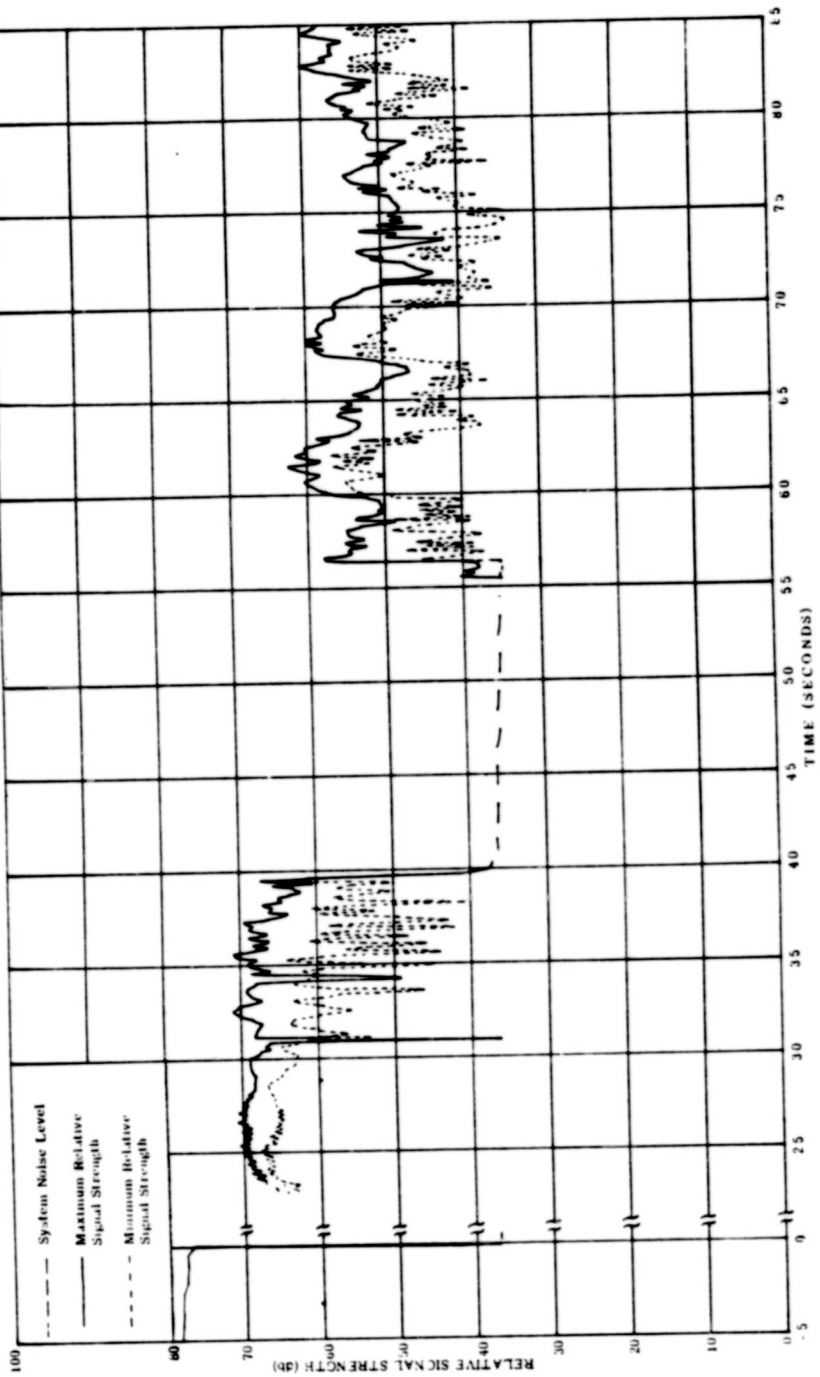

Figure 2.10 L-band relative signal strength envelopes, Blue Gill, Missile A, interferometer.

Page 143 deleted.

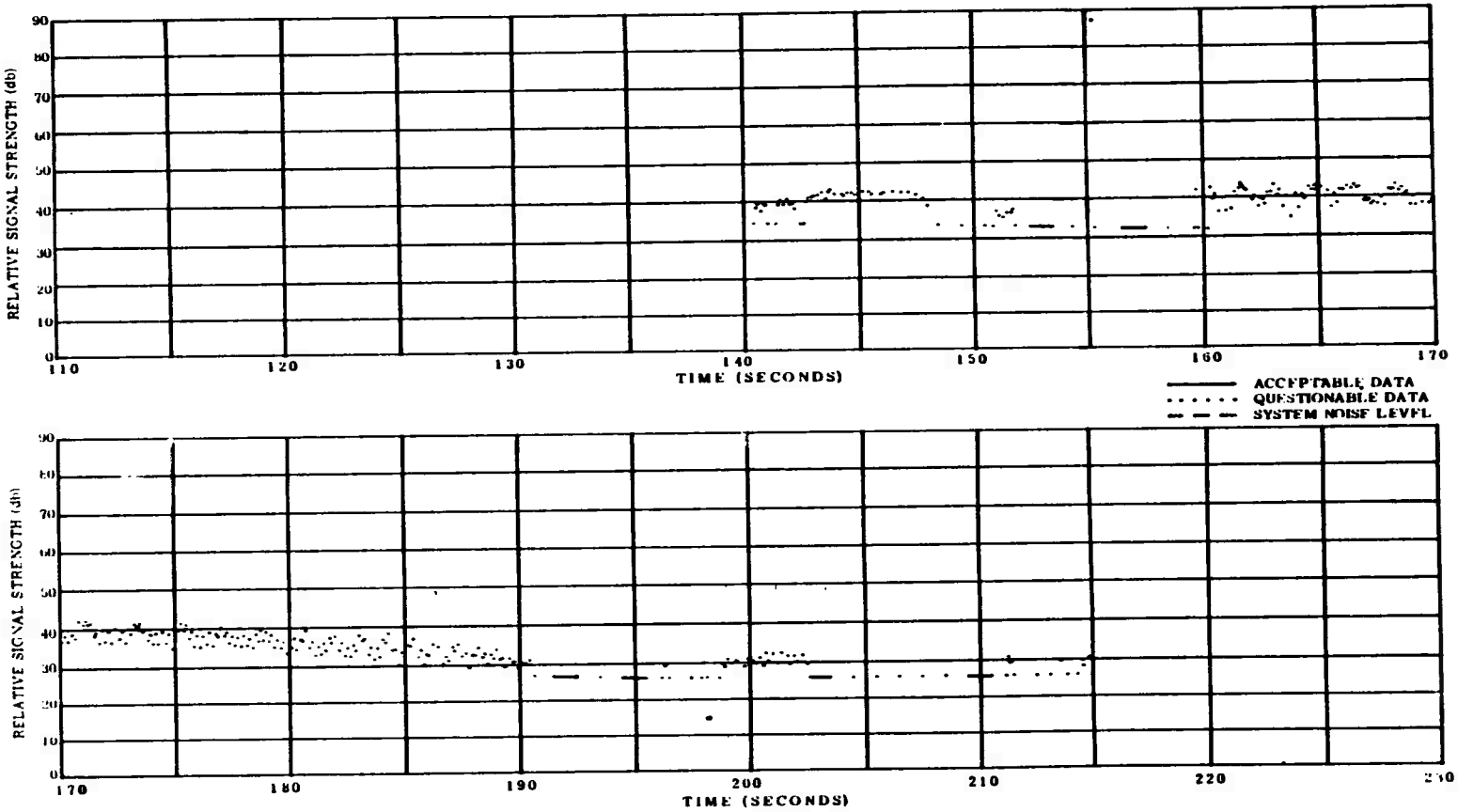

Figure 2.12 X-band relative signal strength, Blue Gill, Missile C, interferometer.

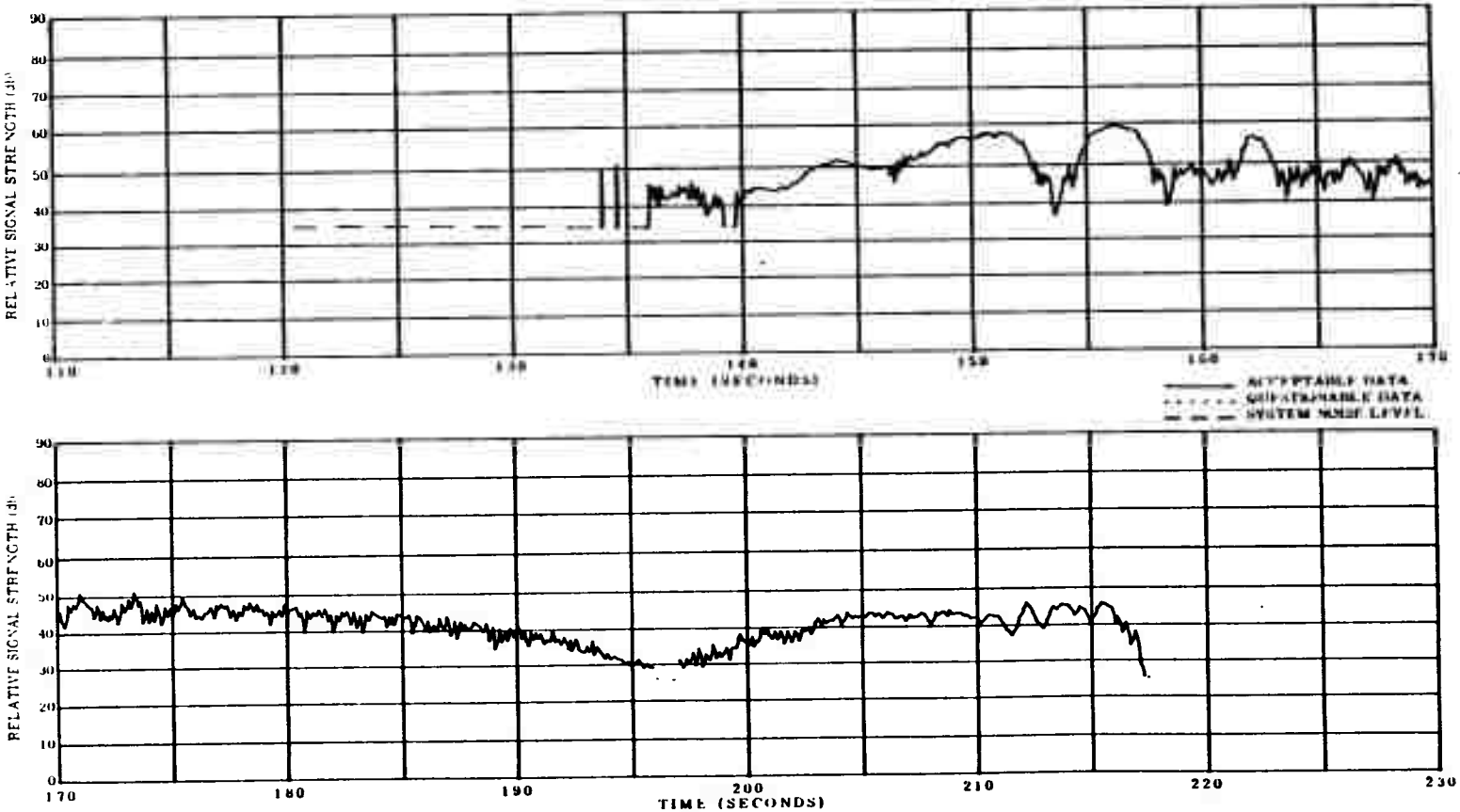

Figure 2.13 C-band relative signal strength, Blue Gill, Missile C, interferometer.

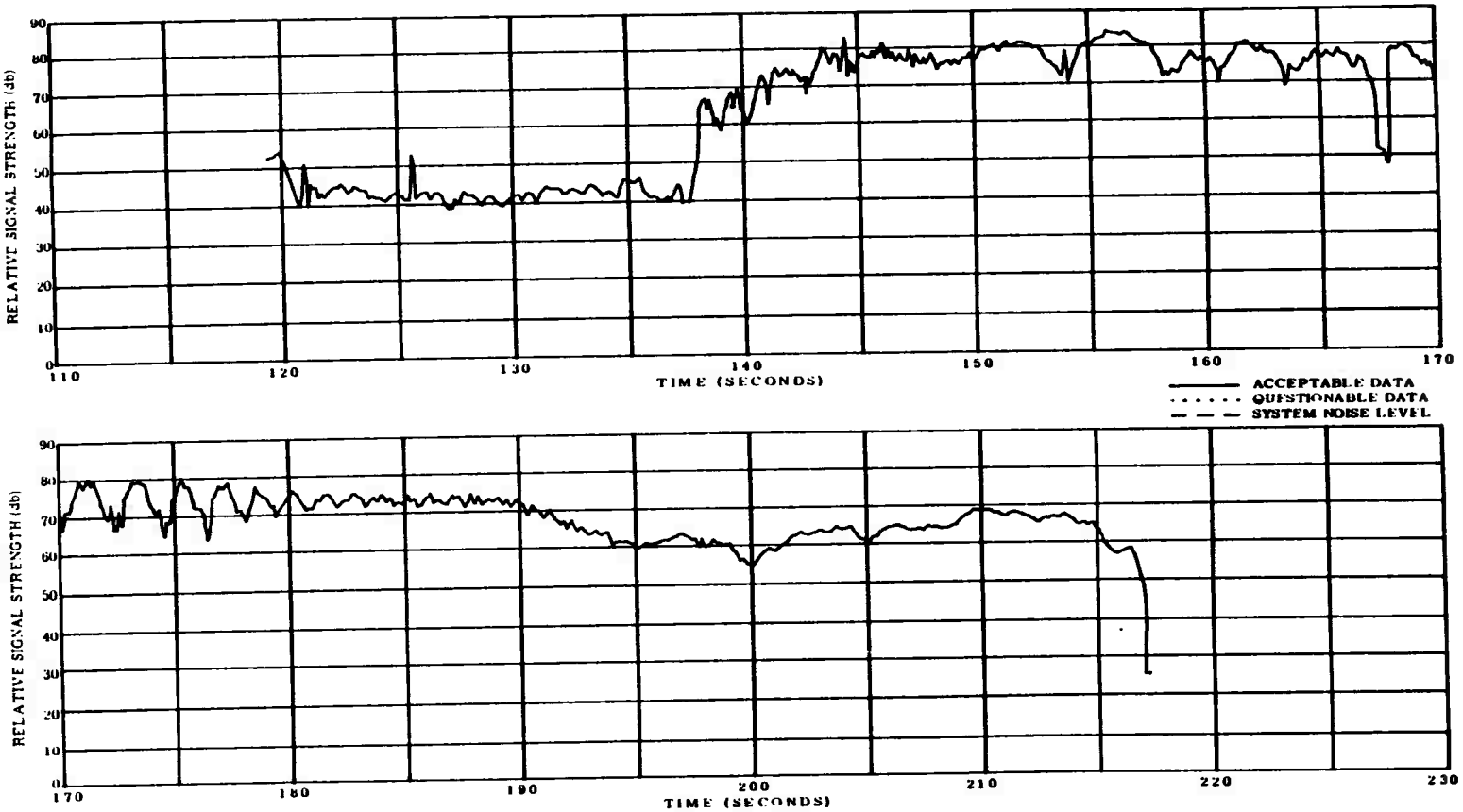

Figure 2.14 L-band relative signal strength, Blue Gill, Missile C, interferometer.

Page 147 deleted.

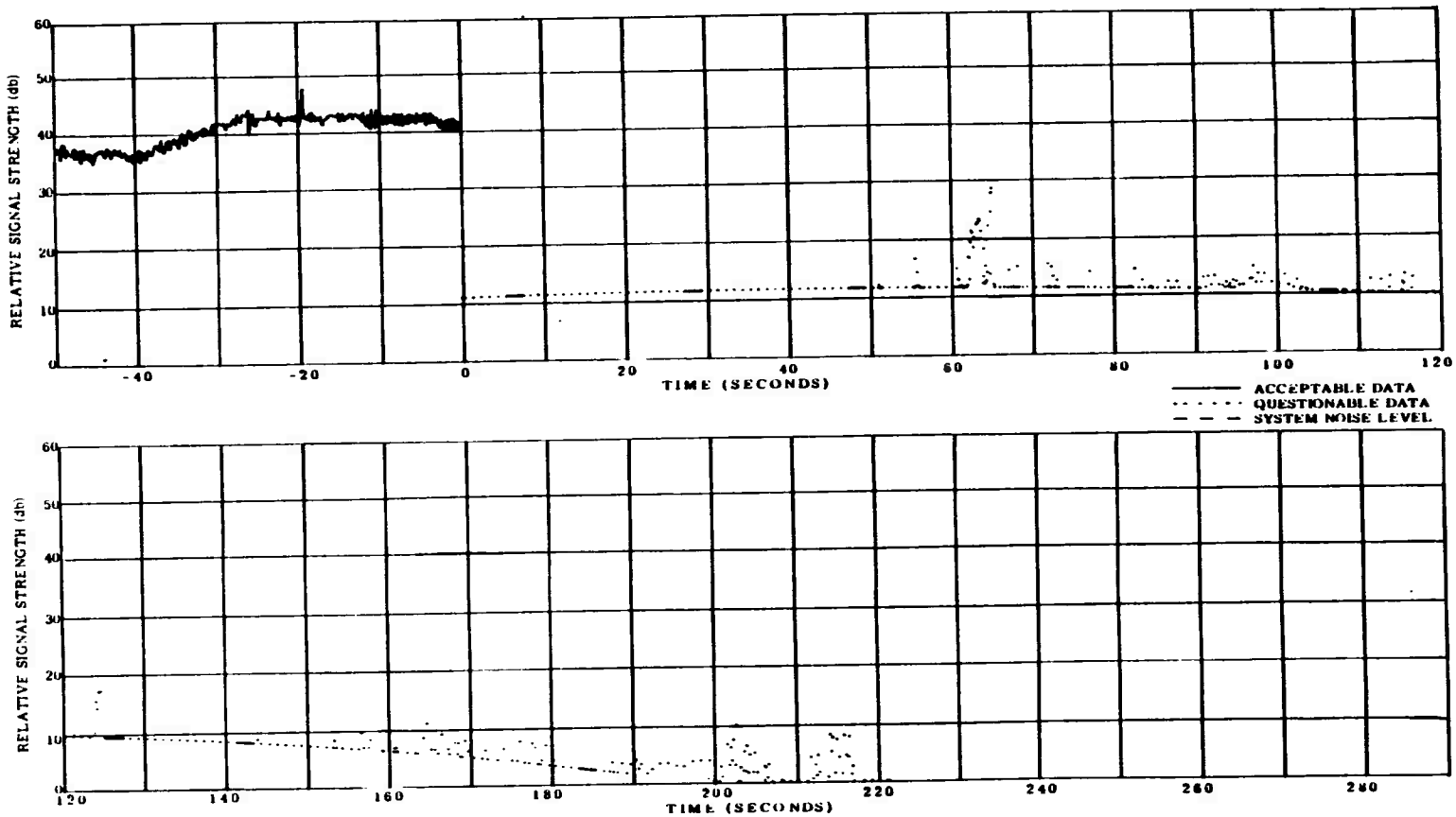

Figure 2.16 X-band relative signal strength, Blue Gill, Missile C, Ship 1.

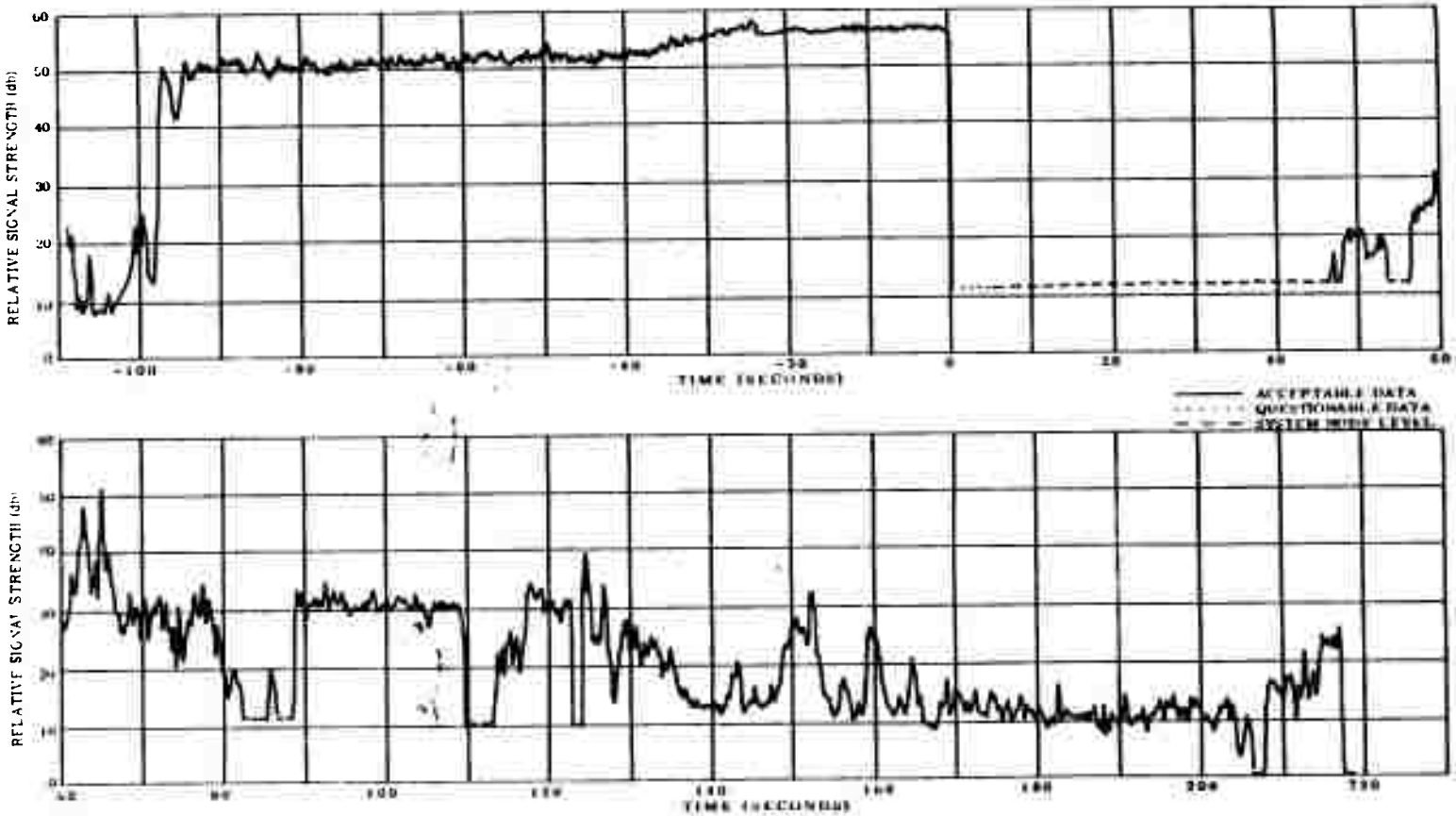

Figure 2.17 C band relative signal strength, Blue Gill, Missile C, Ship 1.

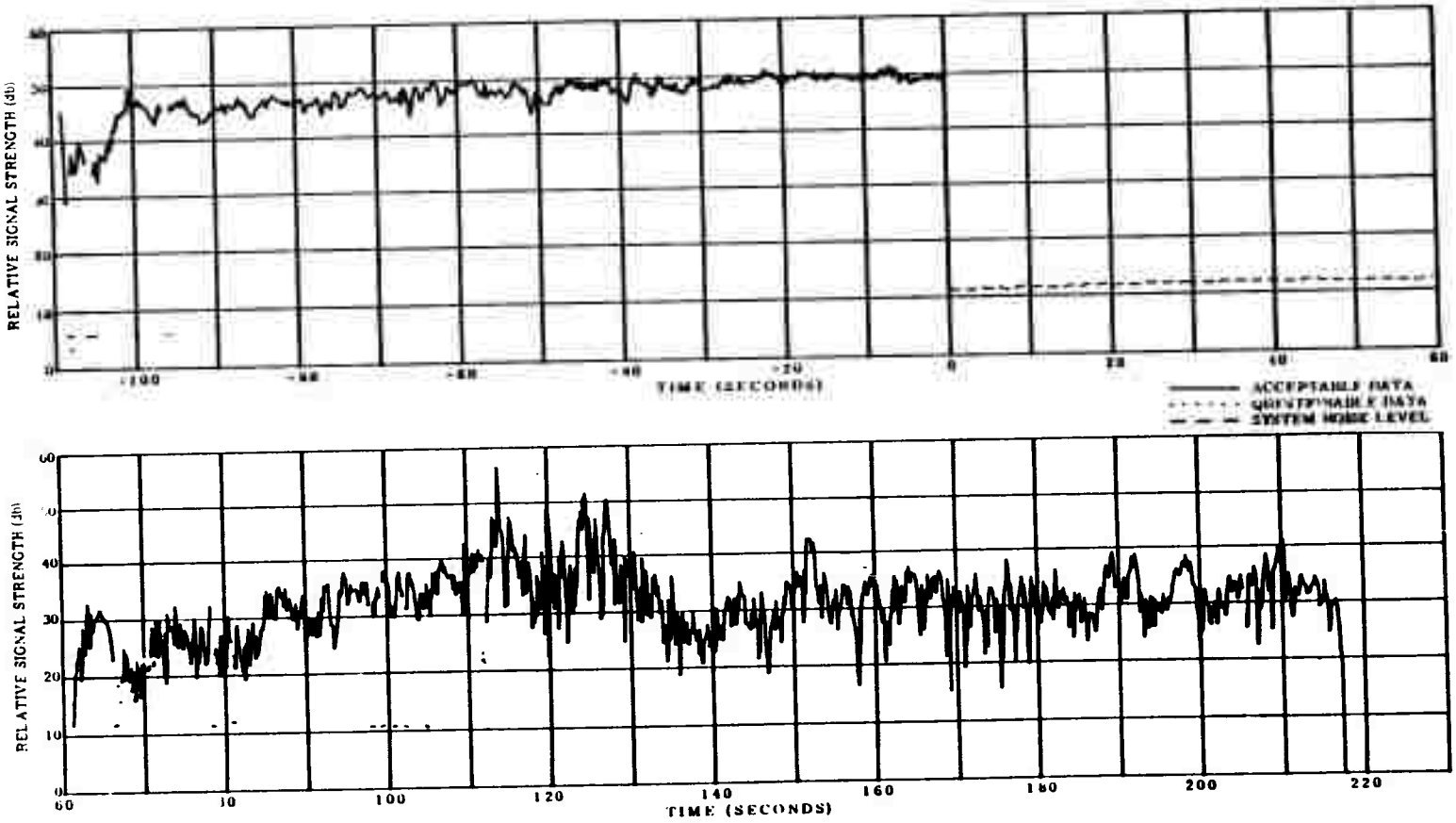

Figure 2.18 L-band relative signal strength, Blue Gill, Missile C, Ship 1.

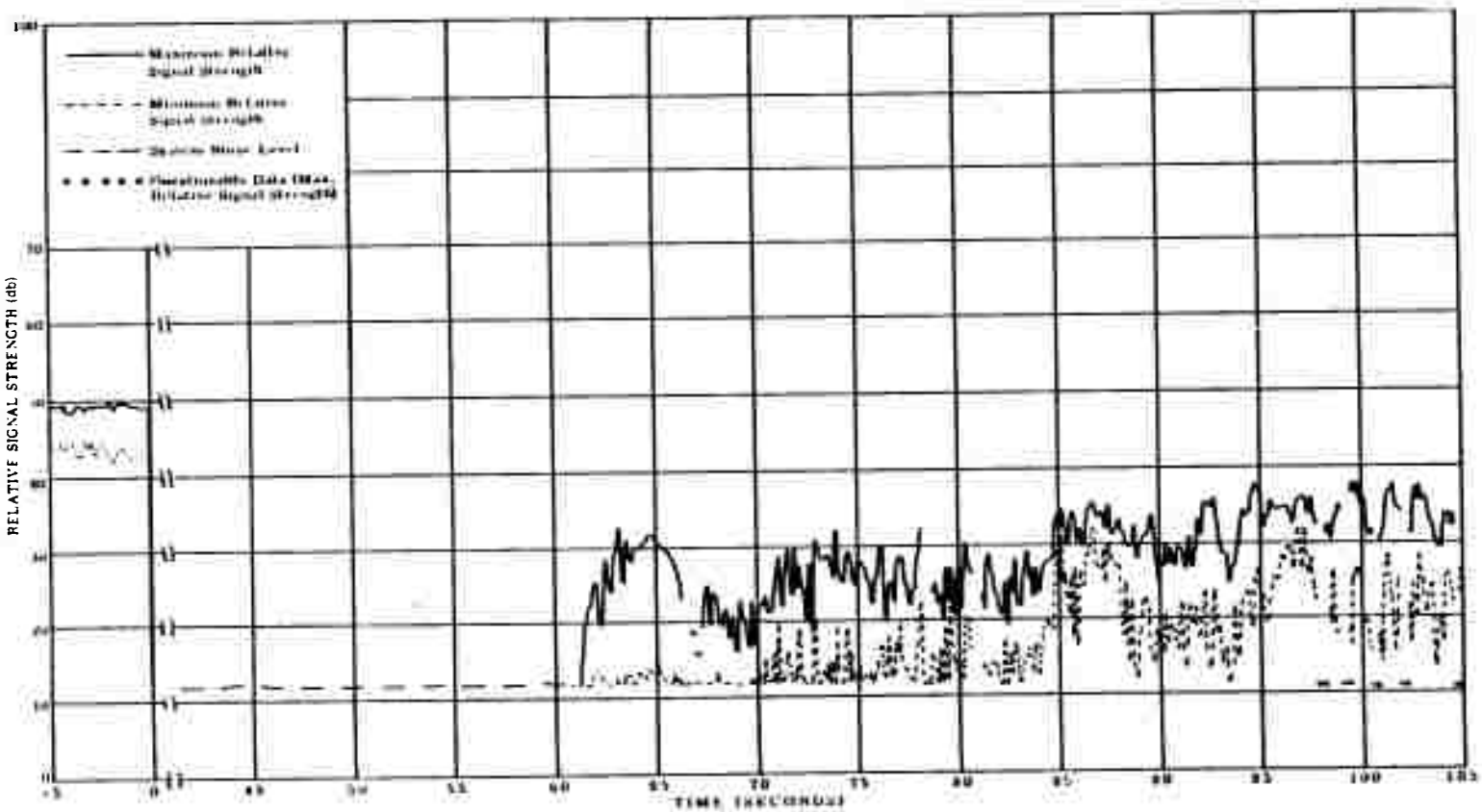

Figure 2 20 L-band relative signal strength envelopes, Blue Gill, Missile C, Ship 1.

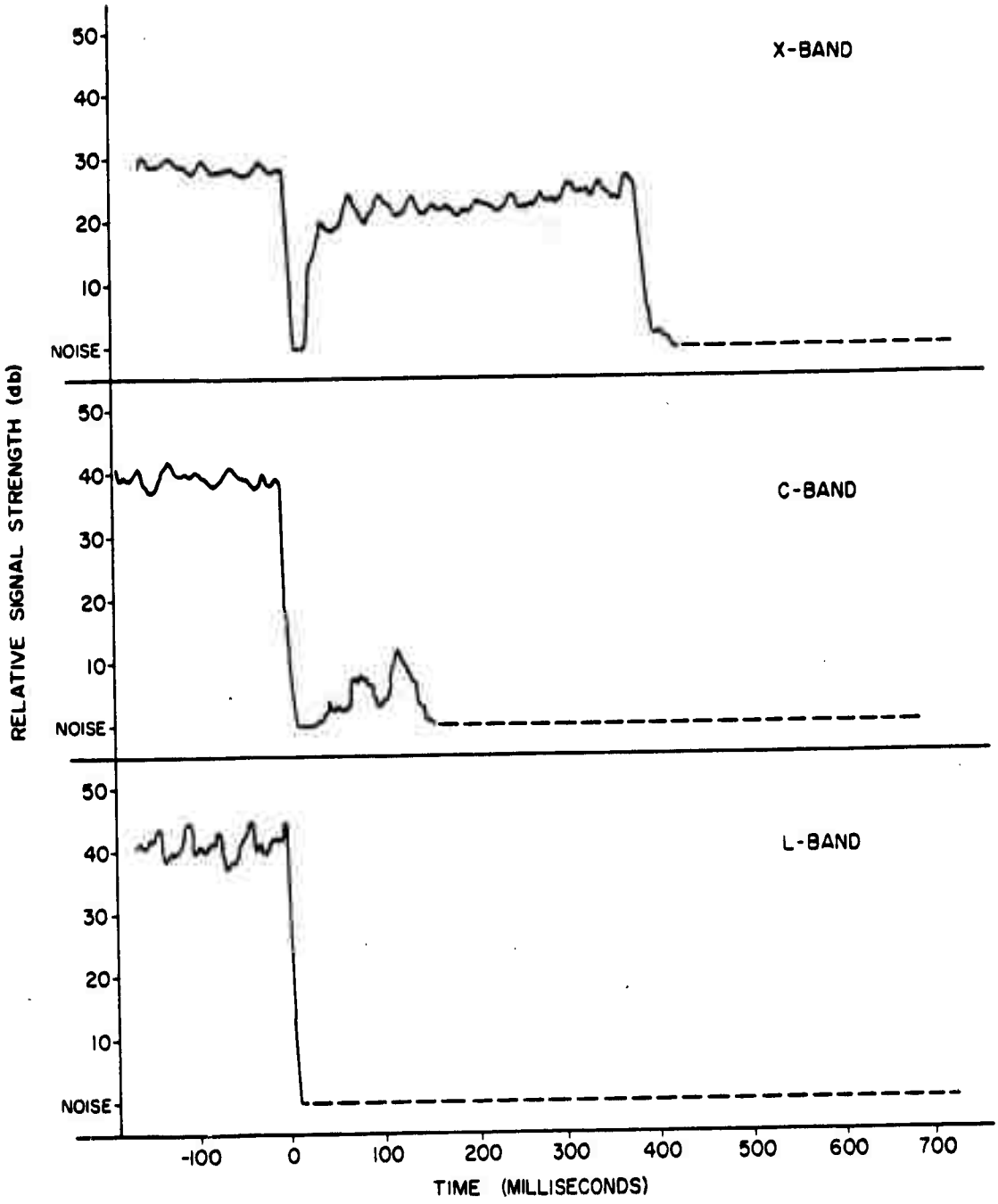

Figure 2.21 Relative signal strength, Blue Gill, Missile C, Ship 2.

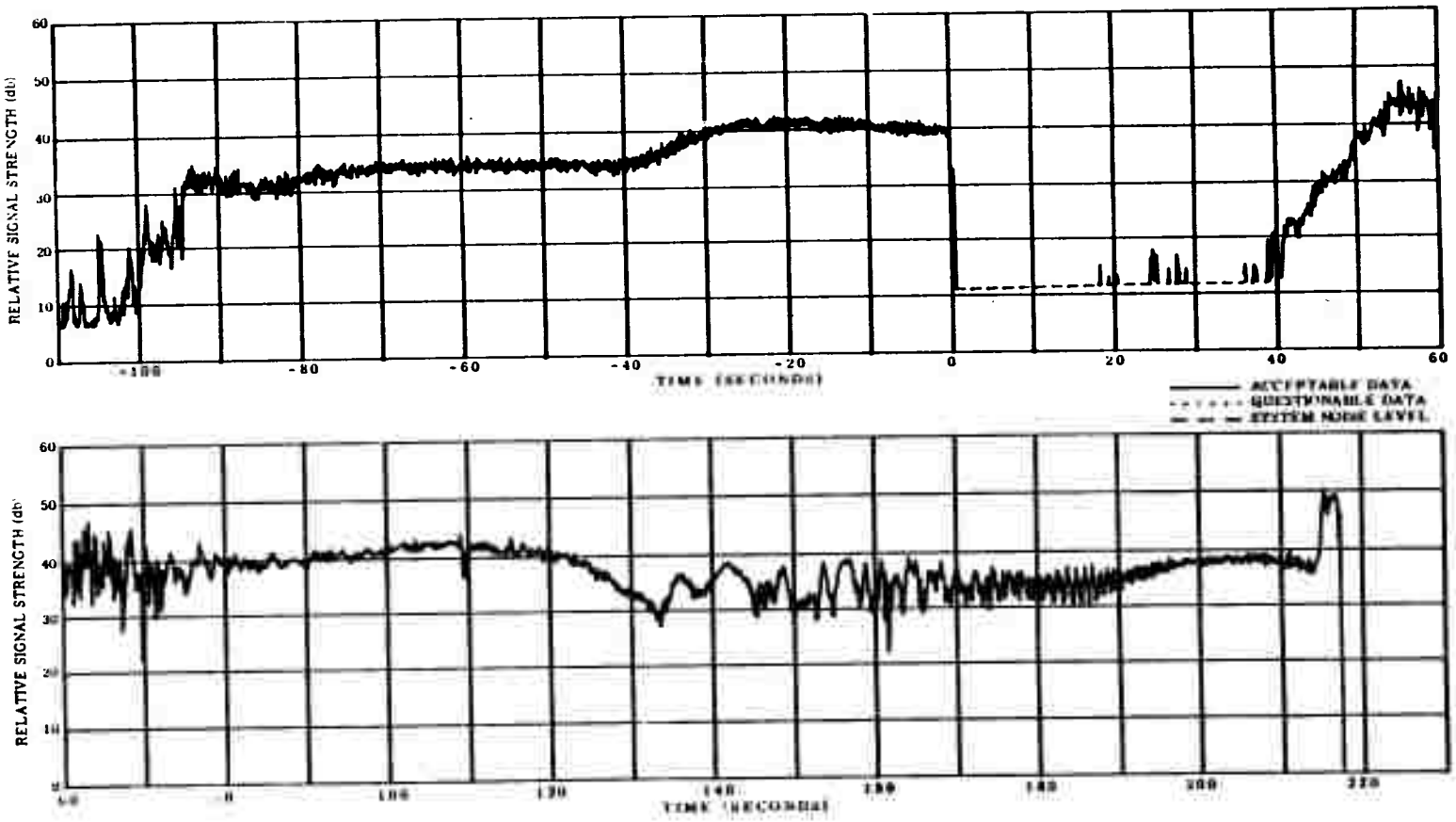

Figure 2.22 X-band relative signal strength, Blue Gill, Missile C, Slap 2.

Page 155 deleted.

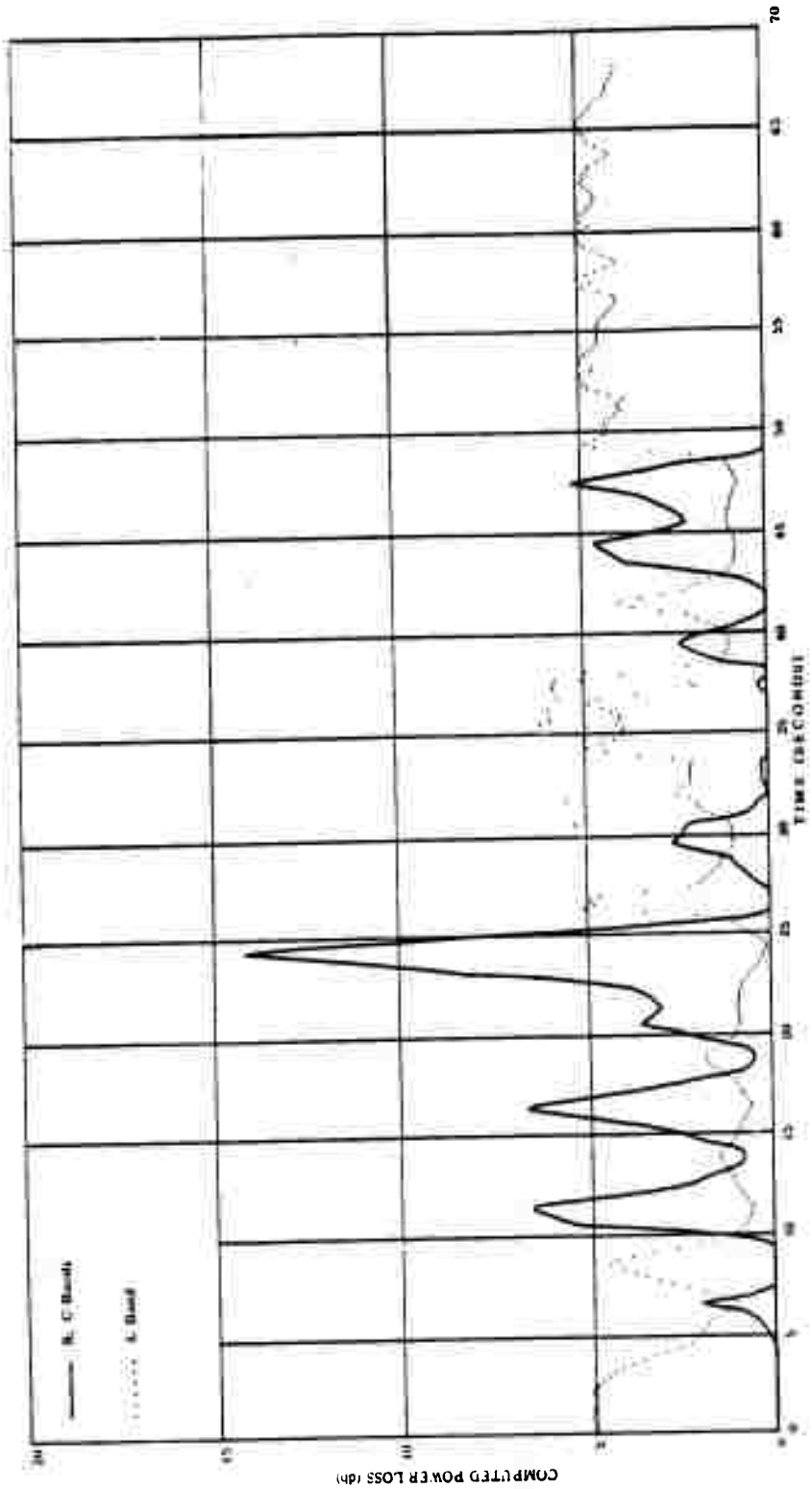

Figure 2.24 Computed power losses due to antenna-pointing errors, Blue Gill, Missile C, Ship 2.

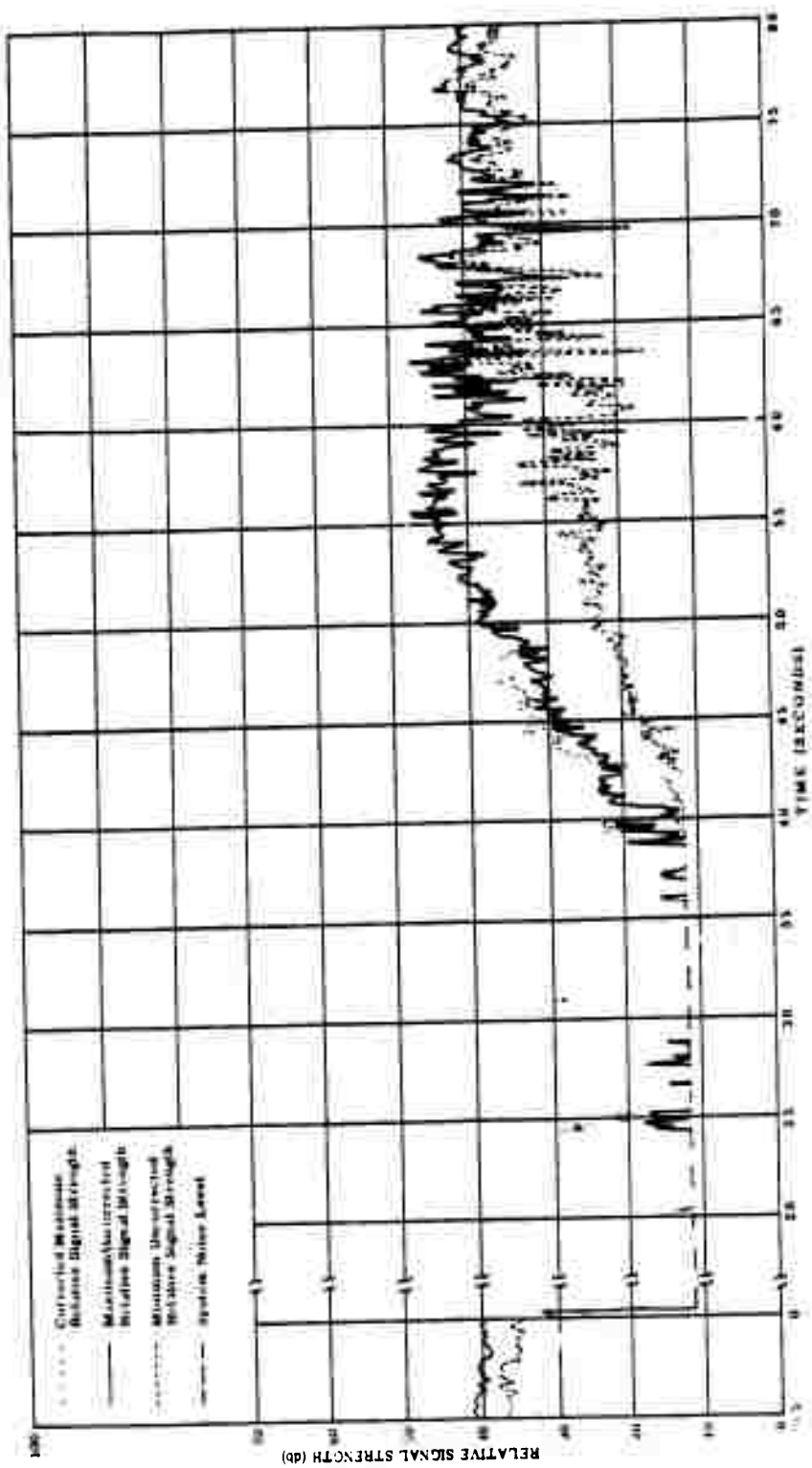

Figure 2.25 X-band relative signal strength with corrections for antenna-pointing errors, Blue Gill, Missile C, Ship 2.

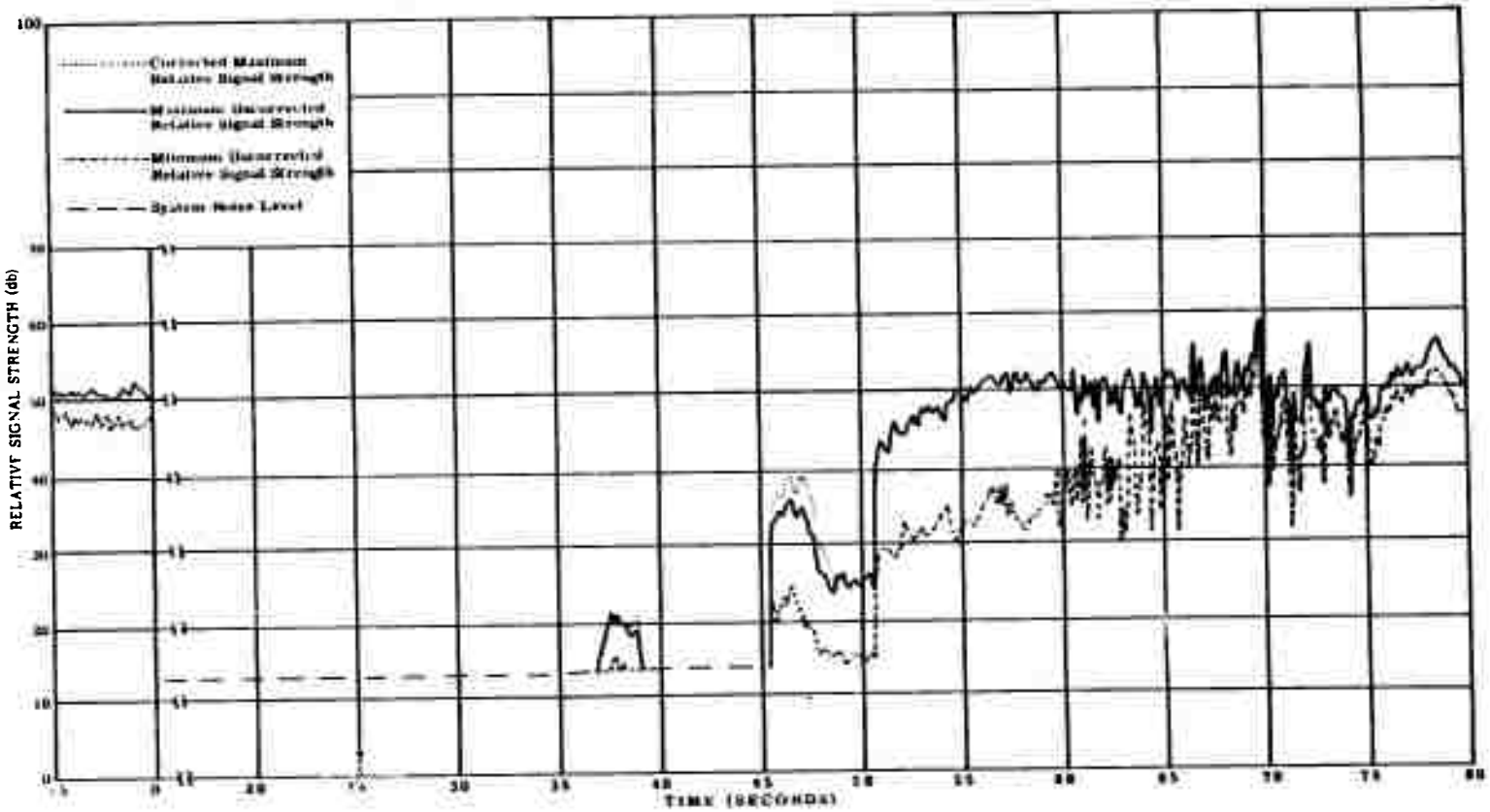

Figure 2.26 C-band relative signal strength with corrections for antenna-pointing errors, Blue Gill, Missile C, Ship 2.

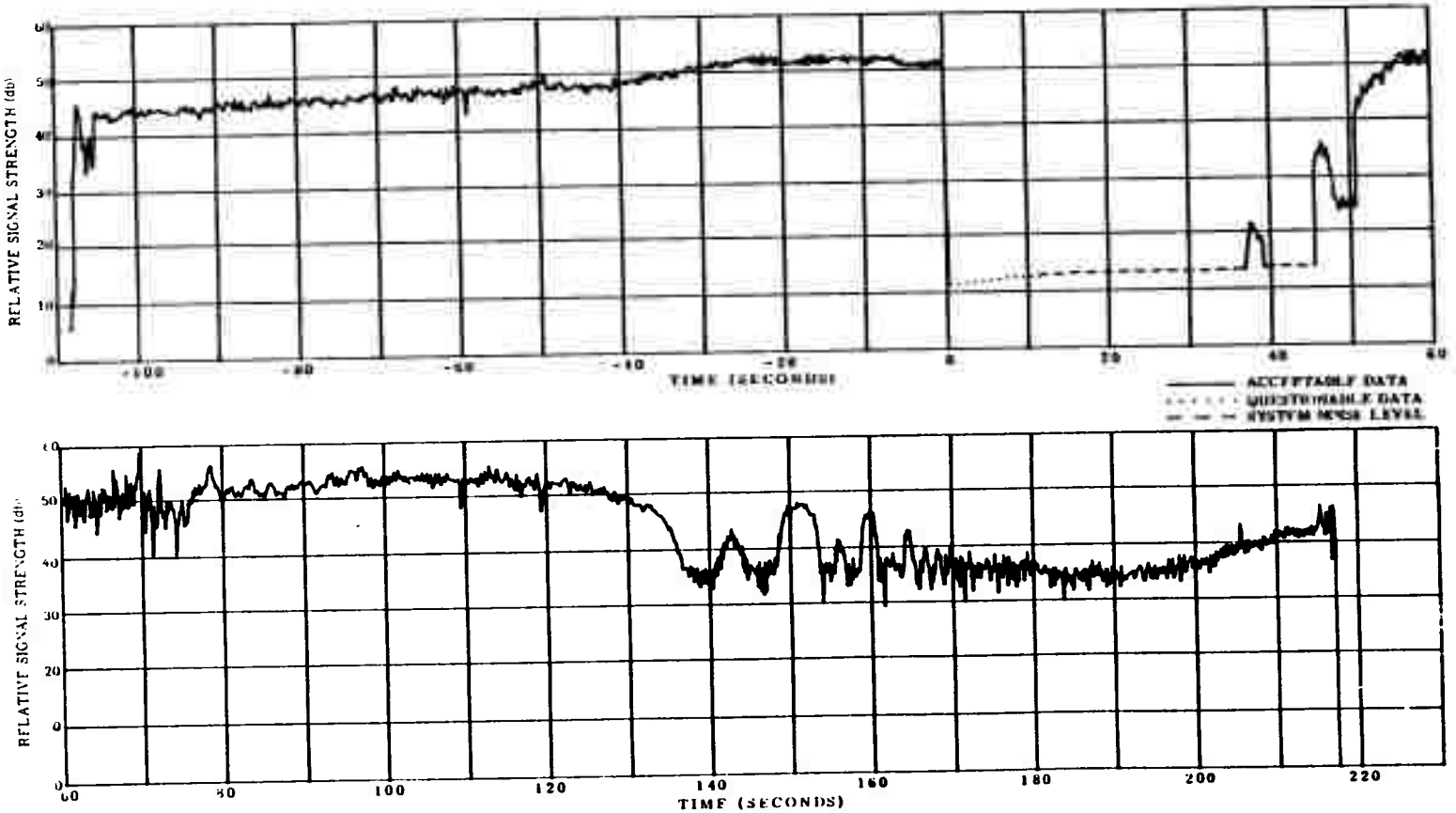

Figure 2.27 C band relative signal strength, Blue Gill, Missile C, Ship 2.

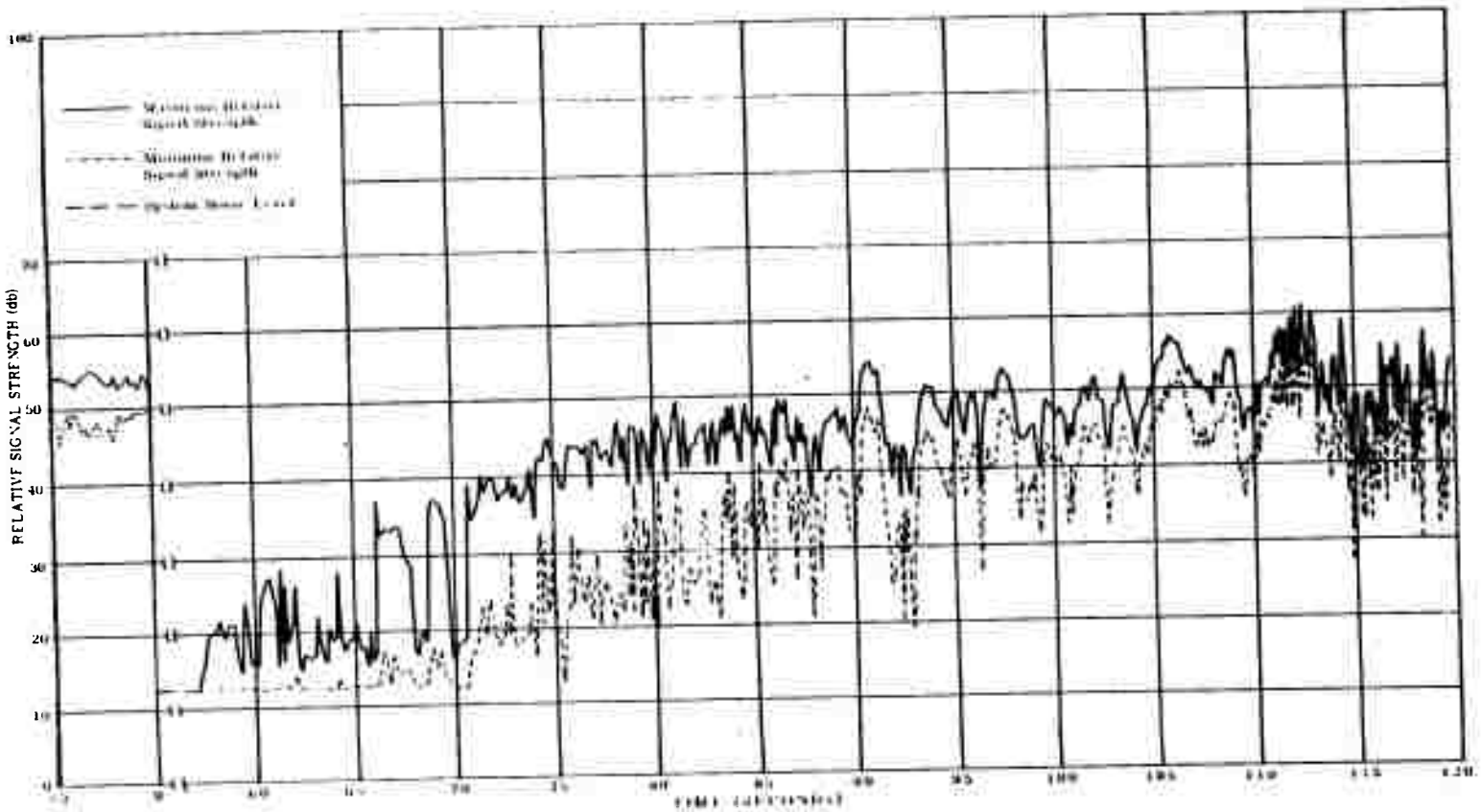

FIGURE 2.28 L BAND RELATIVE SIGNAL STRENGTH ENVELOPES, BLUE GILL, MISSILE C, SHIP 2.

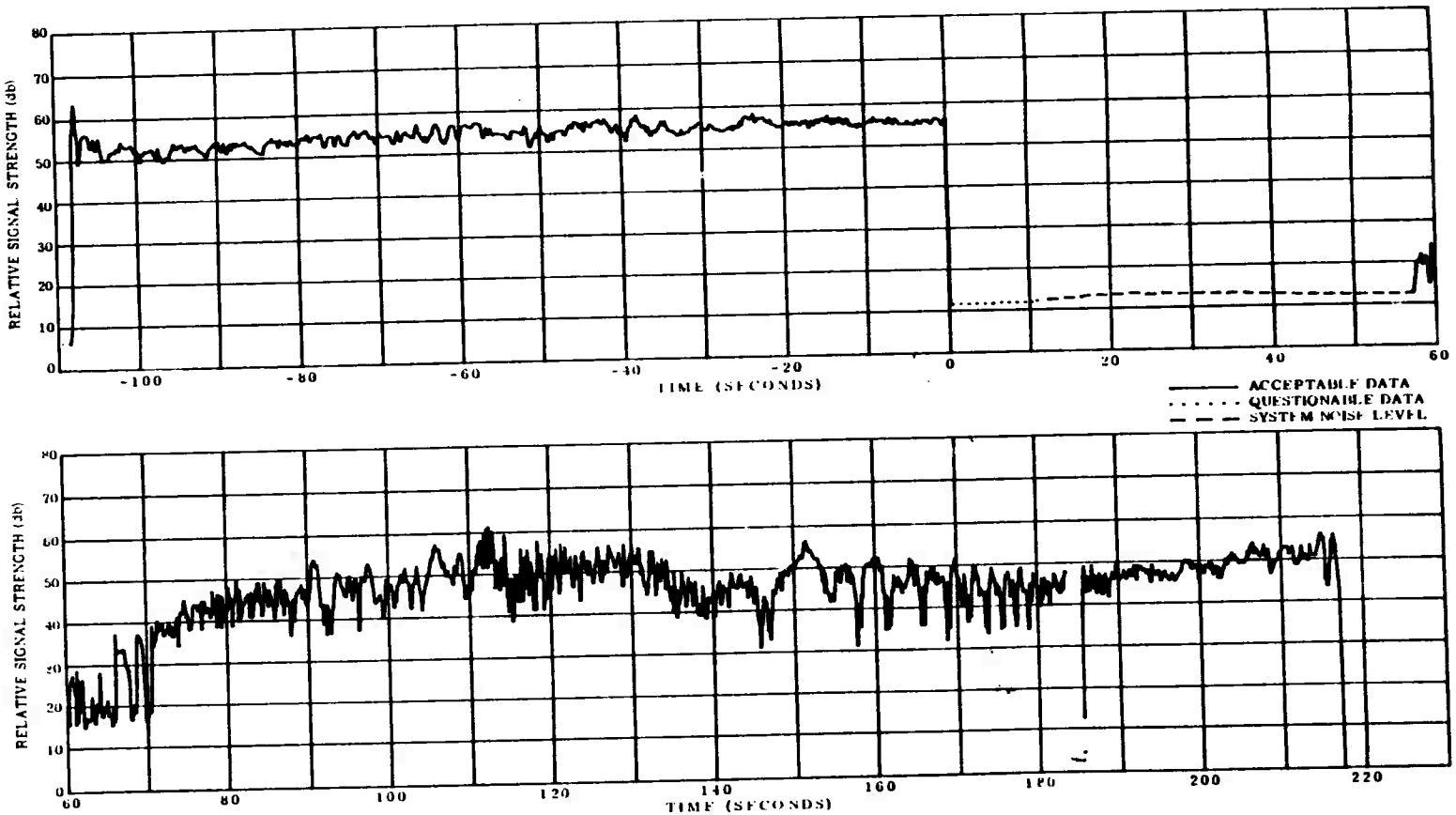

Figure 2.29 L band relative signal strength, Blue Gill, Missile C, Ship 2.

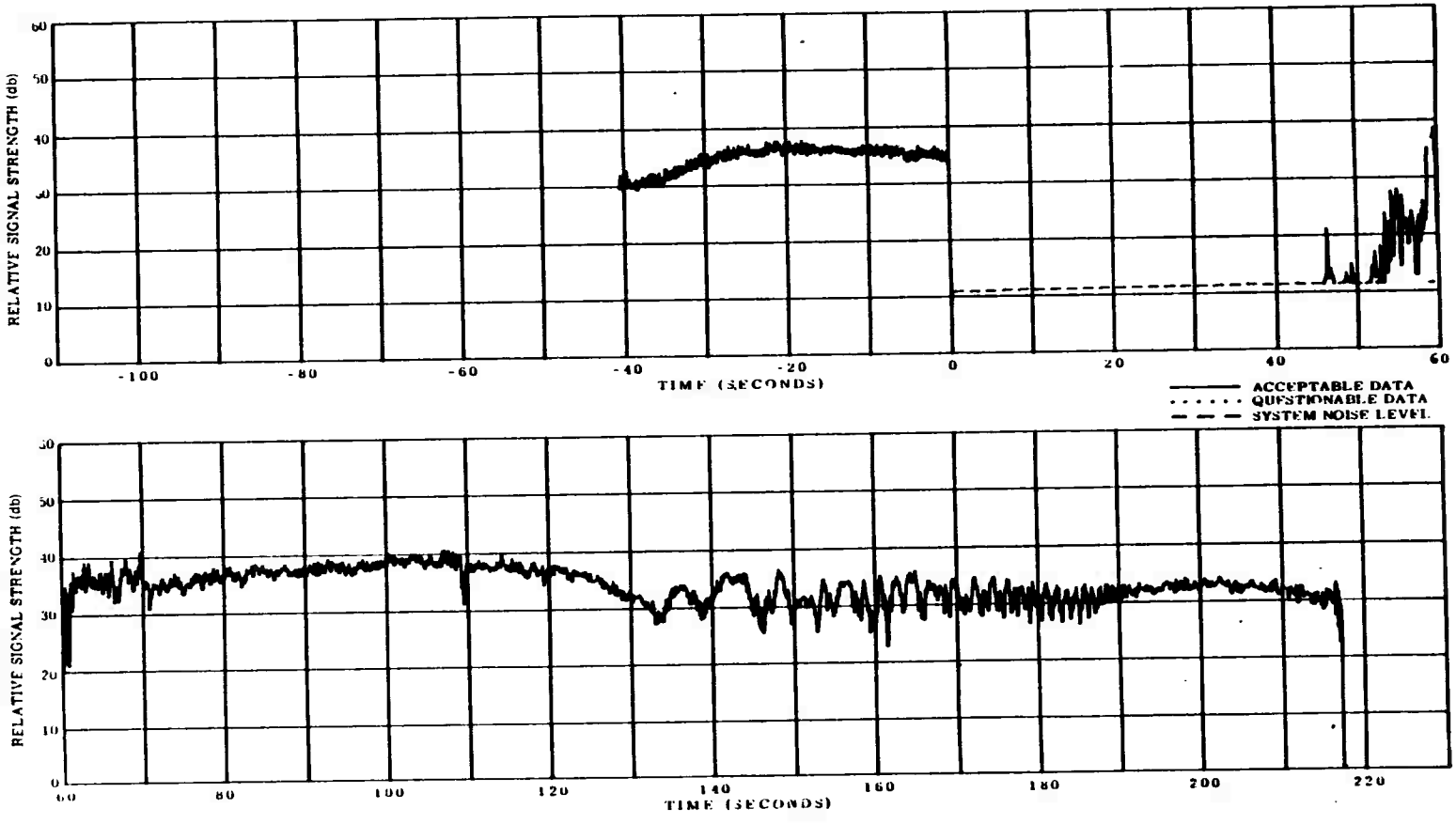

Figure 2.30 X-band relative signal strength, Blue Gill, Missile C, Ship 3.

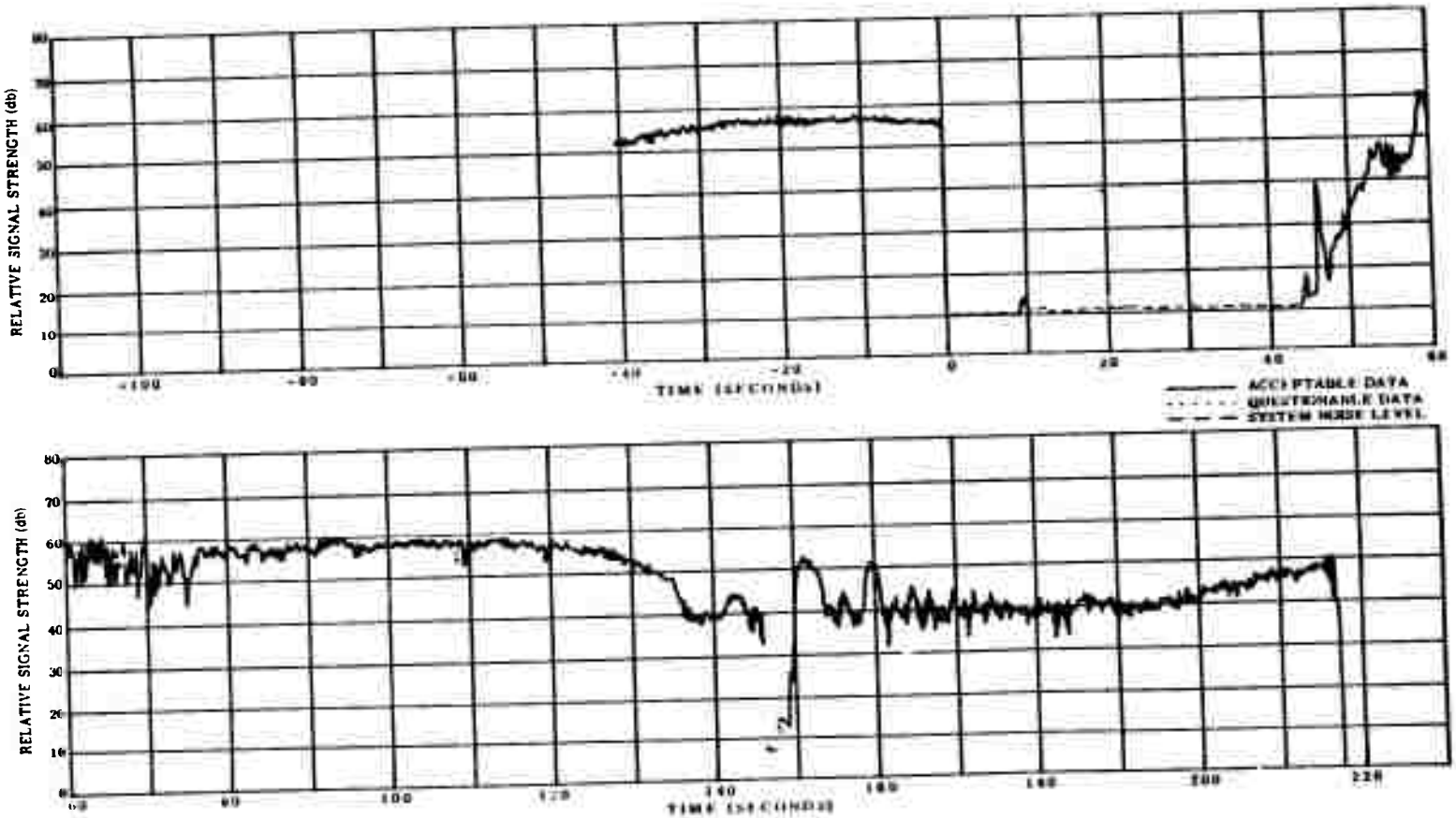

Figure 2.31 C-band relative signal strength, Blue Gill, Missile C, Ship 3.

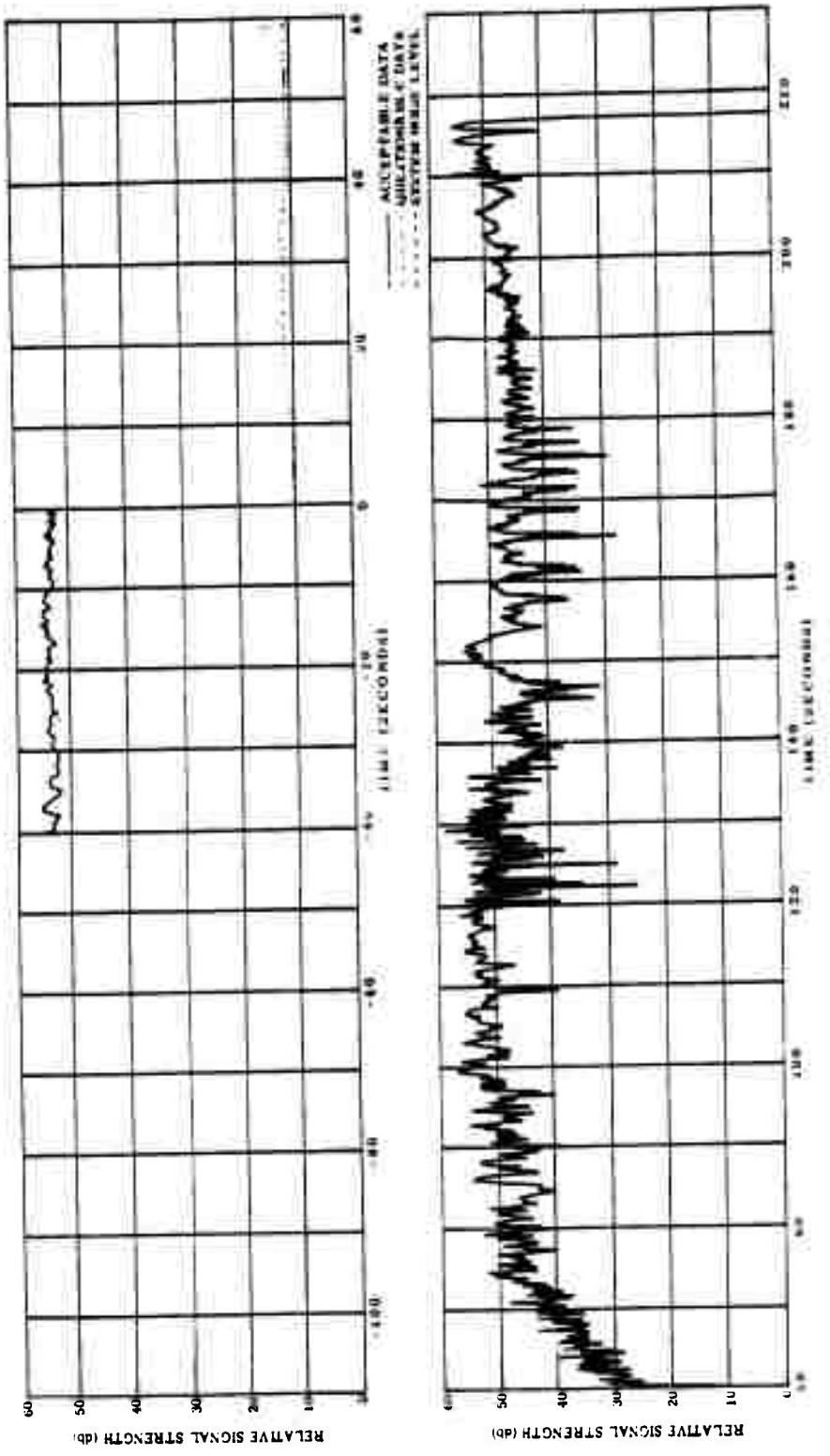

Figure 2.32 L-band relative signal strength, Blue Gill, Missile C, Ship 3.

Page 165 deleted.

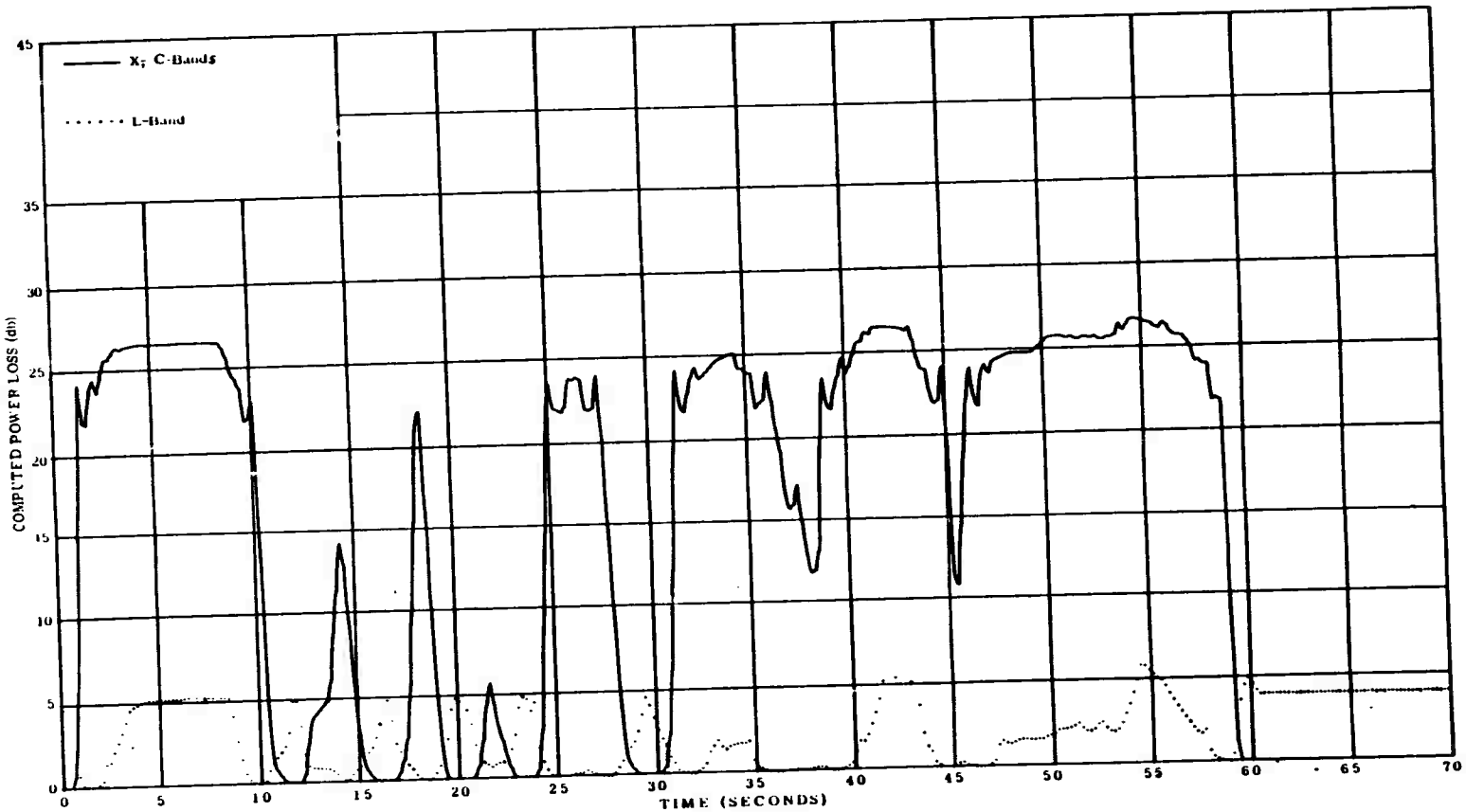

Figure 2 34 Computed power losses due to antenna-pointing errors, Blue Gill, Missile C, Ship 3

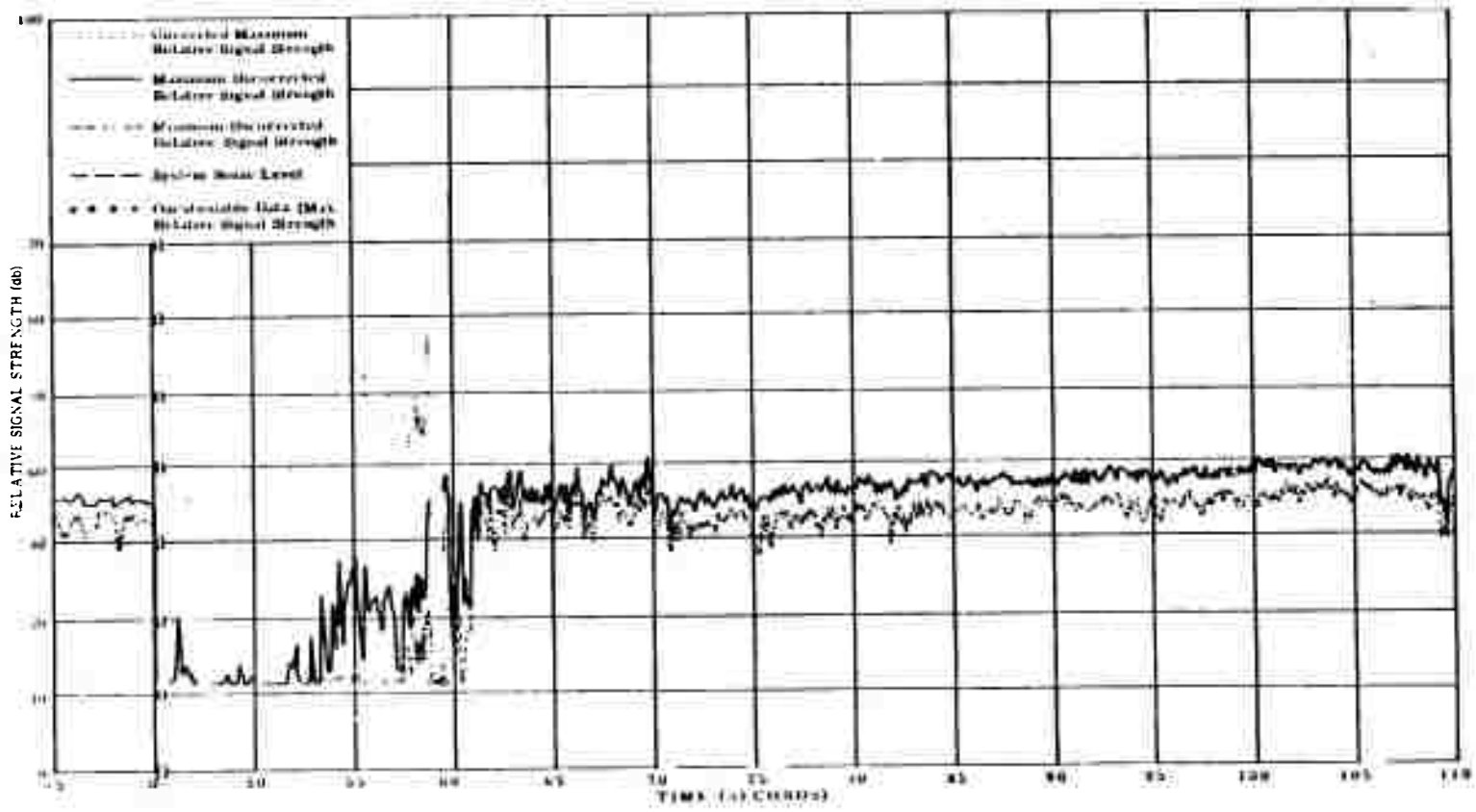

Figure 2-35 X Band relative signal strength with corrections for antenna pointing errors, Blue Gill, Missile C, Ship 3.

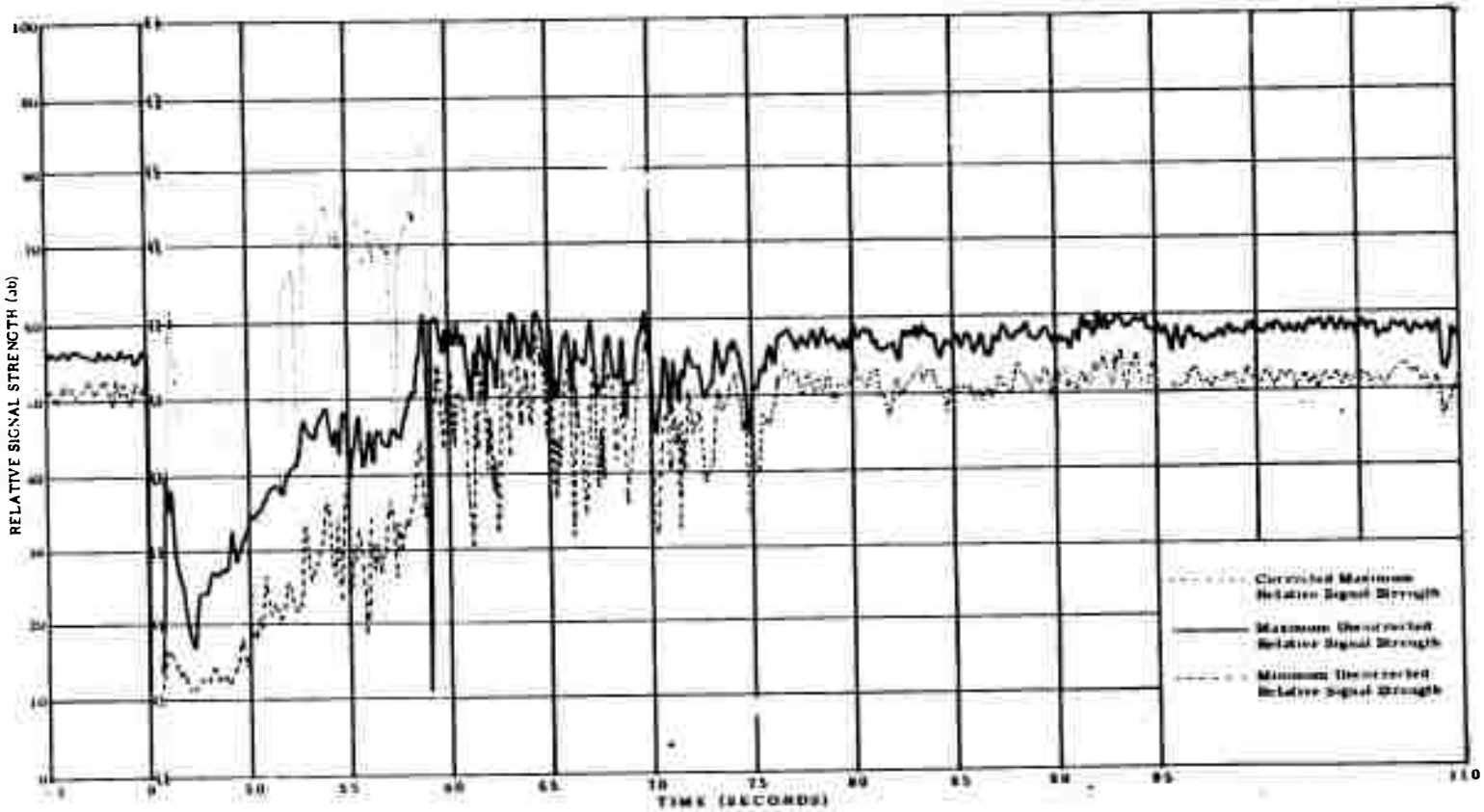

Figure 2 36 C-band relative signal strength with corrections for antenna-pointing errors, Blue Gill, Missile C, Ship 3.

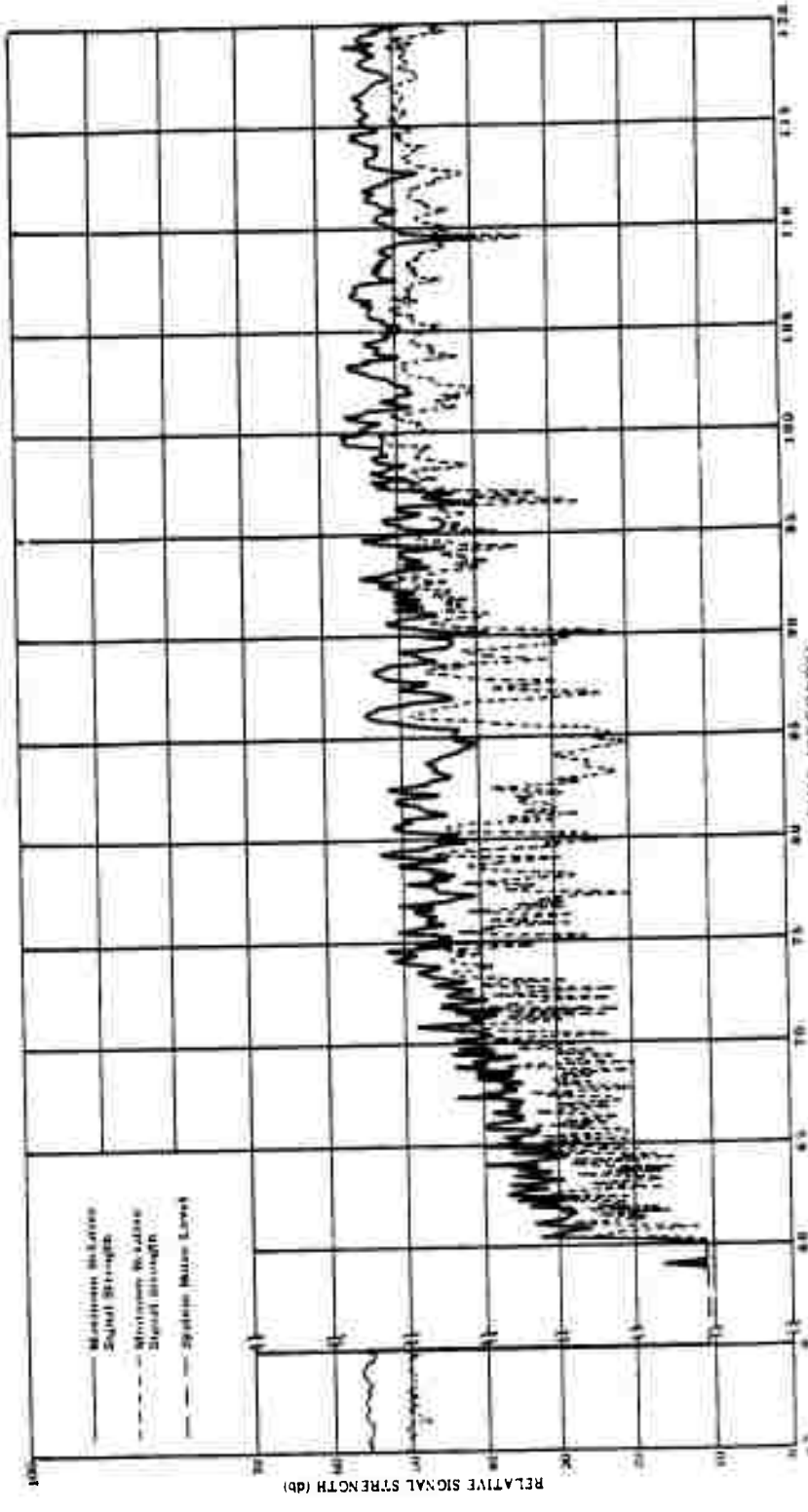

Figure 2.37 L-band relative signal strength envelopes, Blue Gill, Missile C, Ship 3.

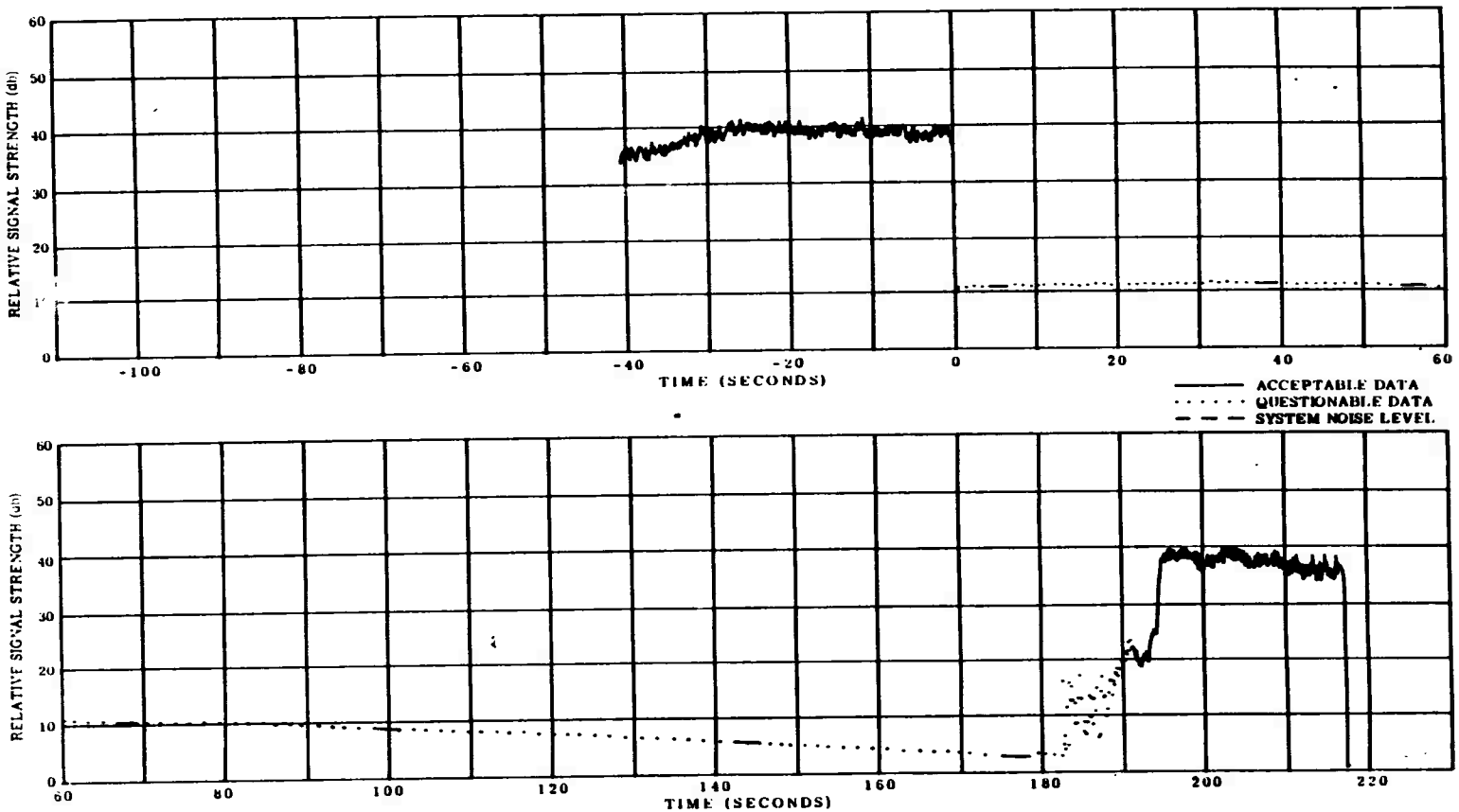

Figure 2.38 X-band relative signal strength, Blue Gill, Missile C, Ship 4.

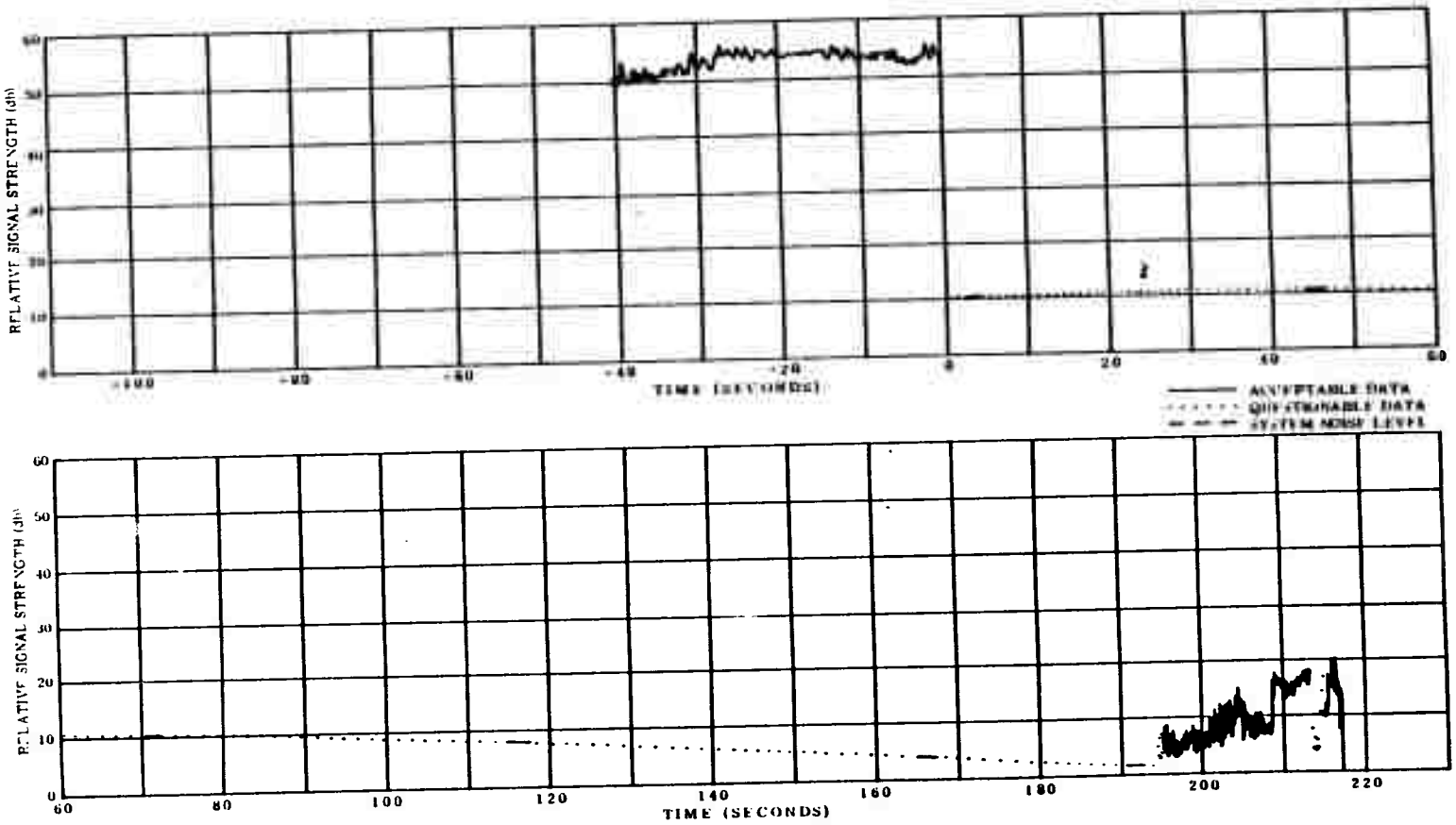

Figure 2-39 C band relative signal strength, Blue Gill, Missile C, Ship 4.

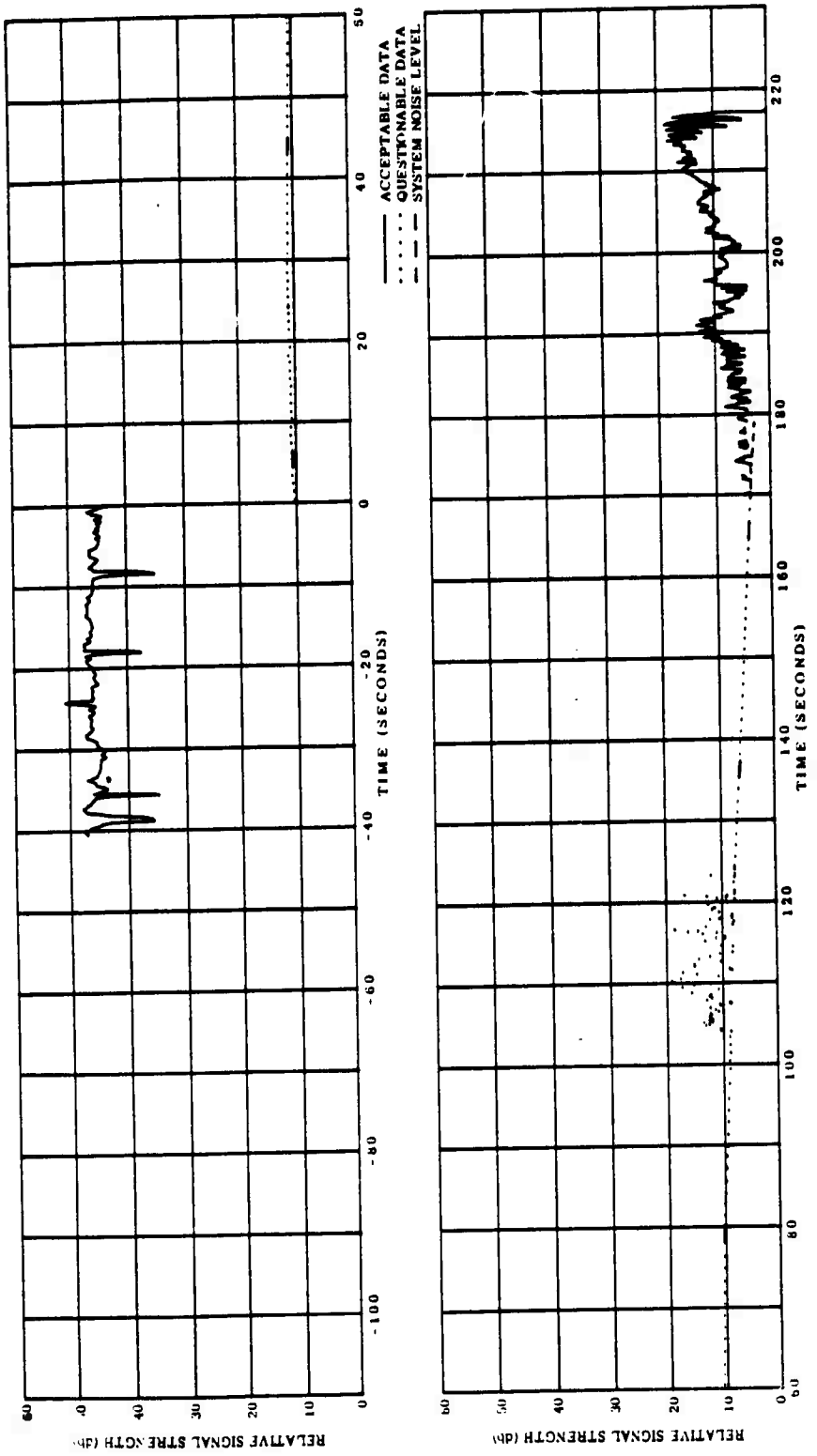

Figure 2.40 L-band relative signal strength, Blue Gill, Missile C, Ship 4.

Page 173 deleted.

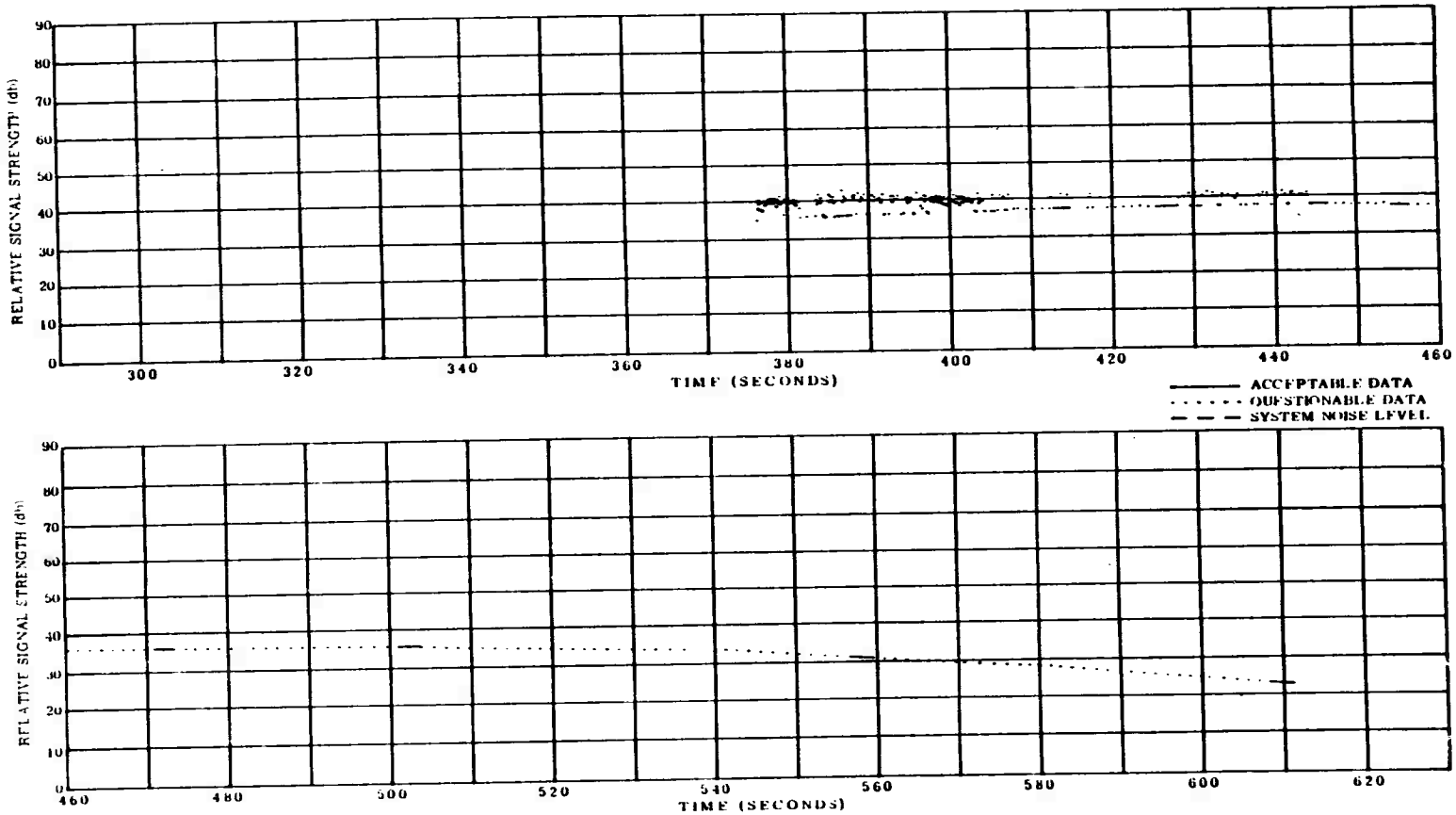

Figure 2.42 X-band relative signal strength, Blue Gill, Missile E, interferometer.

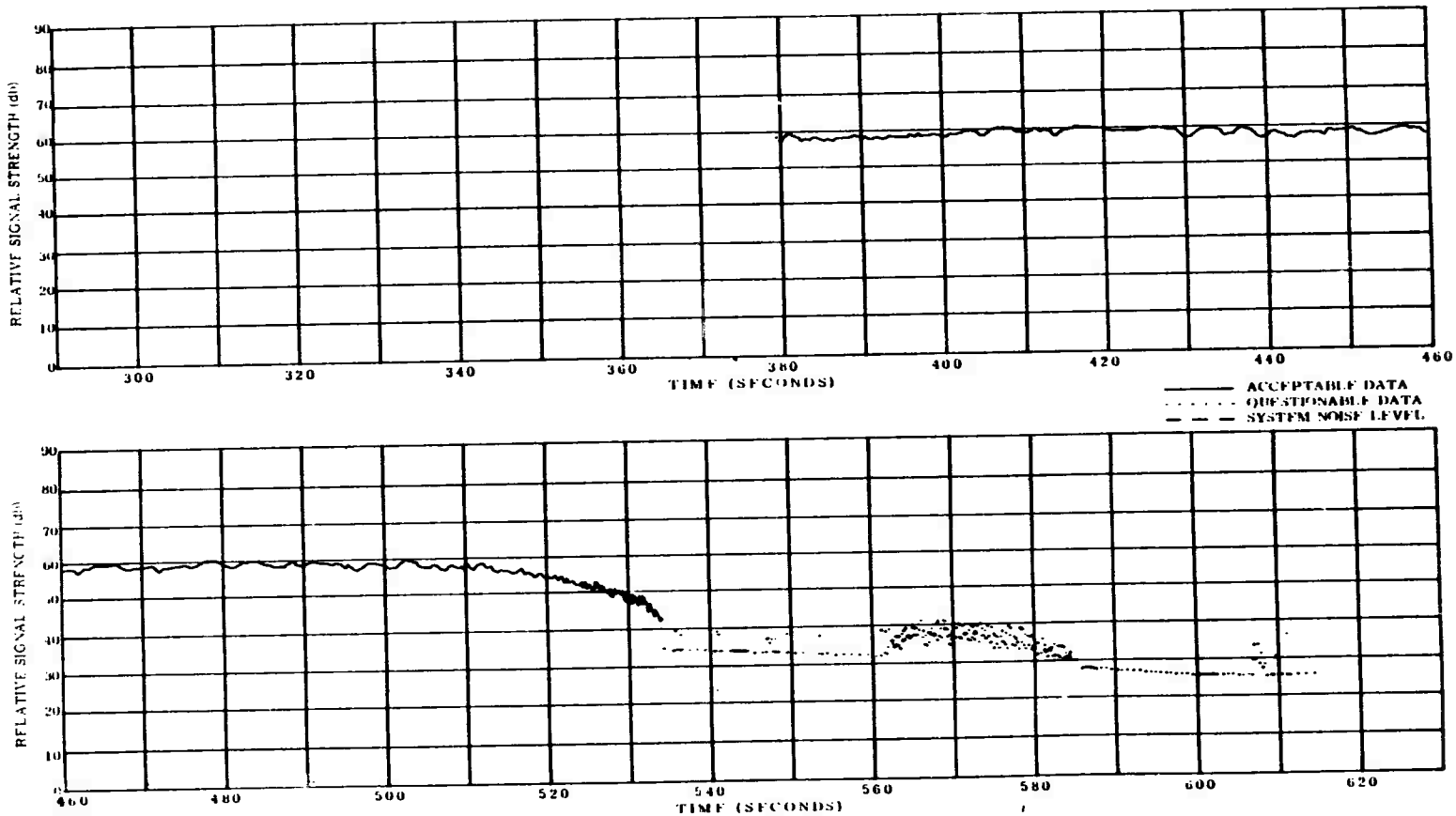

Figure 2.43 C-band relative signal strength, Blue Gill, Missile E, interferometer.

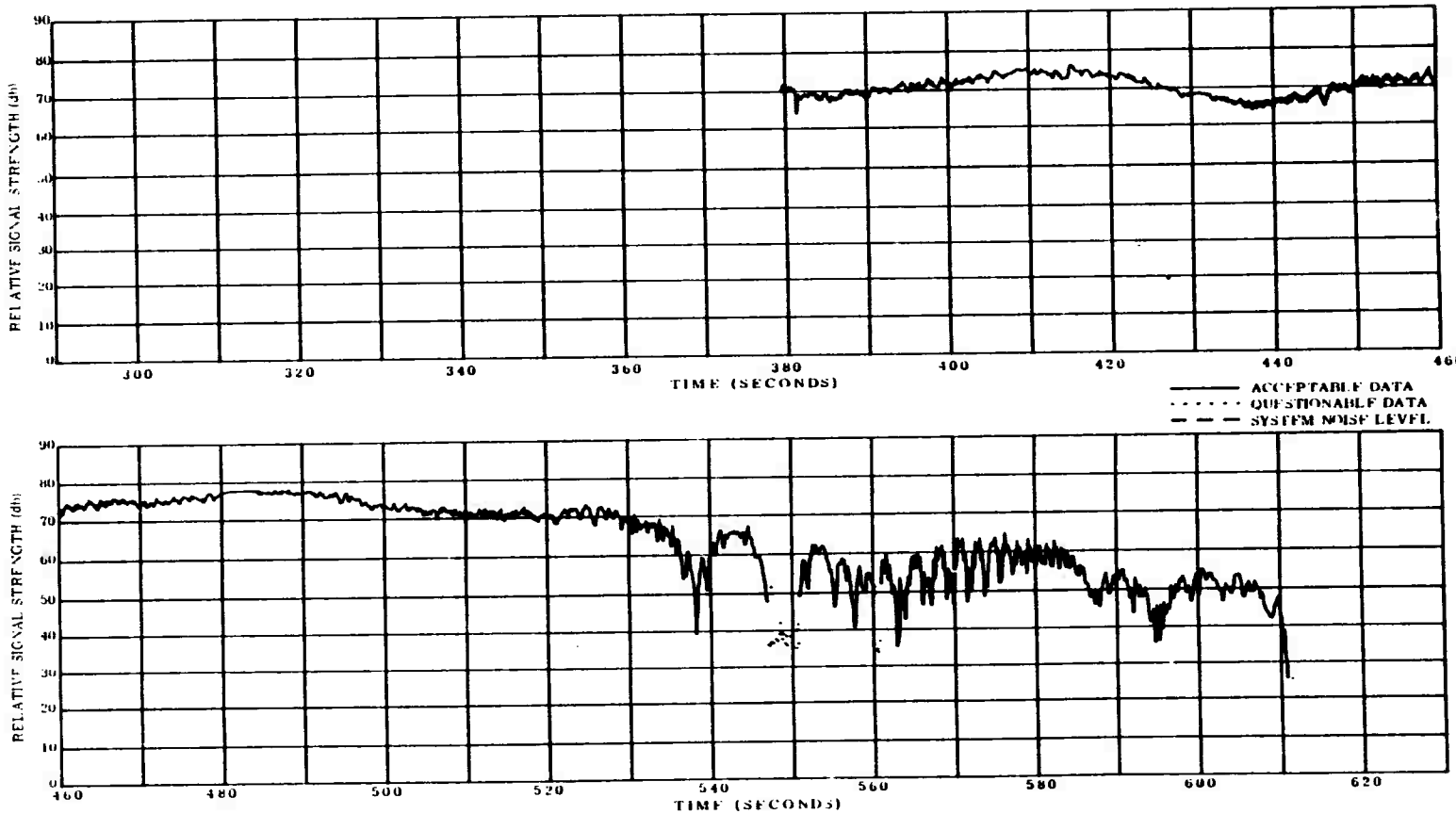

Figure 2.44 L-band relative signal strength, Blue Gill, Missile E, interferometer.

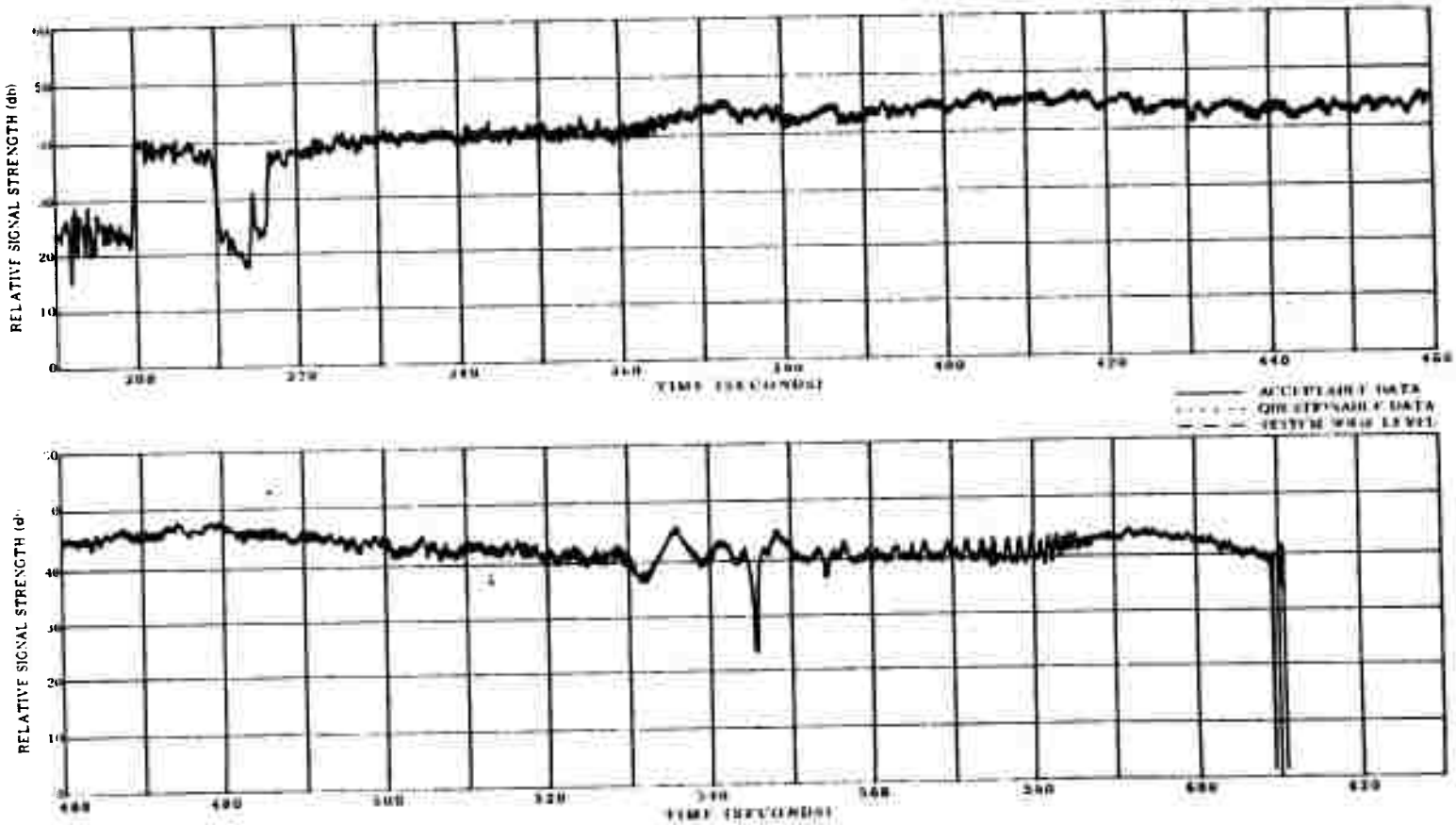

Figure 2.45 X-band relative signal strength, Blue Gill, Missile E, Ship 1.

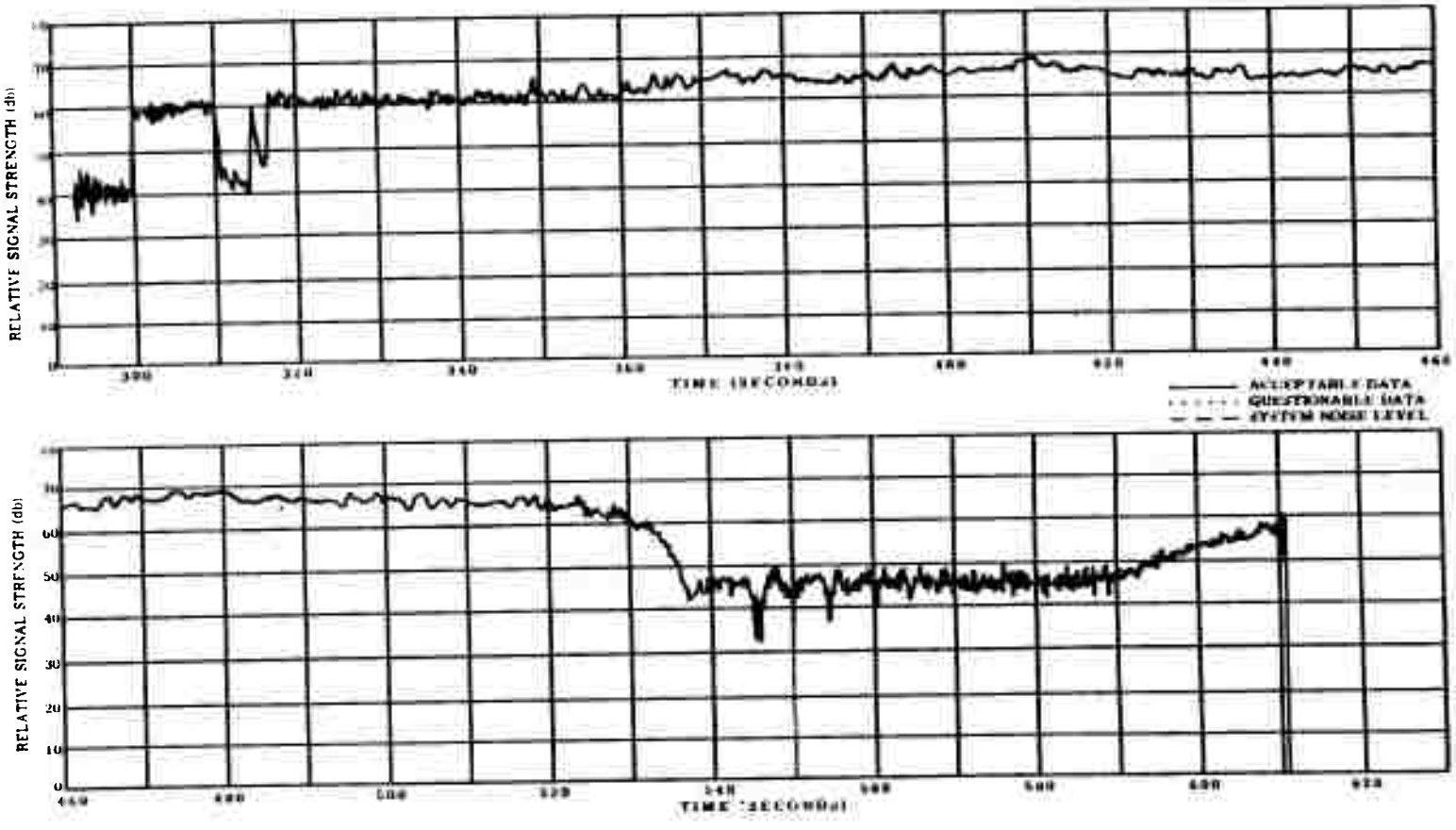

Figure 2 46 C-band relative signal strength, Blue Gill, Missile E, Ship 1.

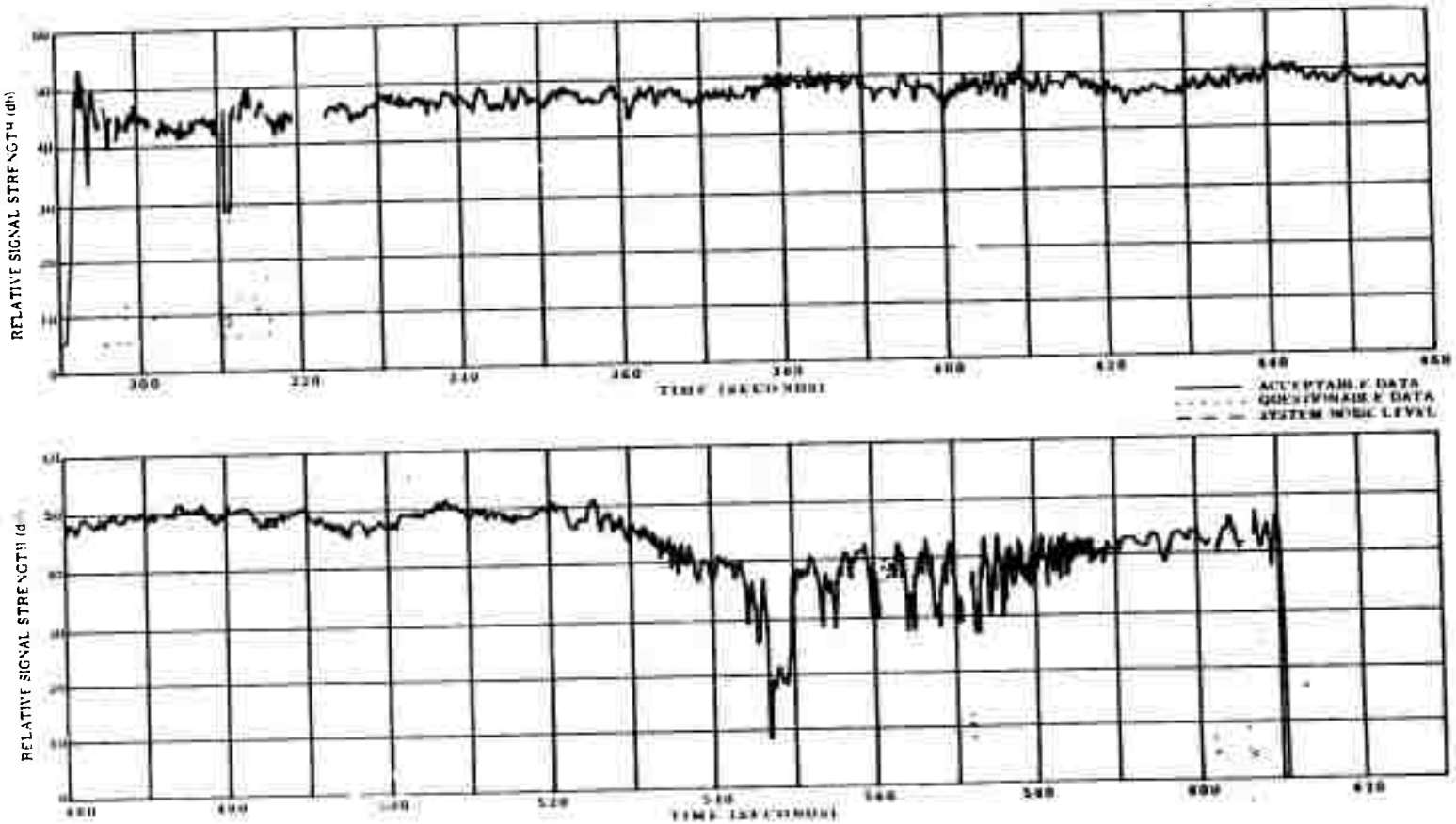

Figure 2-47 L-band relative signal strength, Blue Gill, Missile E, Ship 1.

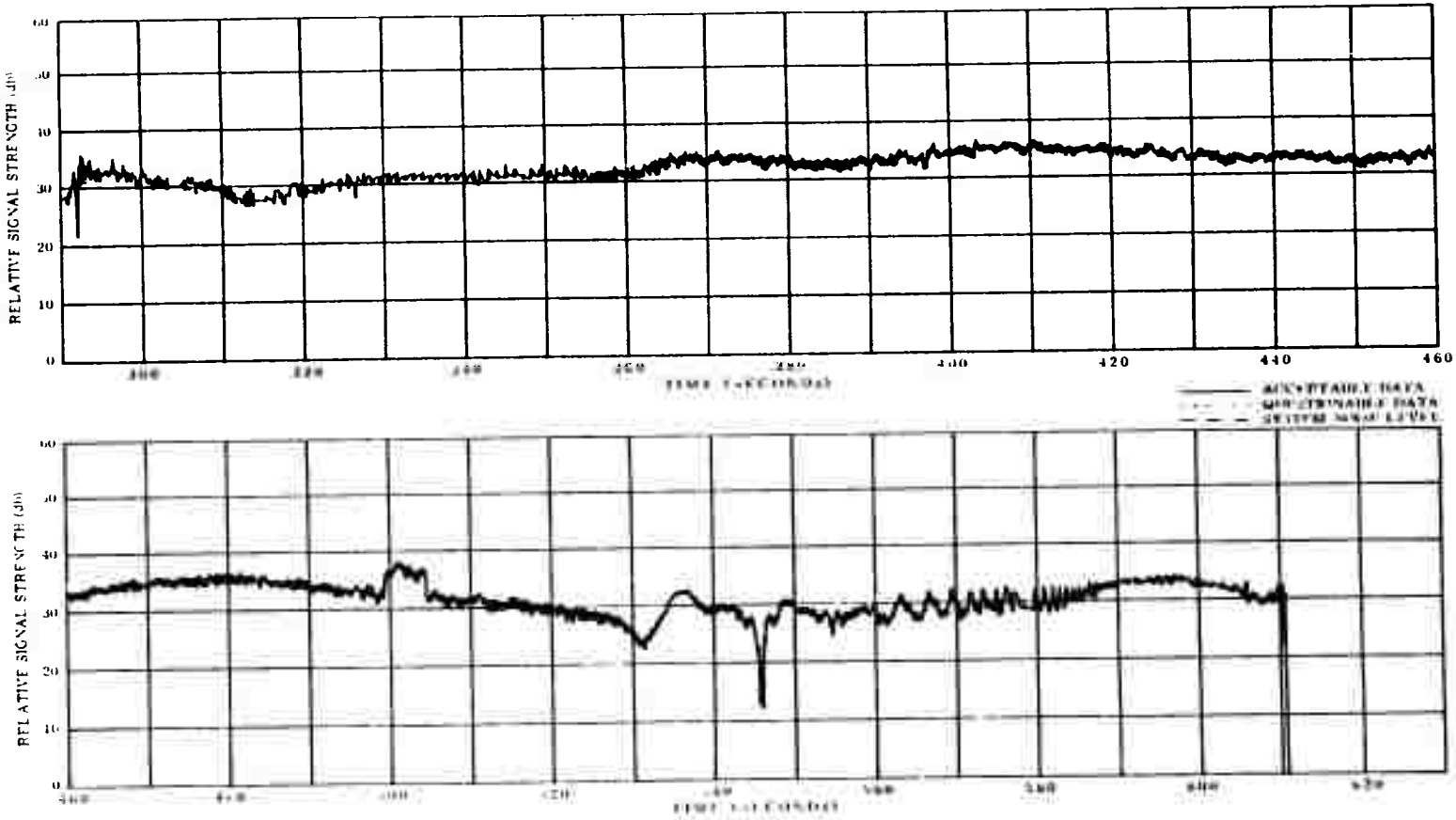

Figure 2.16 X band relative signal strength, Blue Gill, Missile E, Ship 2.

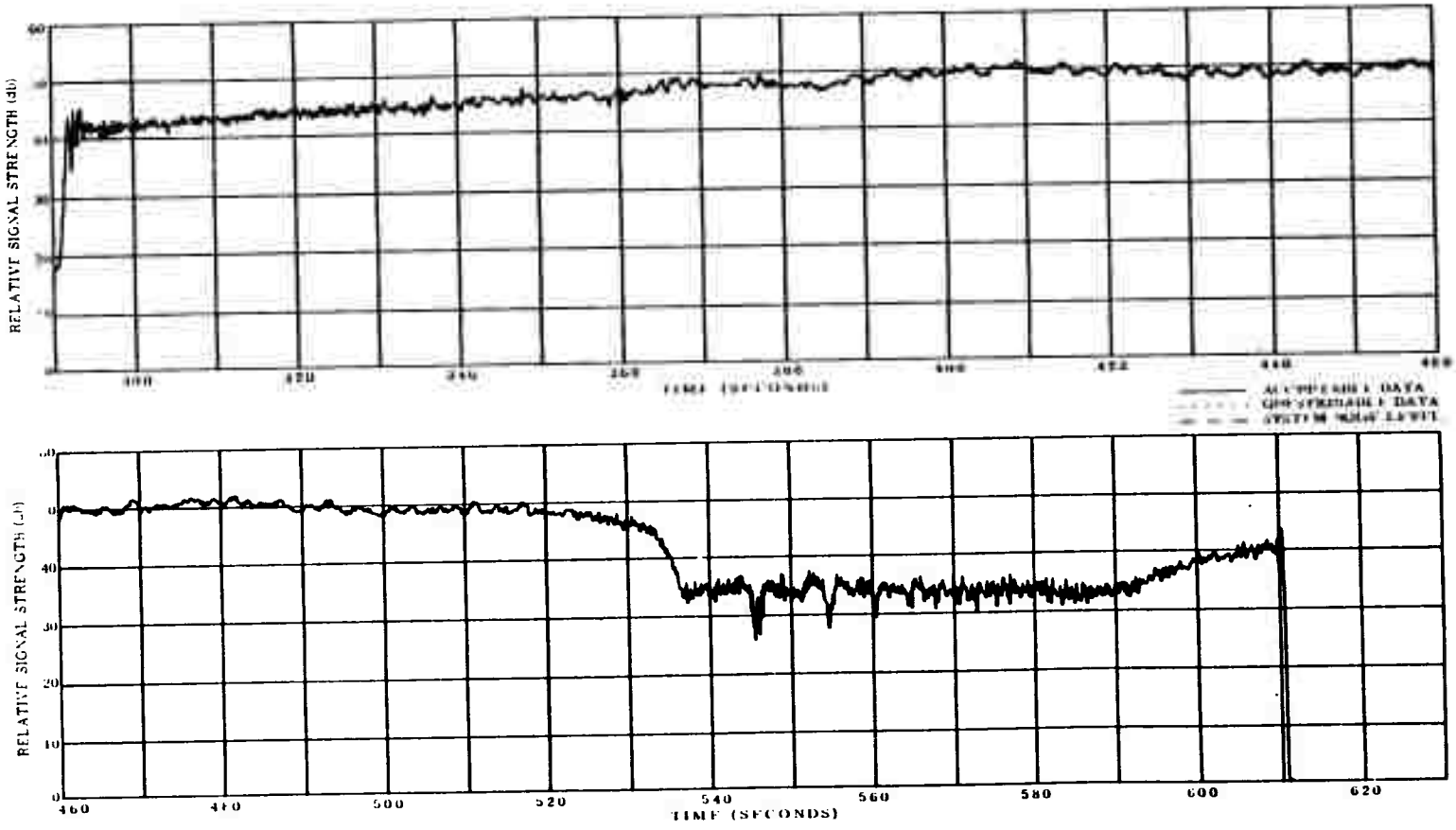

Figure 2.49 C-band relative signal strength, Blue Gill, Missile E, Slip 2.

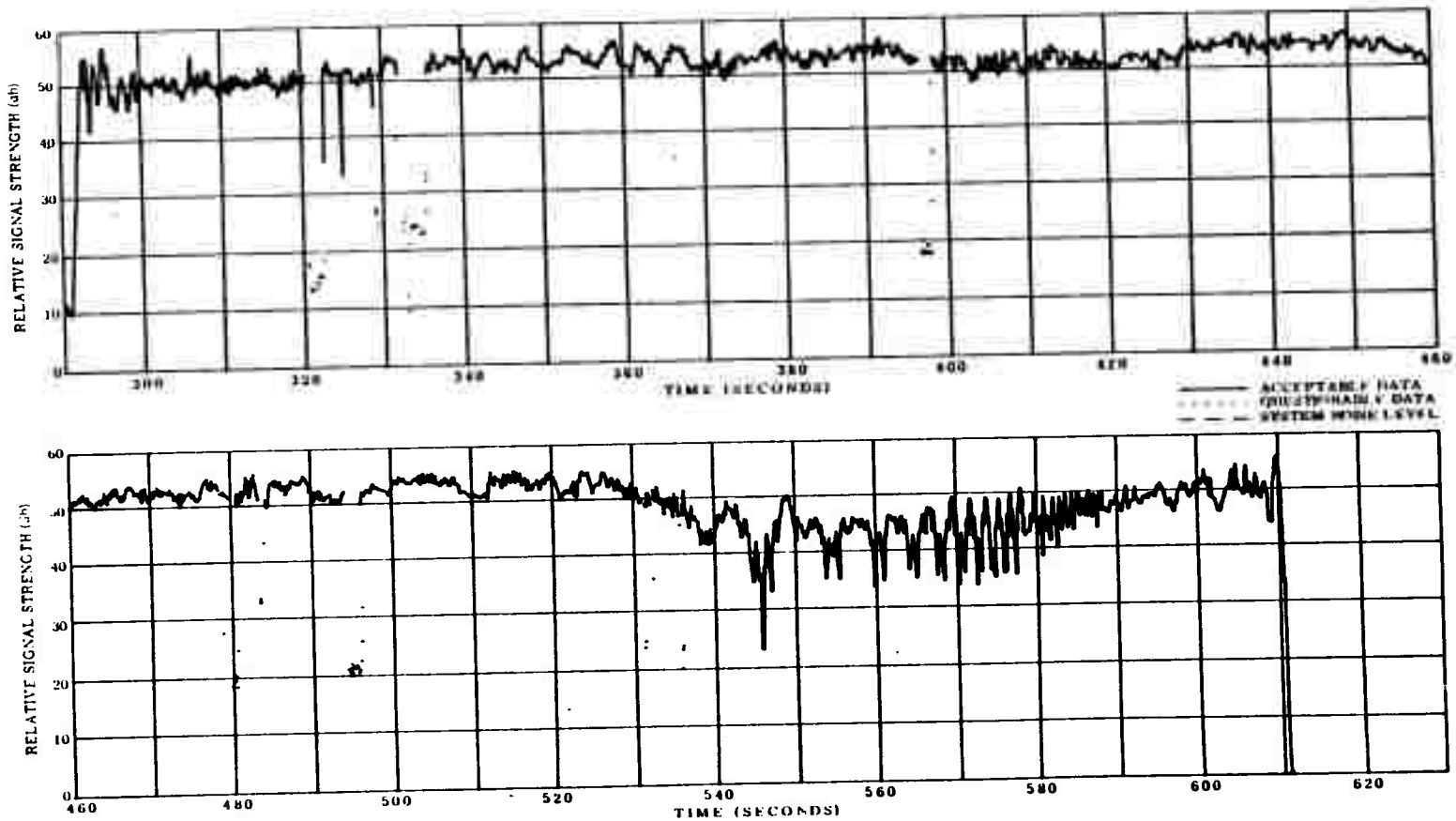

Figure 2.50 L-band relative signal strength, Blue Gill, Missile E, Ship 2.

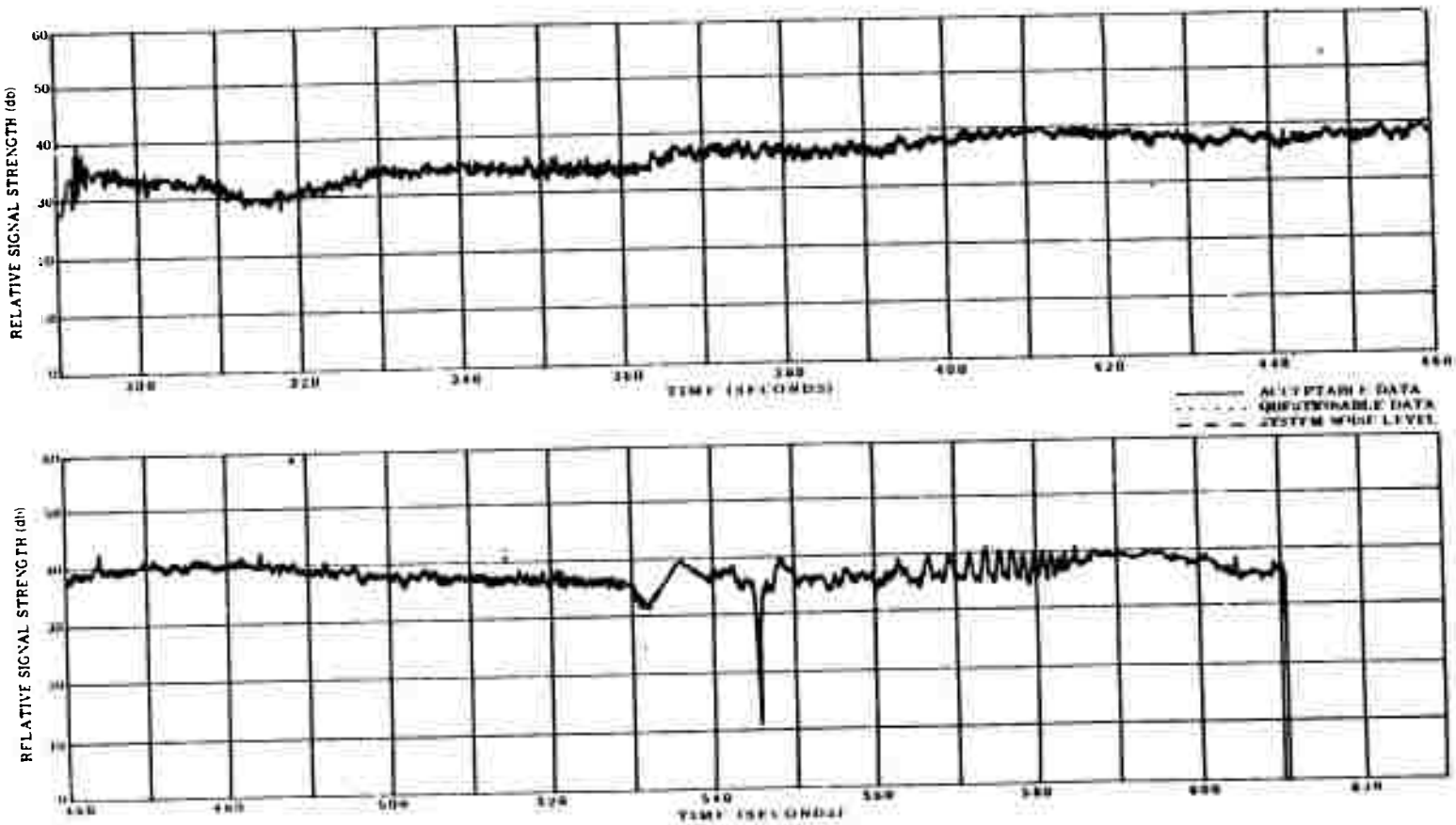

Figure 2.51 X-band relative signal strength, Blue Gill, Missile E, Ship 3.

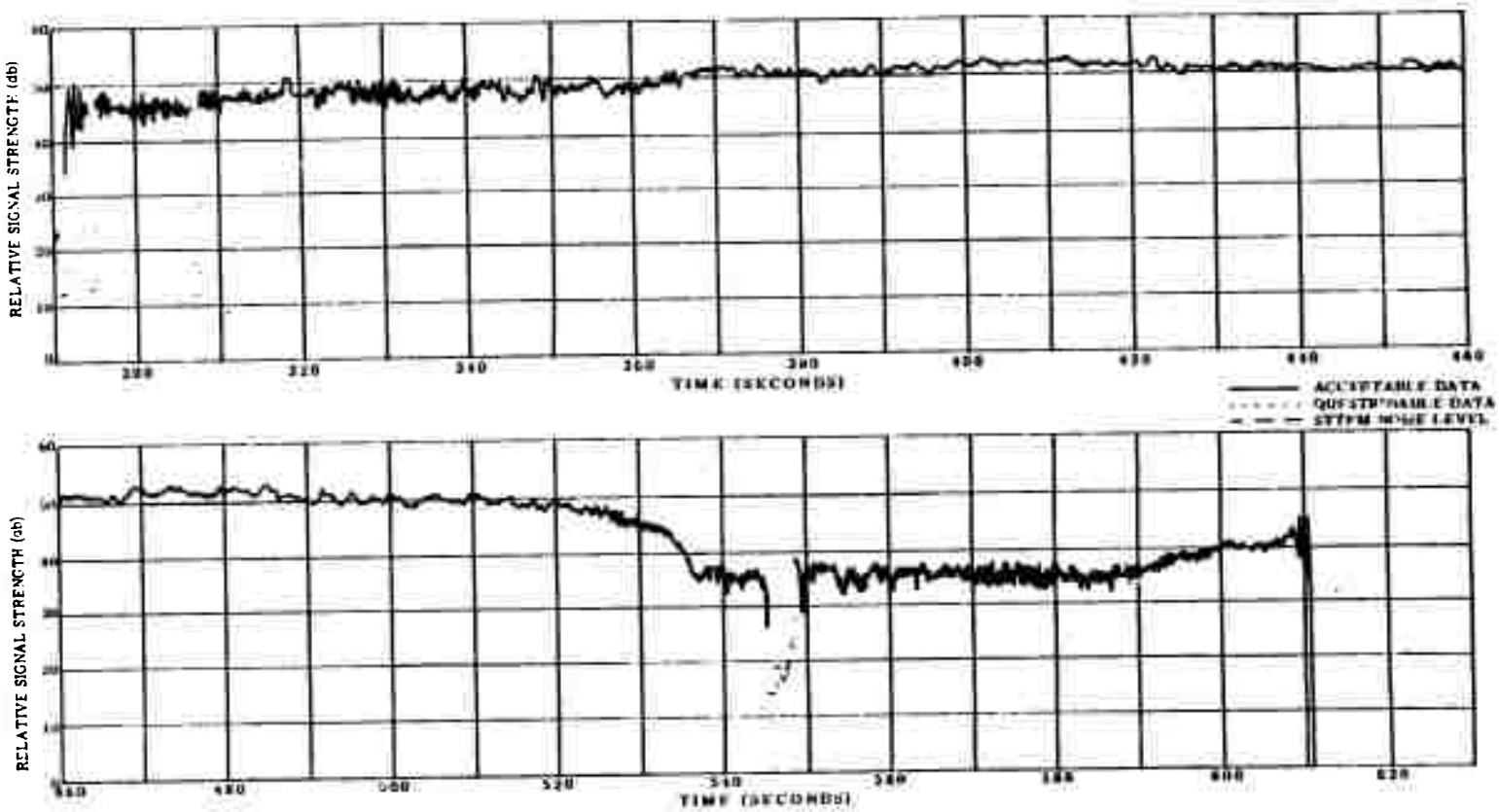

Figure 2.52 C-band relative signal strength, Blue Gill, Missile E, Ship 3.

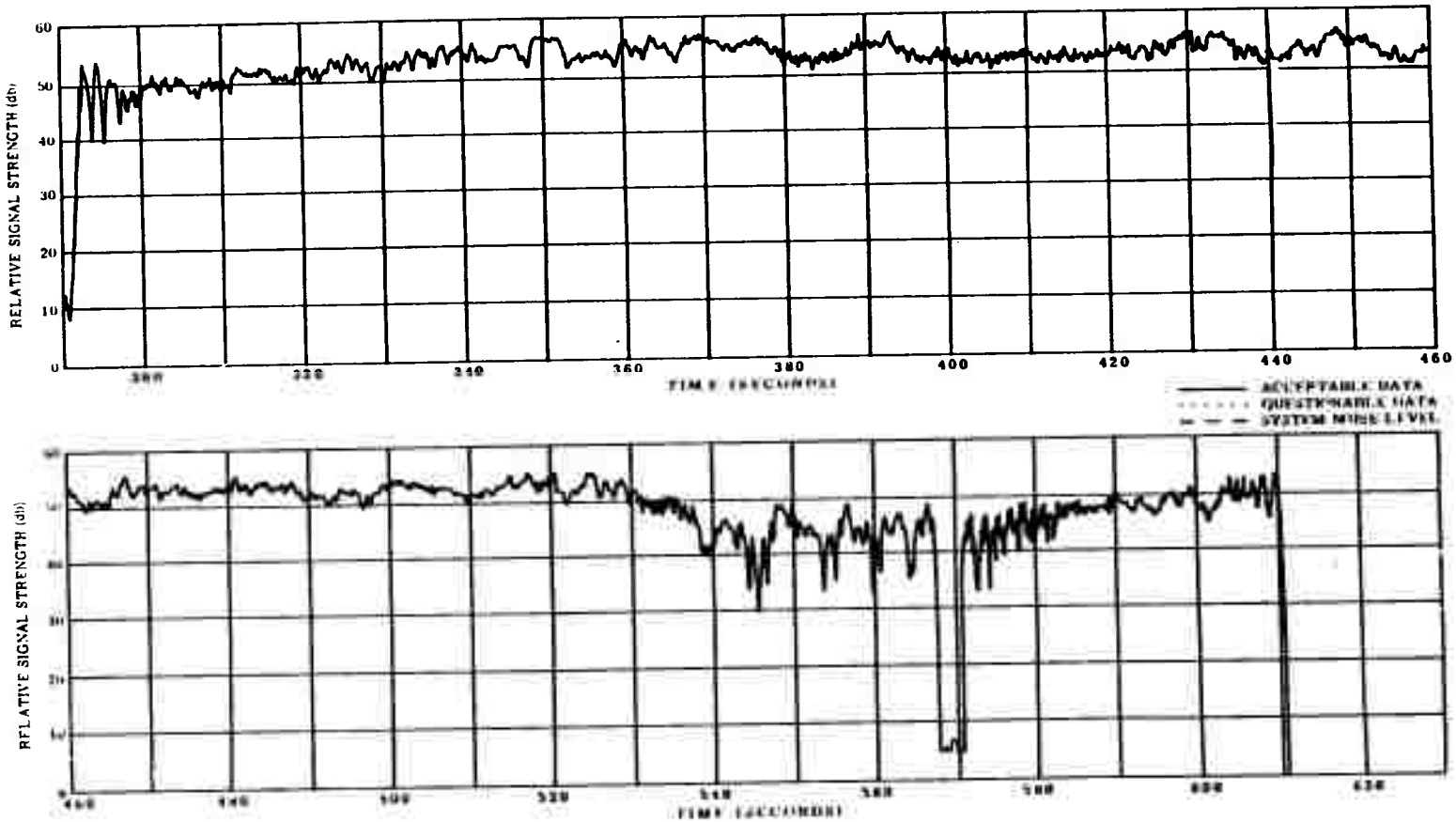

Figure 2.53 L-band relative signal strength, Blue Gill, Missile E, Ship 3.

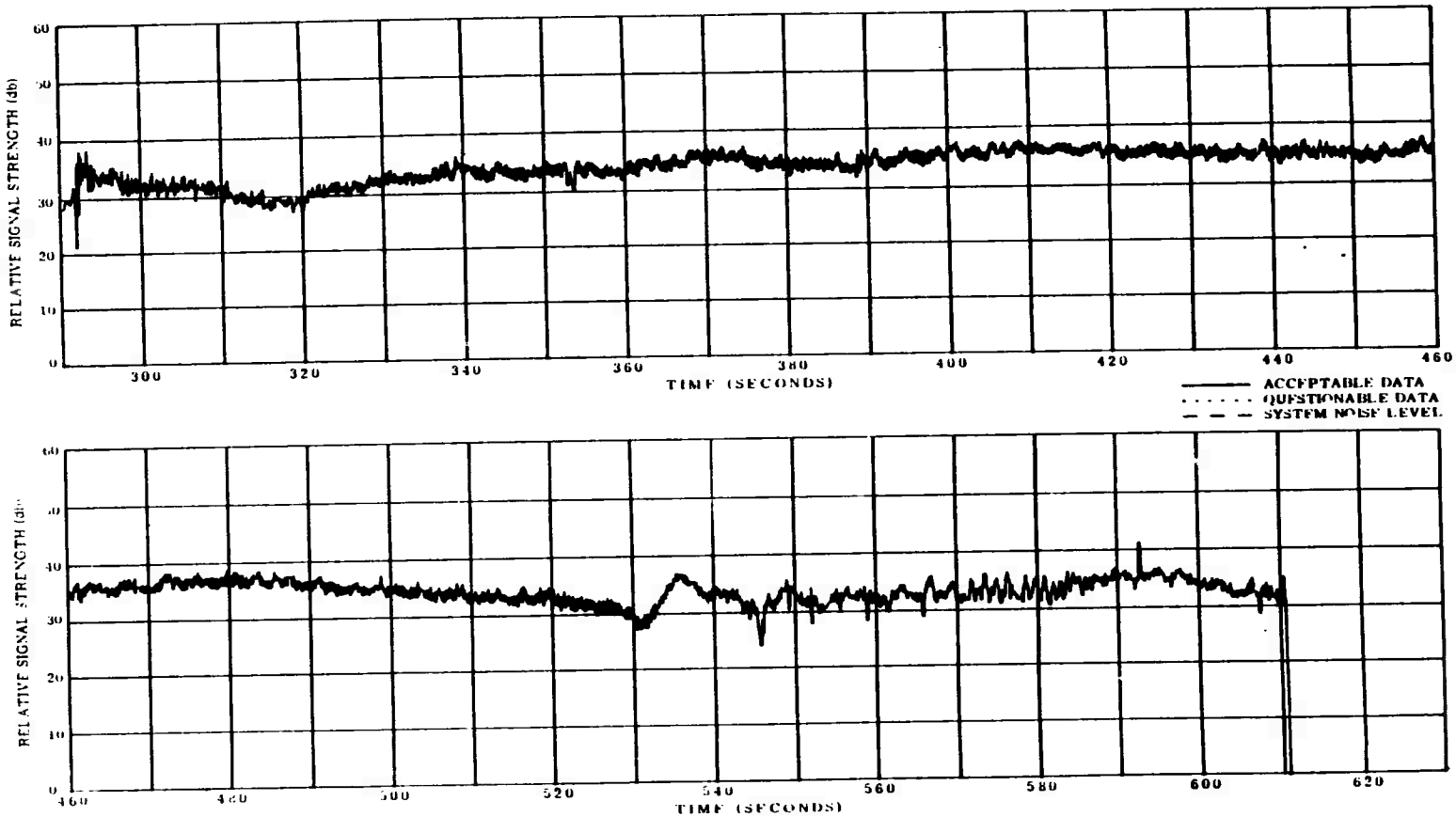

Figure 2.54 X-band relative signal strength, Blue Gill, Missile E, Ship 4.

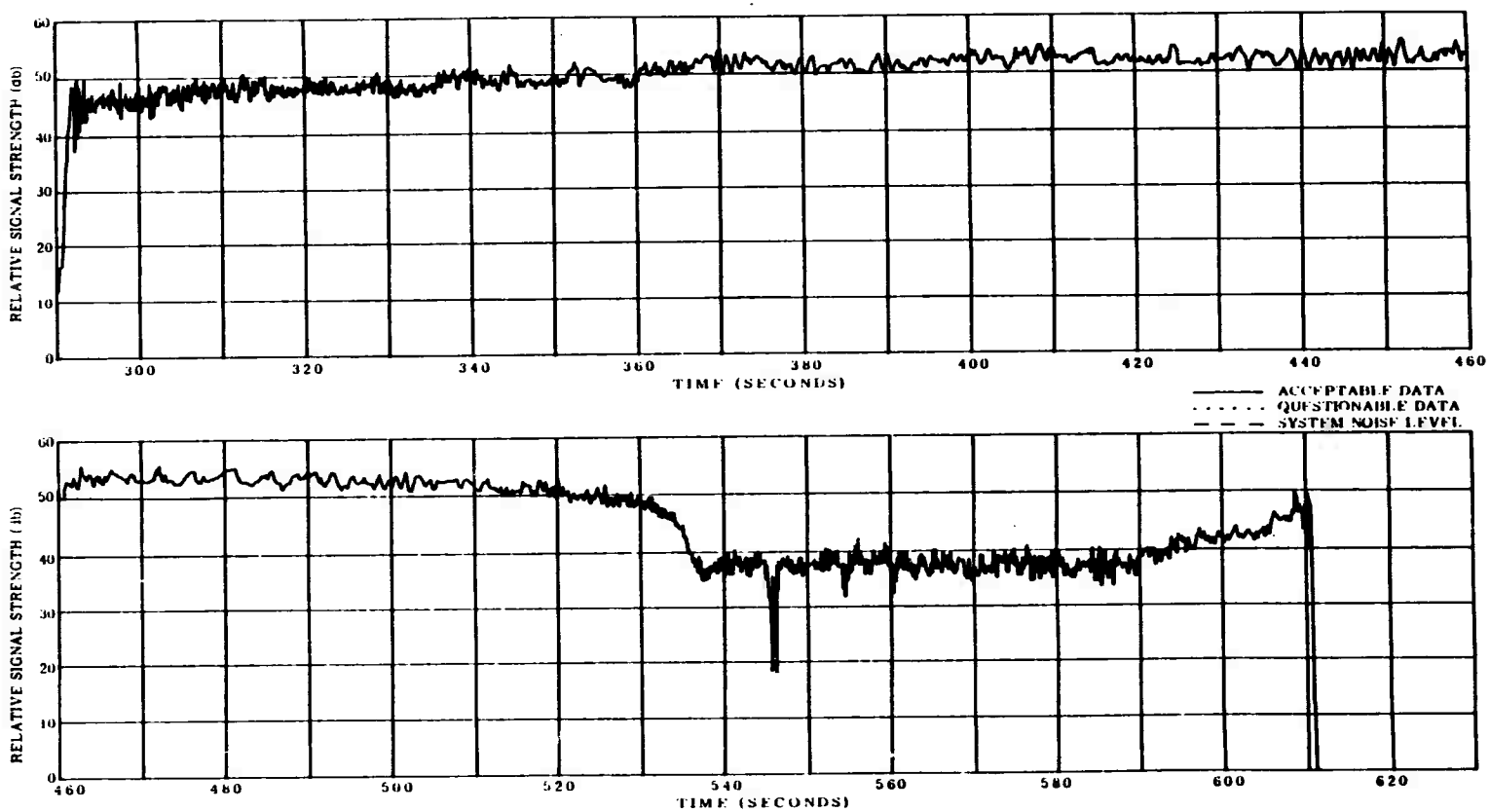

Figure 2.55 C-band relative signal strength, Blue Gill, Missile e, Ship 4.

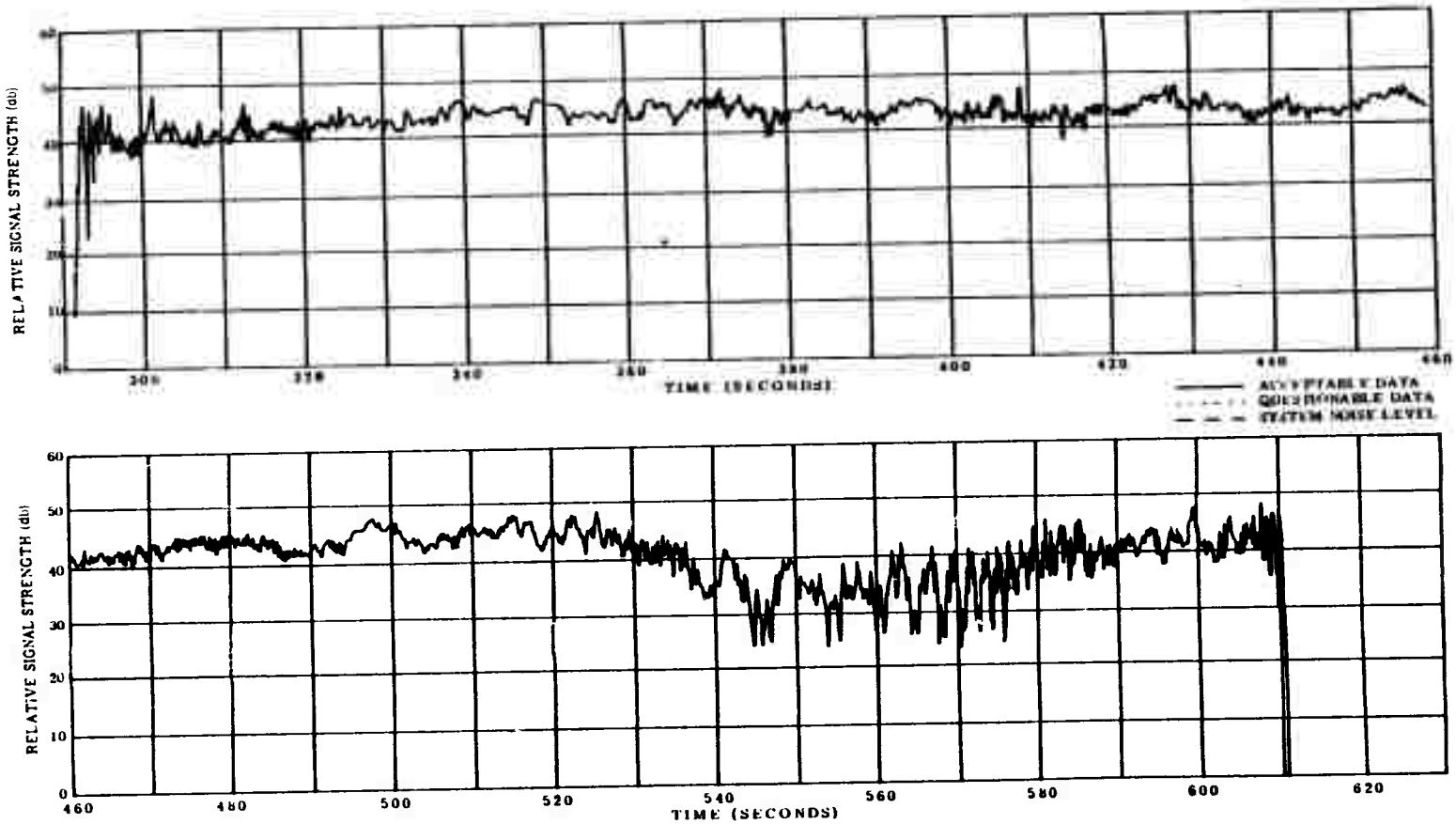

Figure 2.56 L-band relative signal strength, Blue Gill, Missile E, Slap 4.

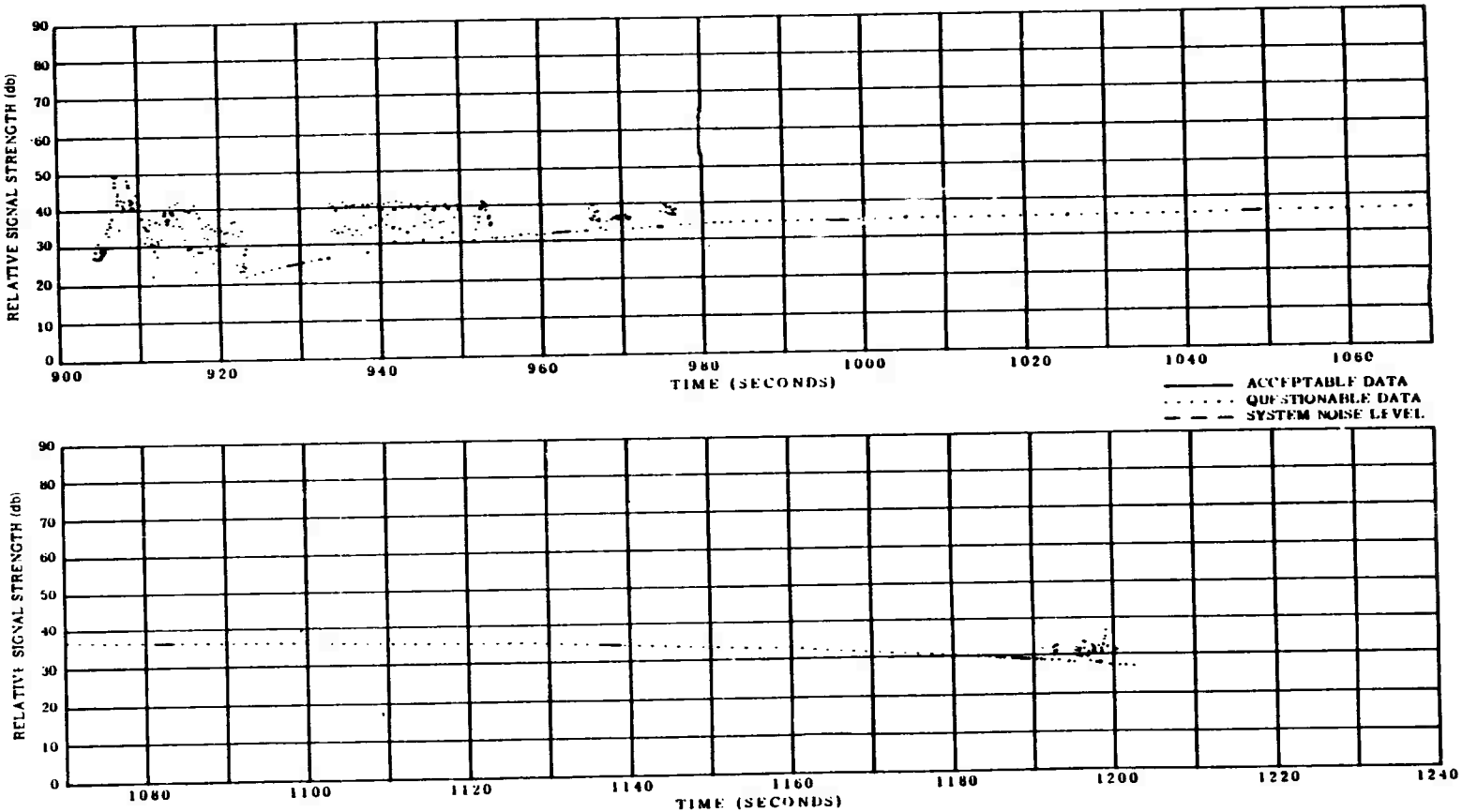

Figure 2.57 X-band relative signal strength, Blue Gill, Missile F, interferometer.

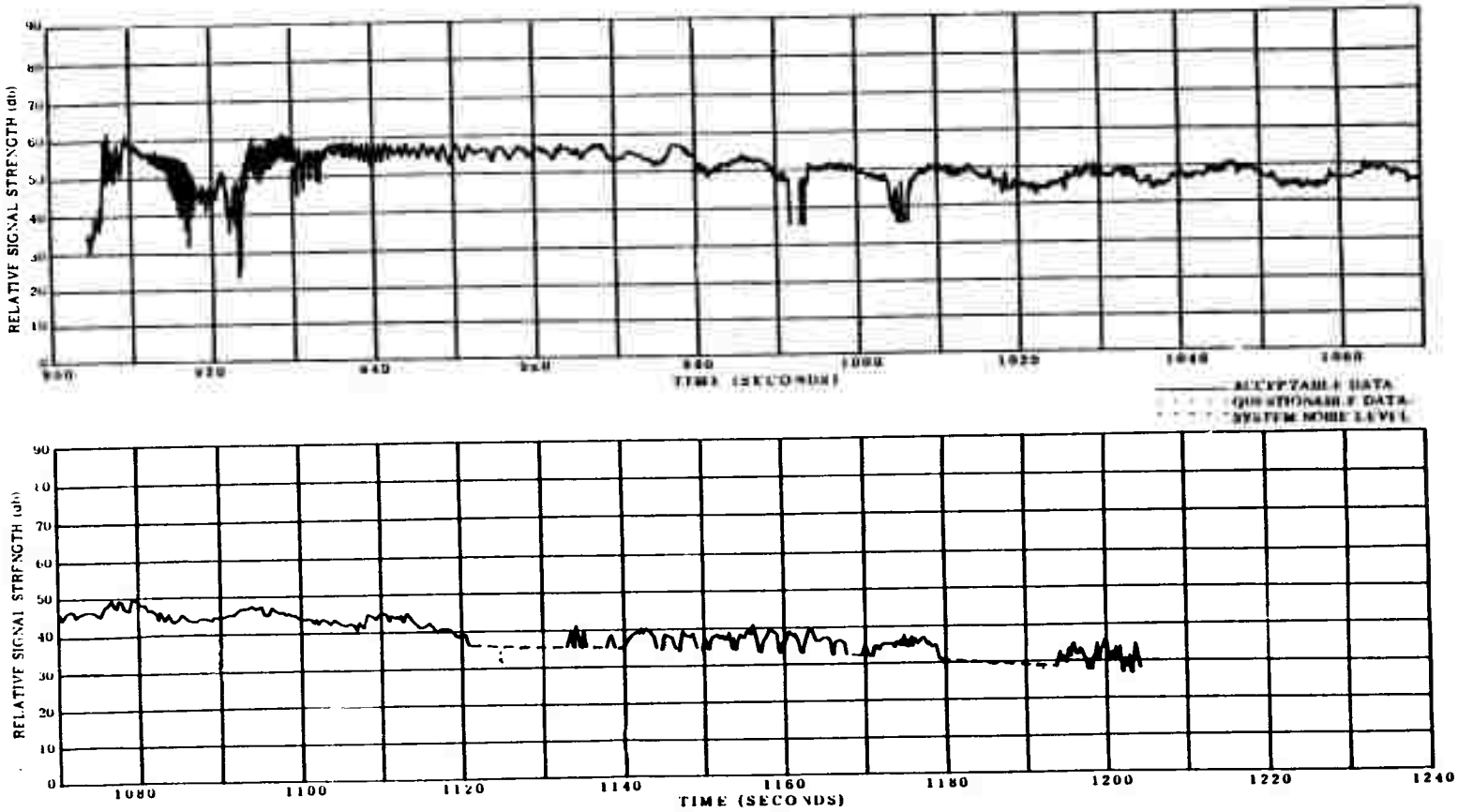

Figure 2.58 C-band relative signal strength, Blue Gill, Missile F, interferometer.

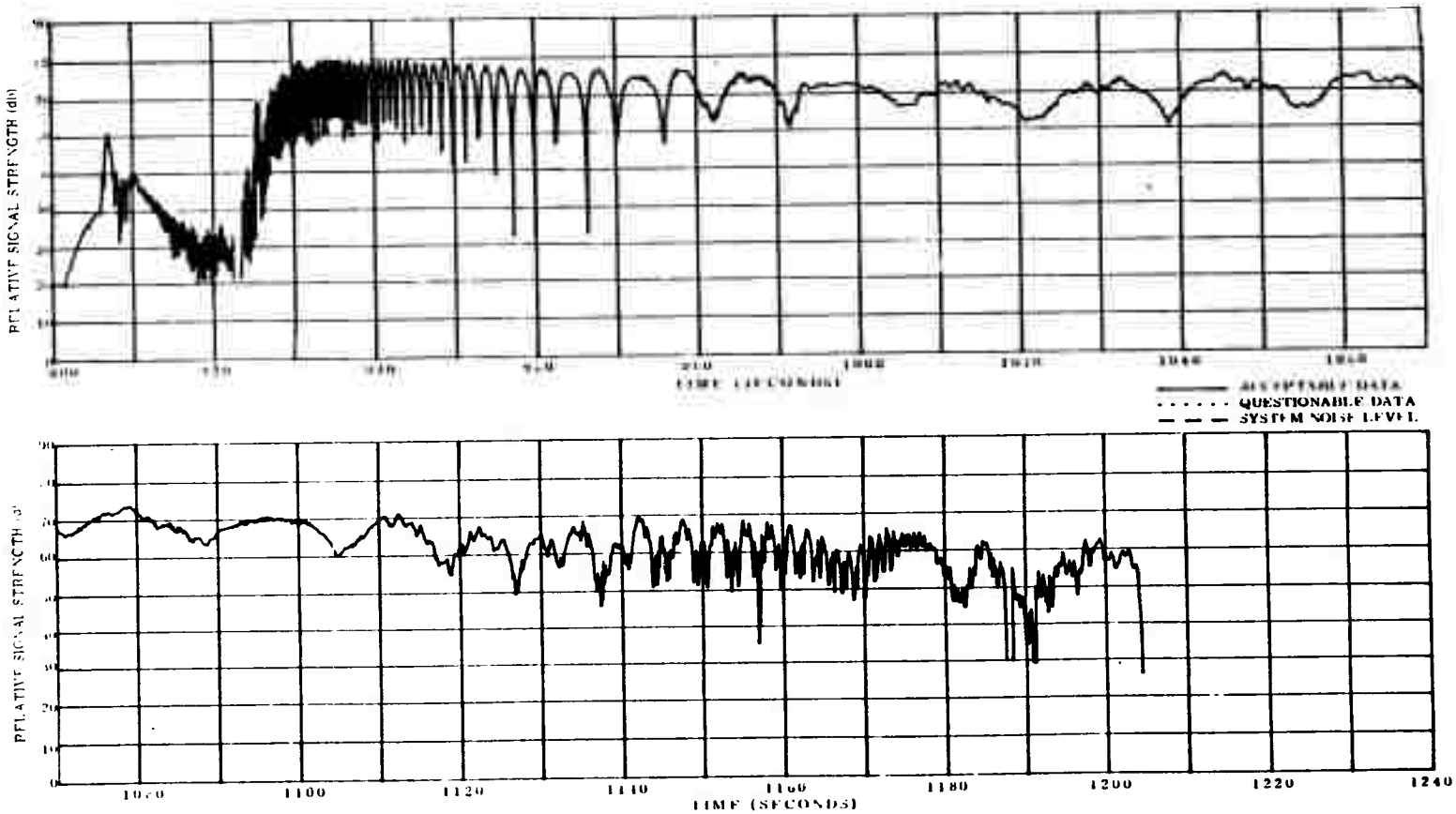

Figure 2.59 L band relative signal strength, Blue Gill, Missile F, interferometer.

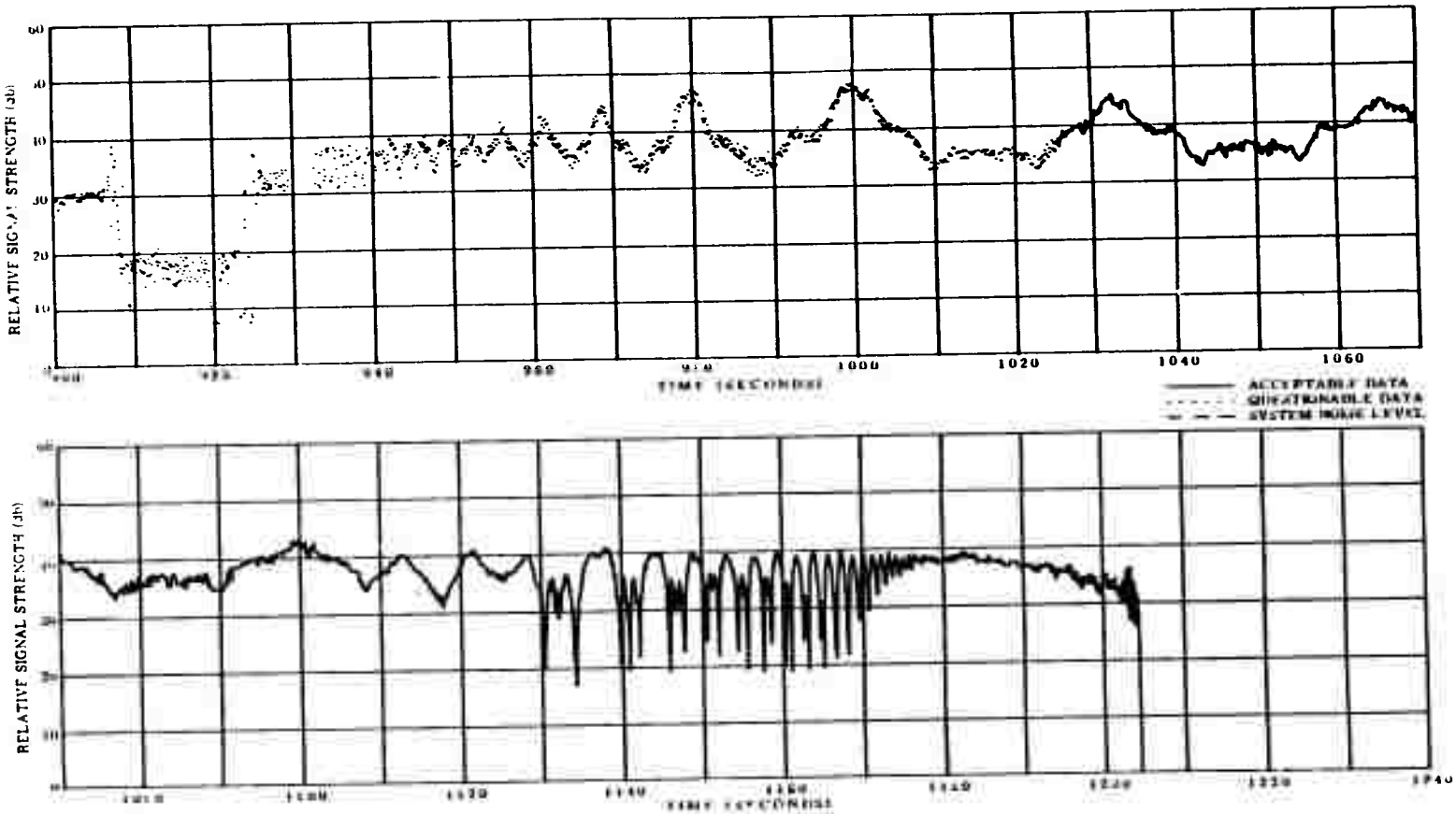

Figure 2.60 X-band relative signal strength, Blue Gill, Missile F, Ship 1.

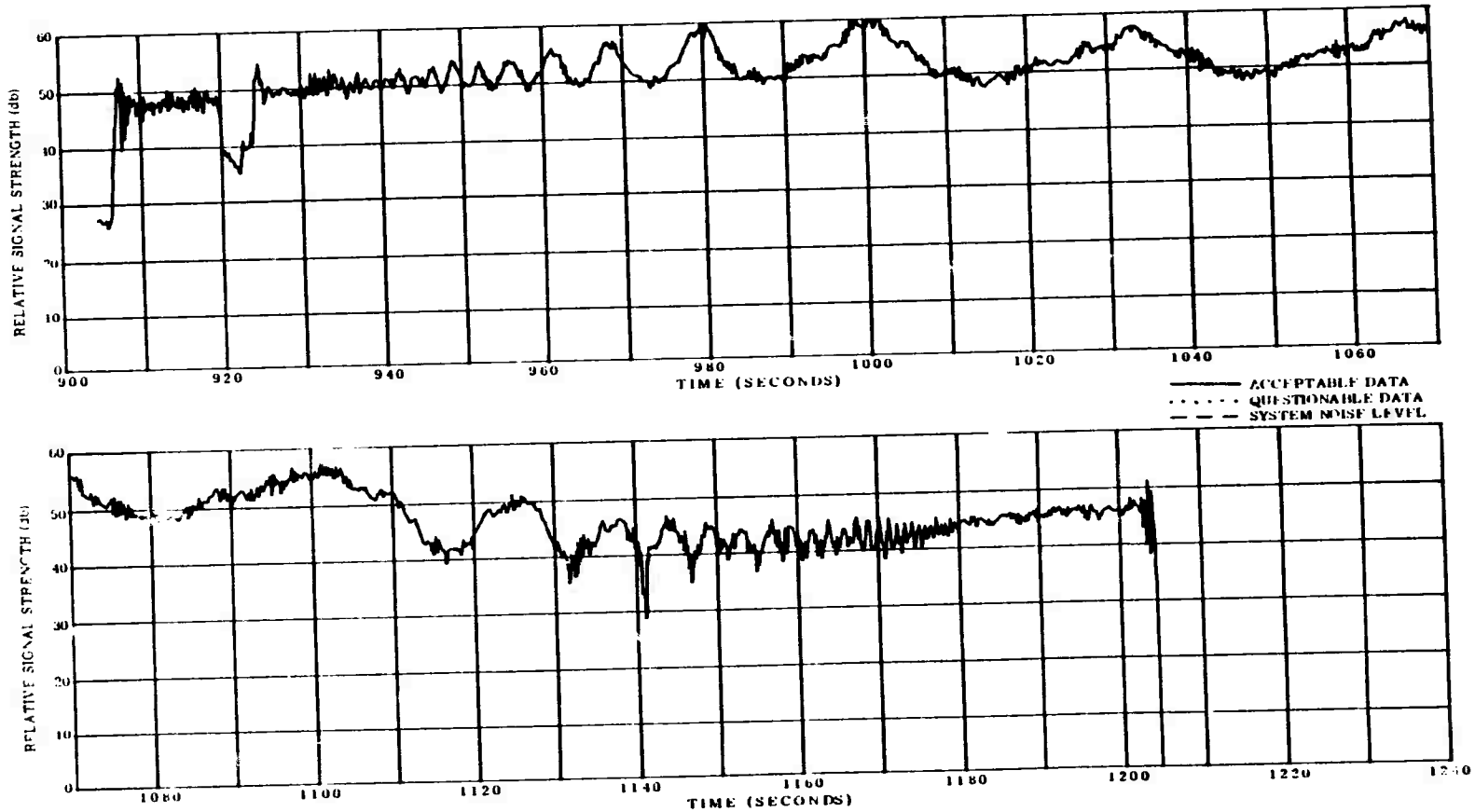

Figure 2.61 C-band relative signal strength, Blue Gill, Missile F, Ship 1.

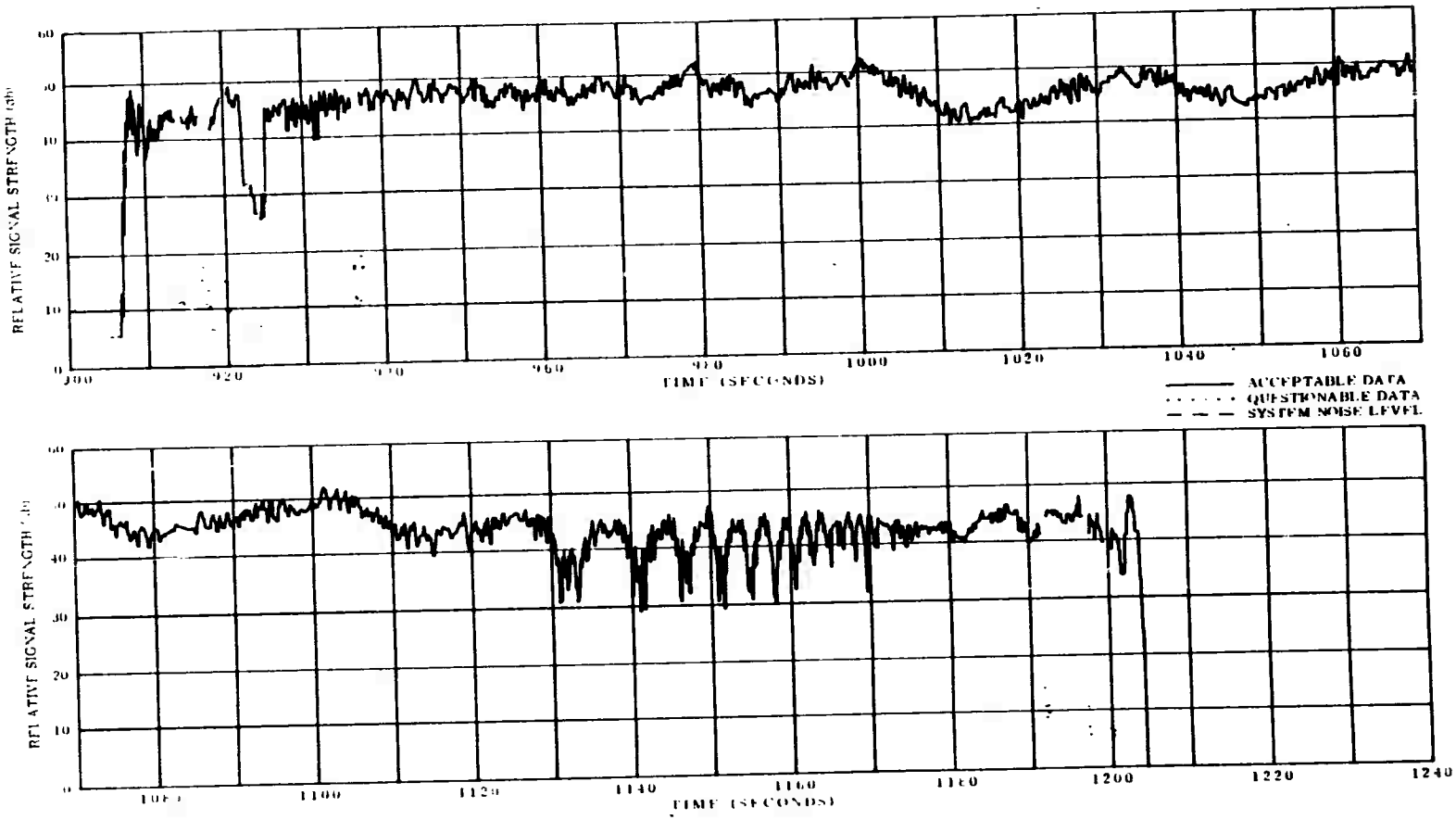

Figure 2.62 L band relative signal strength, Blue Gill, Missile F, Ship 1

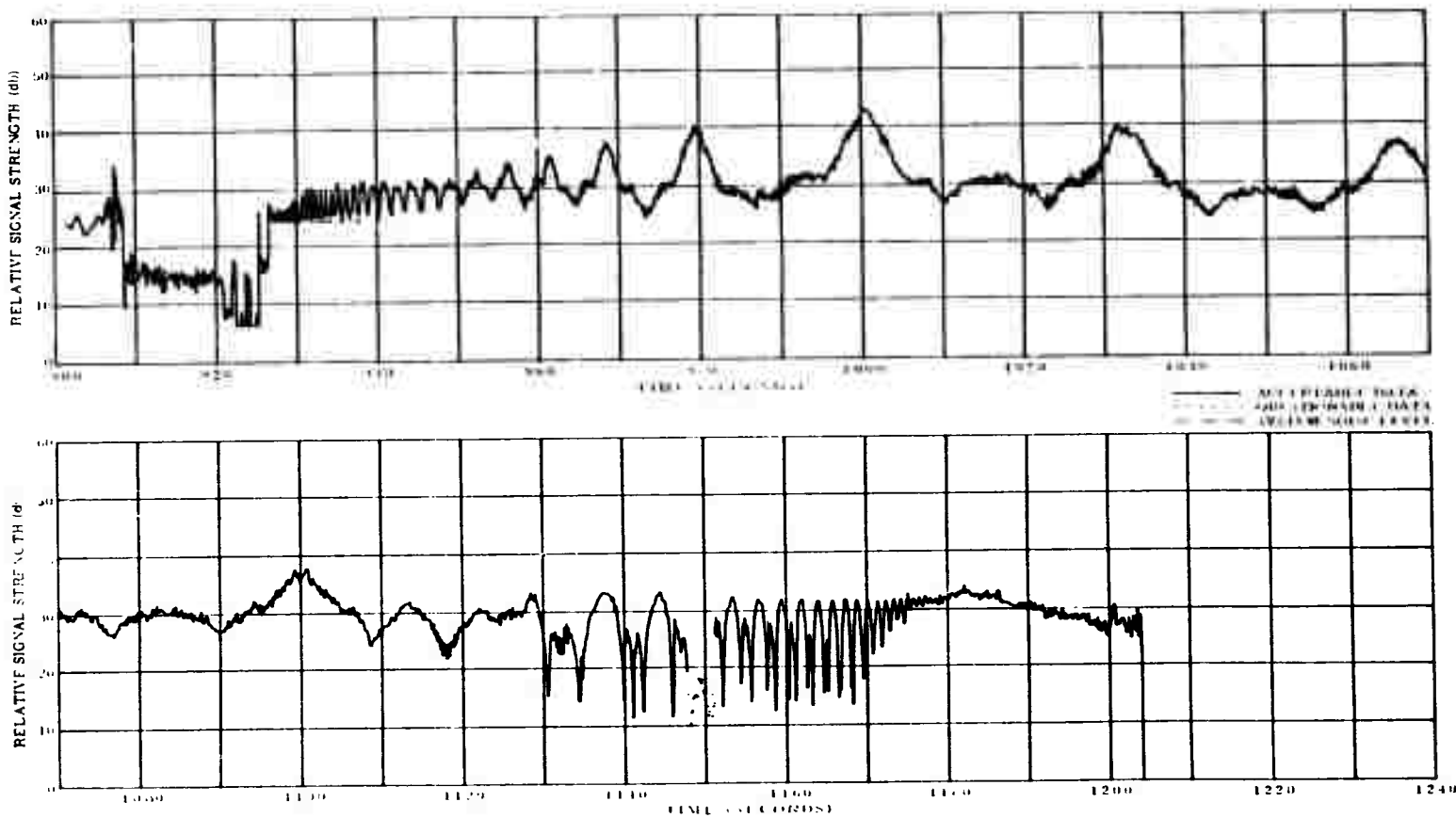

Figure 2.63 X band relative signal strength, Blue Gill, Mesath F, Slap 2

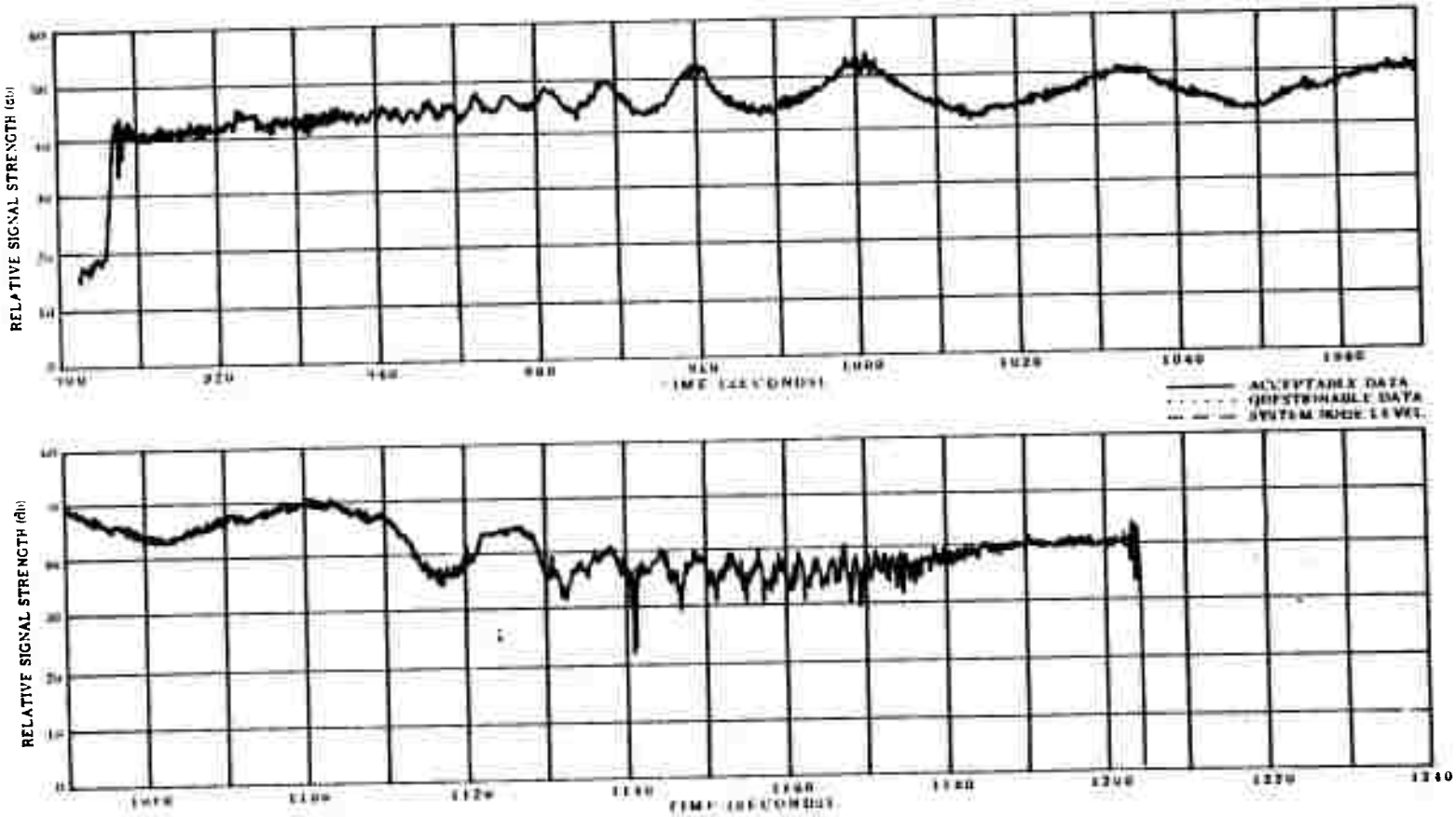

Figure 2.64 C-band relative signal strength, Blue Gill, Missile F, Ship 2.

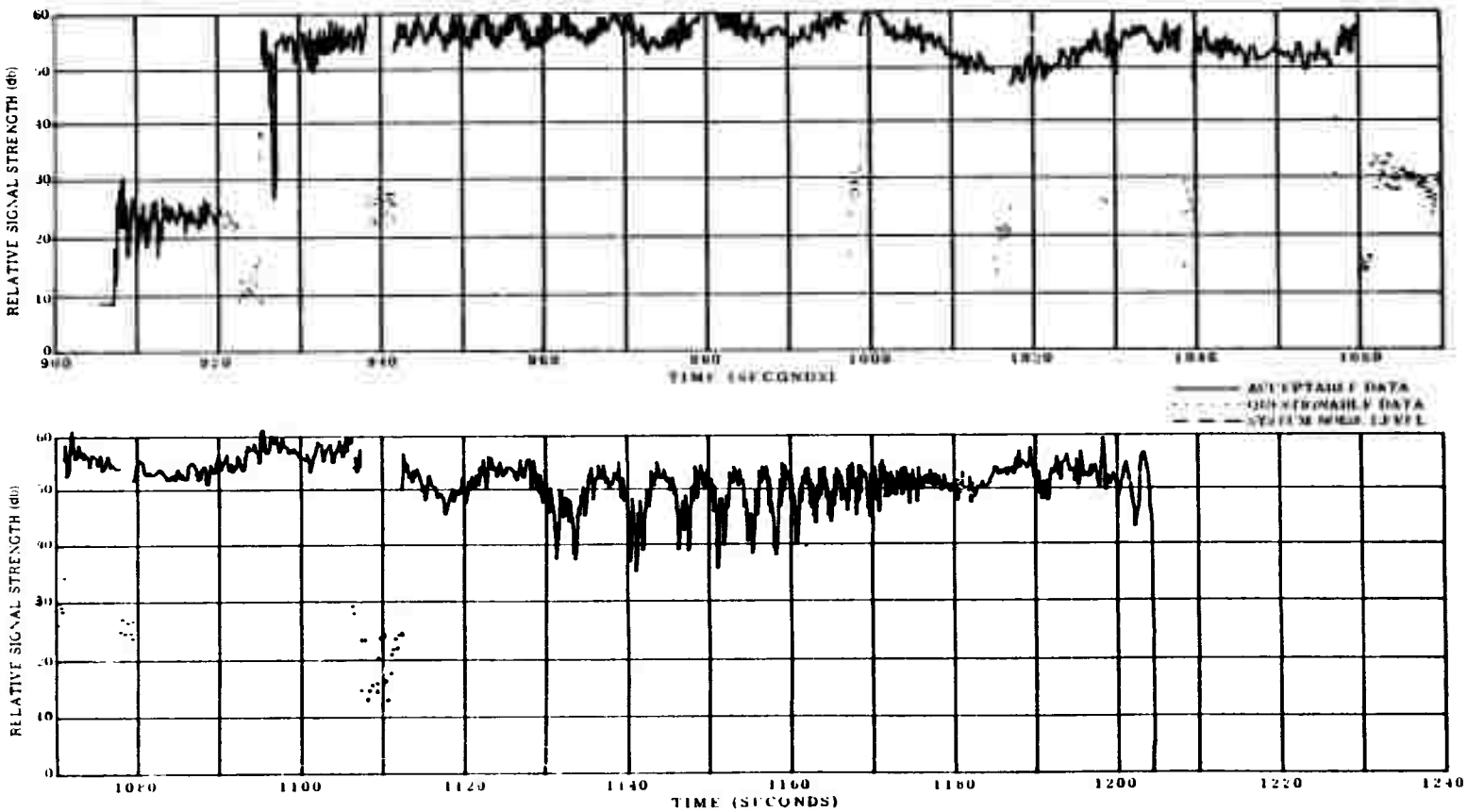

Figure 2.65 L band relative signal strength, Blue Gill, Missile F, Ship 2.

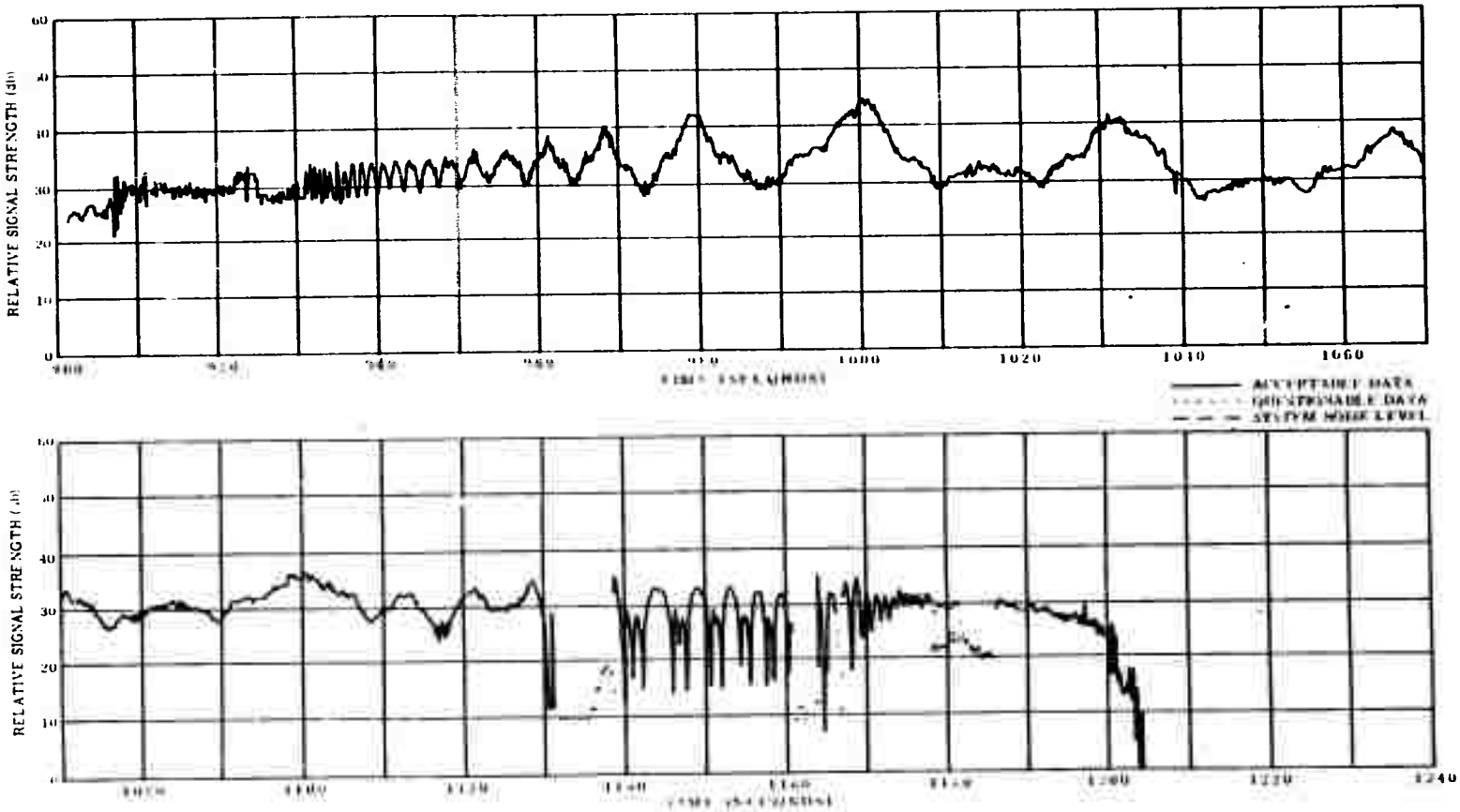

Figure 2.66 X band relative signal strength, Blue Gill, Missile F, Ship 3.

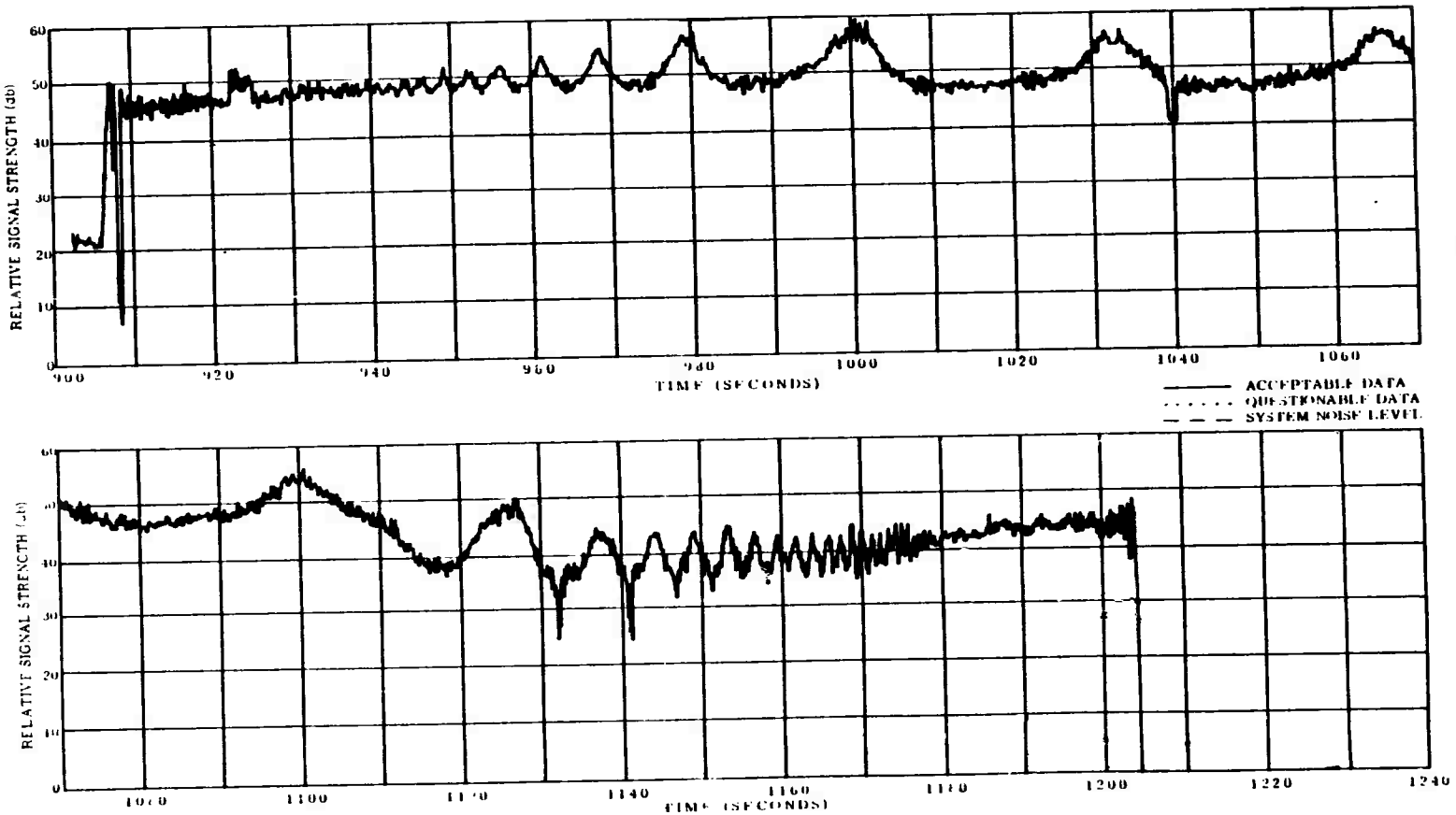

Figure 2-67 C-band relative signal strength, Blue Gill, Missile F, Ship 3.

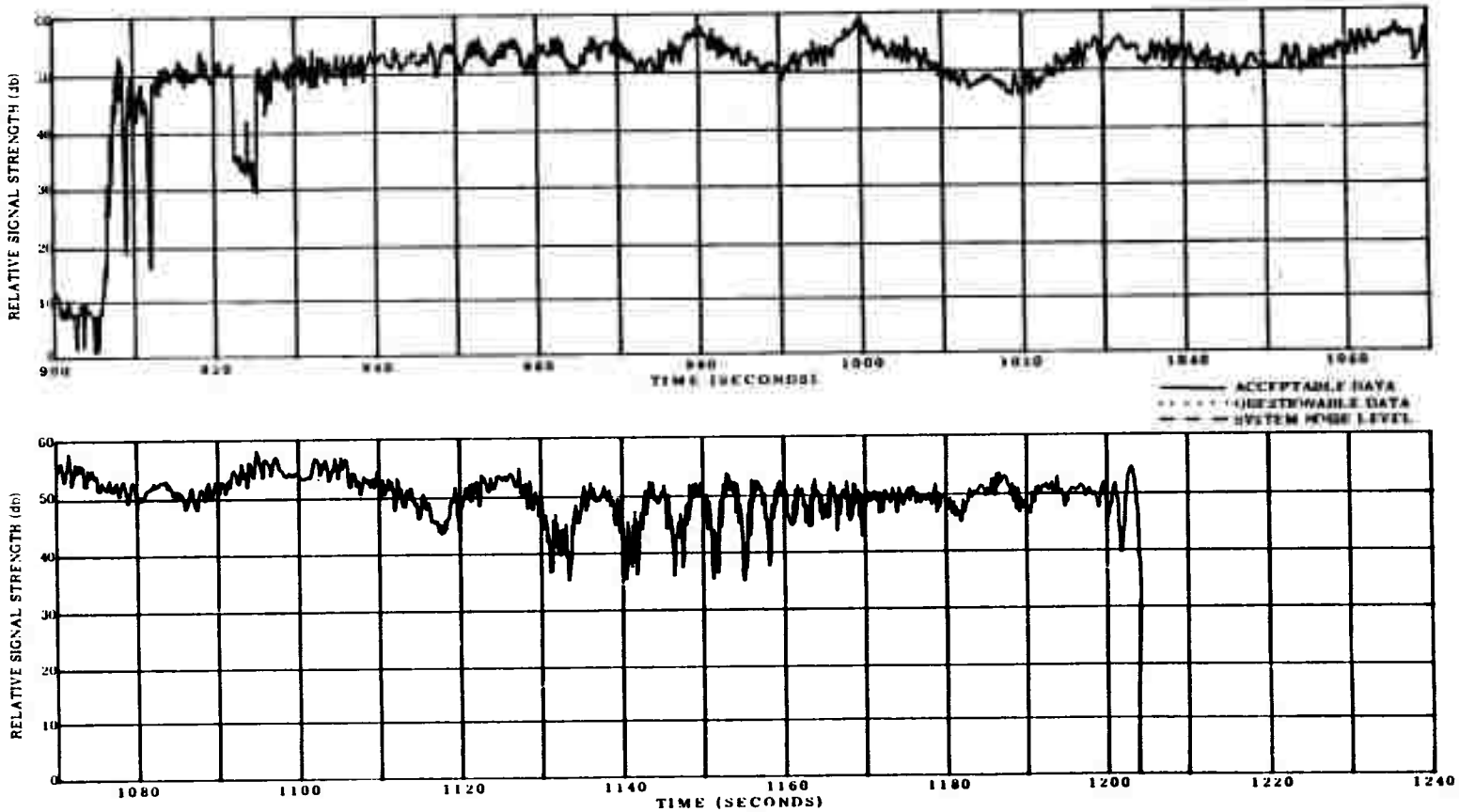

Figure 2.68 L-band relative signal strength, Blue Gill, Missile F, Ship 3.

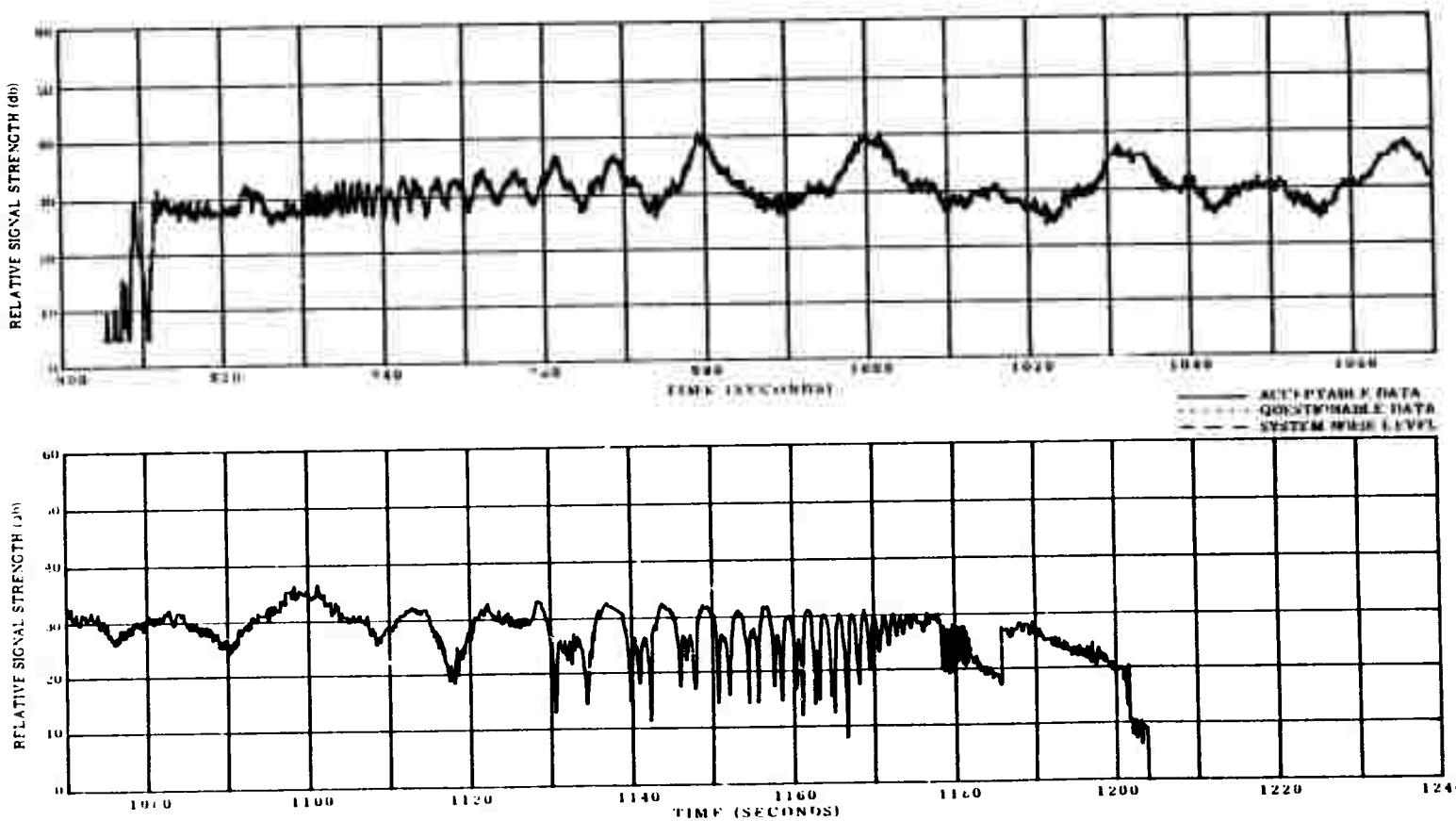

Figure 2.69 X band relative signal strength, Blue Gill, Missile F, Ship 4.

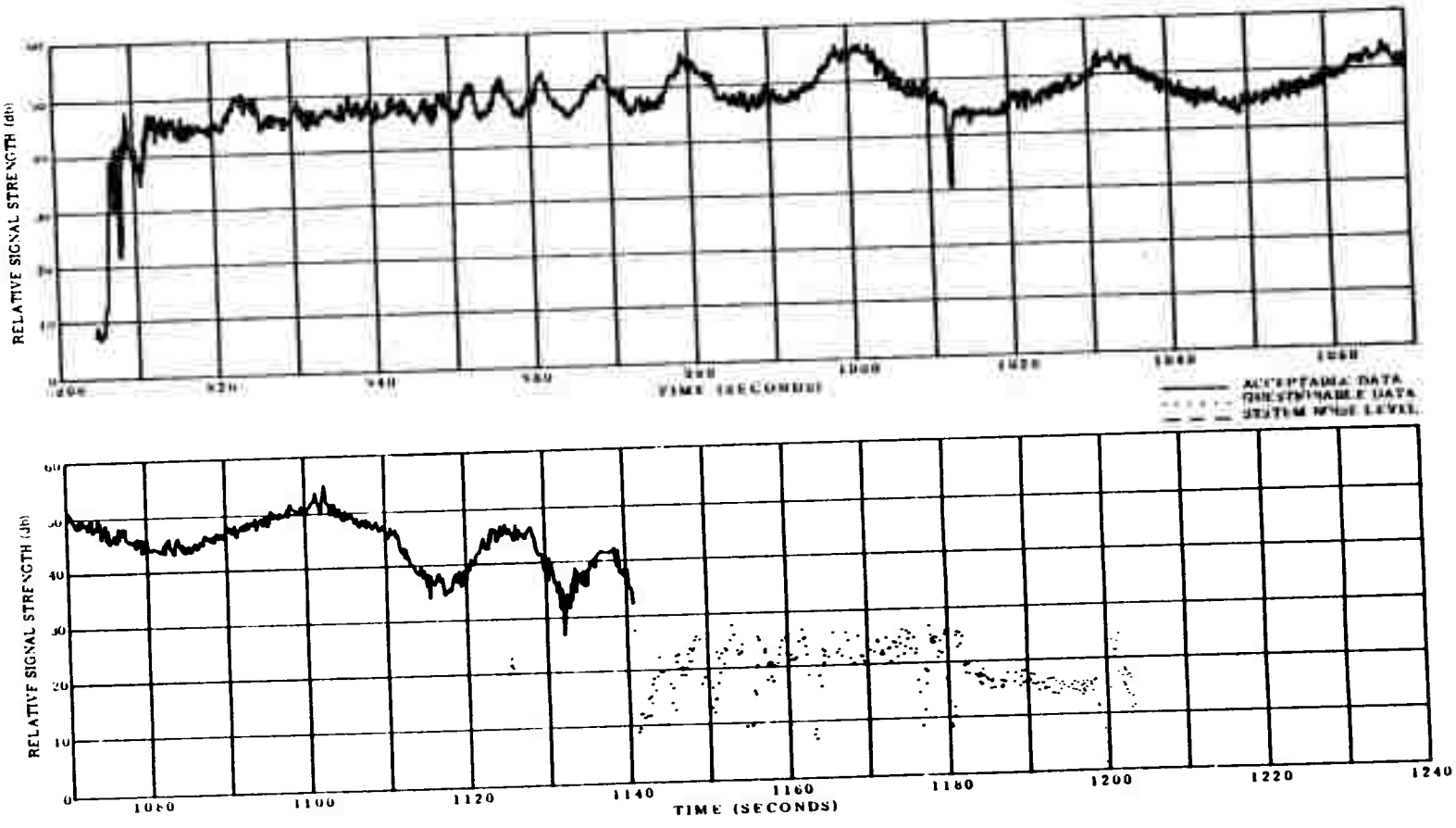

Figure 2.70 C-band relative signal strength, Blue Gill, Missile F, Ship 4.

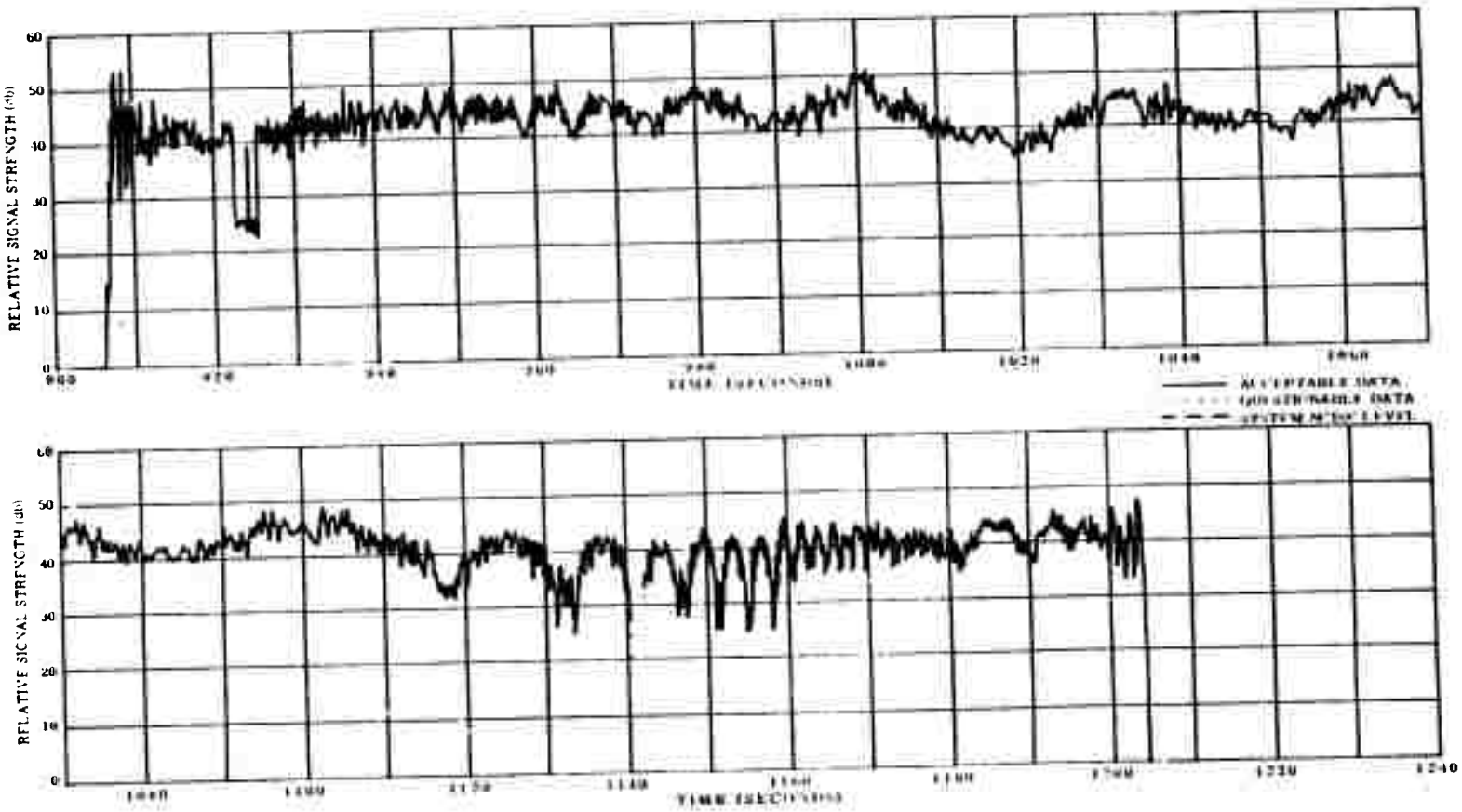

Figure 2-71. L-band relative signal strength, Blue Gill, Minuteman F, Ship 4.

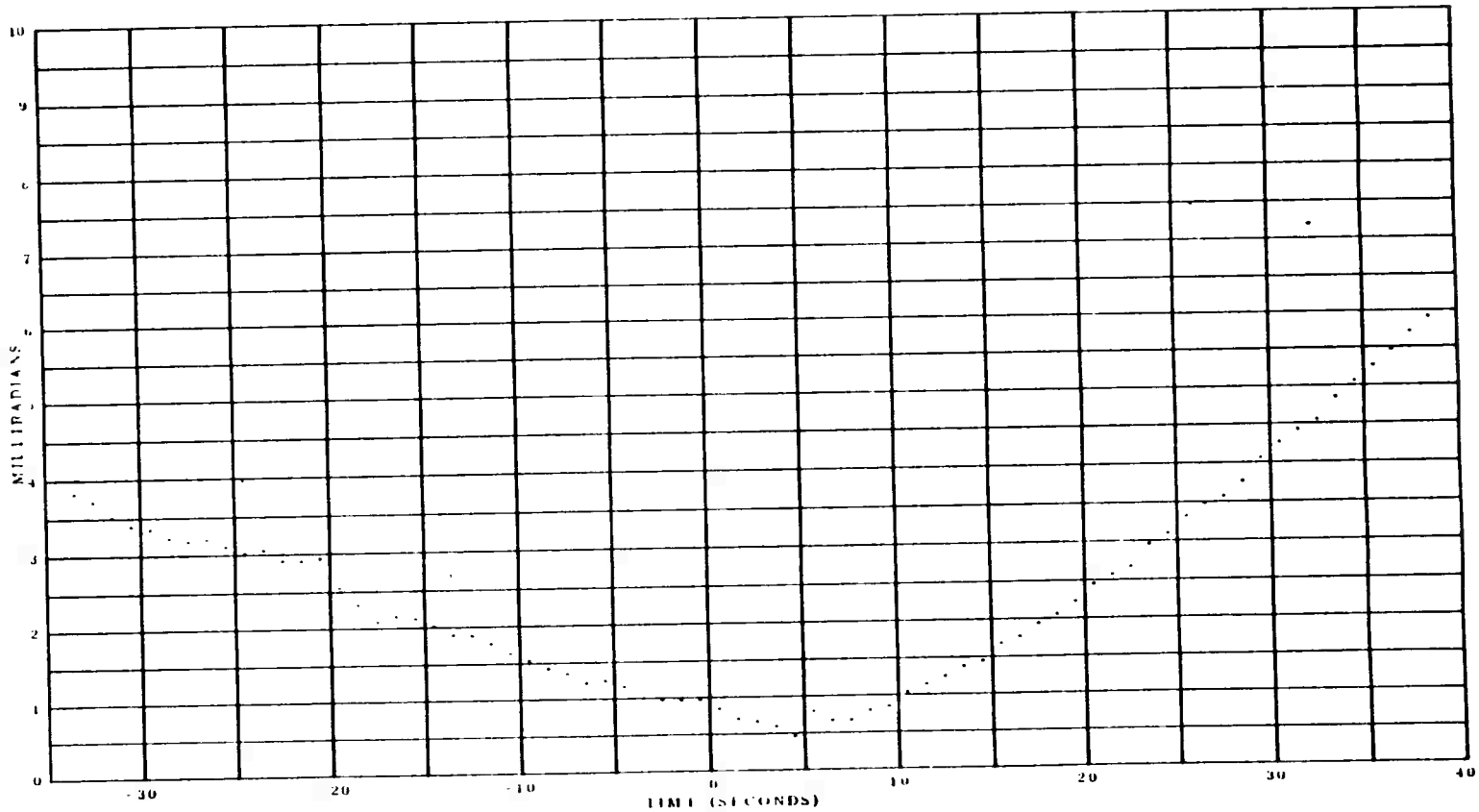

Figure 2-72 Interferometer and trajectory angular comparison, Blue Gill, Missile A, interferometer, least squares combination.

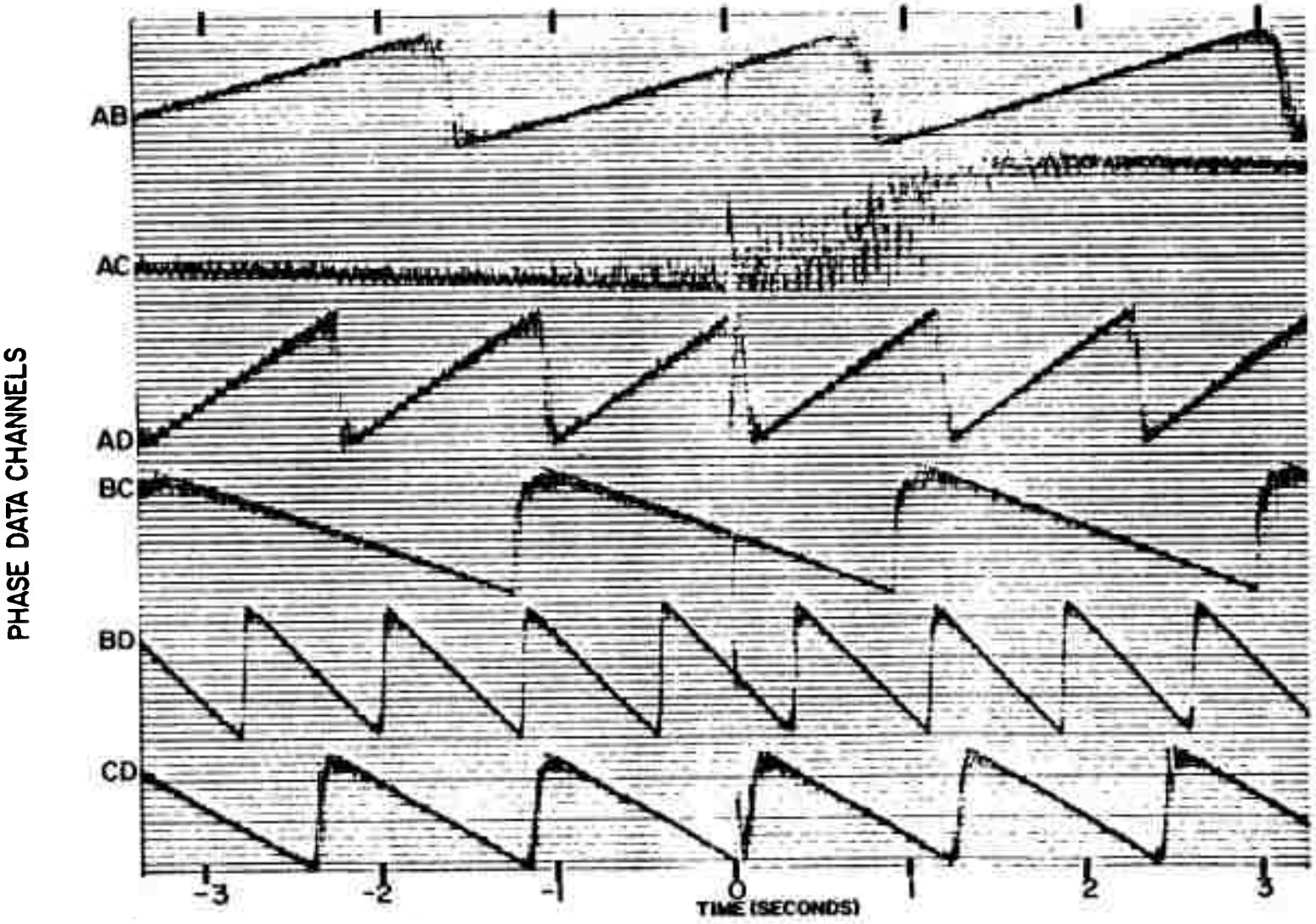

Figure 2.73 Raw phase data at event, interferometer, Blue Gill, C-band.

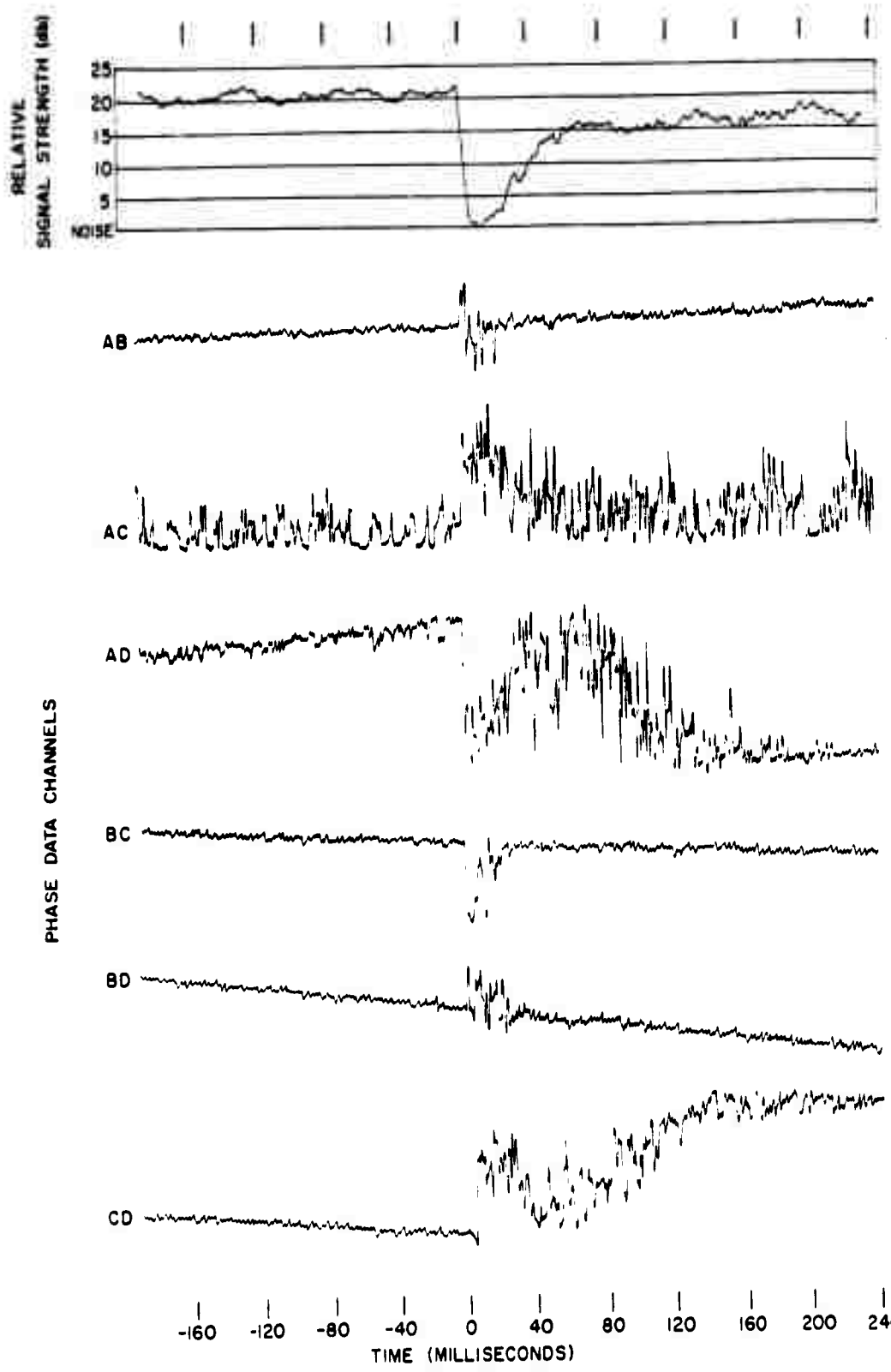

Figure 2.74 Raw phase data and relative signal strength at event, Blue Gill, Missile A, interferometer, C-band.

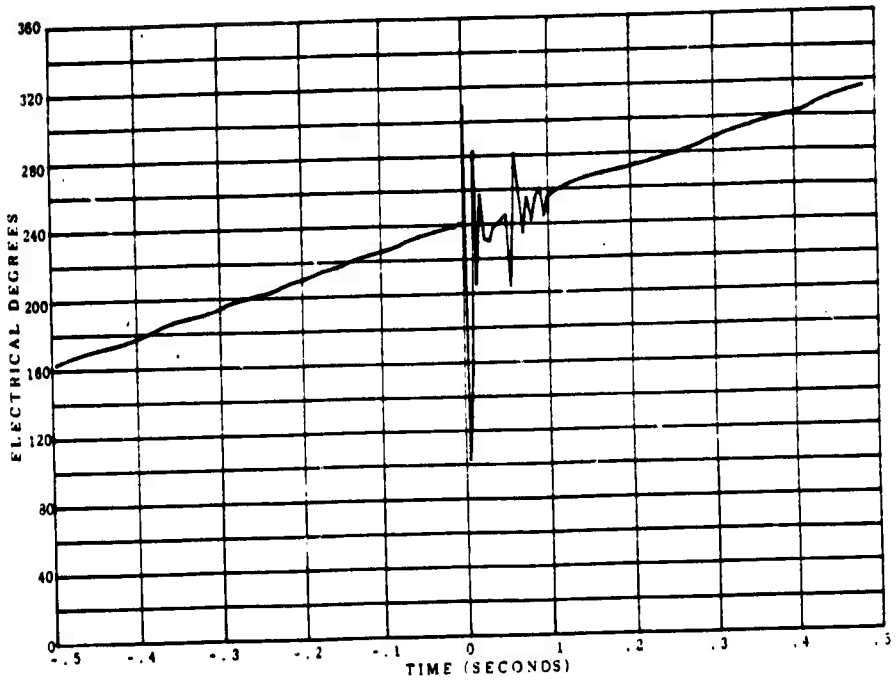

Figure 2.75 Phase perturbation at event, Blue Gill, Missile A, interferometer, Leg AB.

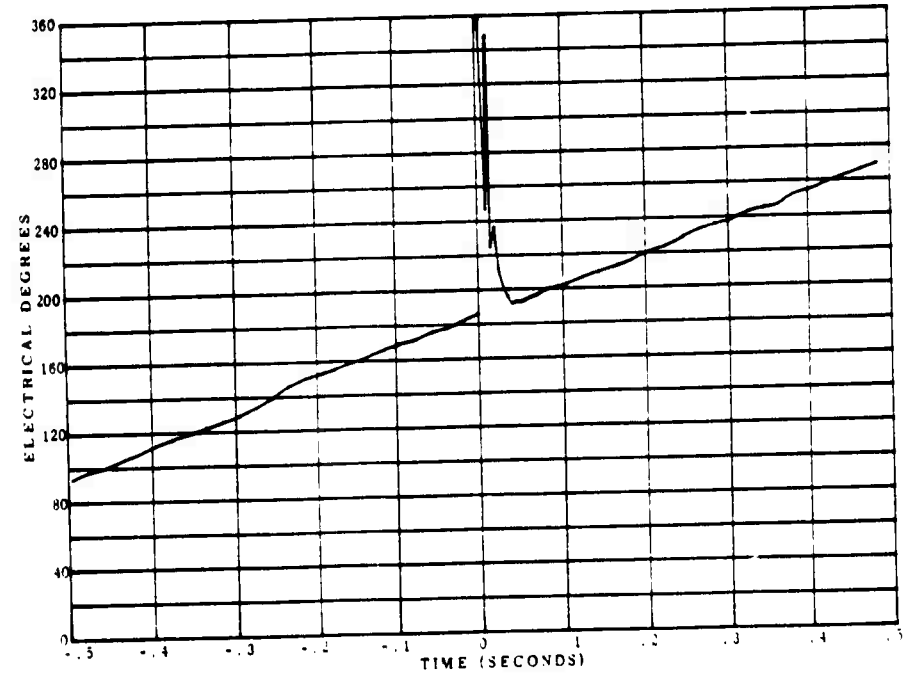

Figure 2.76 Phase perturbation at event, Blue Gill, Missile A, interferometer Leg BC

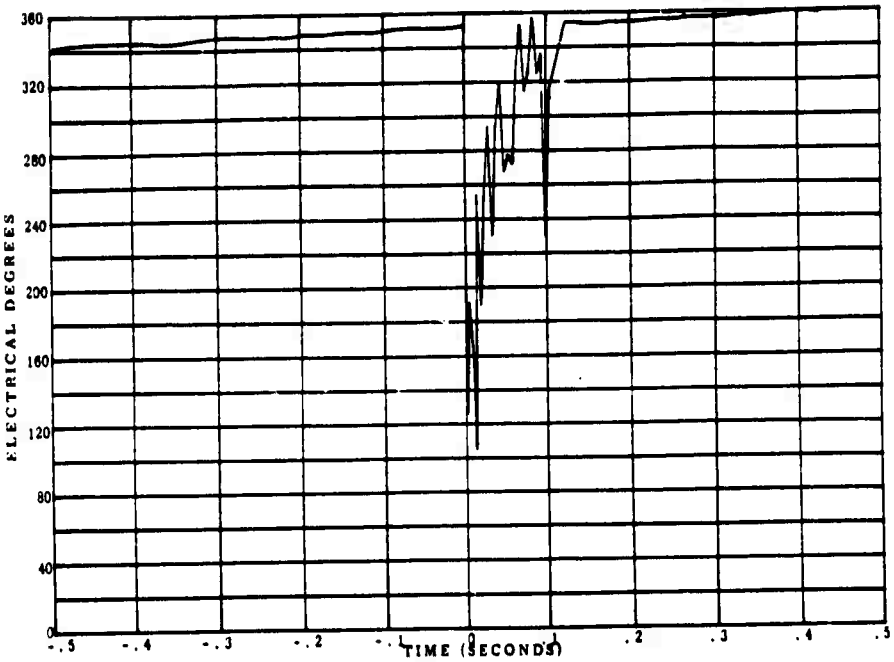

Figure 2.77 Phase perturbation at event, Blue Gill, Missile A, interferometer, Leg AC.

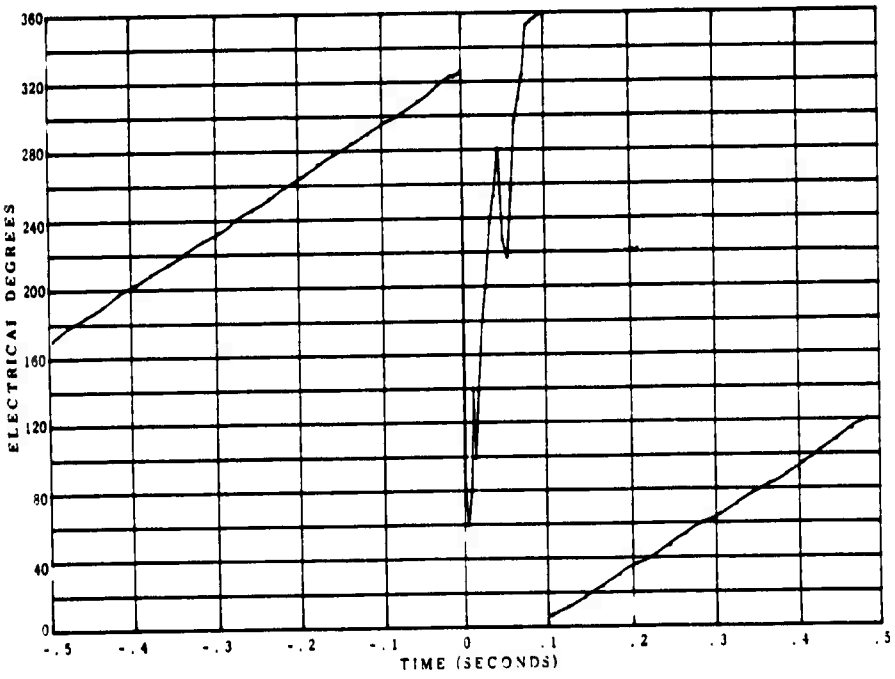

Figure 2.78 Phase perturbation at event, Blue Gill, Missile A, interferometer, Leg AD.

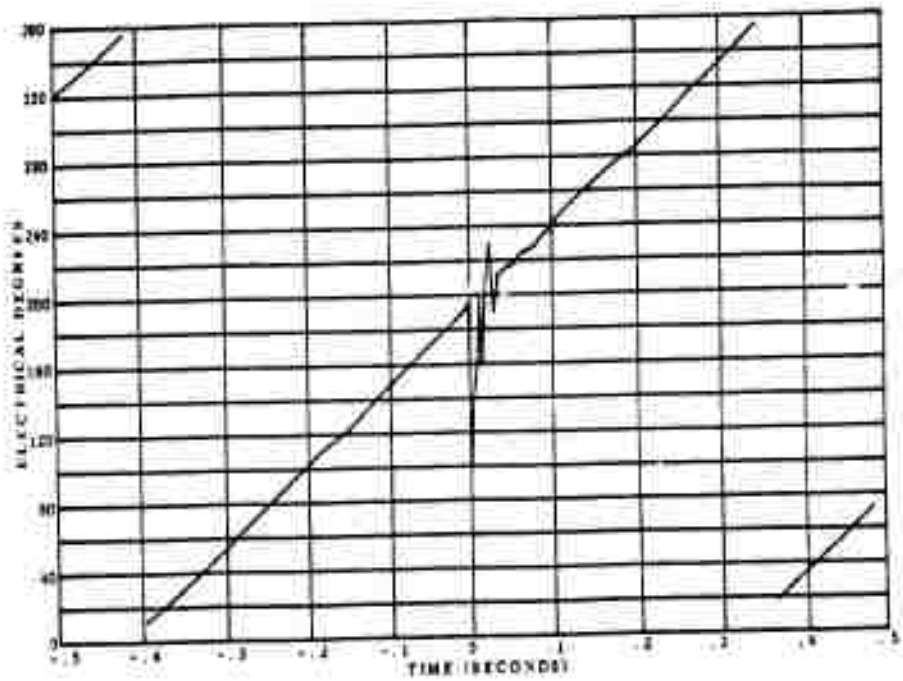

Figure 2.79 Phase perturbation at event, Blue Gill, Missile A, interferometer, Leg BD.

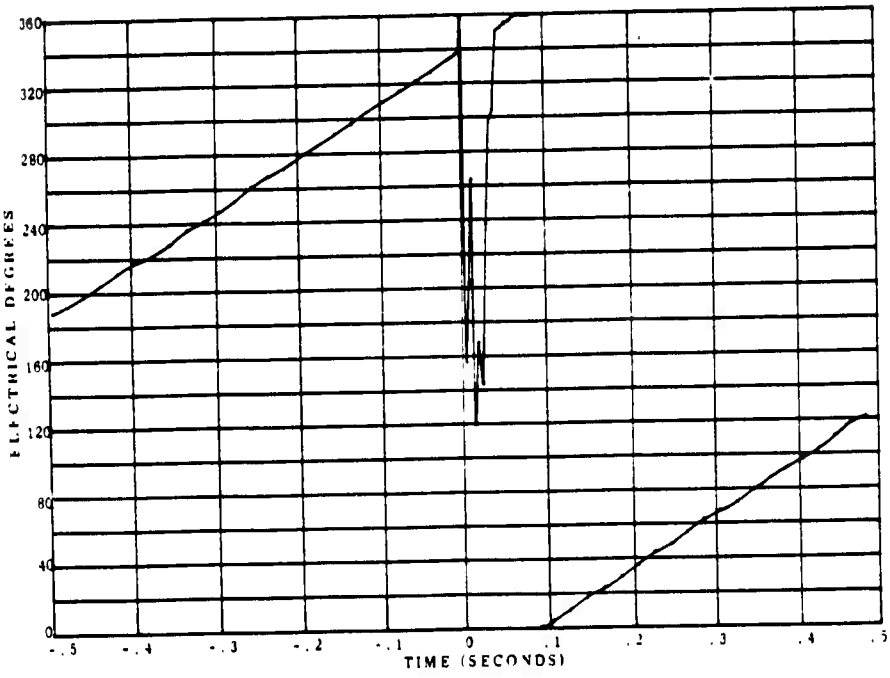

Figure 2.80 Phase perturbation at event, Blue Gill, Missile A, interferometer, Leg CD.

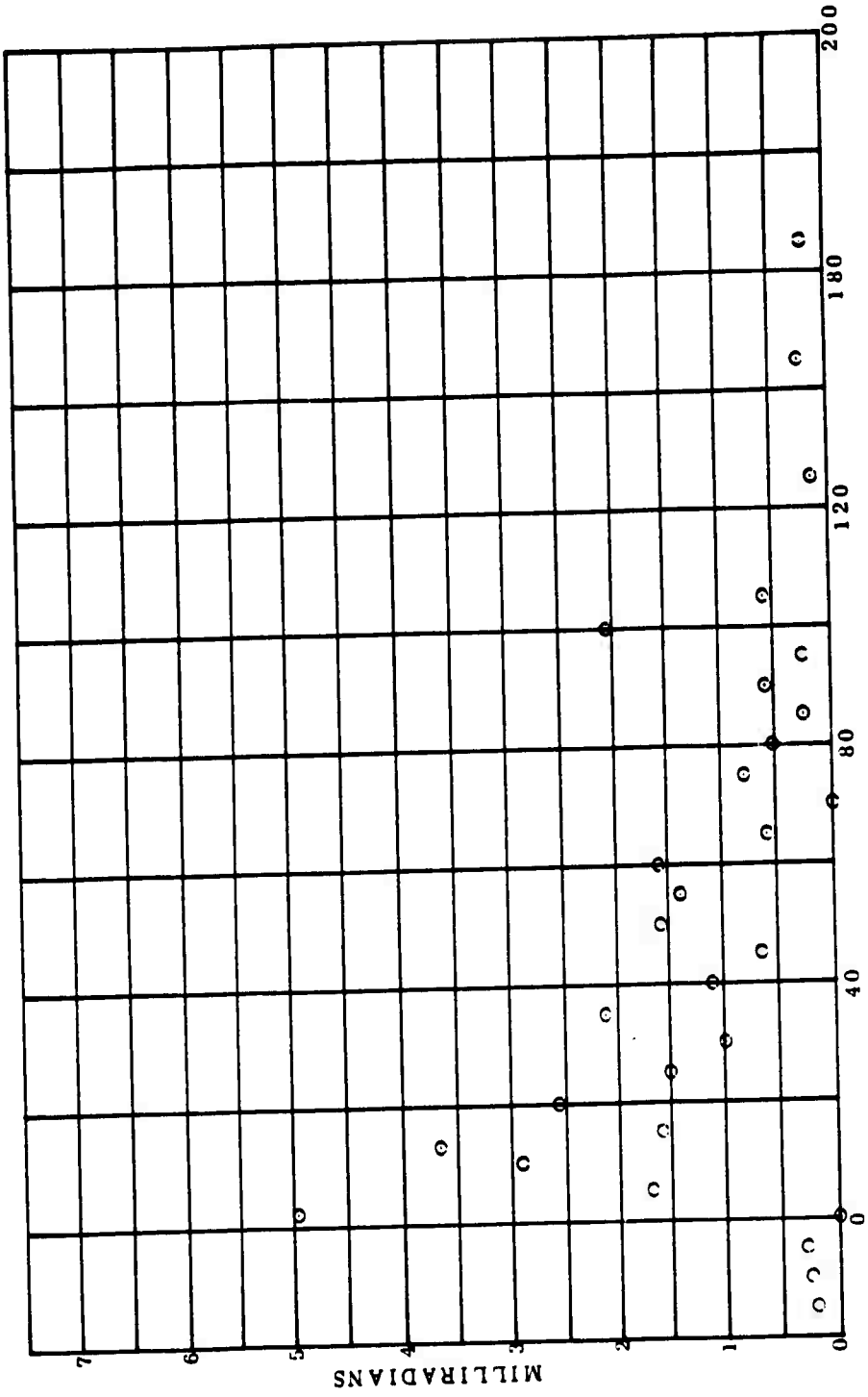

Figure 2.81 Perturbation at event, Blue Gill, interferometer, least-squares combination.

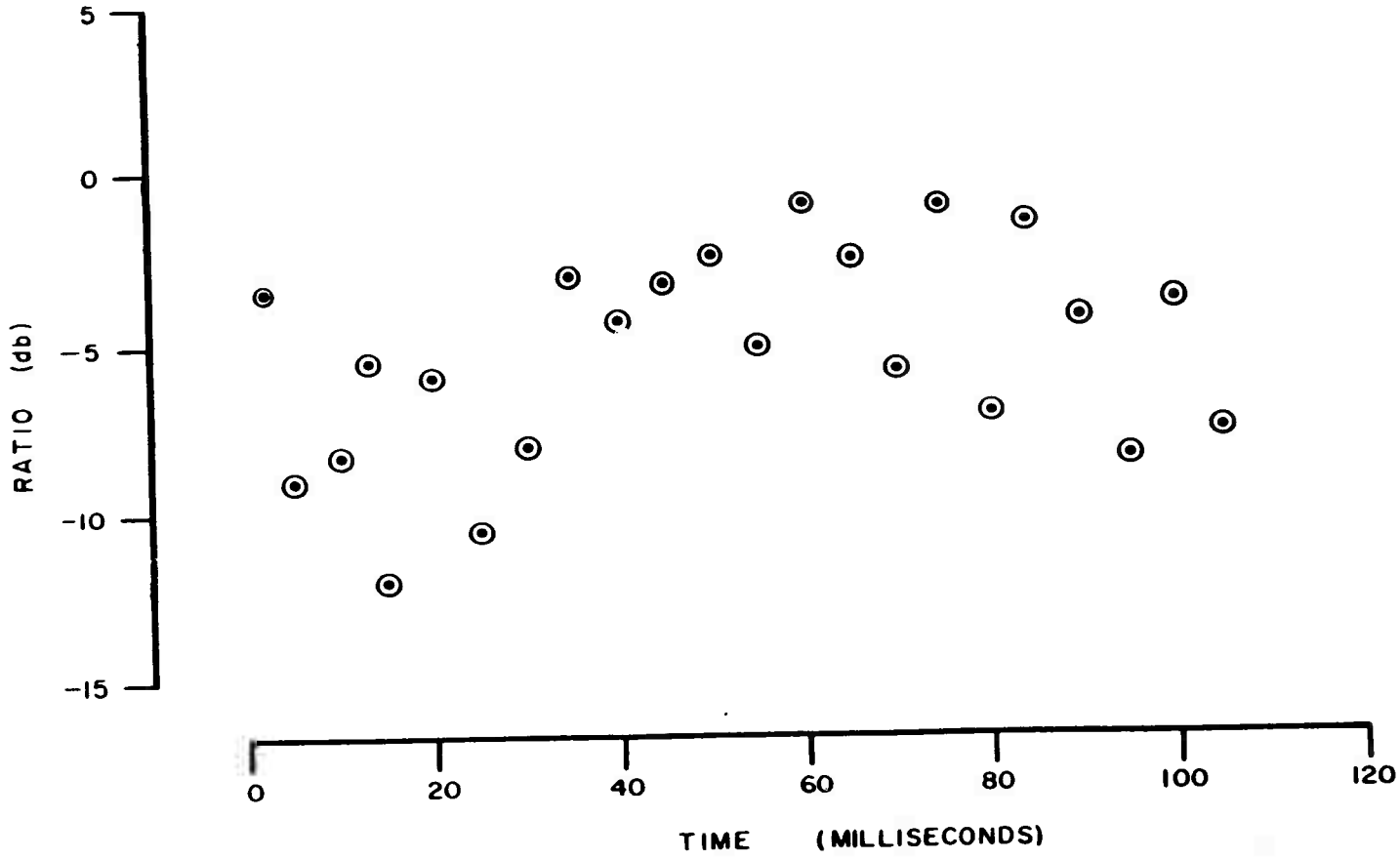

Figure 2.82 Ratio of mean perturbation to dispersion, azimuth plane, Blue Gill.

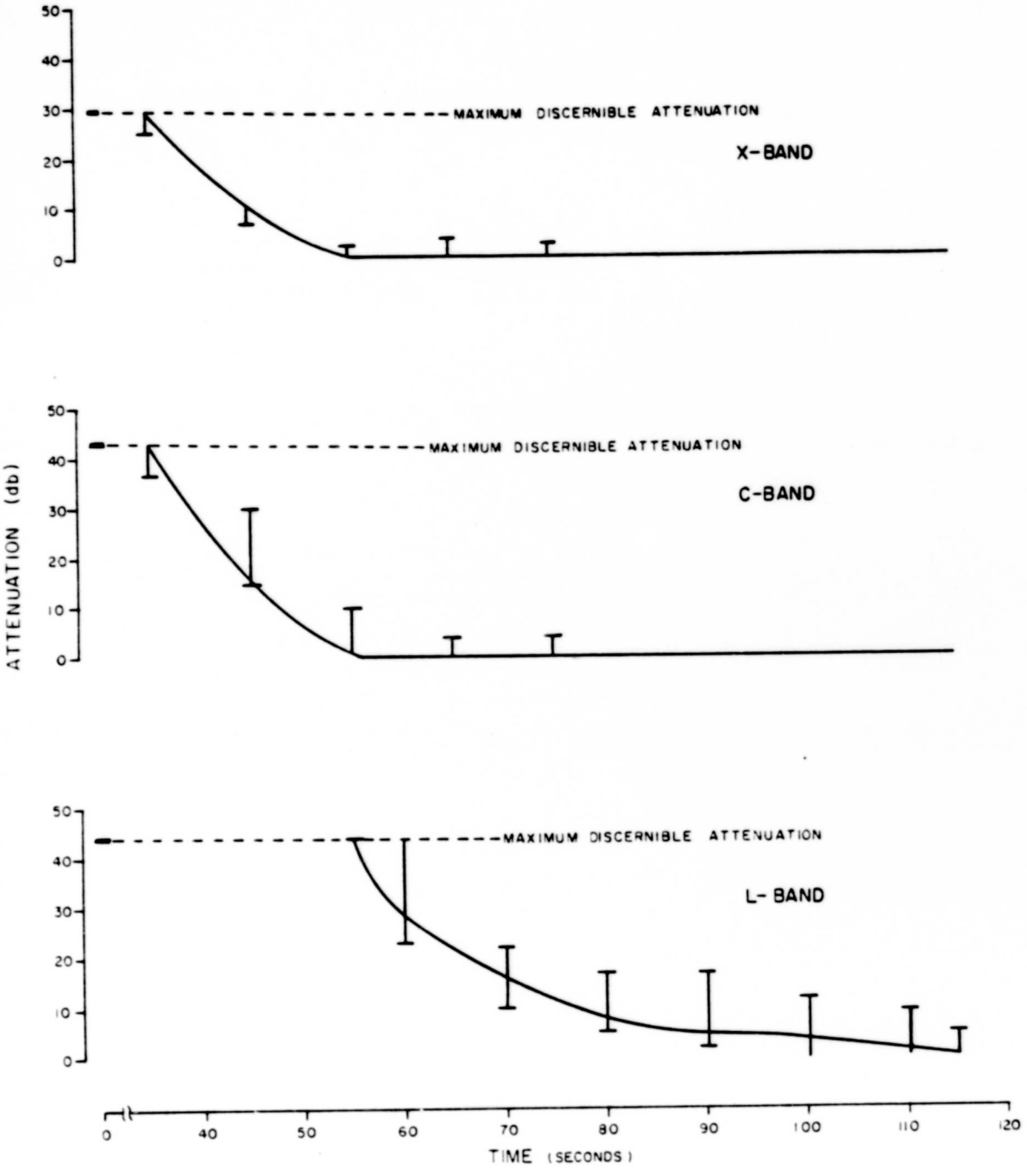

Figure 2.83 Characteristic attenuation through the Blue Gill fireball.

CHAPTER 3

KING FISH

3.1 PHENOMENOLOGY

The King Fish shot was a

at an altitude at

1210:06.1236 Z Greenwich Mean Time, 1 November 1962.

At this altitude, blackout effects were expected from the fireball and its gamma ray aurora and from a patch of ionization, caused by the delayed beta ray emission from the debris, centered at

3.2 OBJECTIVES

Three major objectives, proposed for measuring the effects of the King Fish event on X-, C-, and L-band frequencies, were: quantitative measurements of attenuation through the fireball region proper, attenuation measurements through the beta-induced ionized region that was expected to form just south of Johnston Island, and C- and L-band measurements of apparent angular refraction through the beta patch.

3.3 OPERATIONS

3.3.1 Operational Plan. In general, the operational plan was quite similar to that of Blue Gill. However, because of the interest evidenced in acquiring data from the beta patch, one of the four ships was moved to a position approximately 10 km north of Johnston Island on a bearing of 191 degrees True. This ship, S-2, and the interferometer

station on the island were used to monitor rocket beacons transmitting through the beta patch during the early times after event. The three remaining ship stations were positioned downrange from Johnston Island in a triangular array centered on a bearing of 191.8 degrees True. S-4 was positioned at 134 km from the island, and S-1 and S-3 were 145 km downrange and approximately 12 km apart. These ship stations were positioned in such a manner as to obtain transmission paths from the beacon through the initial fireball and the developing fireball for the first 30 to 40 seconds following event. Figure 3.1 is an artist's concept of the overall geometry of Project 6.1 during this event.

The rocket trajectory which was chosen for interferometer monitoring was determined in such a manner as to allow a transmission path from the beacon to the island station through the early beta-ionized region. In a study directed by Project 6.1c and carried out at the Air Force Special Weapons Center (AFSWC), the following estimated characteristics for fireball and beta patch formation were determined:

Initial fireball radius was expected to be

Fireball rise rate was expected to be approximately

Fireball expansion rate was predicted at about

Initial beta energy deposit was expected to be in a region some 10 to 20 km south of Johnston Island at an altitude of 60 to 70 km.

The beta patch formed by the detonation was expected to move northward along the earth's magnetic field lines at a velocity of approximately twice that of the debris cloud.

Because of the exponential decay in beta emission, the ionization produced during the first ten seconds after event was expected to be most intense and, therefore, was considered the most important time of interest with respect to refractive and attenuation effects.

Considering these limiting conditions, a rocket trajectory for monitoring from the island station was chosen so that the rocket would be south of the island, at approximately the same altitude as the detonation, and yet north of the event at the time of burst. In this manner, a transmission path would be established between the rocket beacon and the island station through the beta patch for the first important seconds of its formation. In order to provide maximum system capability during the times of interest, the principal pointing axes of the interferometer antennas were elevated to 85 degrees, and the X-band helical array was replaced by a horn antenna. Figure 3.1 illustrates

the general geometry of the interferometer rocket position, the island station, and the beta region immediately following detonation. With this geometric arrangement, it was possible for the L- and C-band interferometers to monitor refractive effects occurring in this disturbed region. Attenuation measurements in X-, C-, and L-bands were also made at the island station.

Figure 3.1 also illustrates the rocket trajectory chosen for monitoring from the ship stations. This trajectory was dictated by the fireball and beta patch parameters already mentioned in connection with the interferometer rocket trajectory as well as by the ship-positioning restrictions listed in Section 2.3.1, Operational Plan (Blue Gill). The actual trajectory required the rocket to be above the detonation altitude and just slightly north of the burst at the time of detonation. In this manner, the ship which was positioned north of the island could monitor transmissions through the beta patch while the ships stationed downrange from the island could have transmission paths through the initial fireball and through the developing fireball for several seconds thereafter. This geometry was planned to provide a short-time history of attenuation in X-, C-, and L-bands for both the beta patch and the fireball proper.

Nike-Apaches were utilized as beacon carriers

The probable dispersion of these rockets and the possibility of rocket or beacon catastrophic failure dictated that they be launched in pairs in order to increase the probability of having a successful experiment. Table 3.1 gives the firing schedule for these rockets.

3.3.2 Fixed Station Operation. The technique of correlating real-time azimuth estimates from the Cubic Corporation vans with interferometer signal strength and beacon stability information for a quick-look evaluation of the missile pairs was again applied during King Fish. Two Nike-Apaches were fired for interferometer viewing at H-85 seconds (Missile C) and H-80 seconds (Missile D). The quick-look evaluation indicated better performance on the part of Missile C; therefore, it was monitored throughout this event by the island station. Figure 3.2 presents the plane views of both elevation and azimuth for the H-85-second rocket upon which rough fireball data, furnished by Edgerton, Germeshausen and Grier, Inc., has been superimposed. Note that this is a simulated trajectory.

3.3.3 Shipboard Station Operation. All four ship

stations monitored transmissions from the same rocket during the King Fish event. However, because of the interest expressed in the phenomena associated with the beta-induced ionized region, one ship was stationed north of the island.

Two Nike Apaches were fired: Missile A at H-160 seconds and Missile B at H-155 seconds. The quick-look evaluation by the island station indicated the H-155 rocket was the better of the pair, and it was tracked by all four ship stations. The evaluation information was relayed from the island to the ships via the command link. Table 3.1 gives the firing schedule.

3.3.4 Support Data. Figure 3.2 is the azimuth and elevation plot of Missile C trajectory with the ship locations and fireball dimensions and positions at significant times during King Fish. Missiles B and C, which were selected for tracking during this event, were launched at H-155 and H-85 seconds, respectively.

Due to system operational problems involving the Distance Measuring Equipment (DME), no instrumented trajectory data was available for Missile C (H-85) from Cubic Corporation which provided tracks for Project 6.1 sounding rockets. Unextrapolated data on Missile B (H-155) was from H-155 to H-125

seconds. Cubic Corporation provided an extrapolated trajectory for Missile B. Although there was not sufficient data available to extrapolate a trajectory for Missile C, theoretical trajectory data was utilized in estimating the location of the rocket at event time. This was necessary in order to make any estimate of short-term refraction at event. Final Cubic trajectories are tabulated in Appendix B.

Ship locations during the King Fish experiment, provided by the Navy and determined by radar and flashing light beacon fixes, are given in Table B.5, Appendix B. Positional accuracy for the ships was submitted to be a radial 500 yards. The positional relationships of the ships to ground zero at H-hour is given in Table B.6. During the course of the operation, all ships were under steam, and their changing positions were determined by several estimates of heading and speed (see Table B.7).

Fireball expansion and rise-rate data available from Edgerton, Germeshausen and Grier, Inc., was primarily acquired by photographic analysis. At times of interest, the dimensions, positions, and consistency of the debris cloud are rather nebulous (see Figures B.6 to B.10, Appendix B). In some cases, the data given on the graphs were highly conflicting and could not be readily interpreted.

Data pertaining to the shape of the debris cloud in the Y-Z plane was incomplete and had to be very roughly estimated. The location of the re-entry vehicle at the time of event in the various coordinate systems employed during the King Fish operation is shown in Table B.12, Appendix B.

3.4 RESULTS

A discussion of instrumentation limitations and data interpretation is presented in Sections 1.6 and 1.7.

Interferometer data reduction procedures and sources of interferometer system error are described in Appendix D.

3.4.1 Attenuation Data.

Fixed Station. The X-band receiving system functioned poorly during this experiment, and signal levels remained within a few db of noise for most of the mission. Figure 3.3 is a complete record of maximum X-band signal envelope. Due to the system's inefficiency, no significance is attributed to the data.

At event, C-band signal dropped 32 db to system noise, recovering 20 db within 20 milliseconds. A time-expanded view of the signal at event time is presented in Figure 3.25. Signal levels gradually increased to within about 3 db of pre-event amplitude by H+4.5 seconds where they persisted for the remainder of the flight. A complete record of maximum

C-band signal envelope is presented in Figure 3.4. There are no means to determine whether the residual 3-db loss was caused by beta-patch attenuation or was the result of an equipment malfunction. It is, however, improbable that there was sufficient ionization present to obscure ray paths during the late-time portions of the H-85-second rocket flight. The cause of data anomalies occurring between H+155 seconds and H+162 seconds is not known, although an equipment malfunction is suspected. Figure 3.5 presents the maximum and minimum C-band data envelopes for the primary times of interest. There were no amplitude scintillations such as were associated with the Blue Gill fireball attenuation recovery periods.

At H = 0, L-band signal sustained a 48-db loss to noise where it remained for 15 seconds. A gradual recovery increased the signal to within 11 db of pre-event levels by H+43 seconds where it remained for subsequent periods of interest. A complete record of maximum L-band envelope is presented in Figure 3.6. The observed losses, following H+160 seconds, were caused by receiving antenna patterns and missile reorientation. (The principal axes of the receiving antennas were set at an 85-degree elevation angle.) Figure 3.7 presents the maximum and minimum L-band data envelopes for the primary times of interest. Amplitude scintillations are evident during the recovery period.

Shipboard Stations. The persistence of blackout of Missile B, noted by all ships after event, was undoubtedly due to some malfunction within the missile transmitter. This is substantiated by the simultaneous signal loss and failure to recover by all stations tracking the beacon (Figures 3.[illegible] to 3.19). The extrapolated trajectory furnished by Cubic was compared with the fireball origin. Approximated signal beacon-receiver ray-path distances to the point of fireball origin range from 6 km for S-1 to 47 km for S-2. The fireball-ray-path parameters shown in Figures 3.20 to 3.23 indicate that except for momentary signal losses, due to the effects of prompt radiation, quick recoveries should certainly have been noted by S-2, since the ray path to this station was not obscured by the fireball for some time. Although S-1, S-3, and S-4 signal paths were interrupted by the fireball almost immediately after event, S-2 transmissions were not initially obscured until approximately H+10 seconds. Ray paths to all ships had departed from the cloud by H+30 seconds. All ships attempted signal reacquisition until H+140 seconds at which time all but S-4 tuned to Missile C (H-85). S-4 resumed track of Missile B 167 seconds after event. It is believed that S-4 detected the

resumption of transmissions at the earliest possible time, as reacquisition was preceded by a period of correct tracking antenna orientation.

An examination of pedestal data for all stations (Figures A.25 to A.32) indicates many instances of correct antenna look angles during the extensive period in which reacquisition was attempted. A review of transcripts of station operators' running commentaries reveals that all stations were able to see the transmitted frequencies of Missiles A, C, and D on the panoramic displays during this period but could not find any evidence that Missile B was radiating.

It should be noted that the intense prompt radiation may not have been the only contributing factor to the beacon failure. The difficulty experienced by all shipborne stations in establishing a firm track of Missile B before event suggests the possibility that a faulty operating condition existed within the beacon package at early times and that the prompt radiation aggravated this condition to the point of failure. Although the exact reason for failure can only be postulated, it should be noted that one of the few sections in the beacon common to all three frequencies was the transistorized power supply which appeared to be the most susceptible to radiation during environmental tests.

Although there are a few anomalies in data from the ships following Missile B failure, a careful examination has failed to produce any firm explanation for them.

By H+180 seconds, Ships S-1, S-2, and S-3 had acquired Missile C and continued to track it to splash. Signal ray paths to the ships did not intercept the fireball at any time during the late-time tracks of Missile C. There is no evidence in the data of any obvious attenuation of these signals (see Figures 3.8 to 3.19). During the operation at S-3, an inadvertent disabling of the instrumentation recorder by a station operator caused a total loss of data commencing at H+222 and lasting for 20.5 seconds.

3.4.2 Refraction Data.

Interferometer. No useable trajectory information was available from Cubic Corporation for this event. Therefore, it was impossible to extract any long-term indications of apparent refraction from the data.

With approximate trajectory information, approximate values for apparent refraction during short time intervals can be computed when deviations in the data are sufficient to be differentiated from nonperturbed data. For this purpose, a simulated trajectory (Figure 3.2) was generated which was based upon missile launch parameters, splash time, and late-time azimuth and elevation data from the ship stations.

Refraction results are presented only for C-band because the duration of signal loss in L-band prevented the collection of data during the times of interest immediately following event. Figure 3.24 is a photograph of the raw C-band phase data. Note the change in slopes at event time. Small anomalies at other times in the data are caused by equipment and should be ignored. An expansion of the first 200 milliseconds after event is shown in Figure 3.25. An examination of this phase data, together with the AGC record which is displayed at the top of the figure, has established the first 16 milliseconds of data following event as noise. The behavior pattern of the data during this period is a reflection of the normal reaction of the phasemeters to low signal levels.

Figures 3.26 to 3.31 present refined expansions of this phase data in which the amplitudes of the recorded deviations are calibrated in electrical degrees. In some cases noise spikes were read from the data and should be recognized as such. From this data, together with extrapolated data during the period of interest and an estimation of beacon location, equivalent space angular deviations were computed for each of the 14 interferometer combinations.

Figures 3.32 to 3.45 are plots of these computed deviations.

The points representing large refraction values within the first 20 milliseconds should be ignored because the computations for this interval included noise values. These figures indicate peak refraction, for most combinations, of approximately three milliradians, with further indications that this value decreases to about one milliradian or less within 200 milliseconds. The residual value appears because some legs of the raw phase data do not show a return to the pre-event slope. It is not known whether this residual value represents legitimate refraction or an equipment problem.

Figure 3.46 presents least-squares values for the same period following event and indicates the total observed apparent angular refraction for King Fish. A comparison was made between the mean values of the fourteen combined solutions and their dispersion to establish a confidence factor for the data. A ratio of this comparison appears in Figure 3.47. It can be seen that noise levels in the first few milliseconds of data obviate the value of any refraction measurements for that initial period. Subsequent values, after approximately 20 milliseconds, appear justifiable.

Component apparent refraction angles in the azimuth and elevation planes are given in Figure 3.48. Arithmetic mean values for the various phase comparisons are point-plotted,

and standard deviations for the dispersion of measurements comprising these means are indicated.

The least-squares solution of Figure 3.46 and a discussion of interferometer data consistency appear in Appendix D.

Shipboard Stations. Due to tracking error signal calibration difficulties, no refraction effects could be measured from shipboard station data. A discussion of attempts to obtain shipboard station refraction measurements is given in Section 2.4.2.

3.5 DISCUSSION

3.5.1 Data Reliability. Accuracies for Project 6.1 and support data are discussed in Section 2.5.1 and presented in Table 2.4.

3.5.2 Attenuation. If the residual signal losses (3 db in C-band and 11 db in L-band (at the fixed station) were the result of fireball-associated attenuation, then the $1/f^2$ frequency-attenuation relationship would have to be revised. It is believed that the long-term decreased signal levels in both bands were caused in whole, or in p , by operational changes in equipment which probably resulted from radiation damage to the beacon.

It is assumed that the attenuation observed at event was

caused by the initial radiation. The delay in L-band recovery is probably the result of beta-patch ionization, since signal ray paths to the fixed station did not intercept the fireball at any time during the flight of Missile C (H-85).

The King Fish beta patch produced very little effect on C-band transmissions. L-band attenuation in excess of 48 db for 15 seconds and the subsequent slow recovery appear to be significant if caused by beta-patch ionization. The relationship between L-band recovery and beta-patch movement is not certain. Estimates of beta-patch movement (Reference 5) related to L-band recovery suggest that the ionization level is decreasing even before the beta patch moves north. It should be noted that there are no large C-band amplitude scintillations during recovery, such as were associated with the Blue Gill fireball. Scintillations in L-band existed but were relatively small compared to those of Blue Gill. This suggests fairly uniform ionization and also indicates fewer operational problems for radar systems attempting operation through such a region.

3.5.3 Refraction. Initial radiation produced apparent angular refraction of three milliradians or less in C-band. If long-term apparent refraction exists through the beta patch (and its existence is undetermined), it would appear to have a maximum value of about one milliradian.

TABLE 3.1 FIRING SCHEDULE, KING FISH

Time, Seconds	QE, Degrees	Azimuth, Degrees	Impact Range, km	Monitoring Station
H-160	83	191	100	S-1, S-3, S-4
H-155	83	191	100	S-2
H-85	86	191	56	Interferometer
H-80	86	191	56	Interferometer

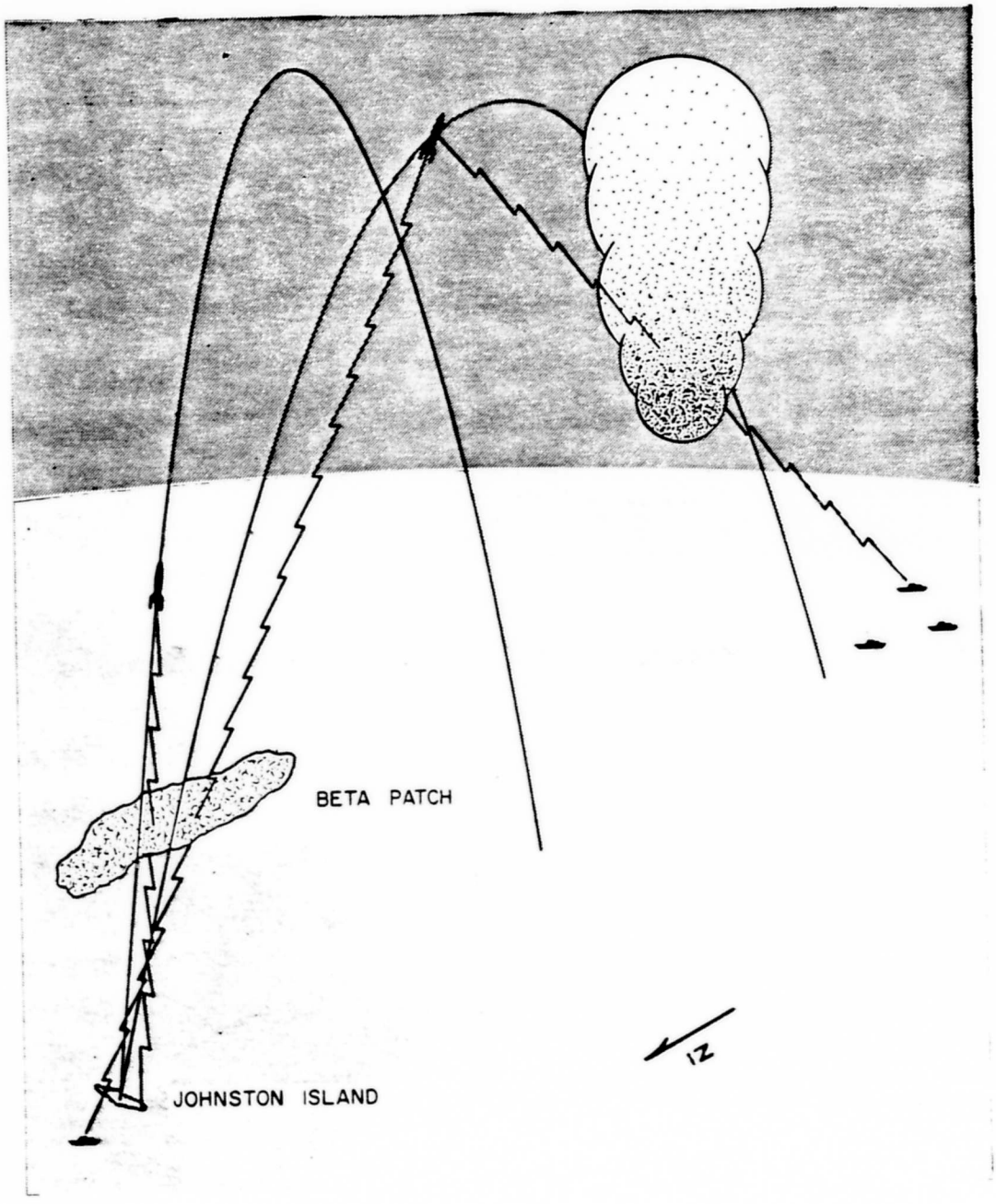

Figure 3.1 King Fish geometry, Project 6.1.

Page 232 deleted.

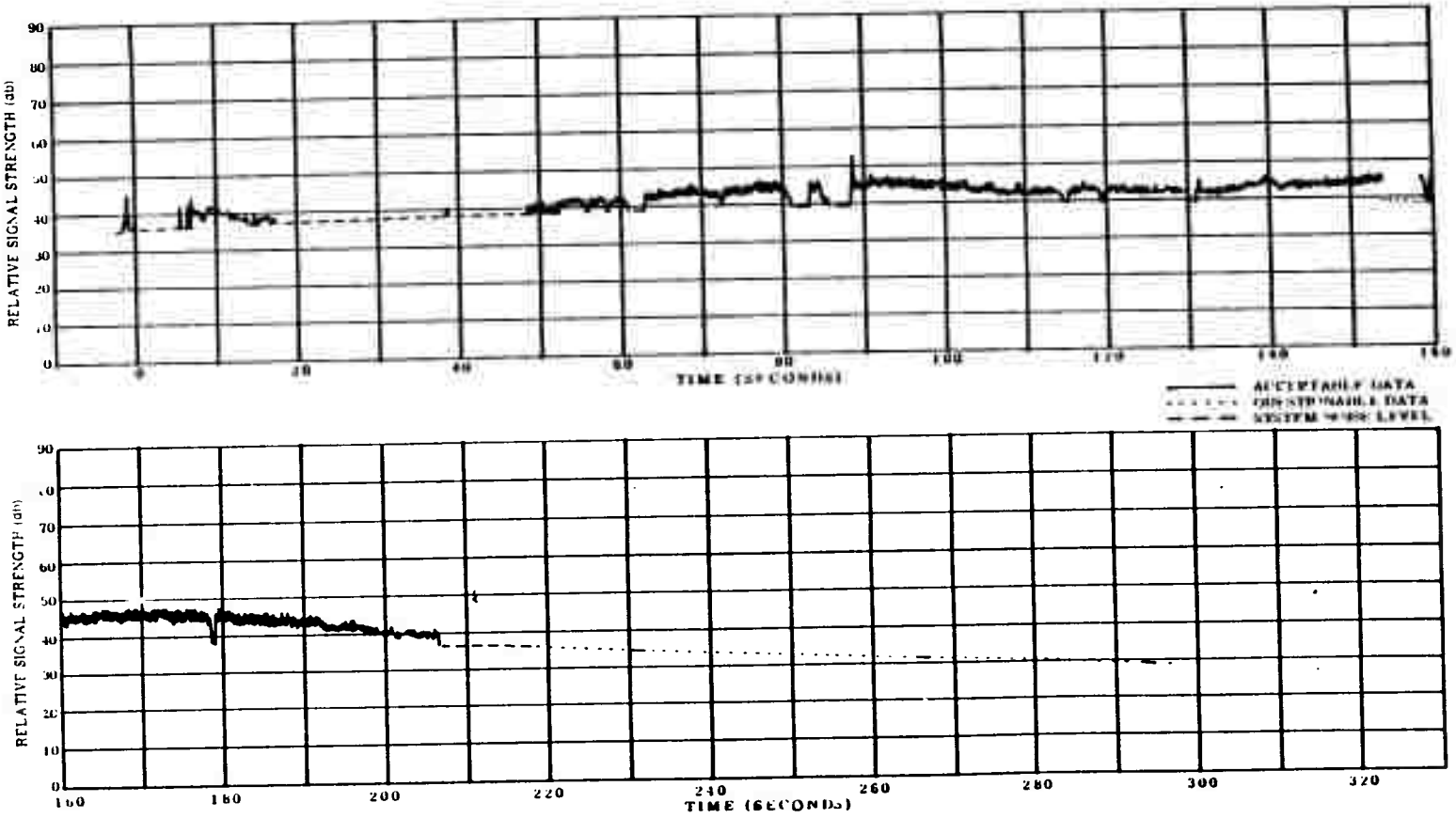

Figure 3.3 X-band relative signal strength, King Fish, Missile C, interferometer.

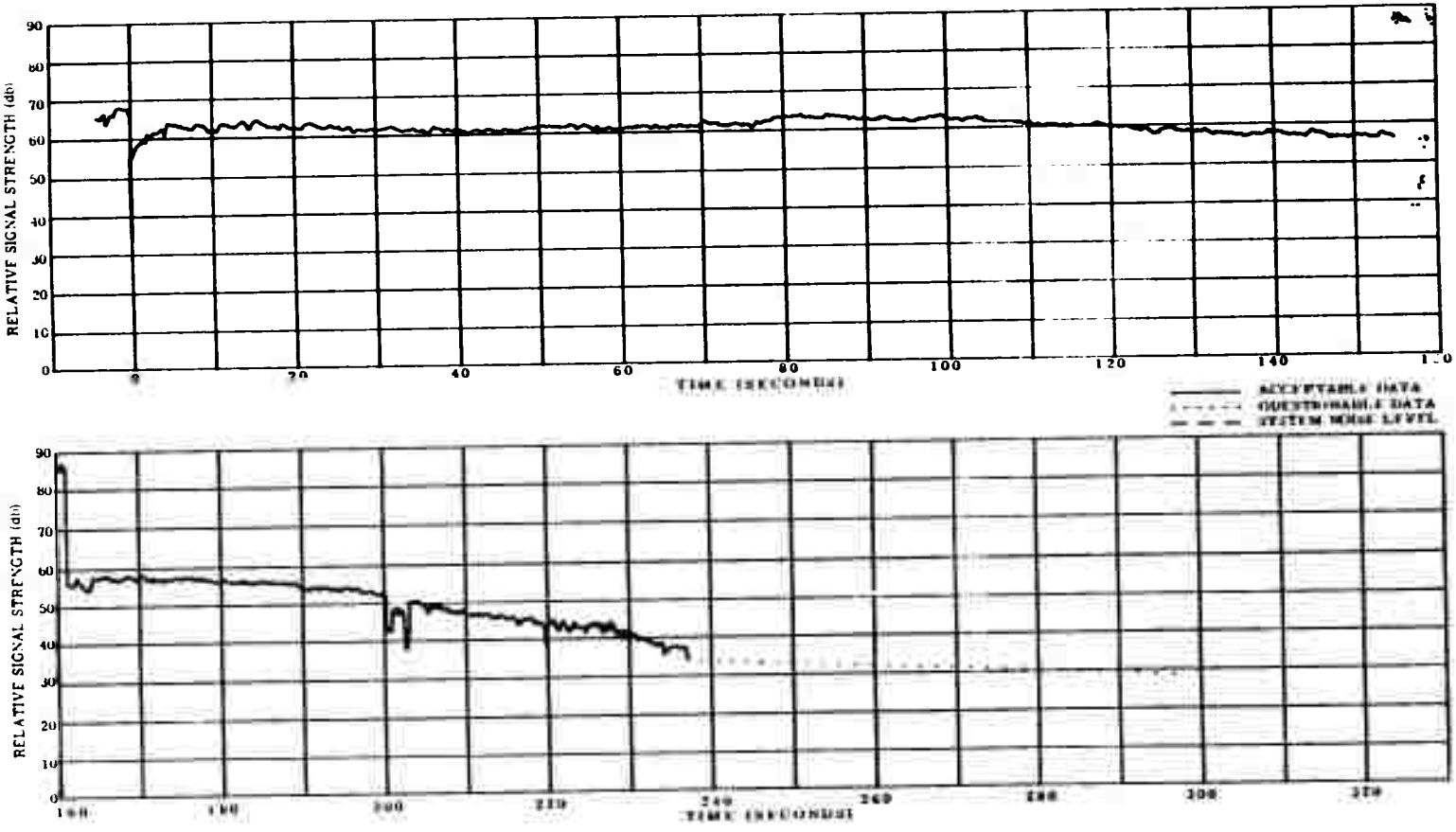

Figure 3.4 C-band relative signal strength, King Fish, Missile C, interferometer.

Figure 3.5 C-band relative signal strength envelopes, King Fish, Missile C, interferometer.

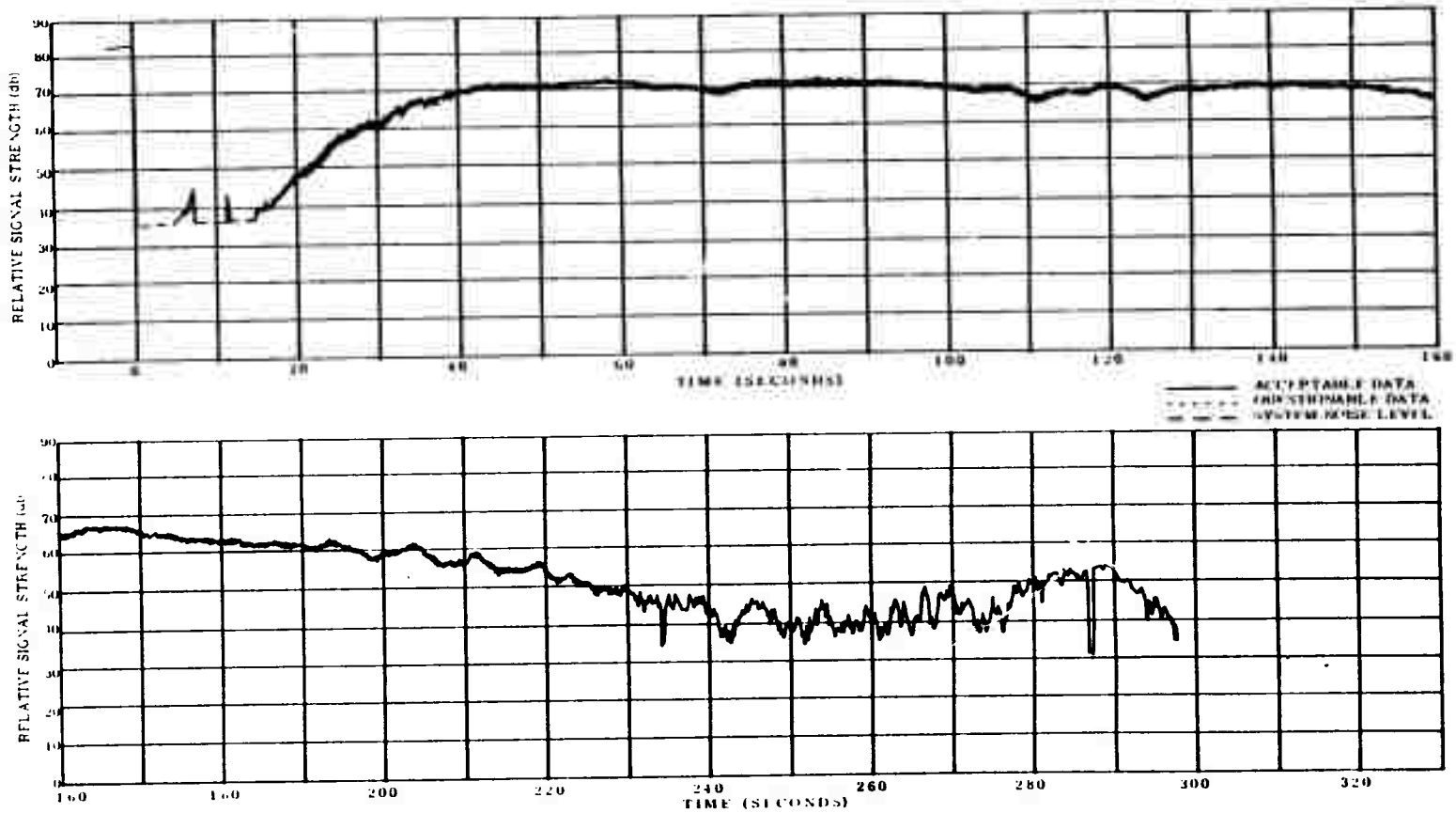

Figure 3-6 L band relative signal strength, King Fish, Missile C, interferometer

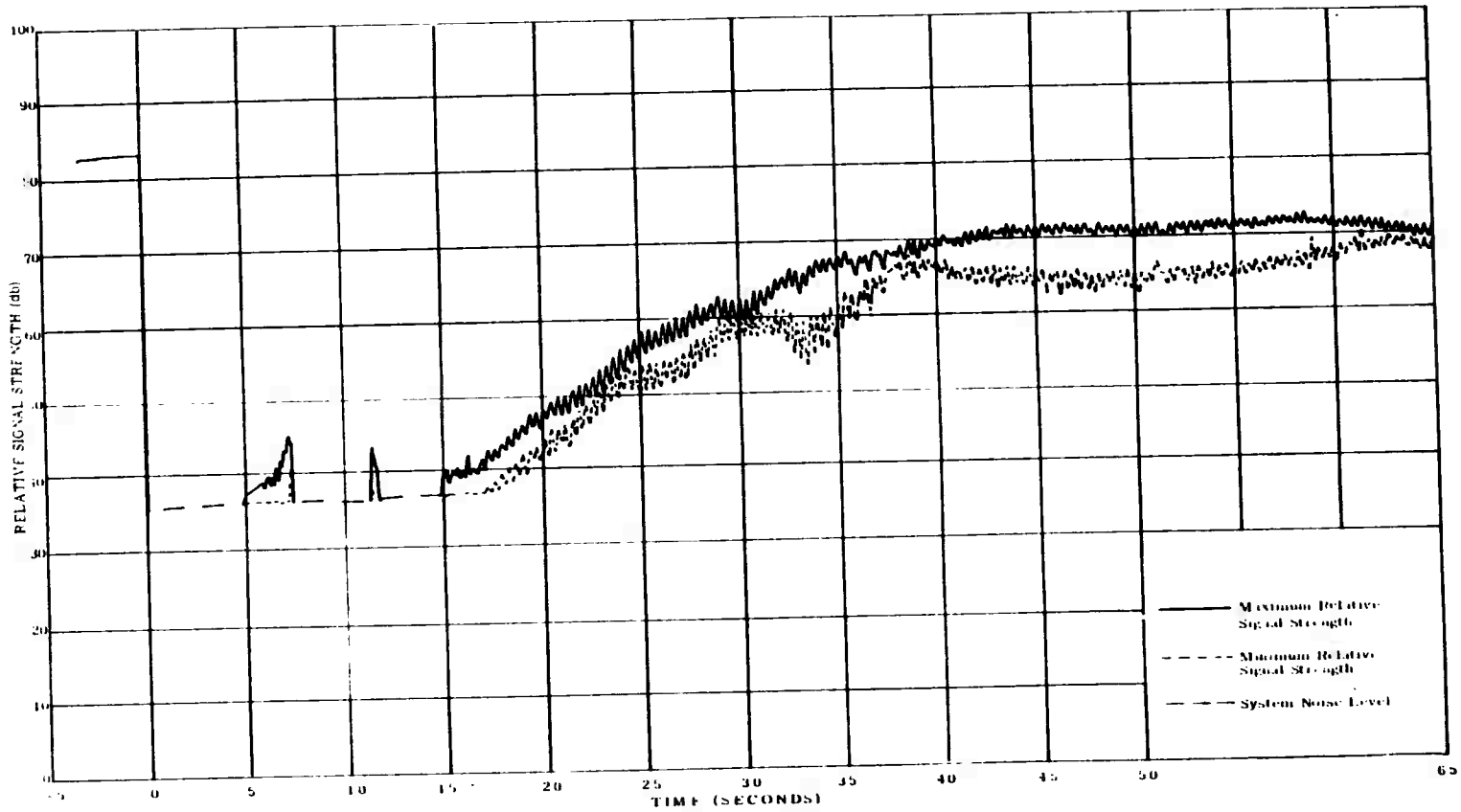

Figure 3.7 L band relative signal strength envelopes, King Fish, Missile C, interferometer

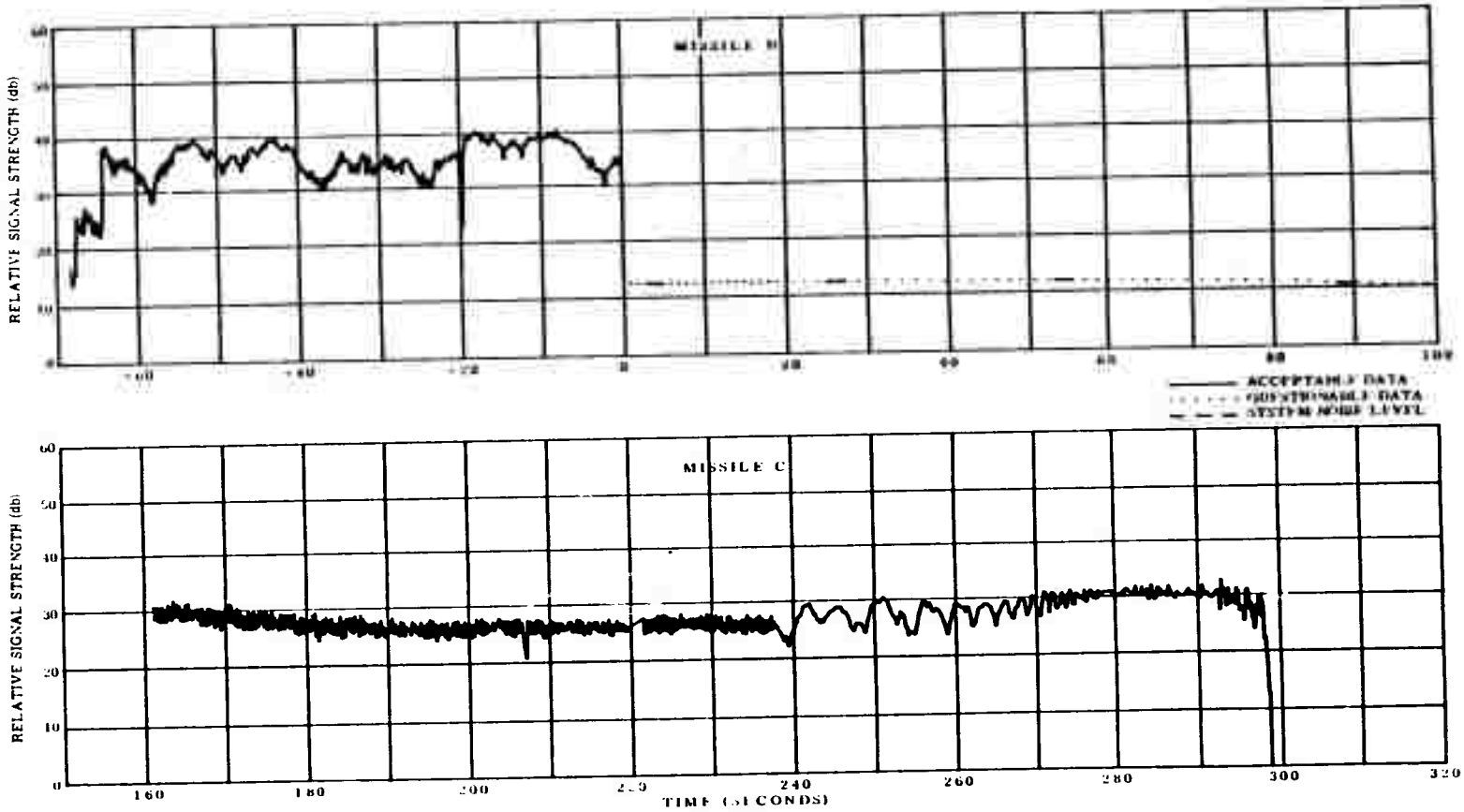

Figure 3.8 X band relative signal strength, King Fish, Missiles B and C, Ship 1

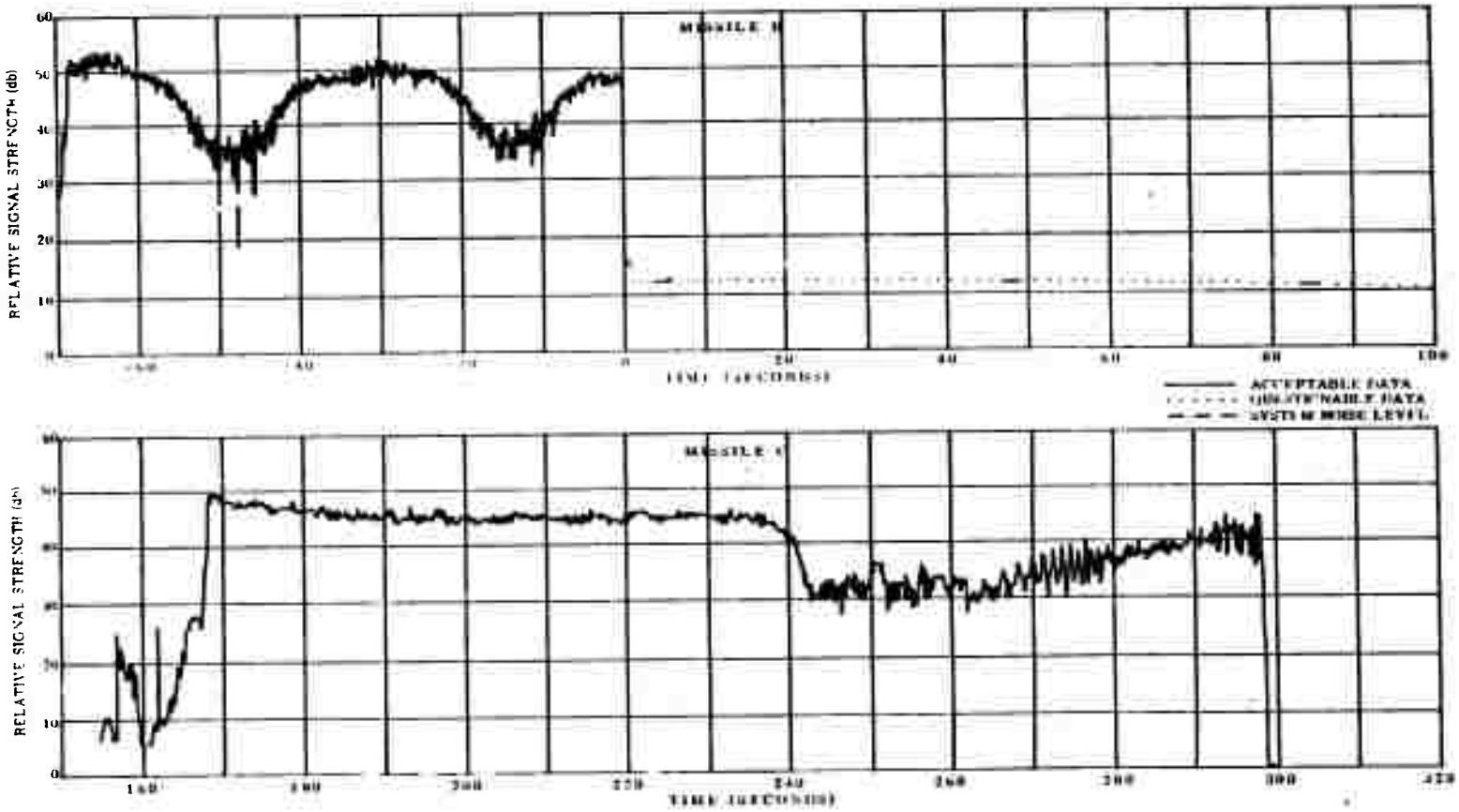

Figure 3.9 C band relative signal strength, King Fish, Missiles B and C, Ship 1.

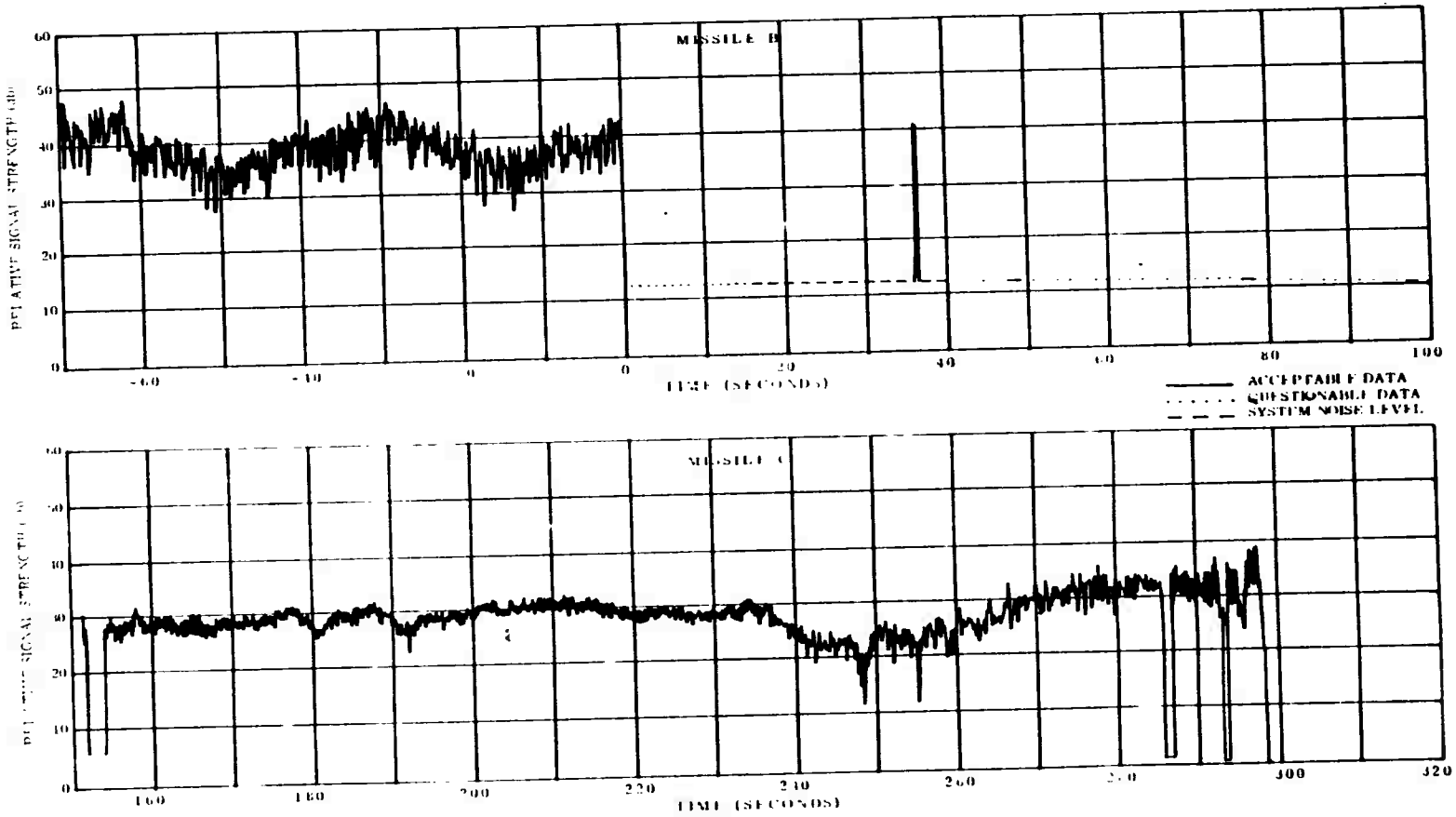

Figure 3-10. L-band relative signal strength, King Fish, Missiles B and C, Ship 1

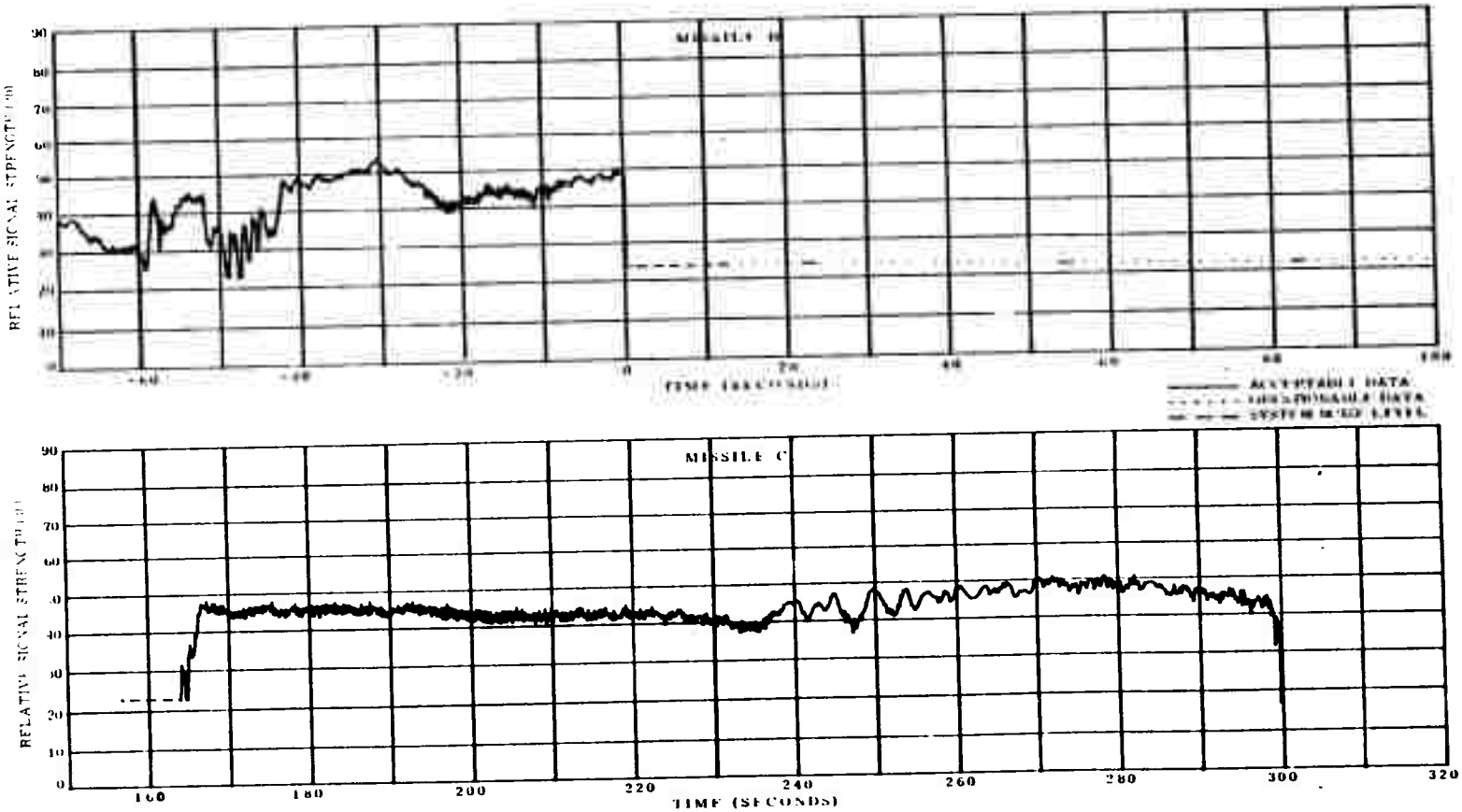

Figure 3.11 X band relative signal strength, King Fish, Missiles B and C, Ship 2.

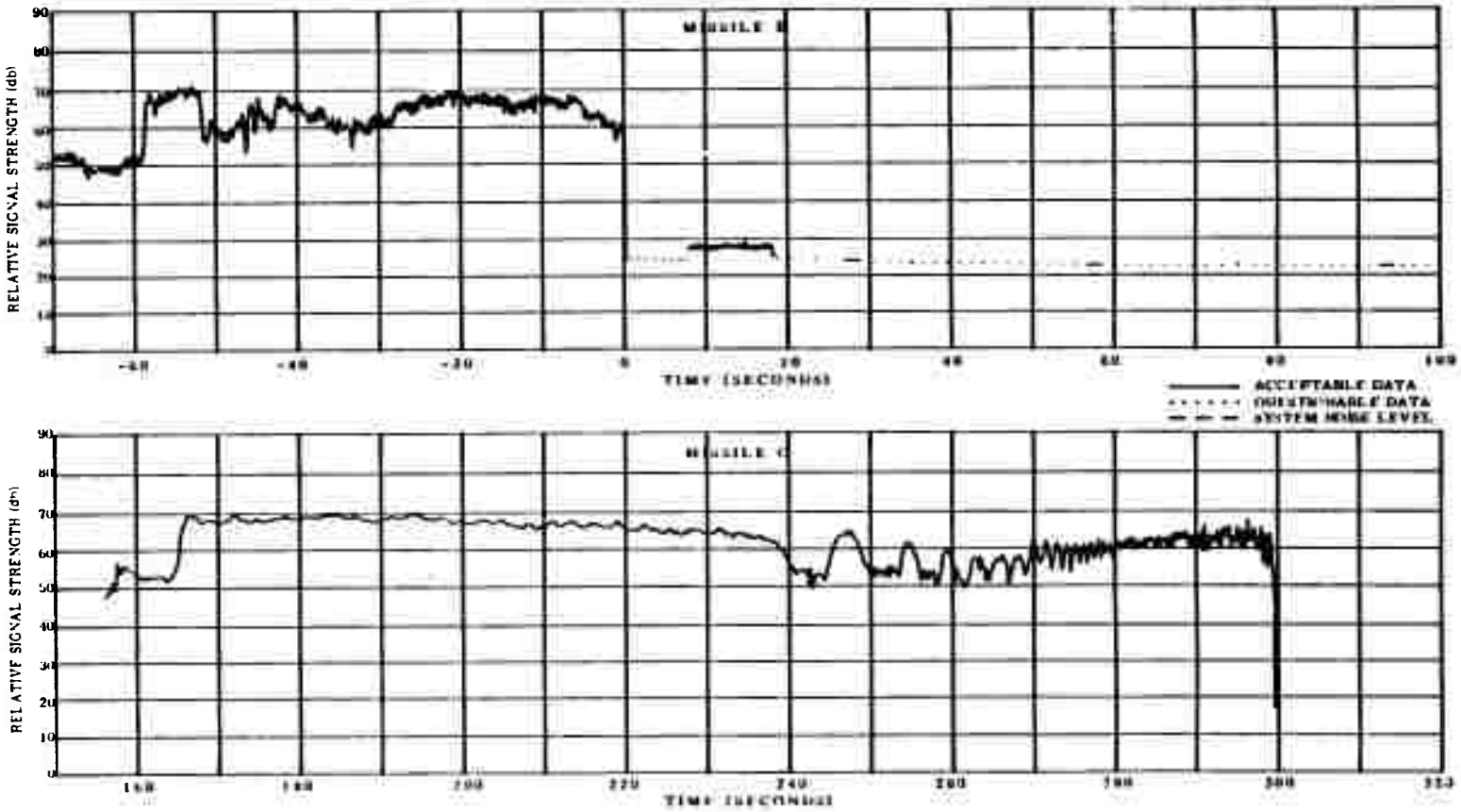

Figure 3.12 C-band relative signal strength, King Fish, Missiles B and C, Ship 2.

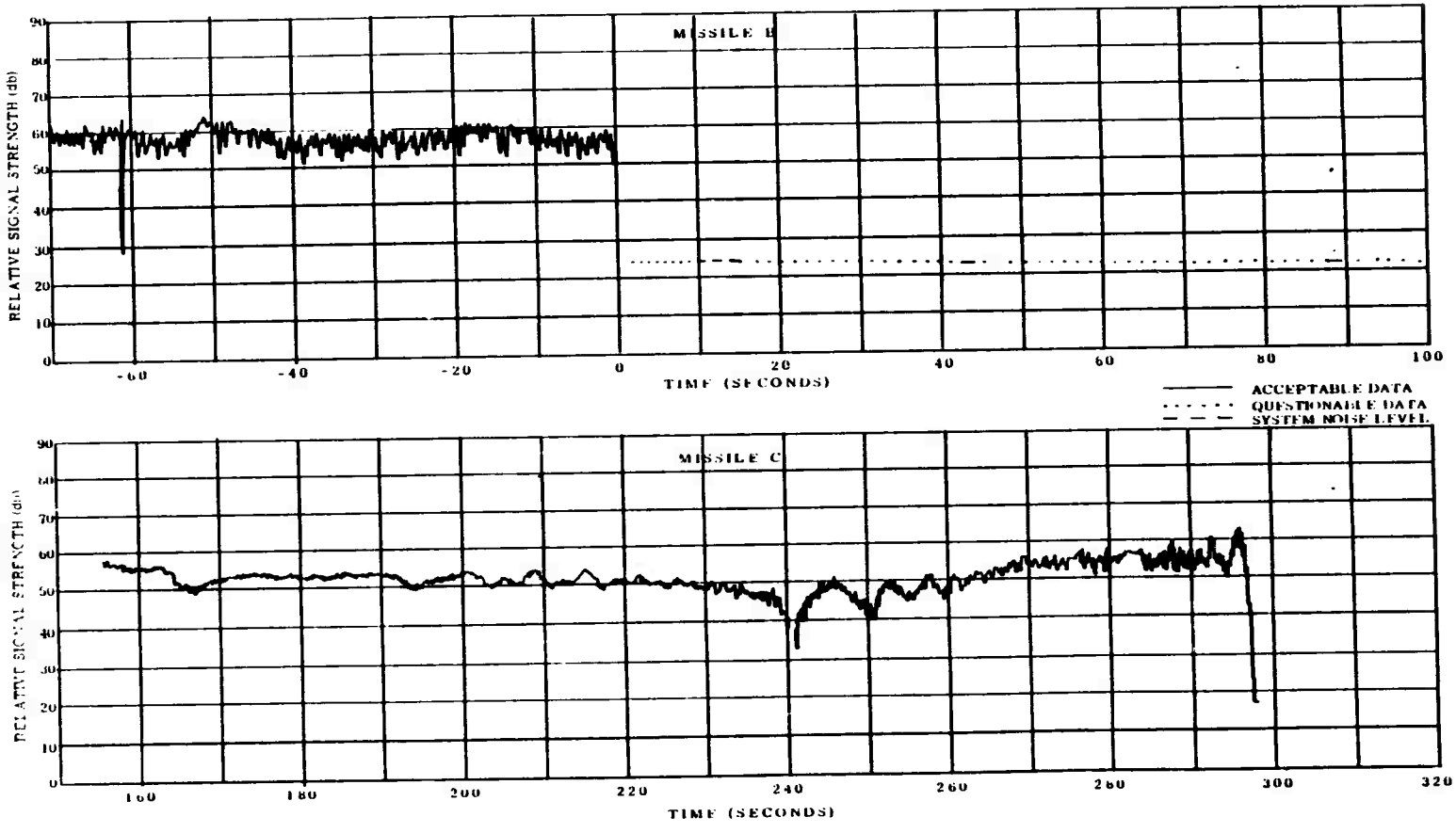

Figure 3.13 L-band relative signal strength, King Fish, Missiles B and C, Ship 2.

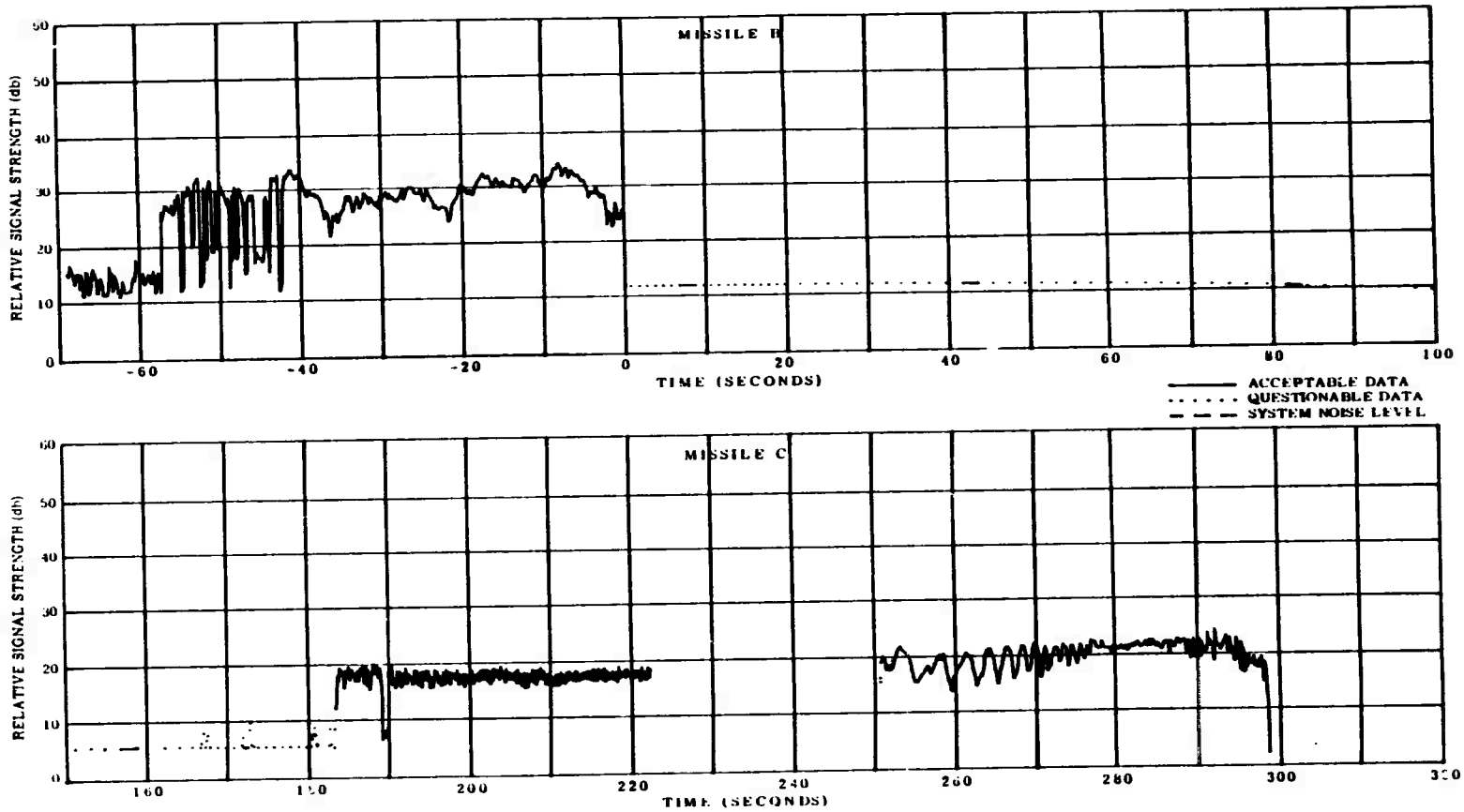

Figure 3.14 X-band relative signal strength, King Fish, Missiles B and C, Ship 3.

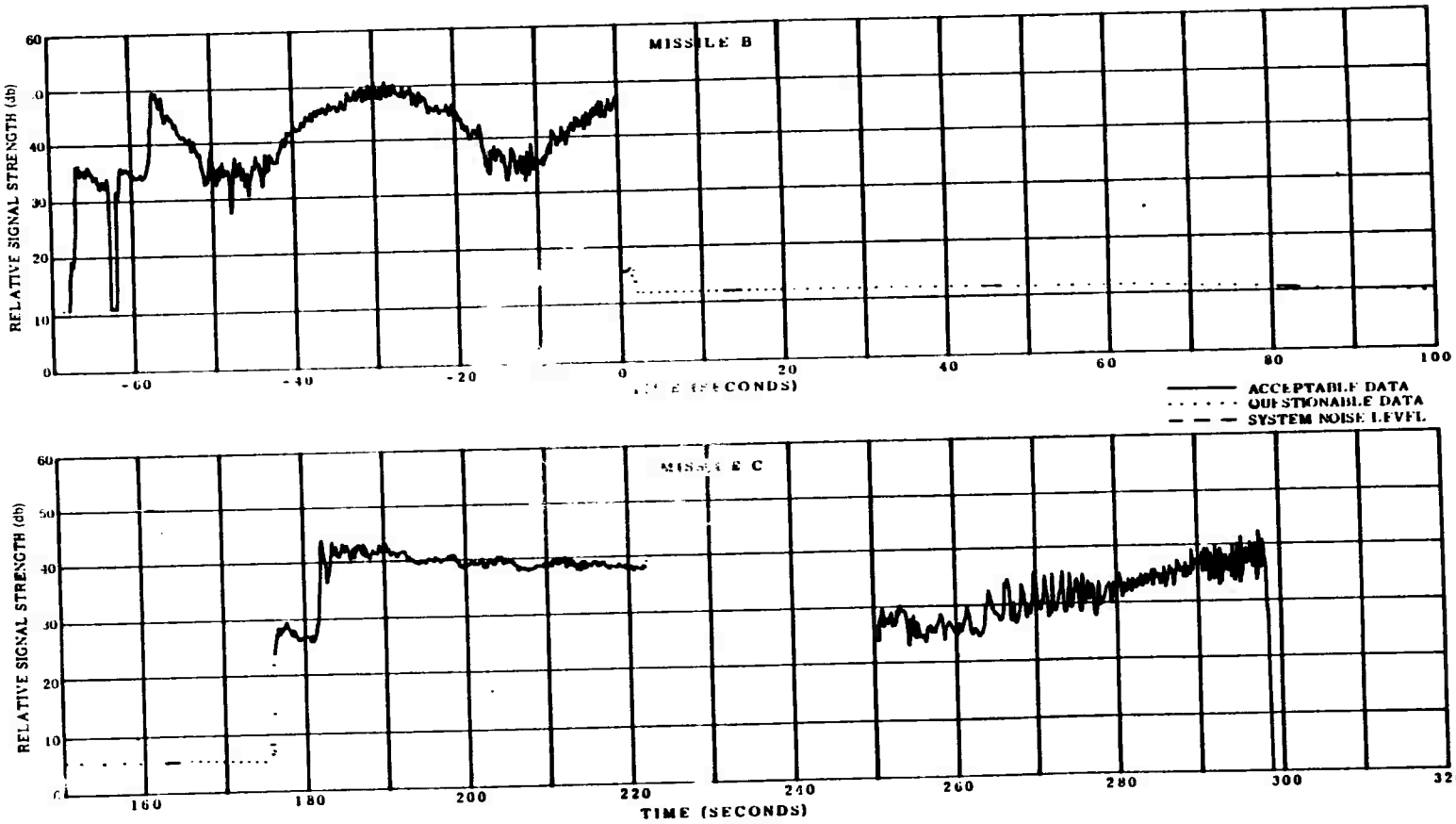

Figure 3.15 C-band relative signal strength, King Fish, Missiles B and C, Ship 3.

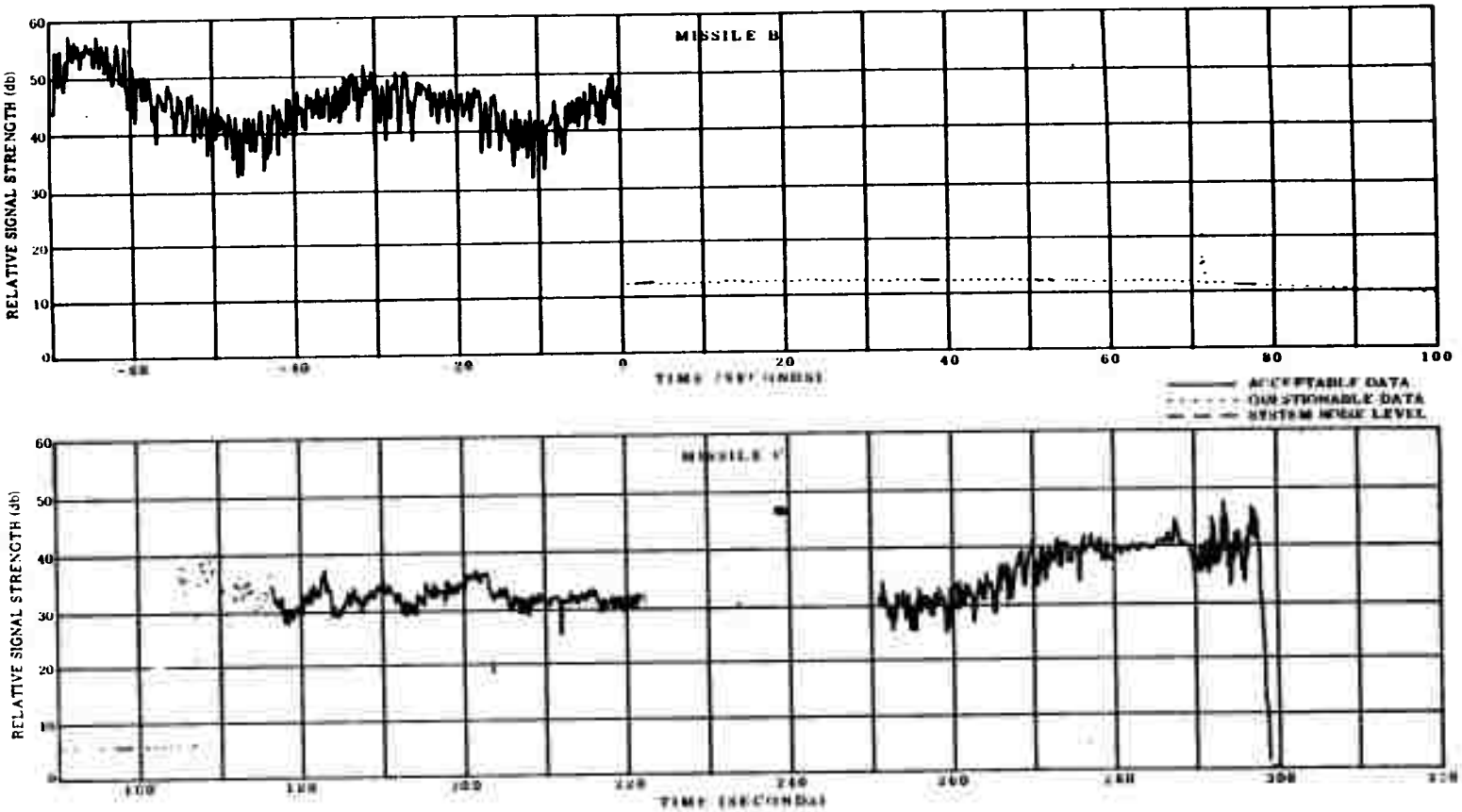

Figure 3.16 L-band relative signal strength, King Fish, Missiles B and C, Ship 3.

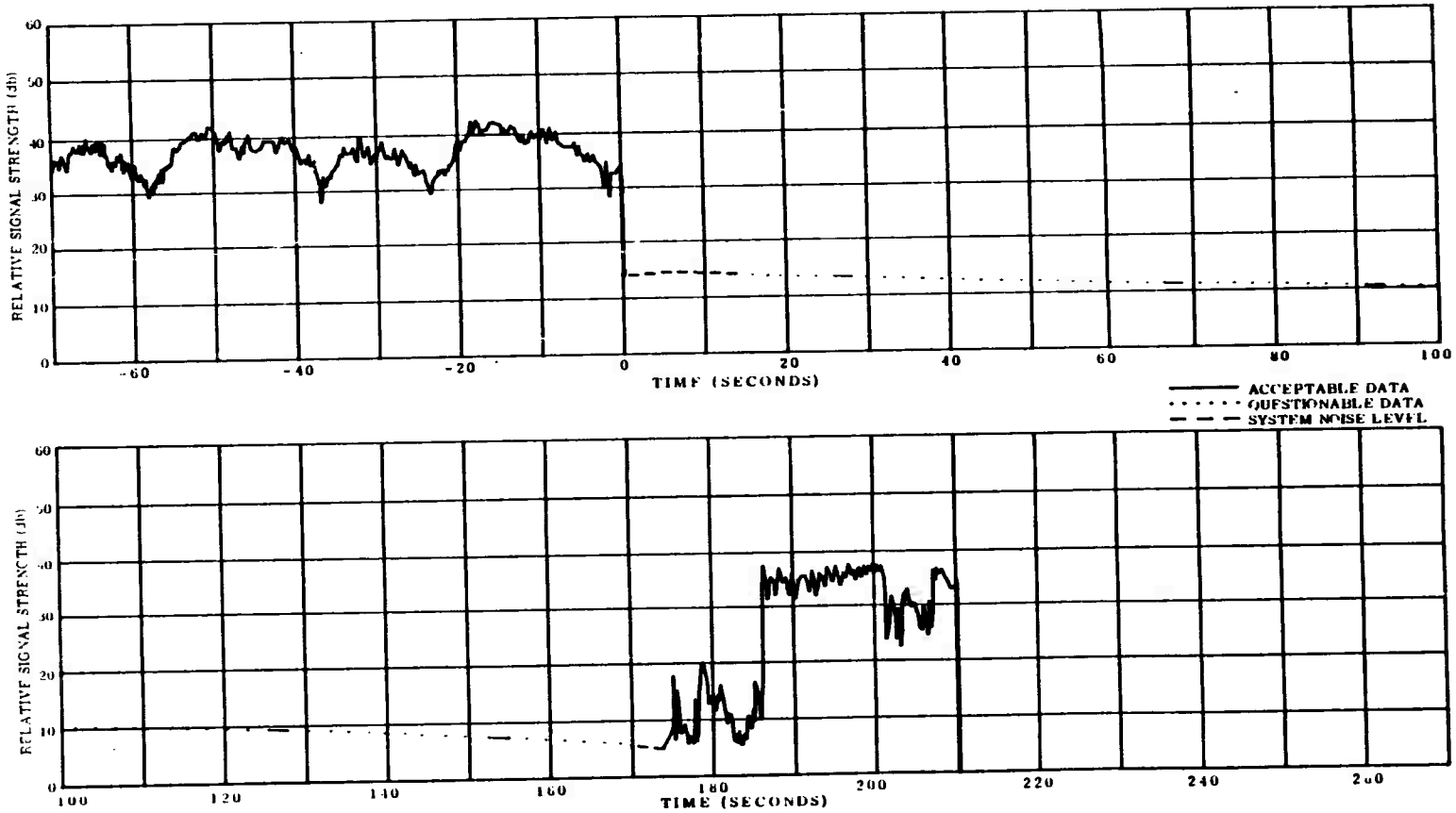

Figure 3.17 X-band relative signal strength, King Fish, Missile B, Ship 4.

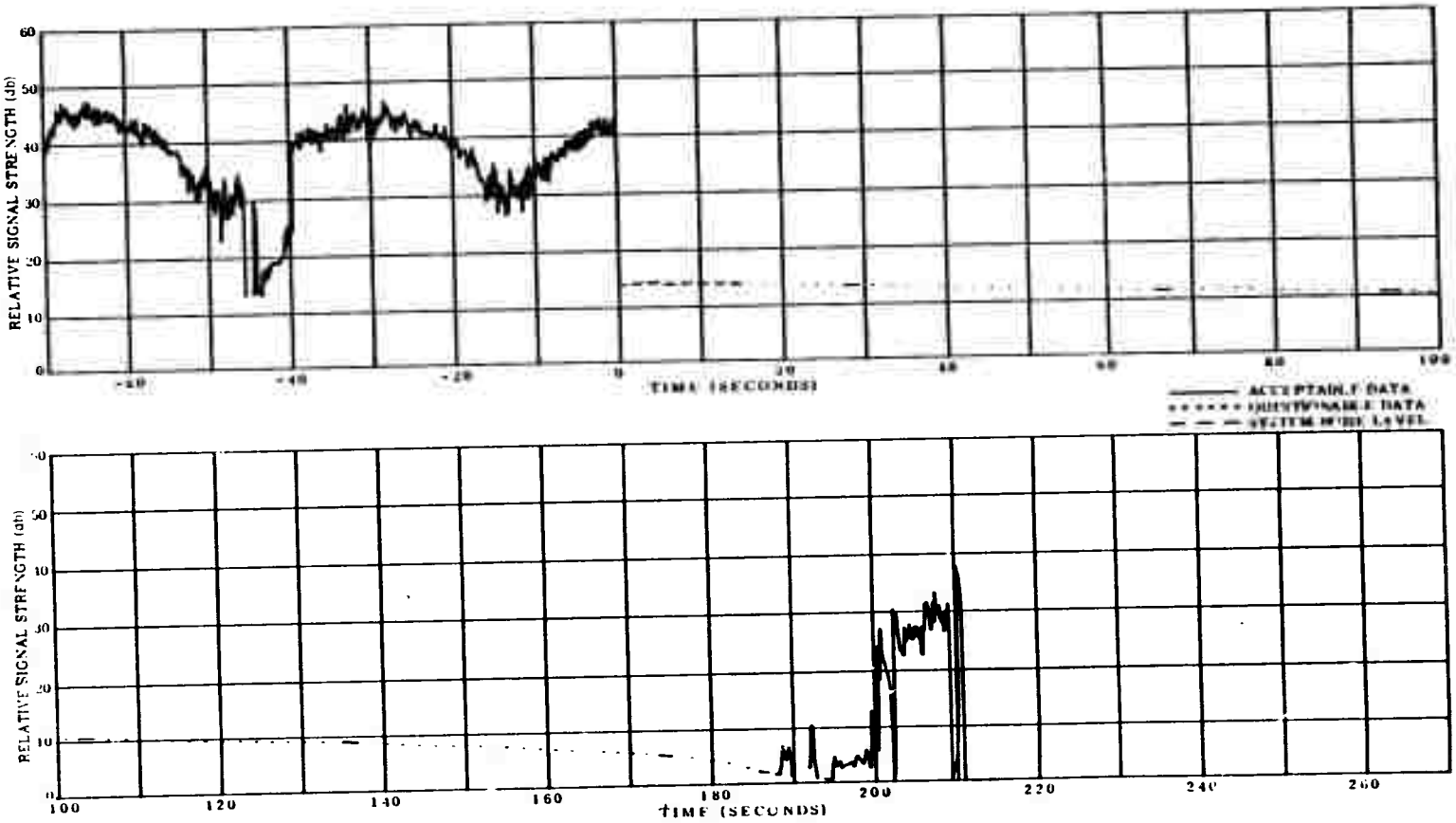

Figure 3.18 C band relative signal strength, King Fish, Missile B, Ship 4.

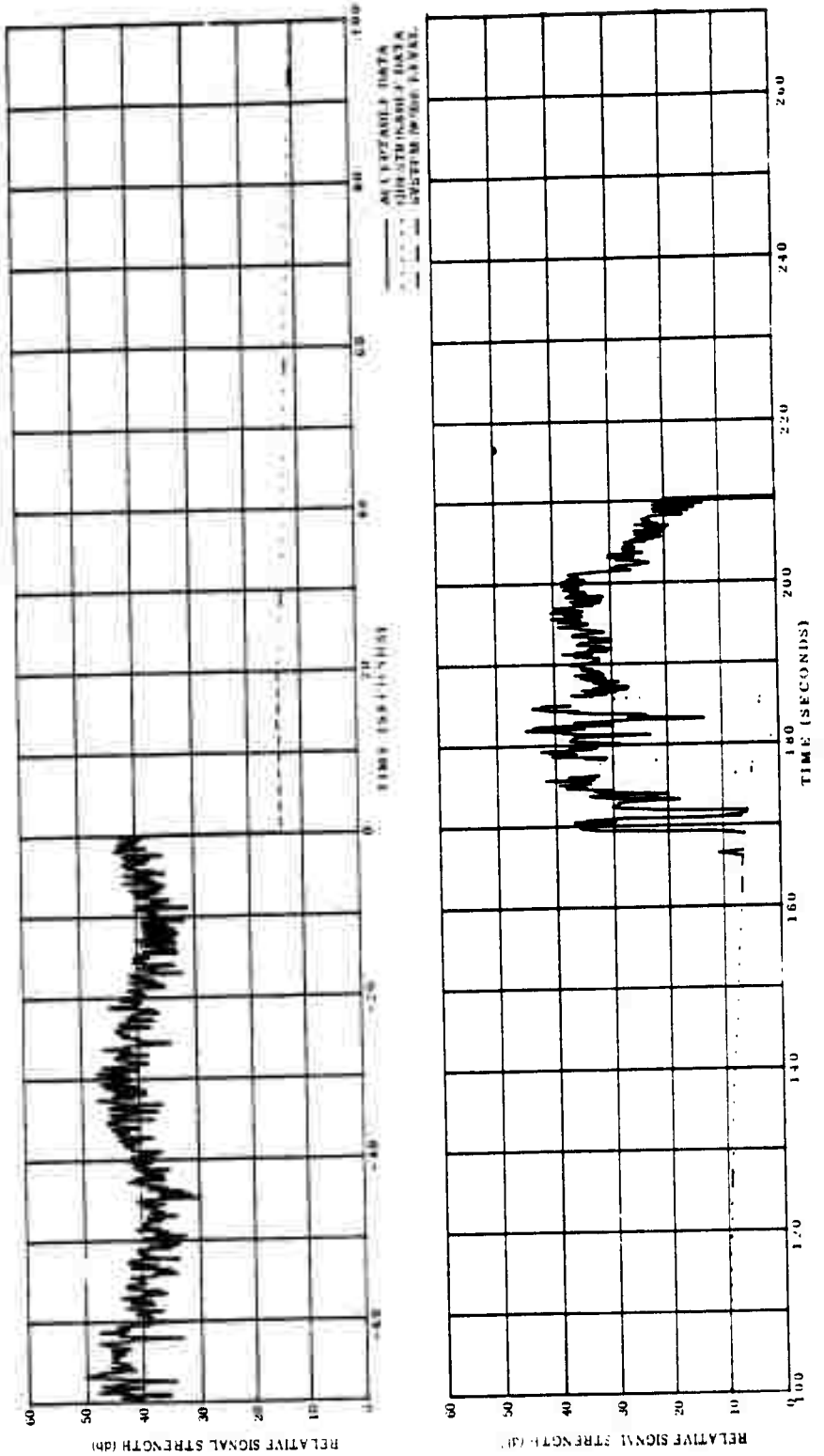

Figure 3-19 L-band relative signal strength, King Fish, Missile B, Ship 4.

Pages 250 through 253
deleted.

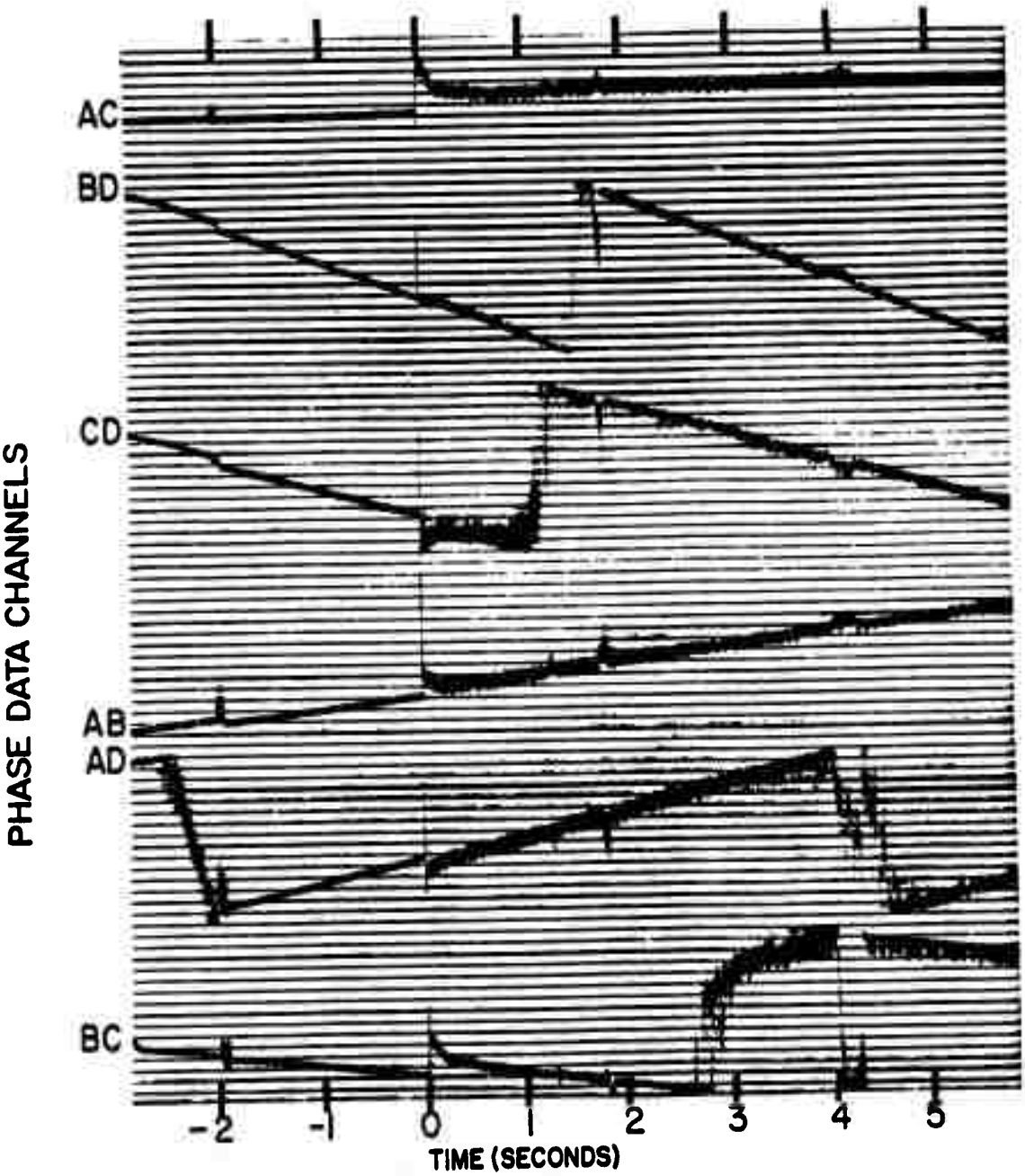

Figure 3.24 Raw phase data at event, interferometer, King Fish, C-band.

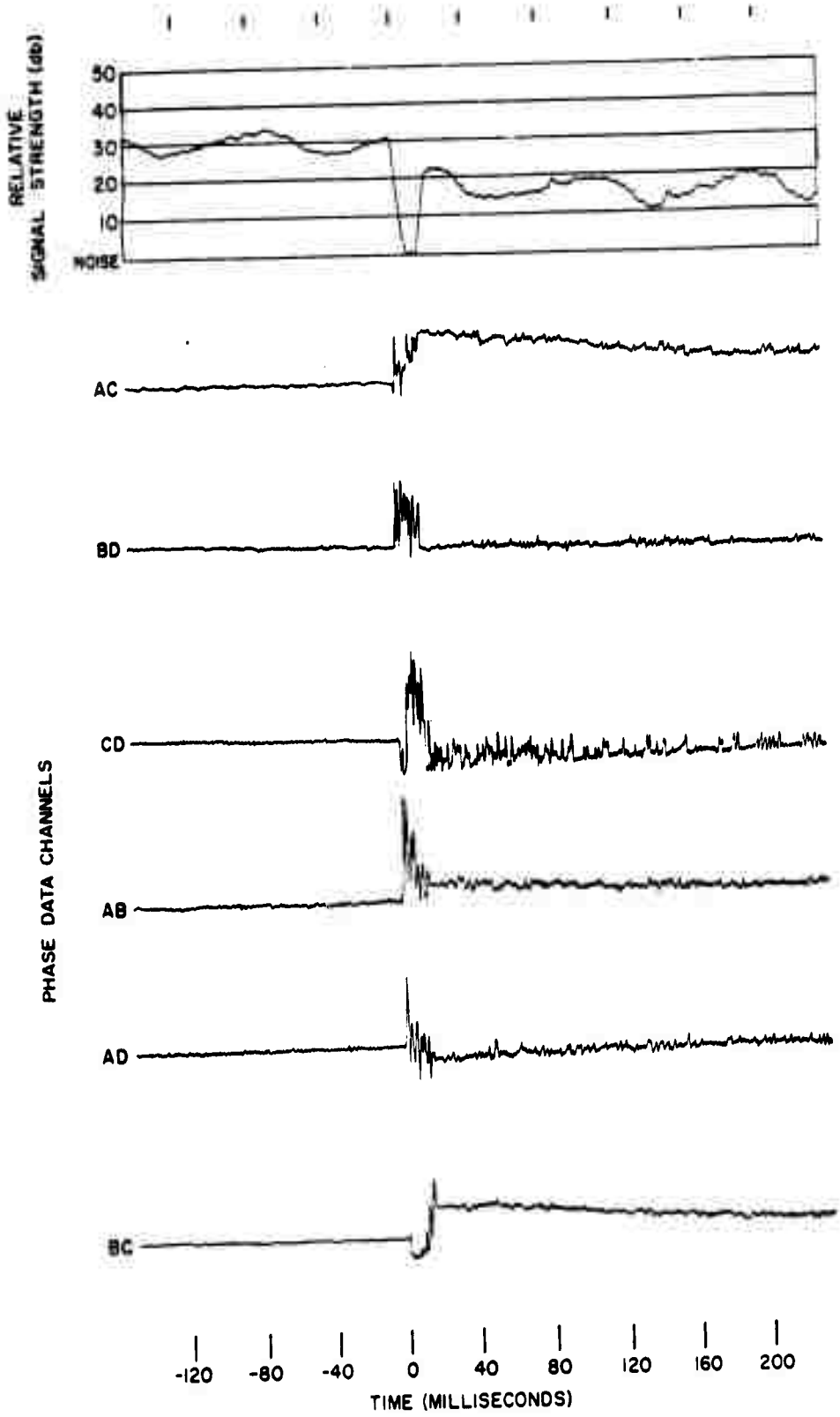

Figure 3.25 Raw phase data at event and relative signal strength at event, King Fish, Missile C, interferometer, C-band.

941

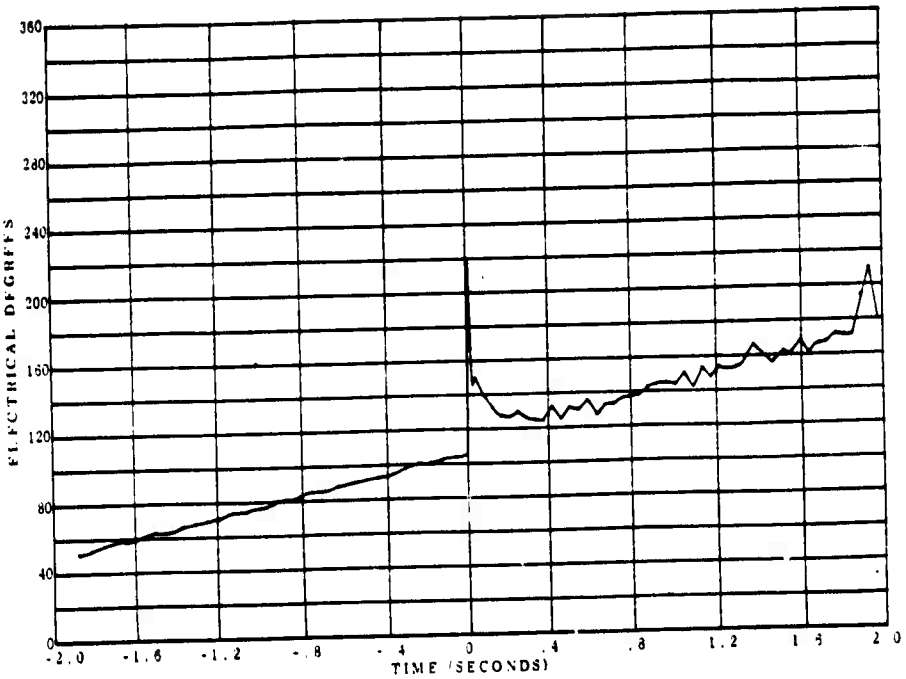

Figure 3.26 Phase perturbation at event, King Fish, Missile C, interferometer, Leg AB.

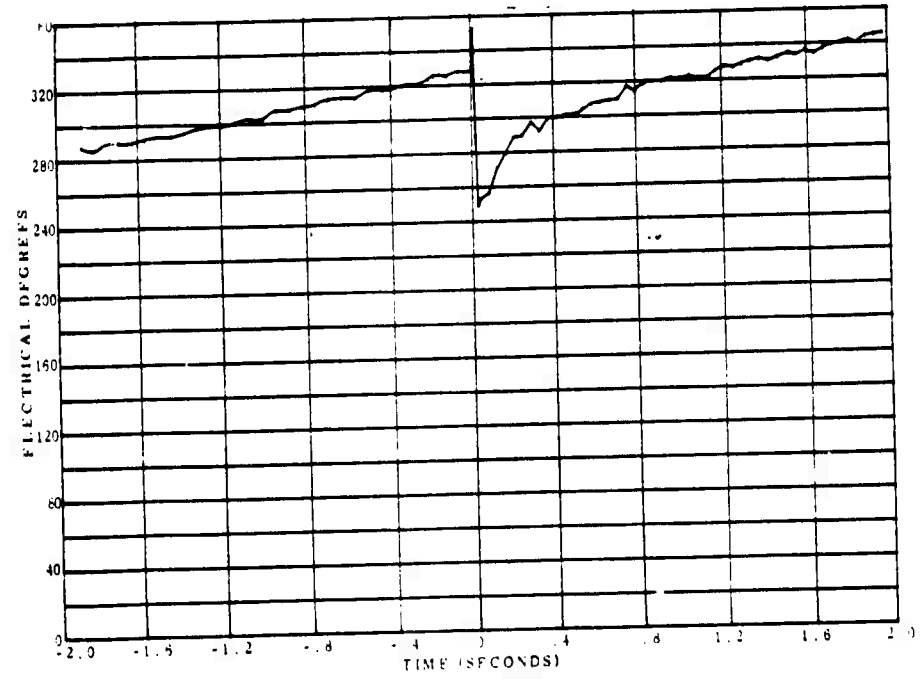

Figure 3.27 Phase perturbation at event, King Fish, Missile C, interferometer, Leg BC.

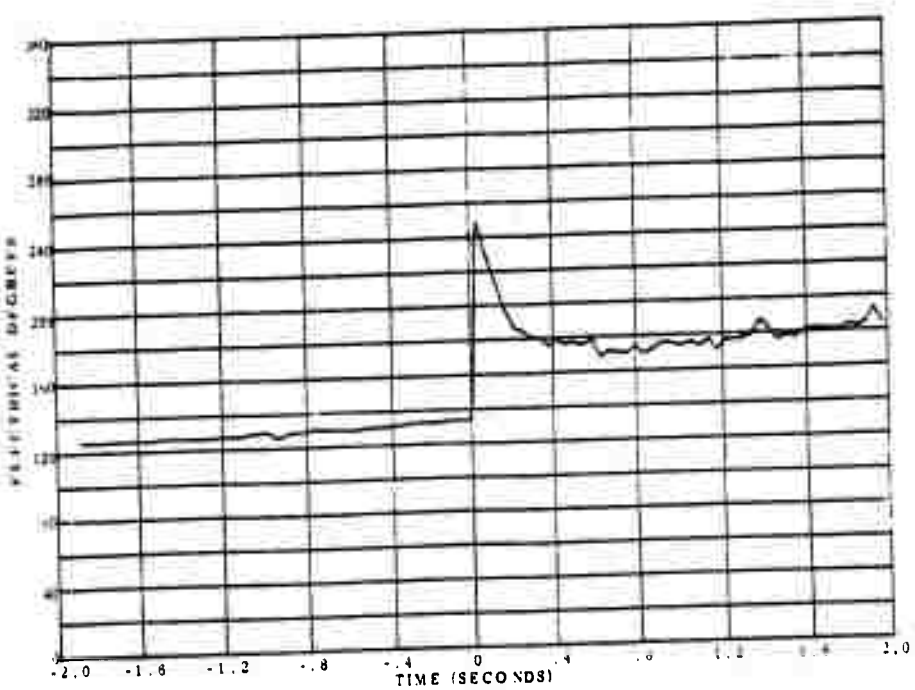

Figure 3.28 Phase perturbation at event, King Fish, Missile C, interferometer, Leg AC.

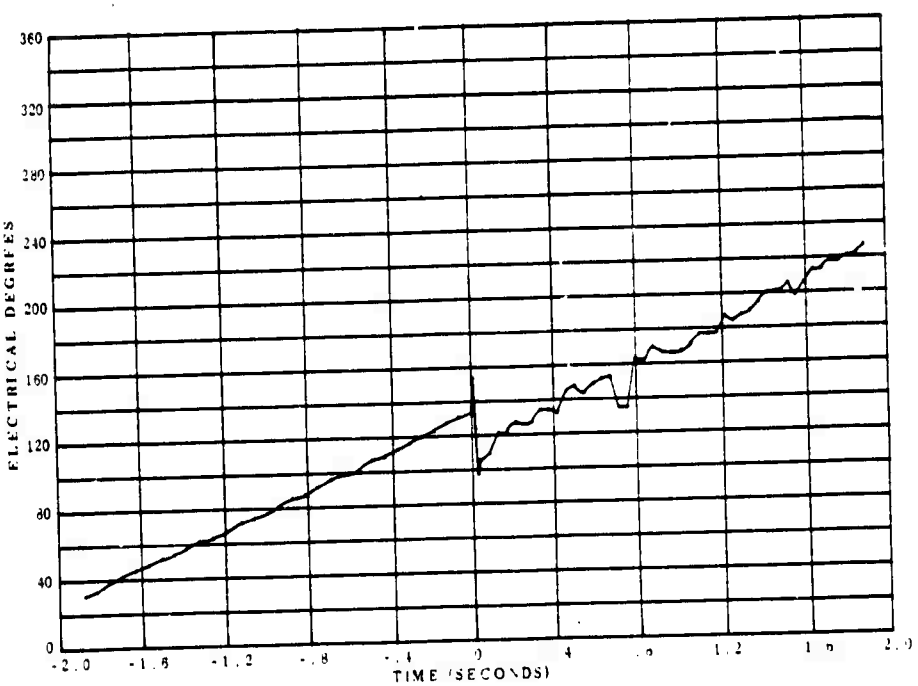

Figure 3.29 Phase perturbation at event, King Fish, Missile C, interferometer, Leg AD

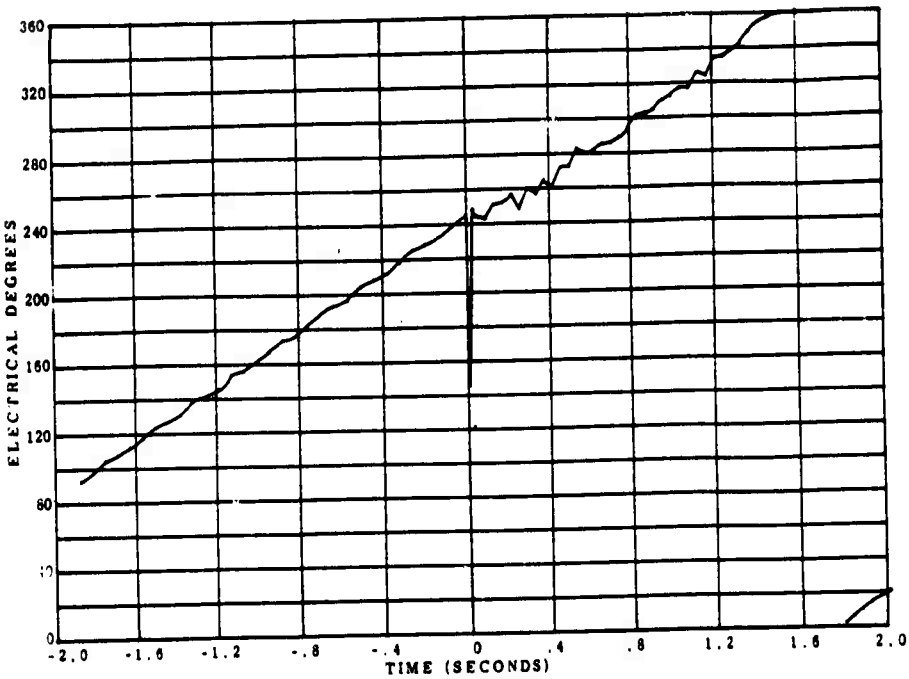

Figure 3.30 Phase perturbation at event, King Fish, Missile C, interferometer, Leg BD.

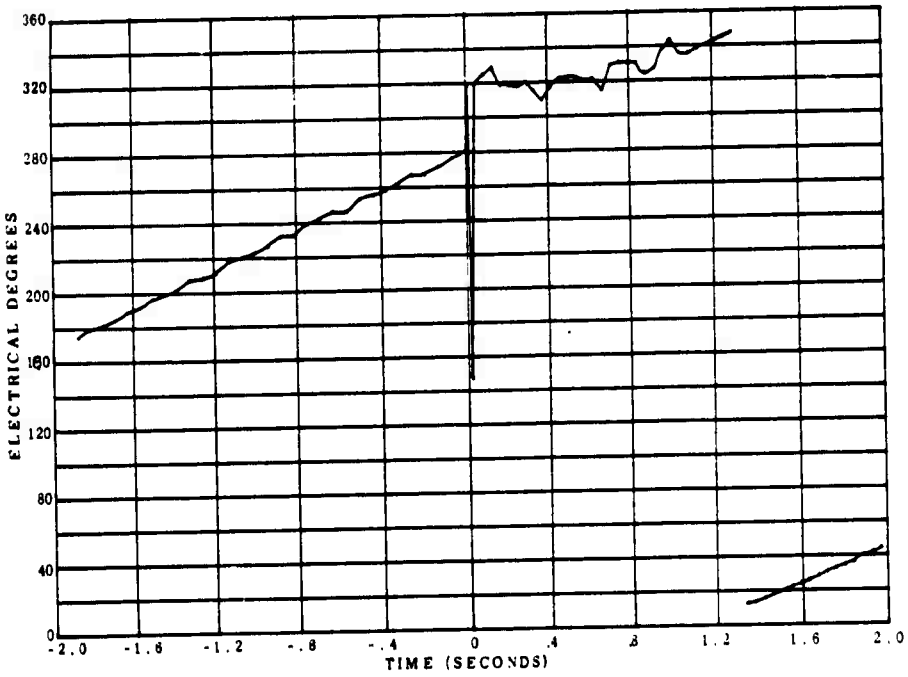

Figure 3.31 Phase perturbation at event, King Fish, Missile C, interferometer, Leg CD.

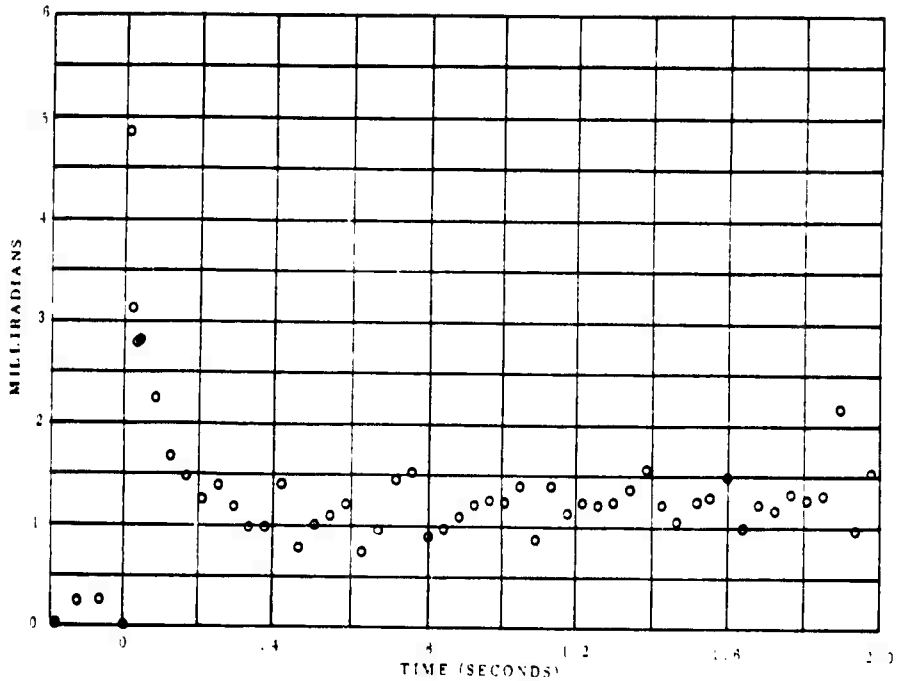

Figure 3-32 Retraction at event, King Fish, Interferometer Combination AB-AD.

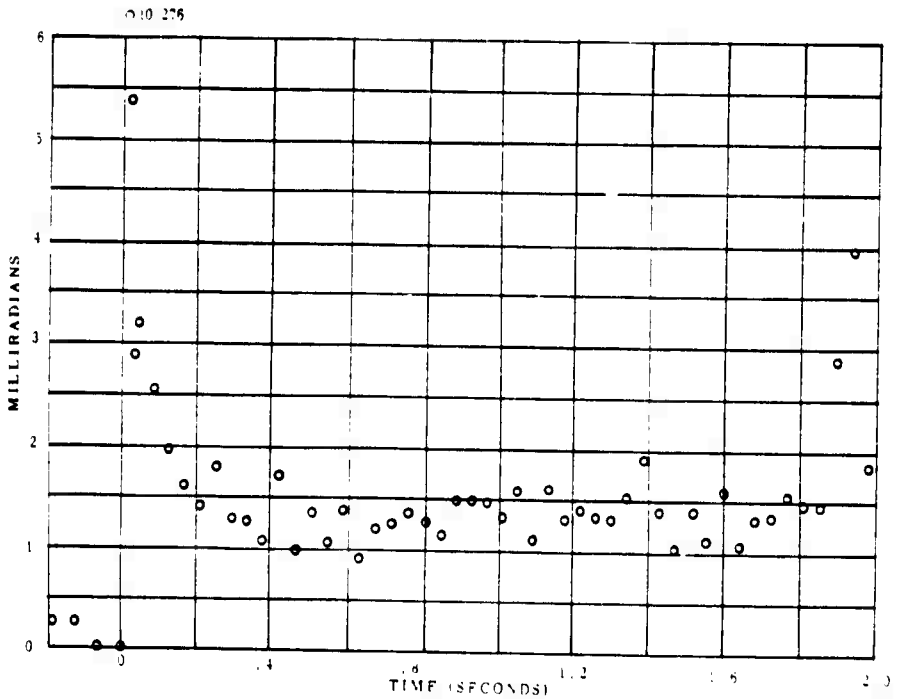

Figure 3-33 Retraction at event, King Fish, Interferometer Combination AB-BC

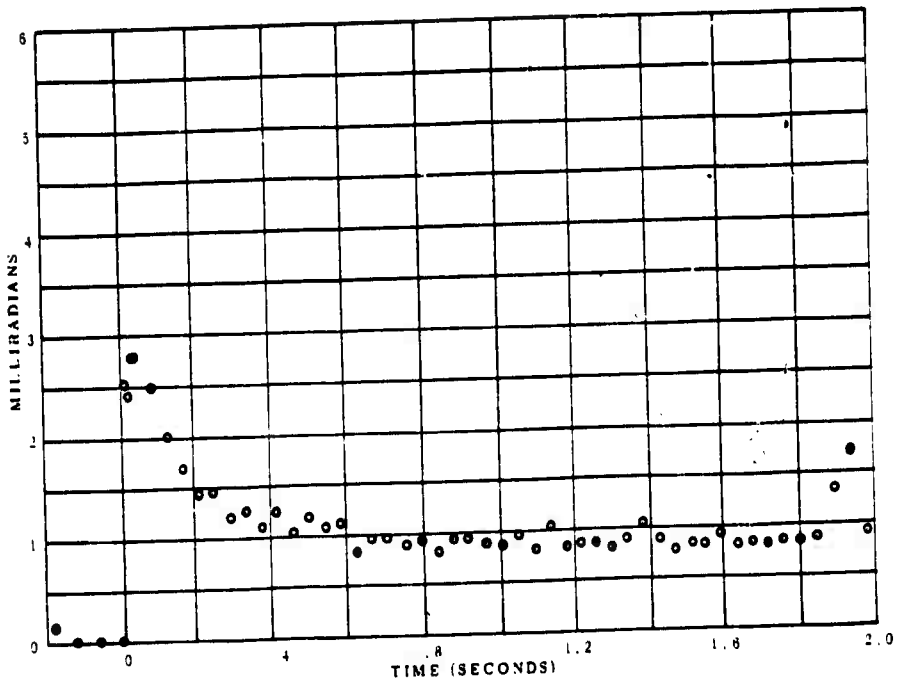

Figure 3.34 Retraction at event, King Fish, Interferometer Combination AB-BC.

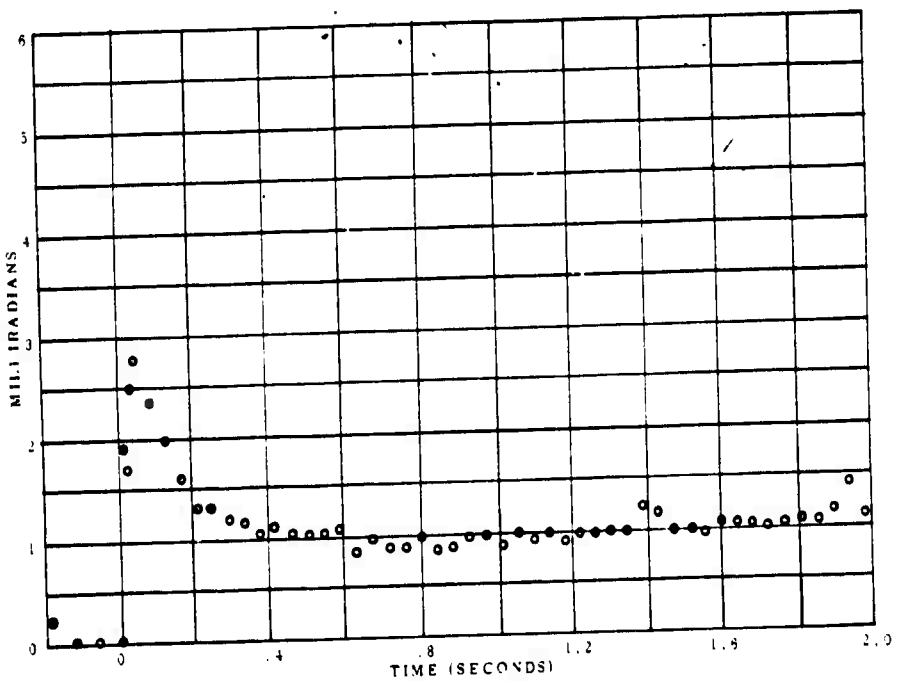

Figure 3.35 Retraction at event, King Fish, Interferometer Combination AB-AC.

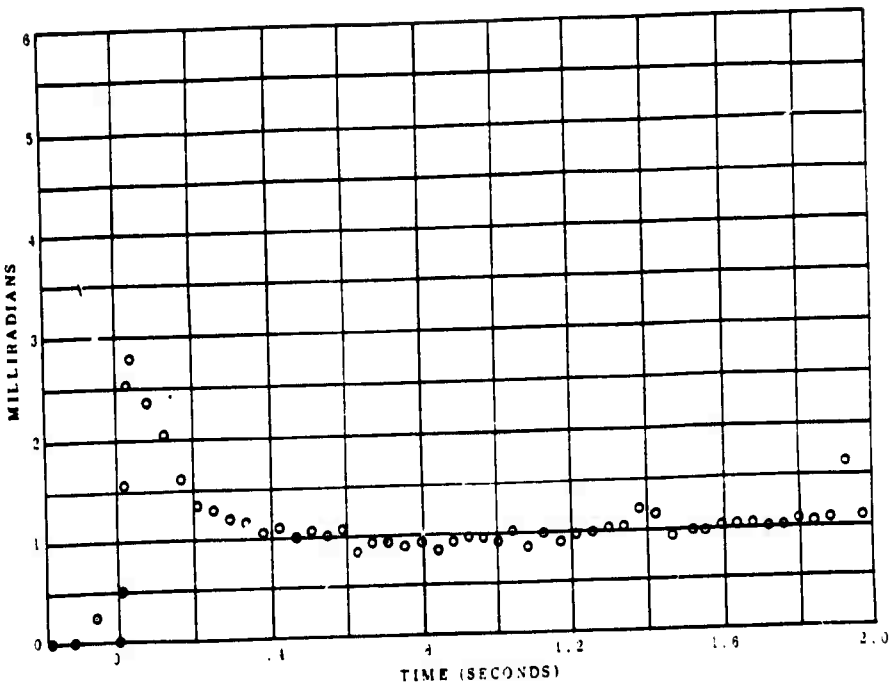

Figure 3.36 Retraction at event, King Fish, Interferometer Combination AC-AD.

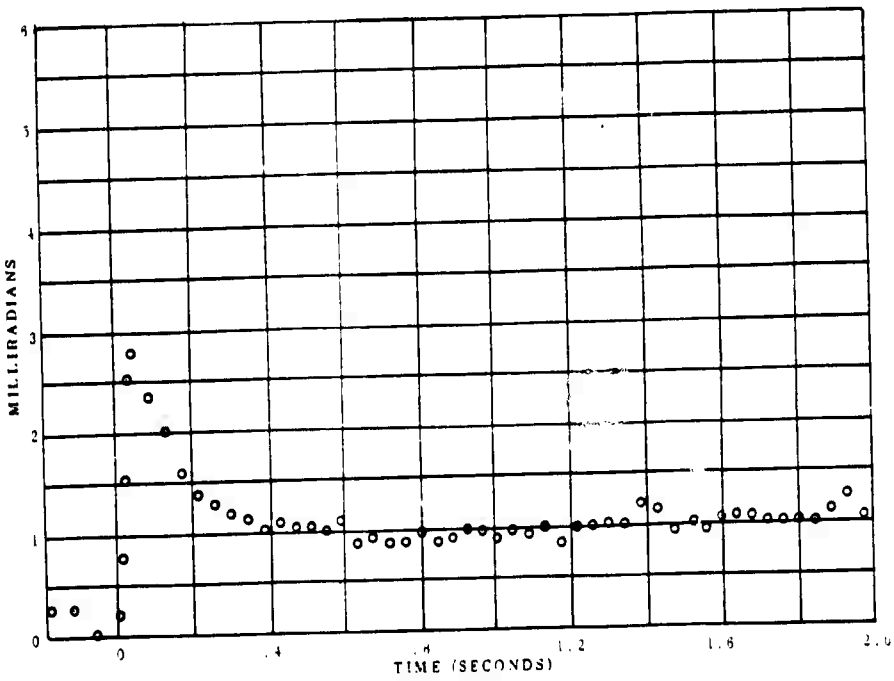

Figure 3.37 Retraction at event, King Fish, Interferometer Combination AC-BD

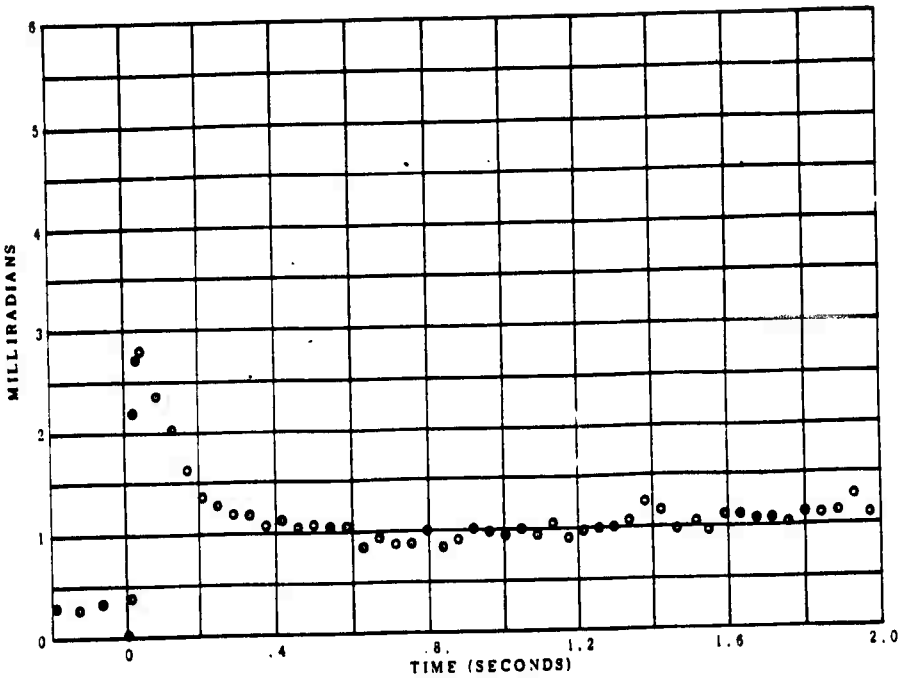

Figure 3.38 Refraction at event, King Fish, Interferometer Combination AC-CD.

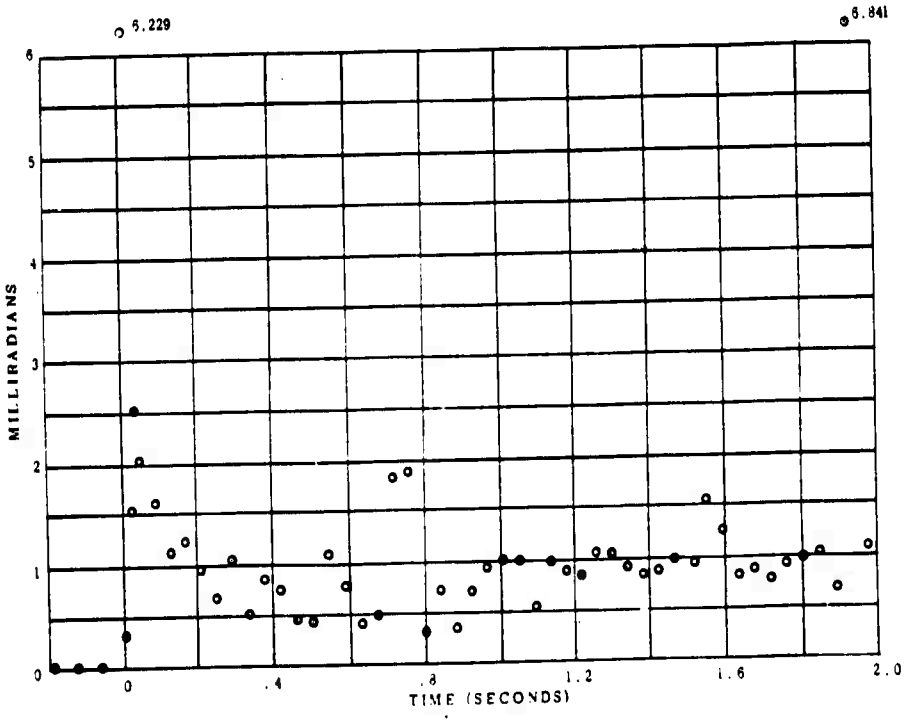

Figure 3.39 Refraction at event, King Fish, Interferometer Combination AD-BD.

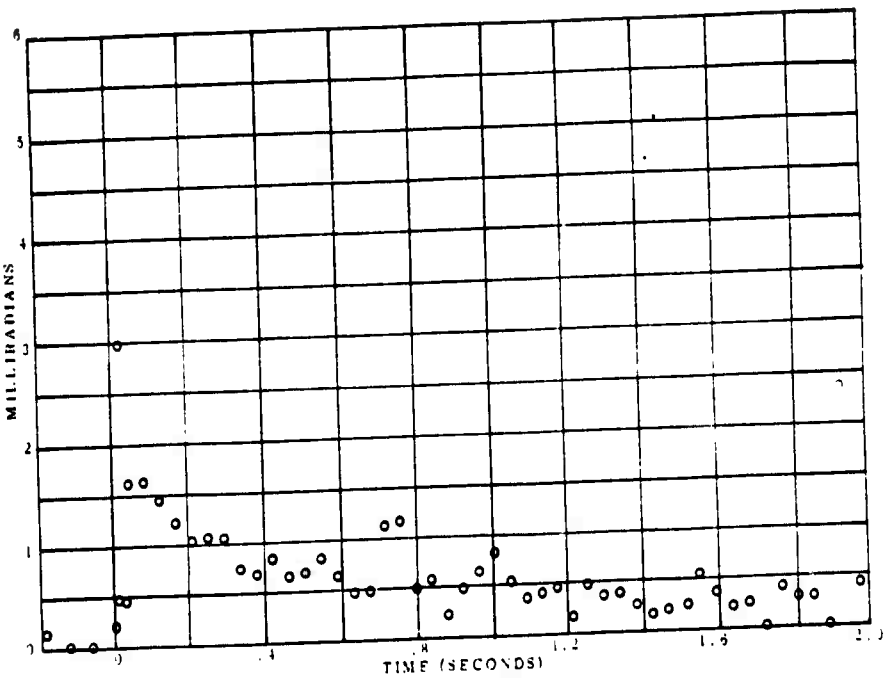

Figure 3.40 Refraction at event, King Fish. Interferometer Combination AD-CD.

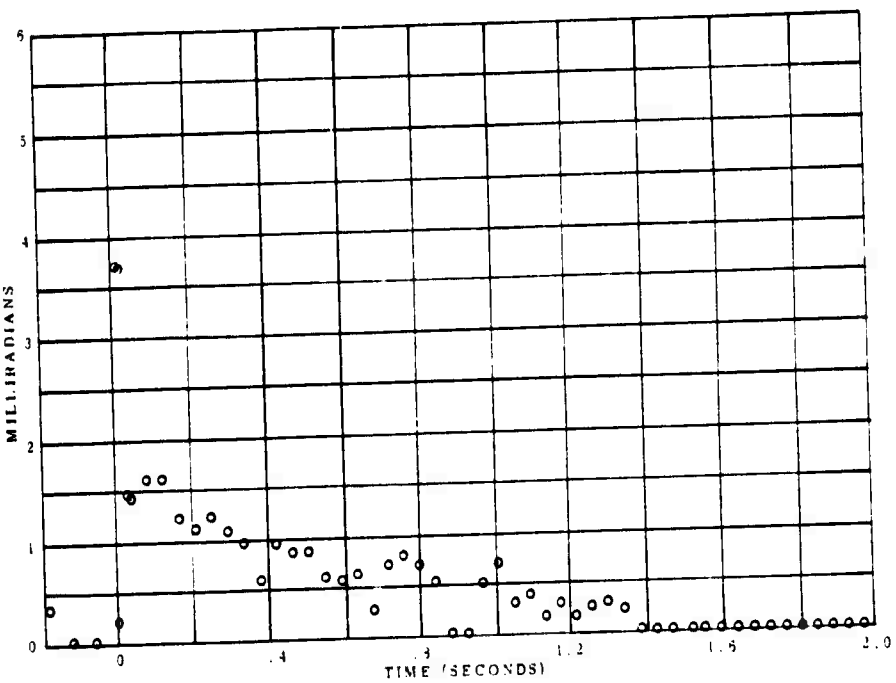

Figure 3.41 Refraction at event, King Fish. Interferometer Combination BD-CD.

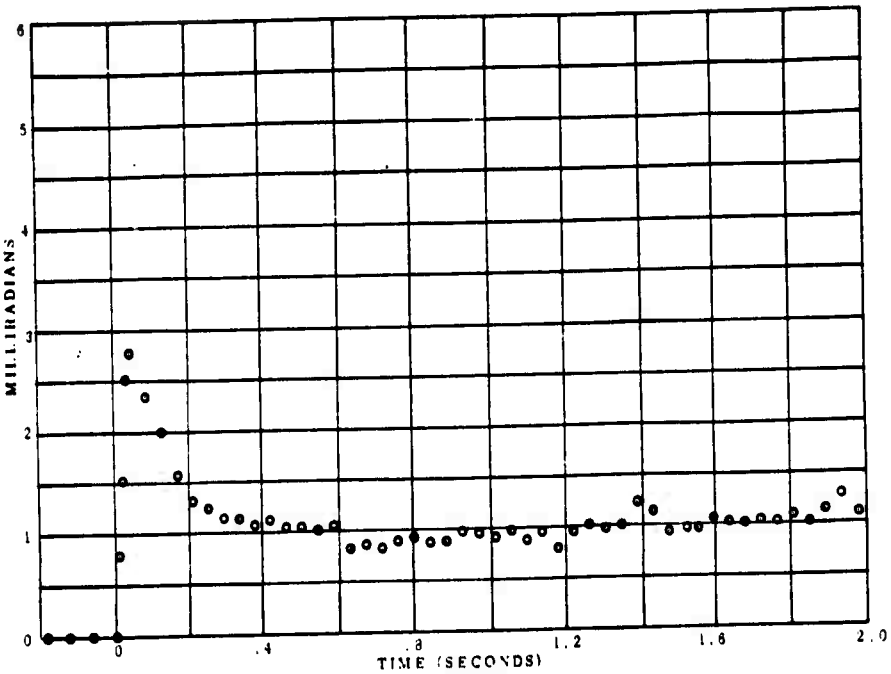

Figure 3.42 Refraction at event, King Fish, Interferometer Combination BC-AC.

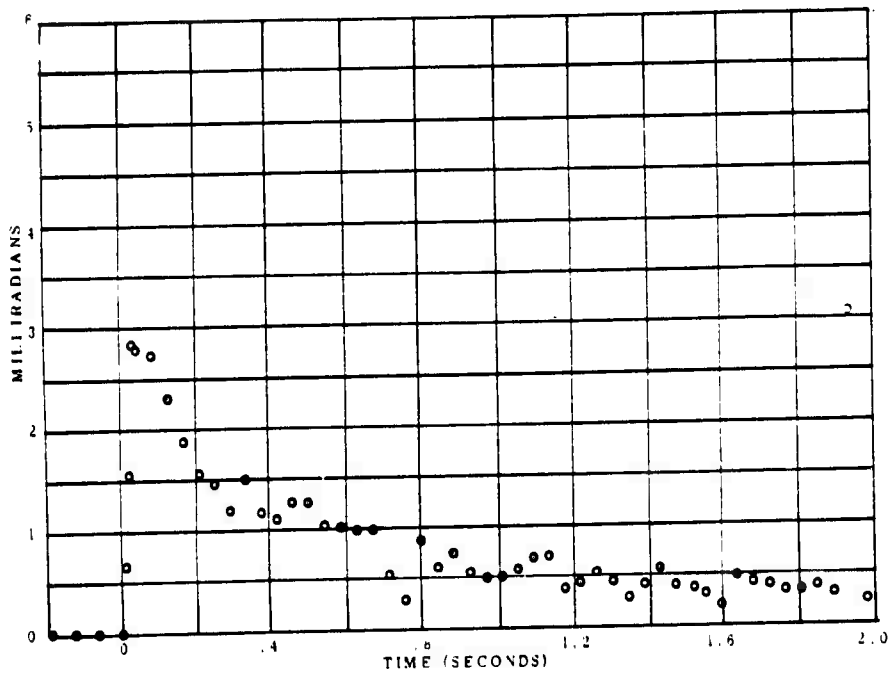

Figure 3.43 Refraction at event, King Fish, Interferometer Combination BC-AD.

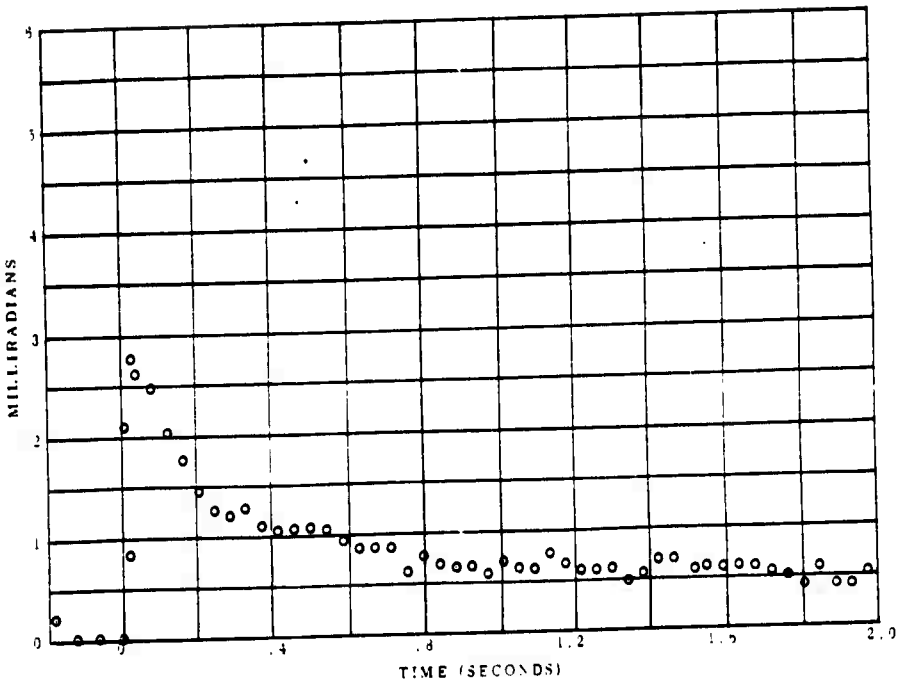

Figure 3.44 Retraction at event, King Fish, Interferometer Combination BC-BD.

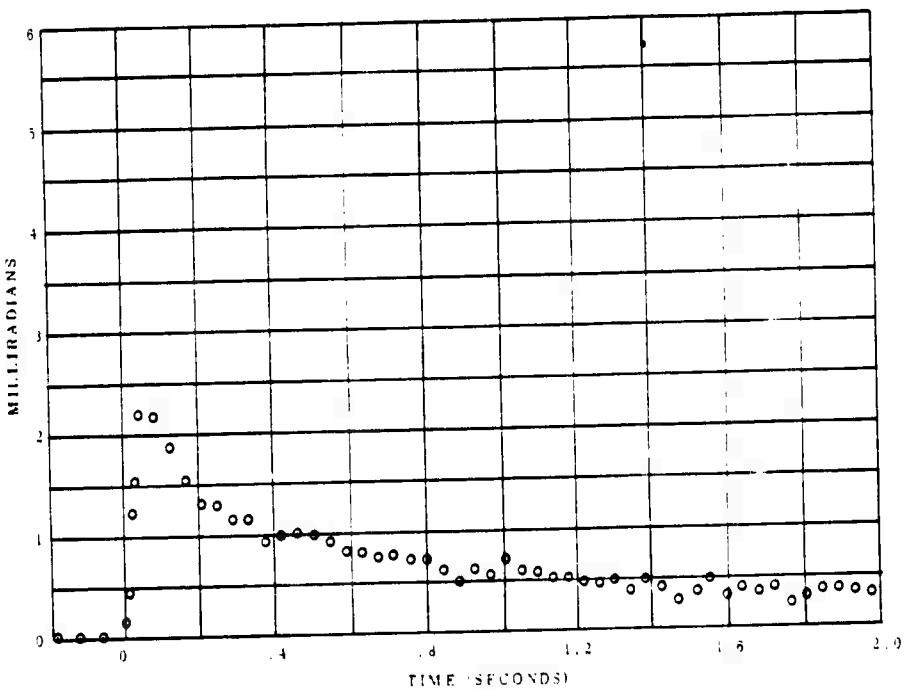

Figure 3.45 Retraction at event, King Fish, Interferometer Combination BC-CD

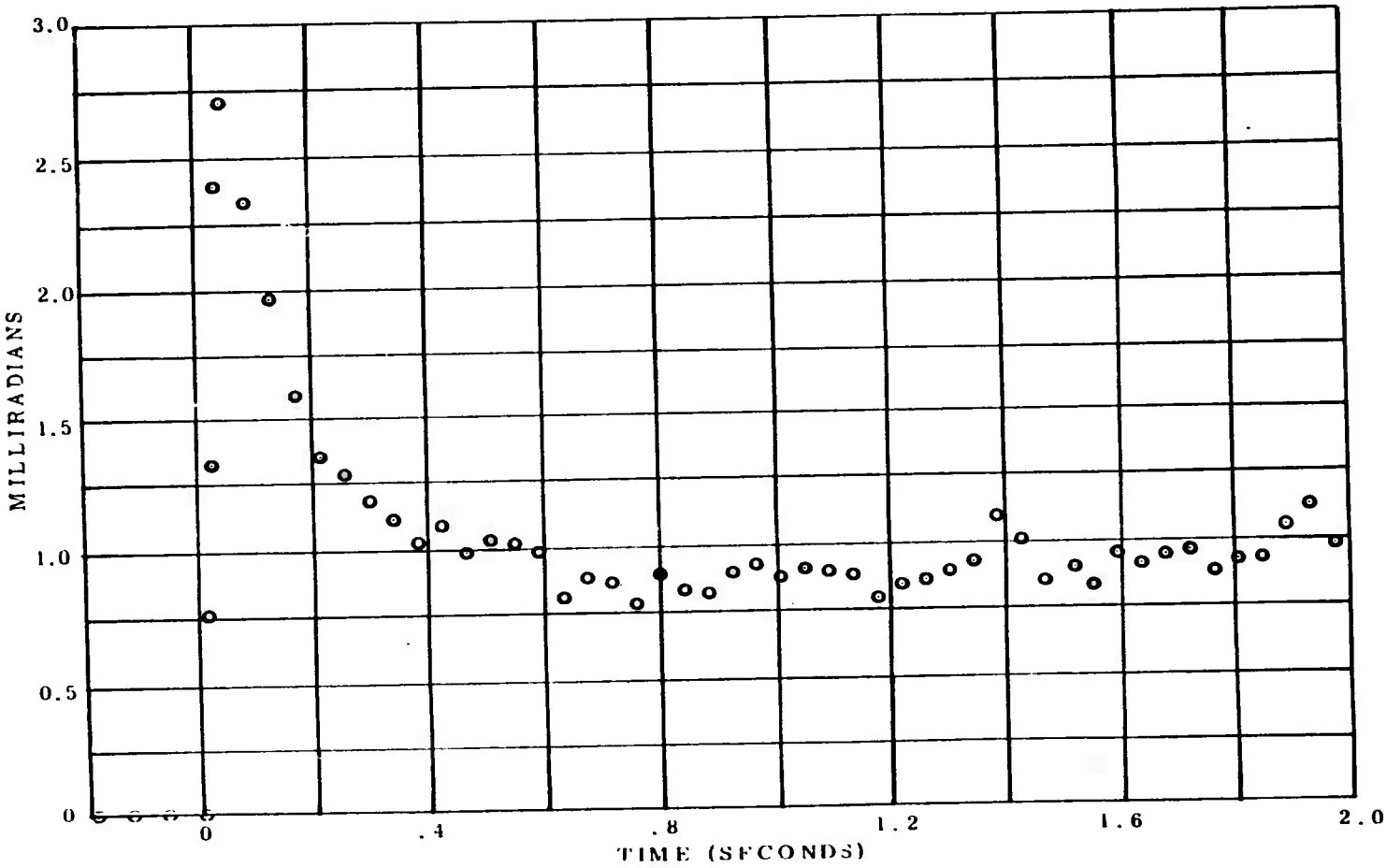

Figure 3.46 Refraction at event, King Fish, interferometer least-squares combination.

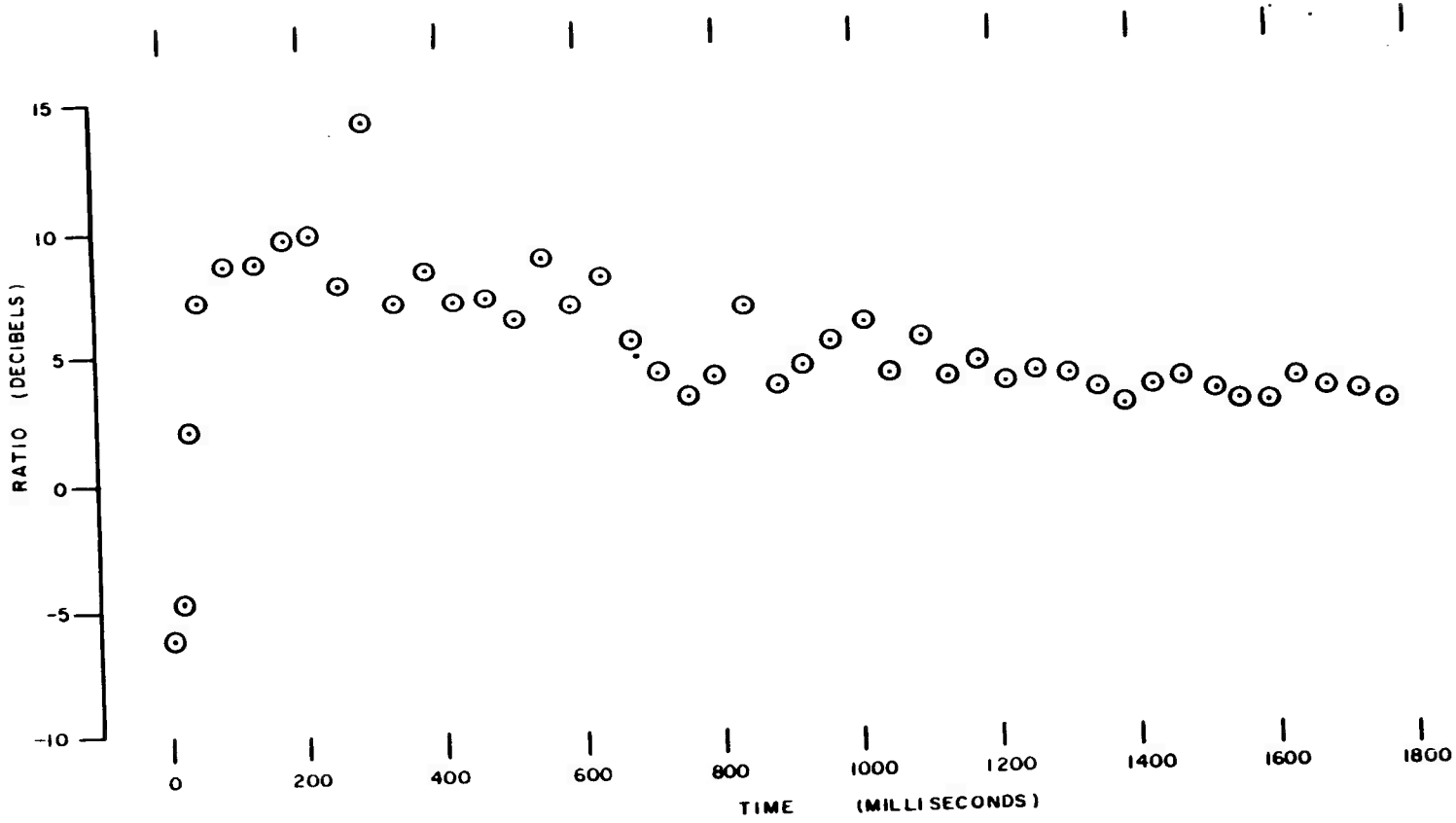

Figure 3.47 Ratio of mean perturbation to dispersion, King Fish, azimuth plane.

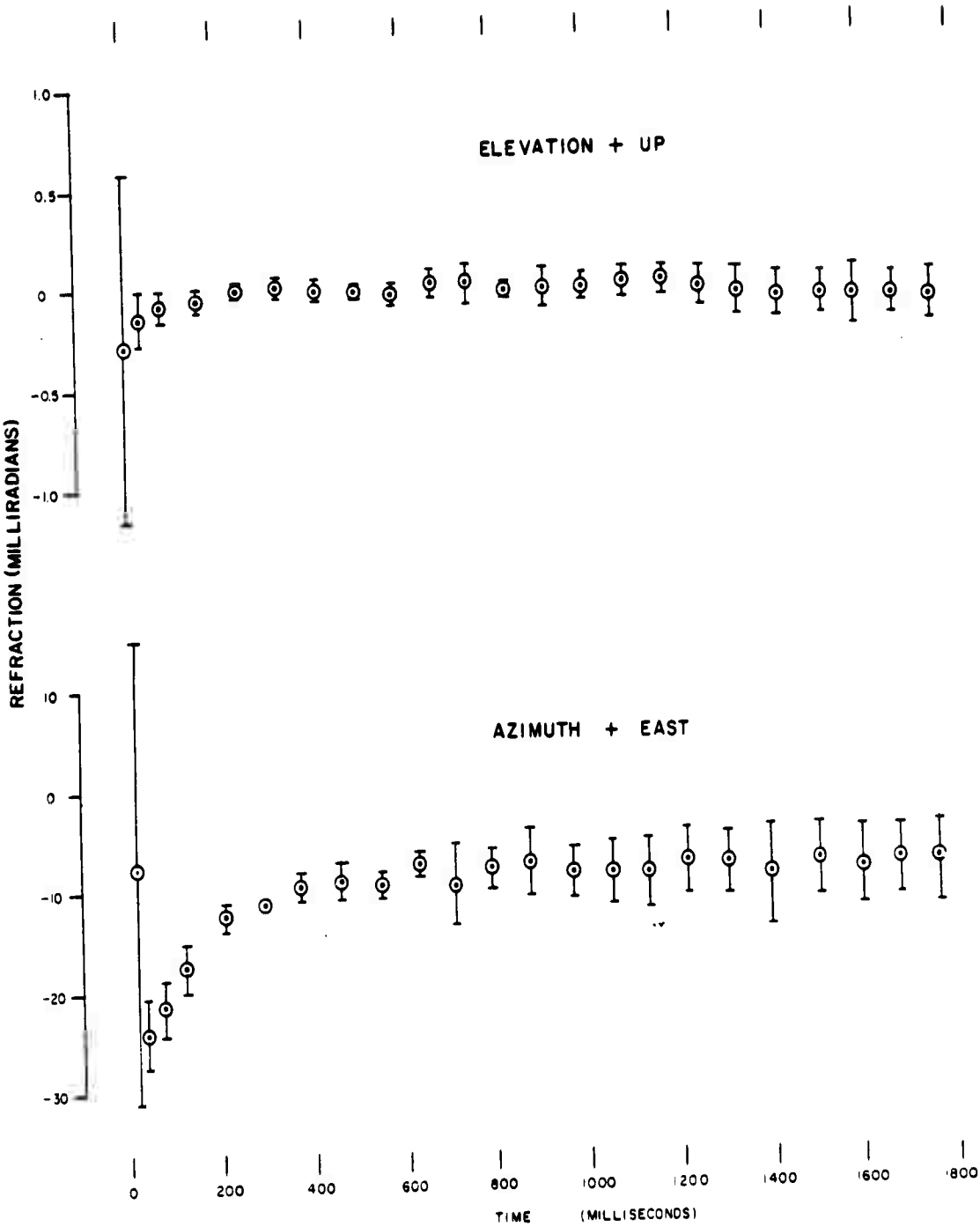

Figure 3.48 Apparent refraction, elevation and azimuth planes, King Fish.

CHAPTER 4

TIGHT ROPE

4.1 PHENOMENOLOGY

Tight Rope was a

detonation at an altitude of at 0730:

00.0678 Z Greenwich Mean Time on 4 November 1962. At this altitude, blackout effects were expected to be entirely a fireball phenomena.

4.2 OBJECTIVES

The objectives of the fixed station were to measure attenuation at X-, C-, and L-bands and apparent refraction at C- and L-bands in the near vicinity of and through the nuclear fireball.

Ship station objectives were to measure attenuation at X-, C-, and L-bands and of apparent relative refraction as a function of frequency.

4.3 OPERATIONS

4.3.1 Operational Plan. Tight Rope was planned as a shot to be detonated at an altitude of km at a downrange distance of approximately 3.3 km from Johnston Island. Considering the relationship between the size of the event and the dispersion of the rockets, it was obvious that the probability of obtaining transmission paths from the carrier vehicles to the shipboard stations or to the fixed station on the island would be small.

Figure 4.1 is an artist's concept of the Project 6.1 geometry for this event. Nike-Cajuns were again utilized as the carrier vehicles. The trajectories chosen for these rockets were planned in such a manner as to place them above and to the south of the event at the time of detonation, in

order to provide paths through the initial fireball. In order to optimize the probability of obtaining any transmission paths through the small fireball, four Nike-Cajuns were fired, and each of the four shipboard stations (S-1 through S-4) tracked a separate rocket for the entire operation. All four ships were positioned north of the island. Ships S-1 and S-3 were stationed in the lagoon approximately 0.5 km from the island, while S-2 and S-4 were about 8 km from the island just outside the reef. Table B.8, Appendix B, gives the positions of the ships with respect to Johnston Island.

4.3.2 Fixed Station Operation. Since all stations were relatively close to the island, and times between launch and event were short, the fixed station was not utilized as a quick-look facility for evaluation of missile trajectories as was done on the previous two events. All fixed station systems were assigned to monitor transmissions from Missile A (H-50) throughout the entire operation. Table 4.1 presents the firing schedule for the missile monitored by the fixed station. The interferometer systems recorded possible refraction data in C- and L-bands. Attenuation data was recorded in X-, C-, and L-bands.

4.3.3 Shipboard Station Operation. As previously stated, each shipboard station tracked a separate rocket throughout the entire Tight Rope operation, to optimize the probability of obtaining a ray path from the rocket through the initial fireball. The four Nike-Cajuns fired for this event were launched in pairs, 10 seconds apart, less than a minute before detonation. Table 4.1 presents the prescribed firing schedule for the rockets and their assigned shipboard tracking stations. The shipboard stations were primarily concerned with monitoring possible signal attenuation in X-, C-, and L-bands.

4.3.4 Support Data. Figures 4.2 and 4.3 are plane views of both elevation and azimuth for Missile A, tracked by S-1 and the fixed station, and Missile C, tracked by S-2. Ship locations and fireball dimensions and positions at significant times during Tight Rope are also illustrated. The precision of any measurements derived from this data is limited by the relative accuracies of the various parameters.

Due to system operational problems, only partially instrumented trajectory data for Missiles A and D are available from Cubic Corporation which provided tracks for Project 6.1 sounding rockets. From short-time samples

for Missiles A and D, it was necessary to extrapolate trajectories before and after event (see Table 4.2). No trajectory data were available for Missile B. It has been estimated that the elevation profile of Missile B was similar to that of Missile A, with only the azimuthal path being significantly different. Tabulations of final Cubic trajectories are found in Appendix B.

Ship locations during the Tight Rope experiment were provided by the Navy and were determined by radar and LORAN positional fixes (Table B.8). Positional accuracy for the ships was submitted to be a radial 500 yards. The positional relationships of the ships to ground zero at H-hour is given in Table B.9. During the course of the operation, Ships S-1 and S-3 were anchored at their respective locations. Ships S-2 and S-4 were under steam, and their changing positions were determined by several estimates of heading and speed (Table B.10).

Table B.13, Appendix B, lists the location of the re-entry vehicle at the time of event in the various coordinate systems employed during the Tight Rope operation. Fireball data is presented in Figures B.11 to B.14.

4.4 RESULTS

A discussion of instrumentation limitations and data interpretation is presented in Sections 1.6 and 1.7.

Interferometer data reduction procedures and sources of interferometer system error are described in Appendix D.

4.4.1 Attenuation Data.

Fixed Station. All systems tuned to Missile A (H-50) experienced large signal amplitude variations prior to event. These variations were caused by an unfavorable beacon antenna pattern during a missile coning motion. Section 1.6.1 describes this problem in some detail.

At H = 0, prompt radiation effects caused drops of 5.7 db, 21.1 db, and 51.0 db in X-, C-, and L-bands, respectively. An expanded view of the event time data is presented in Figure 4.4. Initial recovery began immediately in X- and C-bands and within 200 milliseconds in L-band. Figure 4.5 indicates that the normal distance from the ray path to the point of detonation at H = 0 was approximately 0.8 km. This figure also shows that the closest point of ray path approach to the fireball was about 0.12 km at H+15 seconds.

Complete X-band signal strength data is presented in Figure 4.6, and a record of both maximum and minimum

signal envelopes for the principal period of interest is presented in Figure 4.7. There is no evidence of any attenuation of X-band signal except for the brief loss at H = 0. Other deviations from a uniform response are the result of operational problems.

Similar records of C-band data are displayed in Figures 4.8 and 4.9. Again, there is no evidence of attenuation other than the momentary perturbation at event. The signal losses in this band, as in X-band, which are noted after H+200 seconds, were caused by receiving antenna directional characteristics.

Signal strength data presented in Figures 4.10 and 4.11 indicate that the initial radiation-induced attenuation in L-band was more severe than that in X- and C-bands. The L-band recovery description is distorted by signal amplitude variations caused by antenna patterns. An assumption as to the extent of the signal level anomalies and their removal implies a recovery to within 3-5 db of pre-event levels by H+5 seconds. No other attenuation is apparent in this data. L-band signal losses after H+200 seconds were the result of antenna directional limitations, as were those in X- and C-bands.

761

Ship 1. Ship 1 tracked Missile A (H-50) and experienced the same signal level fluctuations as were recorded by the fixed station. Section 1.6.1 describes the beacon antenna characteristics responsible for these amplitude variations.

At H = 0, X- and C-bands experienced losses of 15.1 and 19.2 db, respectively, with quick recoveries noted in both frequencies. L-band dropped 25.7 db to system noise and remained below this level for more than five seconds. Figure 4.12 displays expanded time plots of the three relative signal strengths at the time of event. At event, the normal distance between the signal ray path and the center of the fireball was about 0.8 km. Computed fireball ray-path parameters for S-1 are illustrated in Figure 4.13. Ray-path entry into the fireball is indicated at approximately H+10 seconds and departure at about H+46 seconds. There is some doubt as to the accuracy of this data.

A plot of X-band signal strength in Figure 4.14 indicates that the only period of attenuation following the event existed between H+17 and H+30 seconds. An examination of possible signal loss due to antenna-pointing errors has revealed negligible pointing deviations during

this period (see Figure A.36). Figure 4.15 presents an expanded view of the X-band data with both maximum and minimum signal envelopes. The inhomogeneity of the fireball is well demonstrated by the amplitude scintillations during the attenuation period. Signal characteristics during the recovery period may be attributed to ray-path departure from the fireball rather than to a decrease of ionization in the debris region. This probability is further discussed at the conclusion of this section.

Figures 4.16 and 4.17, respectively, present the maximum and the complete envelopes of C-band signal strength data. Attenuation times favorably agree with those of X-band. Scintillations are also very prominent in this data.

Figure 4.18 is a plot of L-band signal strength data for the complete flight of Missile A. Varying signal levels are noted from event time to approximately H+35 seconds. A time-expanded view of this data is presented in Figure 4.19. The first signal peak noted after event probably represents a legitimate fireball-associated attenuation of approximately 10 db, the shape being fairly characteristic of beacon antenna-rocket coning. It appears that the ray path was obscured by the fireball

before the next peak reached its maximum value. The final time segment of apparent attenuation abruptly ends within five seconds of X- and C-band recoveries. L-band signal amplitude scintillations are relatively small, not significantly larger than normal pre-event variations. The reason for this departure from expected behavior is not clear. One possible explanation is that L-band transmissions were reflected or refracted from the inner torus area. Such perturbed signals would appear in the main lobe of the wide-beam elements of the L-band tracking system, while reflected or refracted transmissions which enter the side lobes of the narrower beam X- and C-band systems could interfere with non-deviated signals and produce the displayed amplitude scintillations.

The agreement of attenuation times between data from all three frequency bands suggests that the return of the signals to normal amplitudes was the result of ray-path departure from the fireball. The ambiguities between this hypothesis and the fireball-ray-path parameters in Figure 4.13 may be reconciled by small corrections to assumptions of fireball, rocket, or ship positions.

Ship 2. Figures 4.20 and 4.21 present the X- and C-band signal strength data relating to the track of Missile C (H-40). A number of problems, including a malfunction in automatic tracking equipment, hindered the operation of this station. All tracking attempted by S-2 was accomplished manually.

No significance concerning X-band data can be attributed to the event phenomena. C-band information displays continuous level variations caused by antenna-pointing errors during the manual track. The extent of legitimate C-band signal loss at H-hour is difficult to assess because of these variations. However indications are that antenna-pointing deviations were not drastically severe at later periods when ray paths intersect the fireball. This assumption is based upon the maintenance of a significantly strong signal at the later times of interest with respect to the narrow beamwidth of the C-band tracking antenna.

Figure 4.22 illustrates entry and exit times of the ray path to and from the fireball proper. L-band signal strength data presented in Figure 4.23 is relatively compatible with these computations. A loss of about 29 db is noted at event. In addition, a period of considerable attenuation was observed from approximately H+75 to H+95 seconds.

Because of system operational problems, limited significance should be applied to S-2 data. The attenuation observed in L-band at the late times was real, but its value relative to optimum tracking conditions and fireball phenomena is uncertain.

Ship 3. Tracking Missile B (H-50), S-3, experienced signal losses of 18 db and 27 db at event in X- and C-bands, respectively (Figure 4.24). After a partial recovery, signal levels in both frequencies dropped, going into noise by H+0.5 second. The initial loss of the L-band signal was 49 db to noise.

A complete record of X-band signal strength data is presented in Figure 4.25. Signal level variations noted before event were caused by operational problems. After the initial loss caused by the prompt radiation, a subsequent drop-out resulted from an AFC shift. Gross tracking errors between H+0.2 and H+27 seconds (Figure A.38) were responsible for considerable power losses for that period. The equivalent power losses due to the pointing deviations are illustrated in Figure 4.26. There appears to be valid attenuation data commencing at H+32 seconds and lasting until H+53 seconds. Figure 4.27 presents a time-expansion of both maximum and

minimum X-band data envelopes with signal strength corrections for antenna pointing errors. Although the overall attenuation for this period is not very large, amplitude scintillations do enhance the significance of the data to some degree.

C-band data exhibits characteristics similar to that of X-band (Figure 4.28). Attenuation data, recorded after normal tracking had resumed, appears valid except for the three brief questionable periods noted in the graph. An expansion of this data in which the extent of the overall attenuation and the characteristic amplitude perturbations are indicated appears in Figure 4.29.

The operational problems which degraded early post-event information in X- and C-bands are also reflected in L-band data (Figures 4.30 and 4.31). Because of the wide beamwidth of the L-band tracking system, this data may be significant although a lack of position data for Missile B makes it difficult to evalute. Values for attenuation at H-hour and between H+25 and H+70 seconds are believed to be legitimate reactions to the event phenomena. Average attenuation levels of approximately 40 db exhibit some level fluctuations, although not as prominent as those observed in X- and C-bands.

In the absence of an instrumented trajectory, an analysis was made of photographic data collected by a boresight camera mounted on the station's antenna pedestal to provide information of fireball-ray-path relationships. The reducible portion of the boresight data indicates that ray paths were within the fireball from H+27 seconds to H+61 seconds. Fireball-ray-path parameters, derived from this data, are presented in Figure 4.32. Penetrations of relatively unperturbed X- and C-band transmissions were noted during the first several seconds of fireball obscuration when ray paths lingered close to the inner edge of the developed torus. A pronounced absorption of the more vulnerable L-band signals coincided with the initial fireball intercept at H+27 seconds, although levels for the subsequent period of attenuation were maintained above system noise.

Ship 4. Operational problems prevented the acquisition of any usable data from this station.

4.4.2 Refraction Data.

Interferometer. A comparison of interferometer phase data with the Cubic AME-DME trajectory for Missile A (H-50) has revealed discrepancies which prevent any long-term refraction measurements for the Tight Rope operation.

Figure 4.33 compares the trajectory with a least-squares combination of all Project 6.1 phase data measurements. Most of the disparity noted after H-30 seconds probably can be explained by relative differences in the systems' orientations or inaccuracies in base length measurements.

Trajectory data is adequate, however, to estimate short-term refraction at event time. Figure 4.34 is a time-expansion of the raw phase data at H-hour. It is noted that all major excursions occurred during the signal decay time. Because such rapid decays have been shown to effectively deny suitable inputs to the phasemeters, the first five milliseconds of phase data must be discarded. Refined phase comparisons, calibrated in electrical degrees, are presented in Figures 4.35 to 4.40. All slopes are presented as positive to facilitate comparisons. Subsequent to the initial five-millisecond noise period, small residual deviations may be noted from an extrapolation of the pre-event data. All significant perturbations appear to be dissipated by approximately H+20 milliseconds.

Unit vectors were computed for the deviations and compared with similar vectors derived from the extrapolated data. Results of these 14 comparisons are presented in Figures 4.41 to 4.54. It is noted that all values after

the initial five-millisecond noise interval are relatively small and after H+15 milliseconds, insignificantly different from pre-event data characteristics. A least-squares solution of values for the period of interest is presented in Figure 4.55.

The significance of refraction measurements for Tight Rope cannot be adequately assessed because of the relatively low signal levels that prevailed during the entire perturbation period. Low signal levels will degrade the quality of interferometer phase data. An accuracy for this data is approximated at ±0.2 milliradian.

Shipboard Stations. Due to tracking error signal calibration difficulties, no refraction effects could be measured from shipboard station data. A discussion of attempts to obtain shipboard station refraction measurements is given in Section 2.4.2.

4.5 DISCUSSION

4.5.1 Data Reliability. Accuracies for Project 6.1 and support data are discussed in Section 2.5.1 and presented in Table 2.4.

4.5.2 Attenuation. Data was intermittent for this event, but integration and extrapolation indicate that the observed attenuation was closely confined to the fireball proper. Figure 4.56 presents a time-history of attenuation in X-, C-, and L-band frequencies constructed from data collected by the several stations. Attenuation measurements are indicated only for ray paths directed through the torus, ostensibly the most densely ionized portion of the debris region. Attenuation data was not available prior to H+20 seconds. Complete signal recoveries were noted by H+54 seconds in X-band; H+60 seconds in C-band. L-band transmissions are observed close to, or within, the noise as late as H+60 seconds. Data for this frequency from S-2 indicates some absorption as late as H+95 seconds although the reliability of the information is questionable.

A comparison of Tight Rope data with that of Blue Gill indicates some relative differences and similarities. Characteristic attenuations for both events were compared at H+40 seconds, a time immediately after reacquisition of X- and C-band signals during the Blue Gill operation. The comparison is presented in Table 4.3. Recovery periods and amplitude scintillations for X- and C-bands compare

favorably to those of Blue Gill, although the attenuation effects during Tight Rope were less severe because of the shorter path lengths through the fireball. It was also evident that the center of the Tight Rope torus is virtually transparent to X- and C-band transmissions for times as early as 27 to 30 seconds after the event. For all computations involving the event phenomena, a spherical fireball was assumed.

4.5.3 Refraction. Limited significance should be applied to the Tight Rope refraction data. It is not certain that the observed phase data perturbations were other than noise produced by low signal levels.

TABLE 4.1 PLANNED FIRING SCHEDULE, TIGHT ROPE

Missile	Time Relative to Event, seconds	QE, degrees	Azimuth, degrees True	Monitoring Station
A	H-50	84	201	S-1, Interferometer
B	H-50	84	201	S-3
C	H-40	81	199	S-2
D	H-40	81	206	S-4

TABLE 4.2 TIME SPANS OF RAW TRAJECTORY DATA, TIGHT ROPE

Missile	Time Span of Unextrapolated Data Referenced to Event, seconds
A	H-50 to H-10
C	Complete Track
D	H-40 to H-5

TABLE 4.3 COMPARATIVE CHARACTERISTIC ATTENUATION FOR BLUE GILL AND TIGHT ROPE AT H + 40 SECONDS

Frequency Band	Attenuation, db Blue Gill	Tight Rope
X	19±2	9±4
C	28+8, -2	24±3
L	≥45	≥40

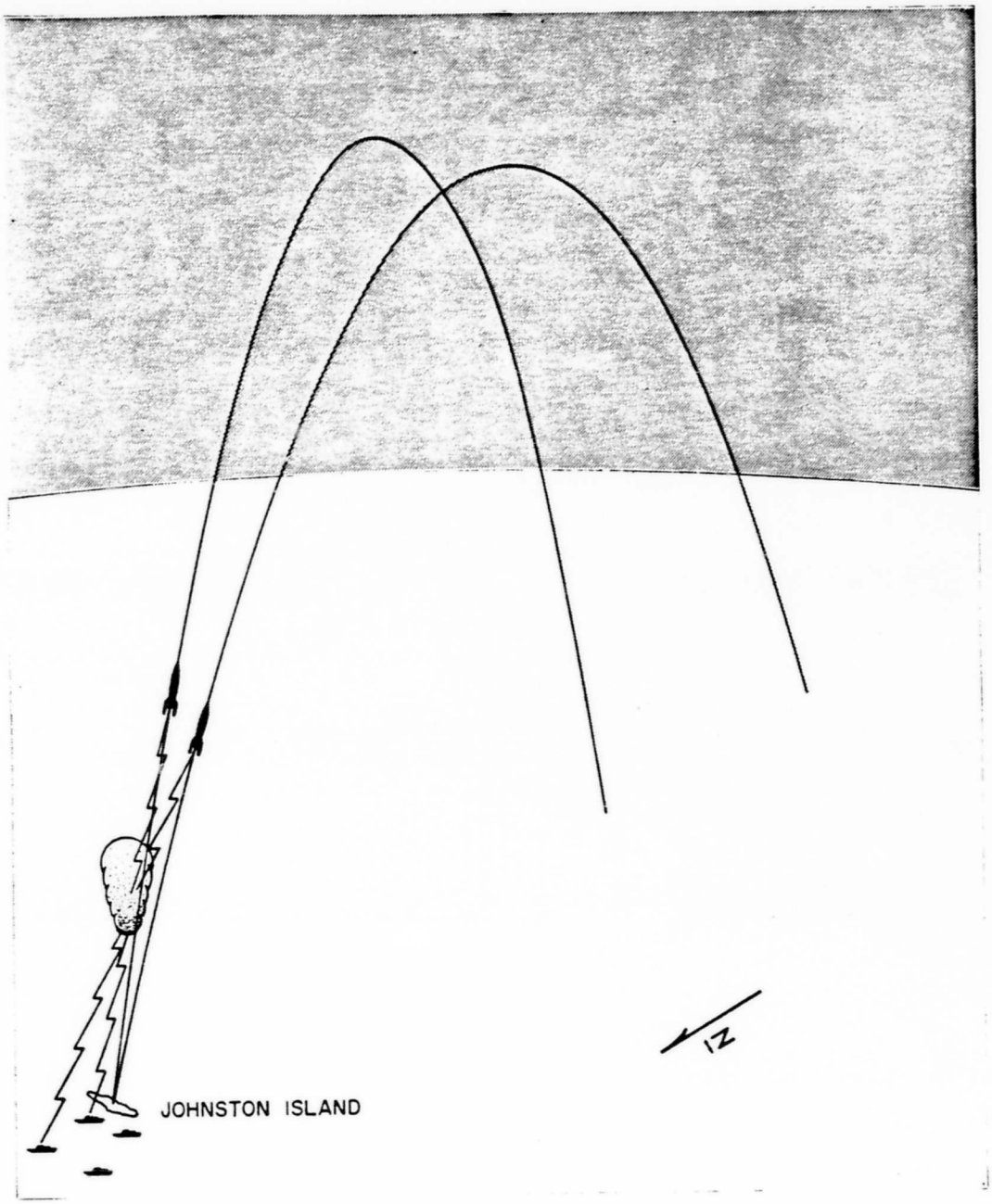

Figure 4.1 Tight Rope geometry, Project 6.1.

Pages 289 and 290
deleted.

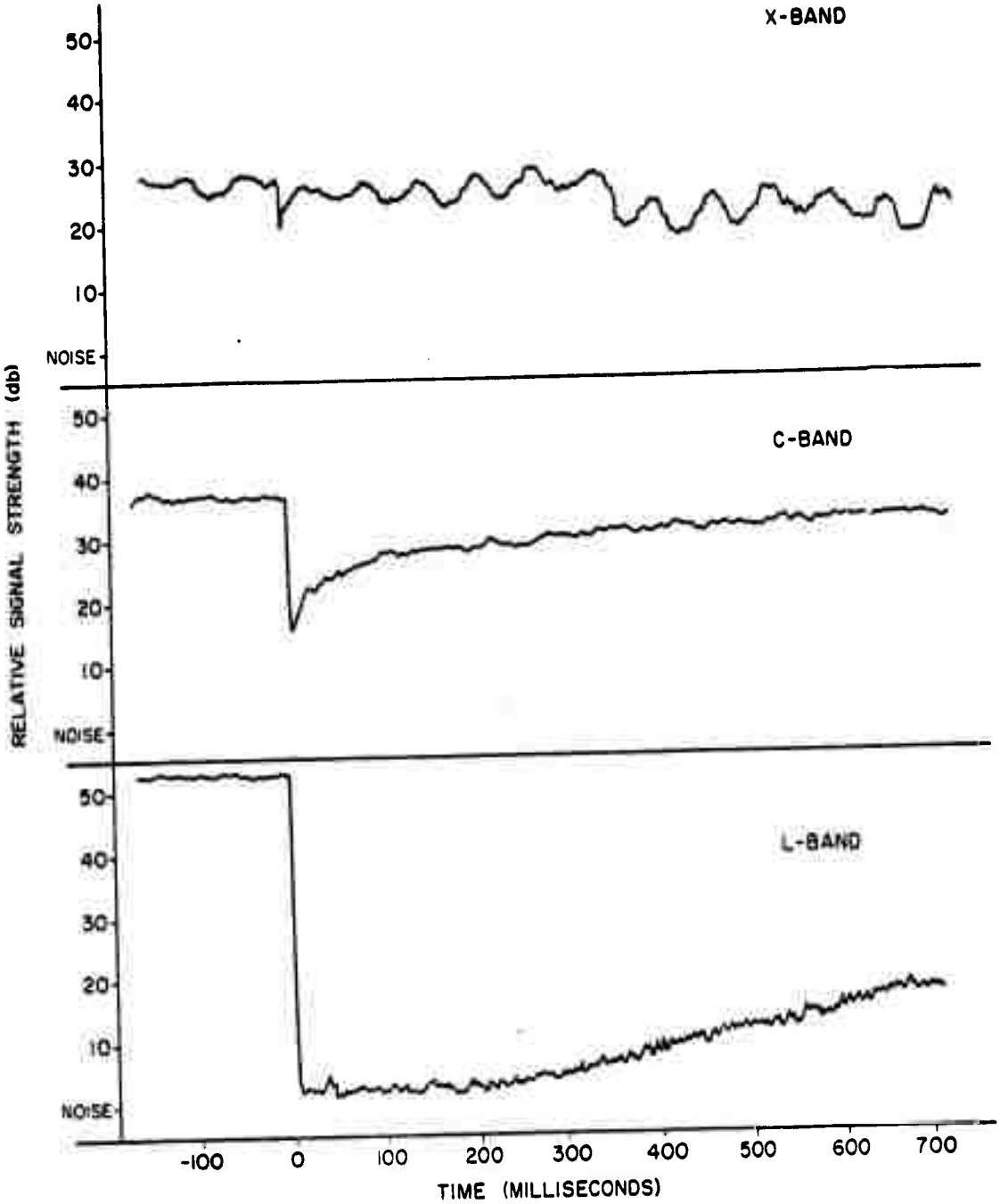

Figure 4.4 Relative signal strength, Tight Rope, Missile A, interferometer.

Page 292 deleted.

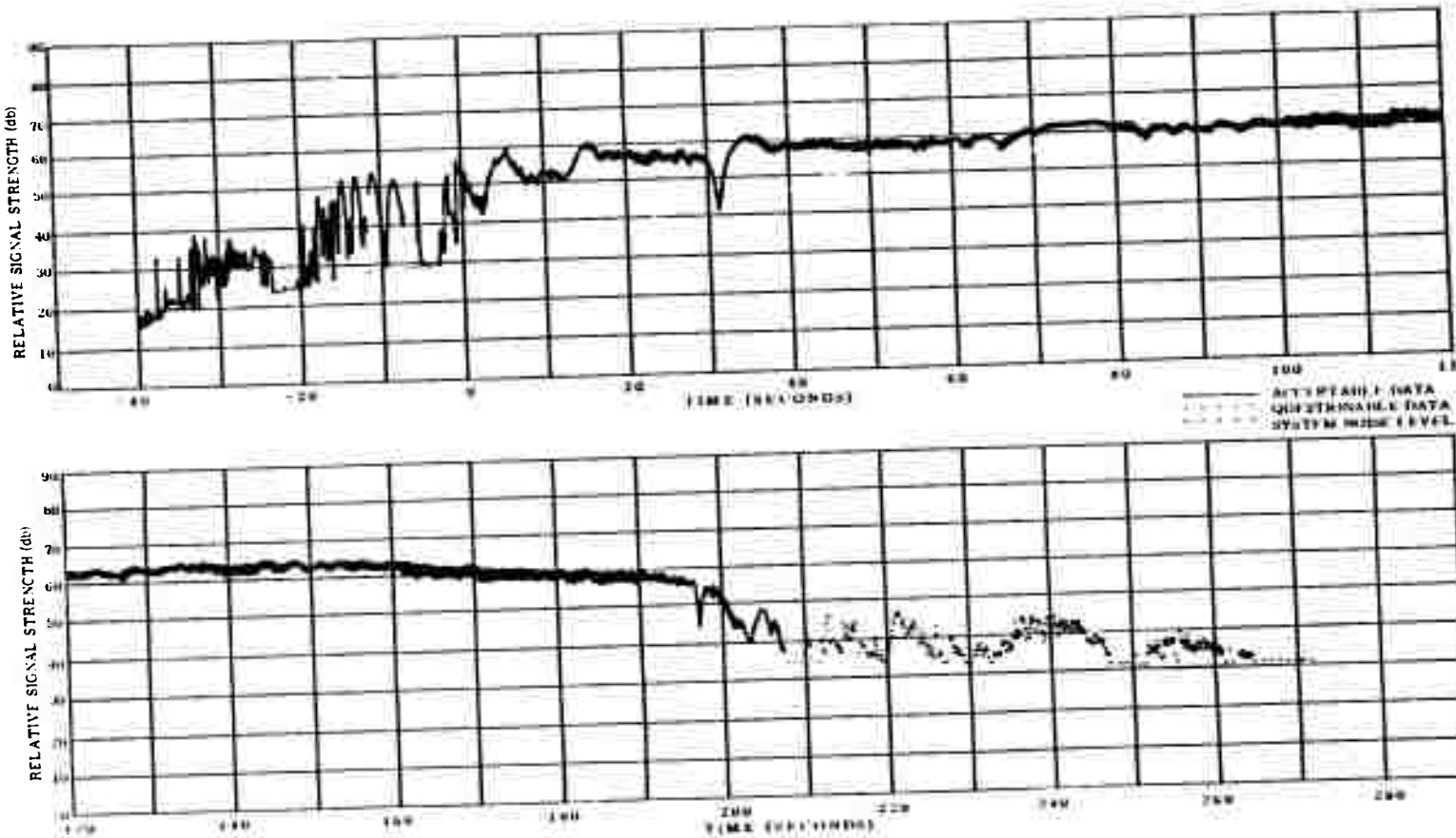

Figure 4.6 X-band relative signal strength, Tight Rope, Missile A, interferometer.

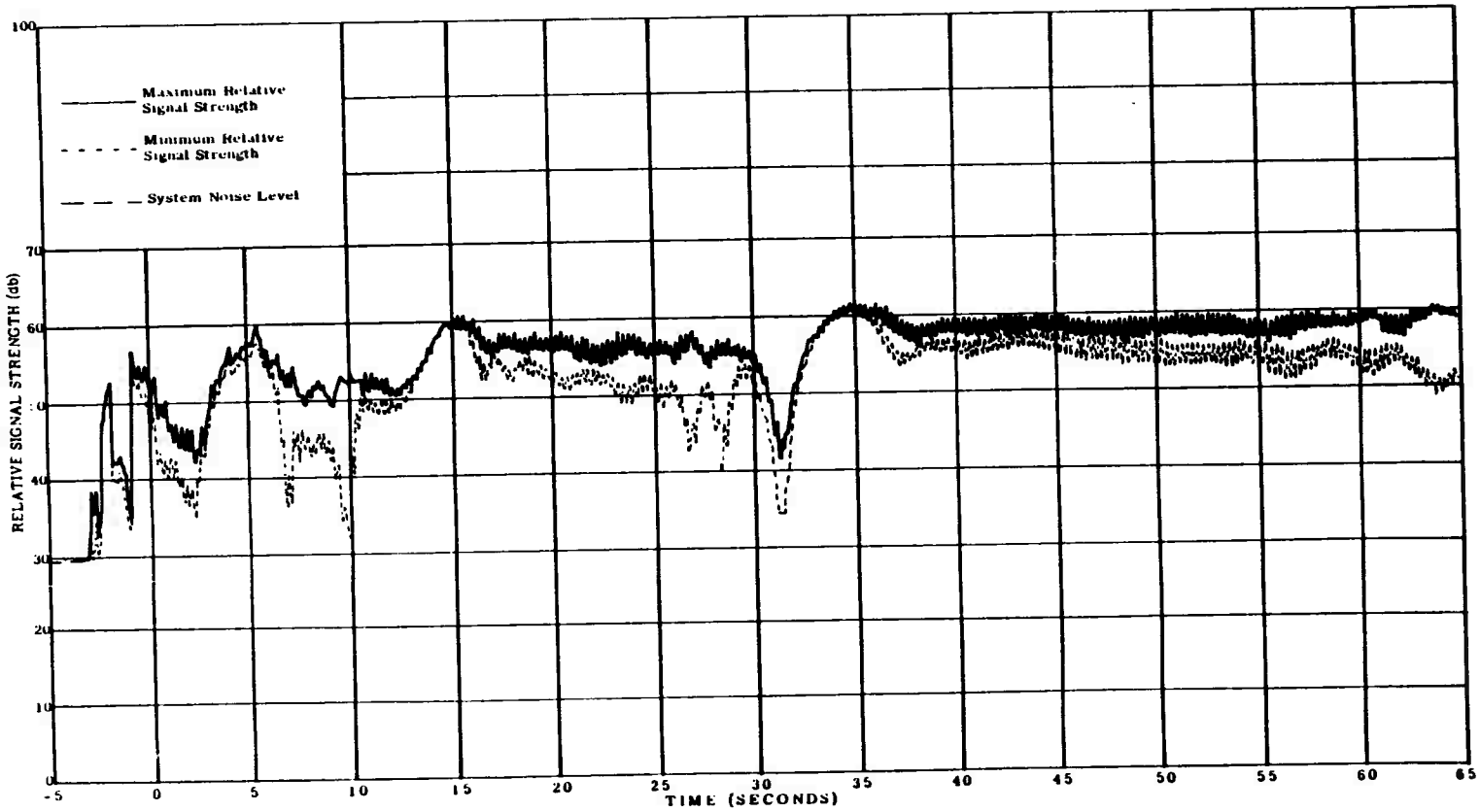

Figure 4.7 X-band relative signal strength envelopes, Tight Rope, Missile A, interferometer.

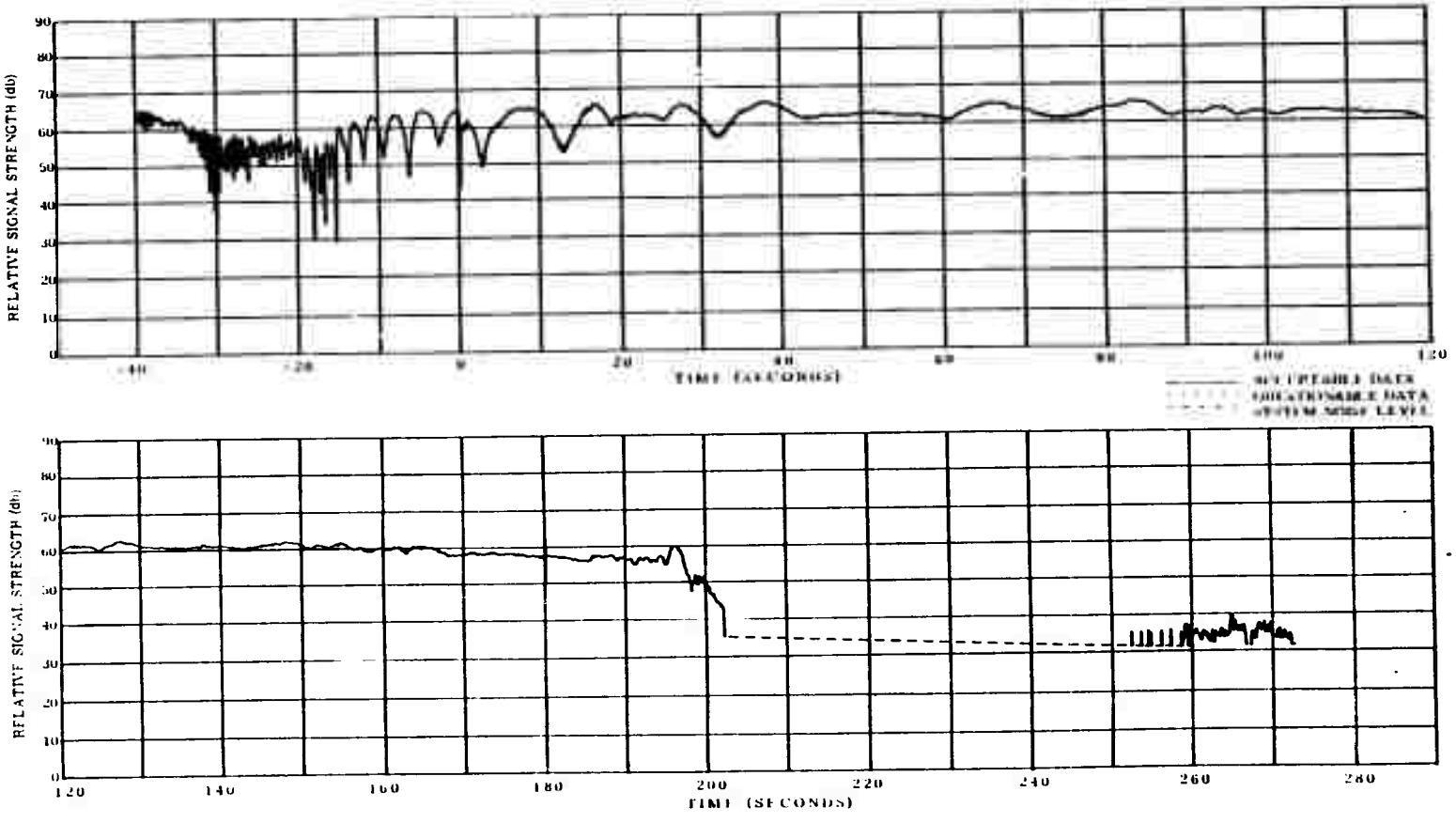

Figure 4.8 C band relative signal strength, Tight Rope, Missile A, interferometer

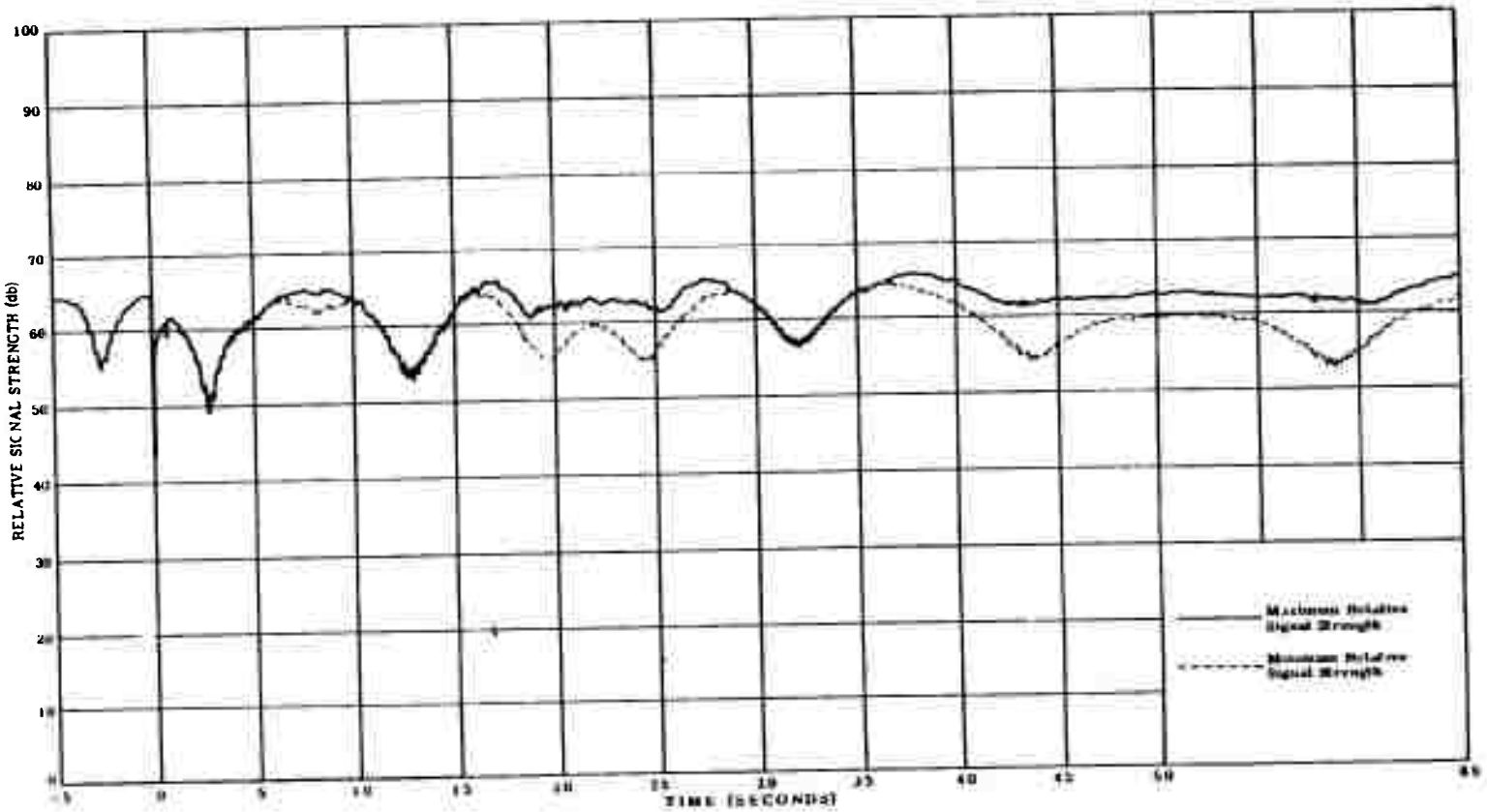

Figure 4.9 C-band relative signal strength envelopes, Tight Rope, Missile A, interferometer.

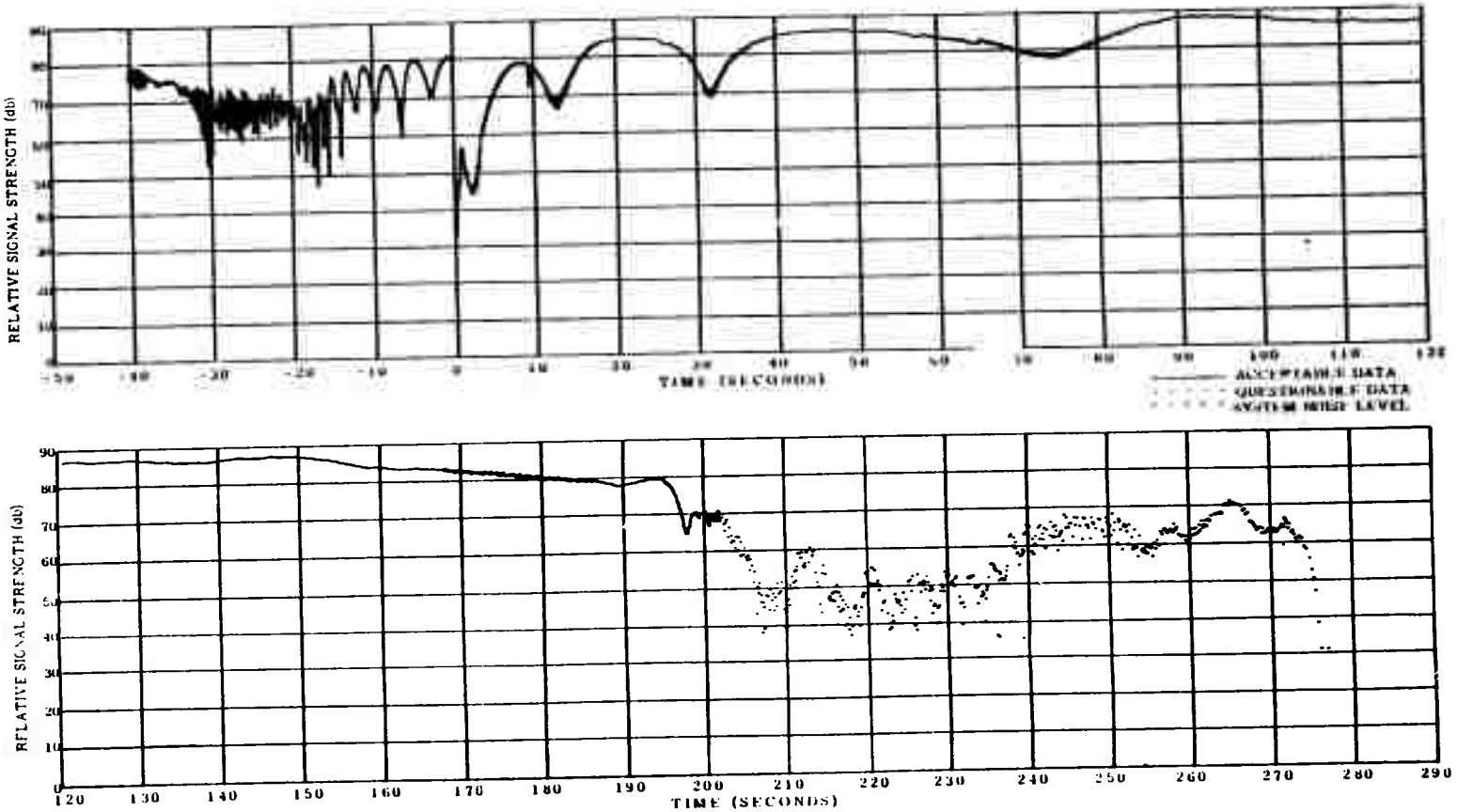

Figure 4.10 L-band relative signal strength, Tight Rope, Missile A, interferometer.

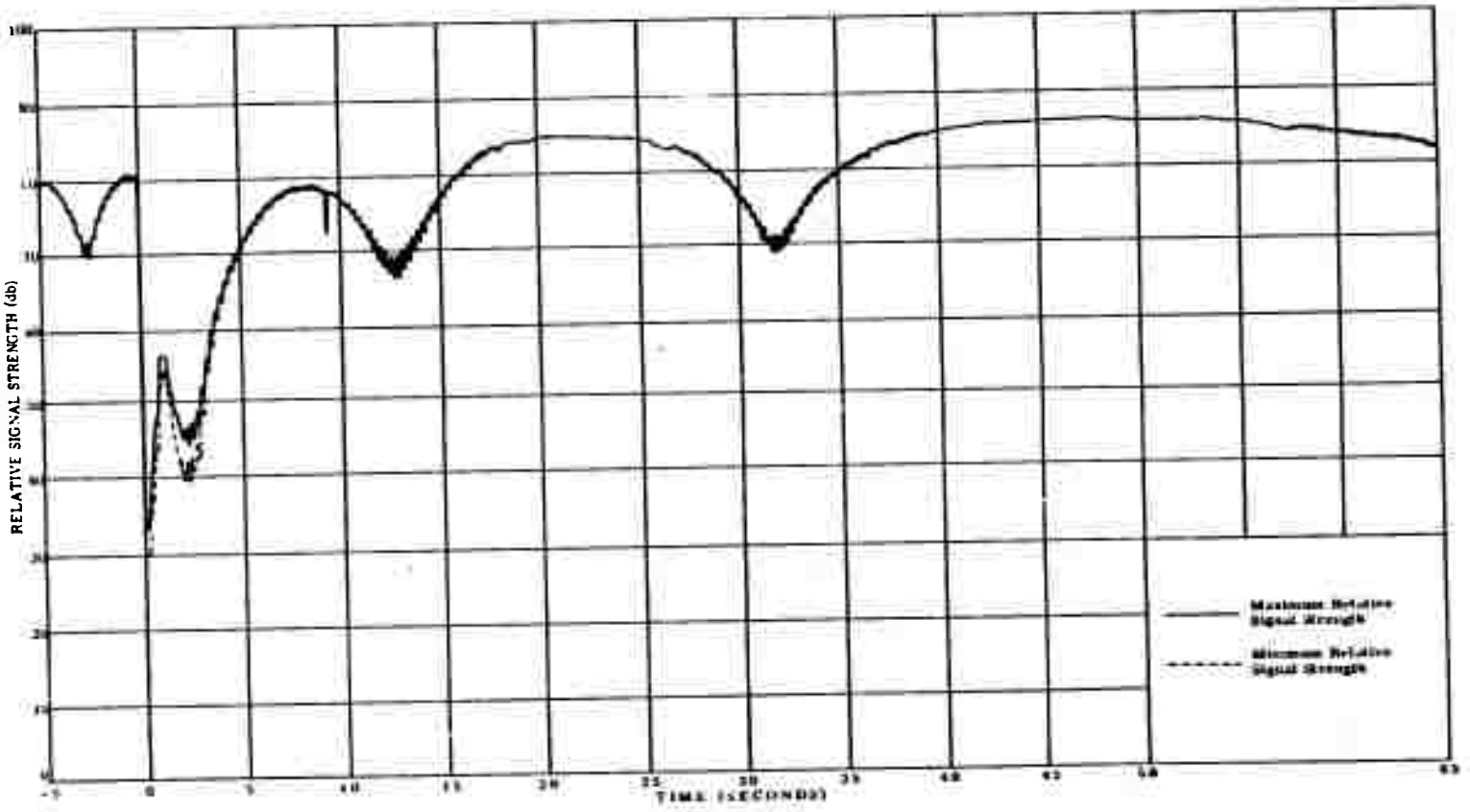

Figure 4.11 L-band relative signal strength envelopes, Tight Rope, Missile A, interferometer.

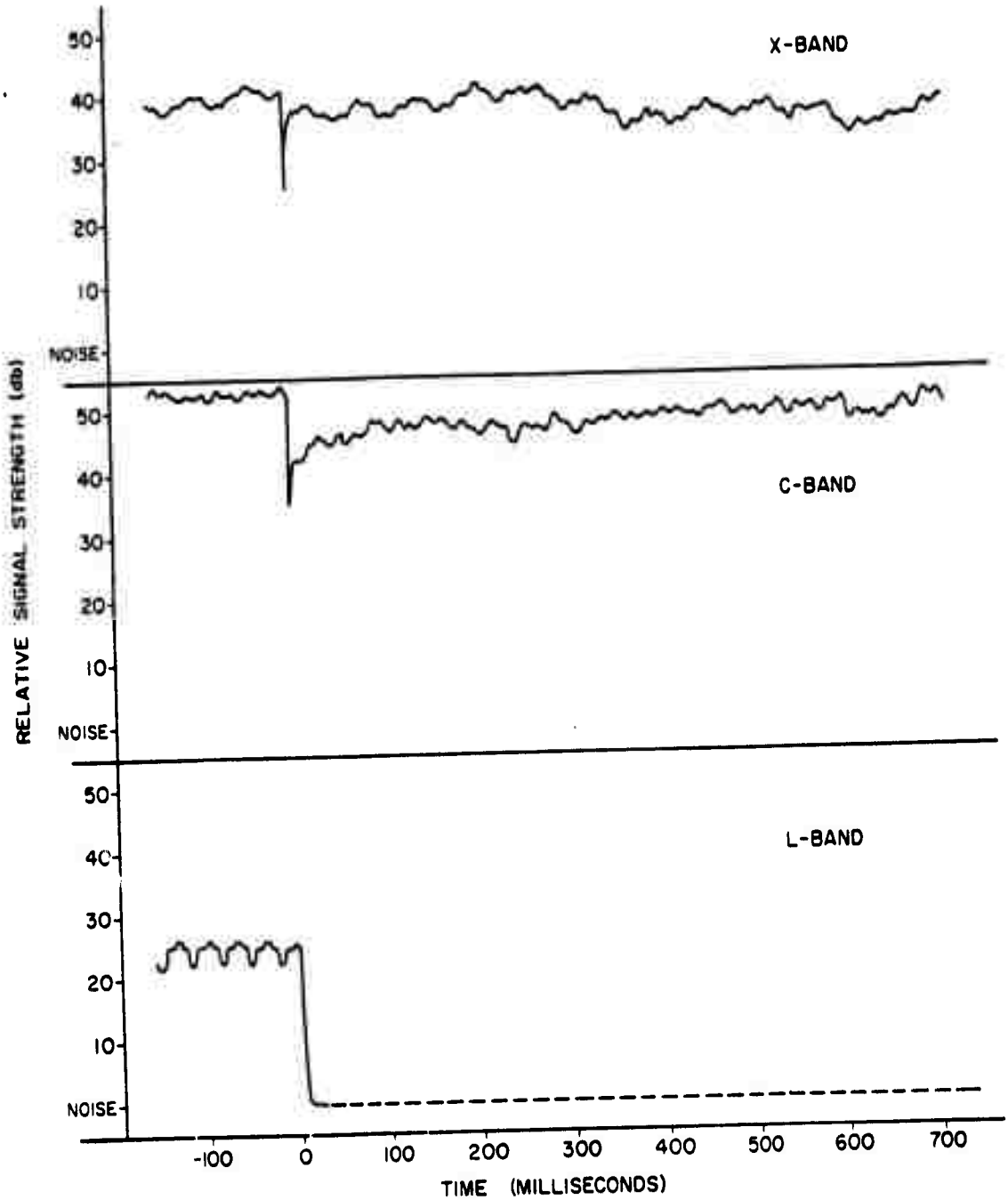

Figure 4.12 Relative signal strength, Tight Rope, Missile A, Ship 1.

Page 300 deleted.

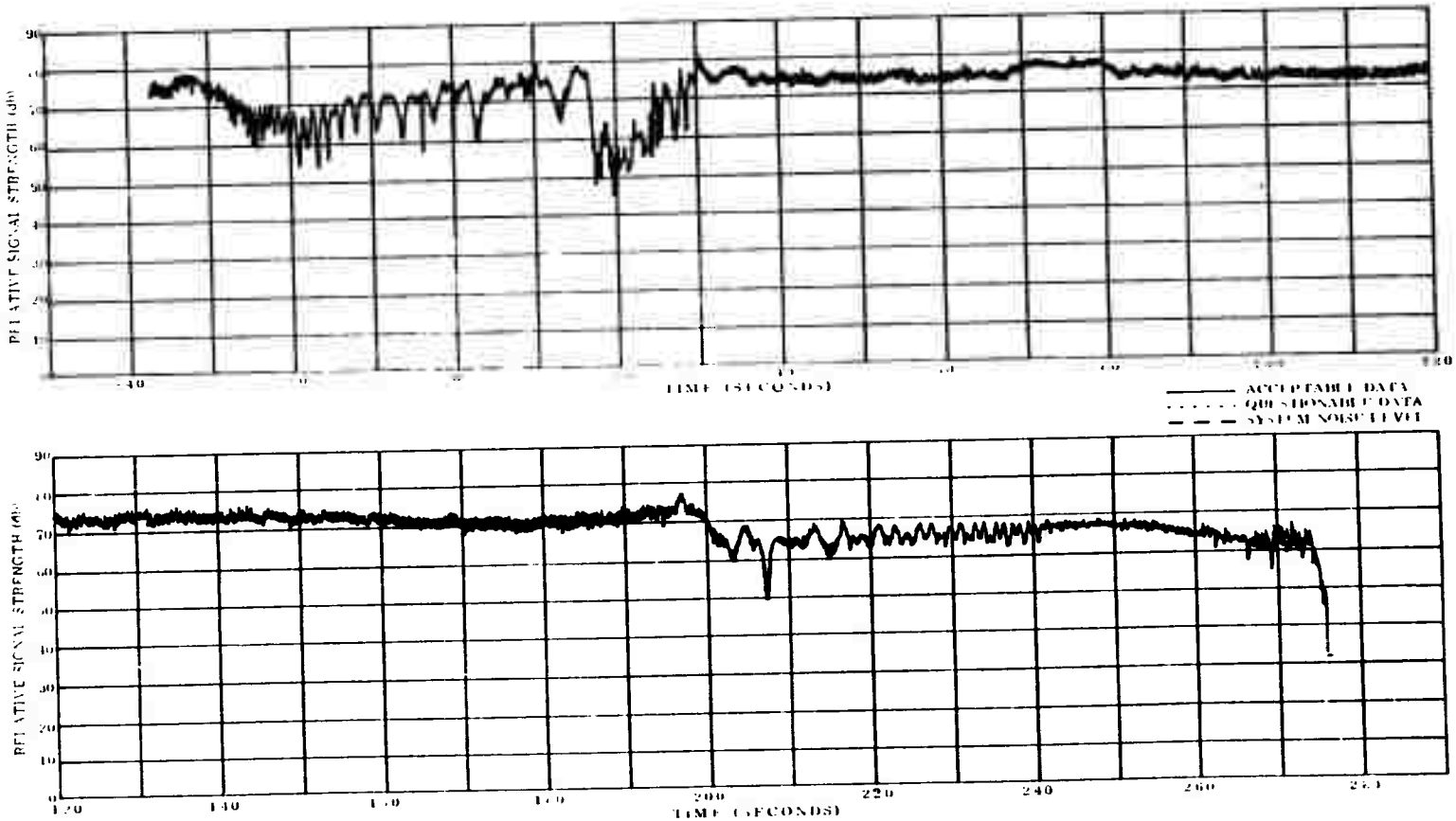

Figure 4.14 X band relative signal strength, Tigal Reps, Missile A, Ship 1.

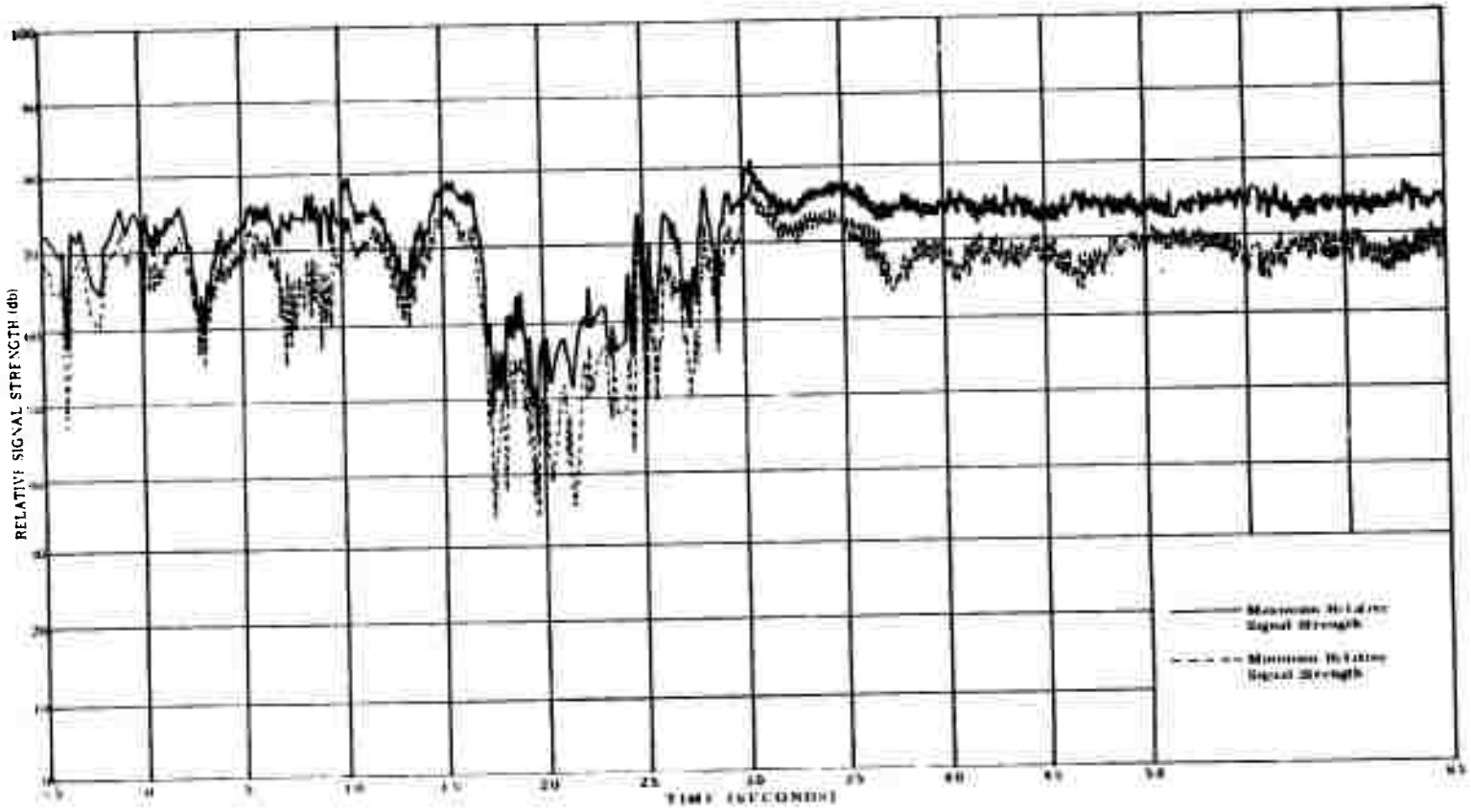

Figure 4.15 X-band relative signal strength envelopes, Missile A, Ship 1.

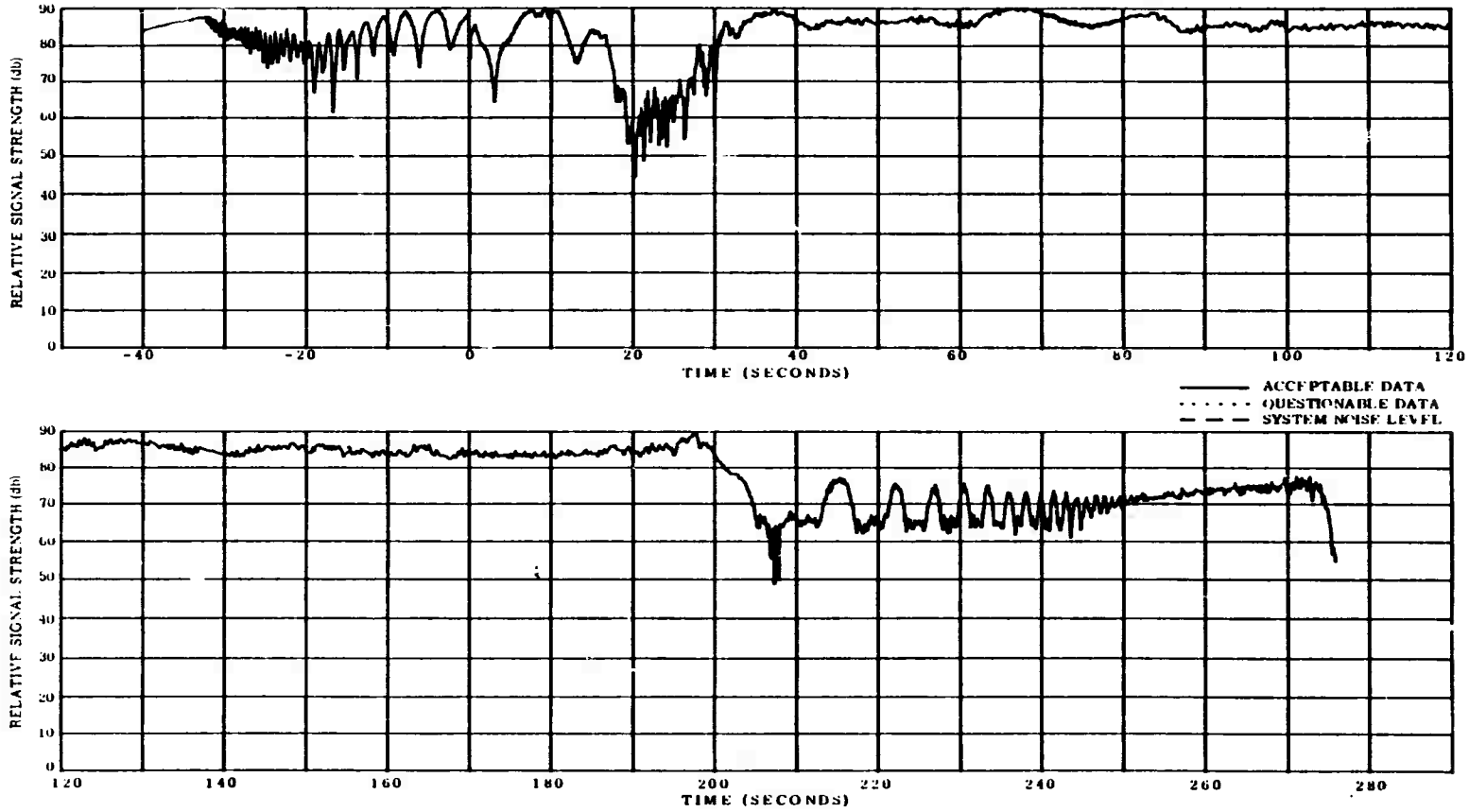

Figure 4-16 C-band relative signal strength, Tight Rope, Missile A, Ship 1.

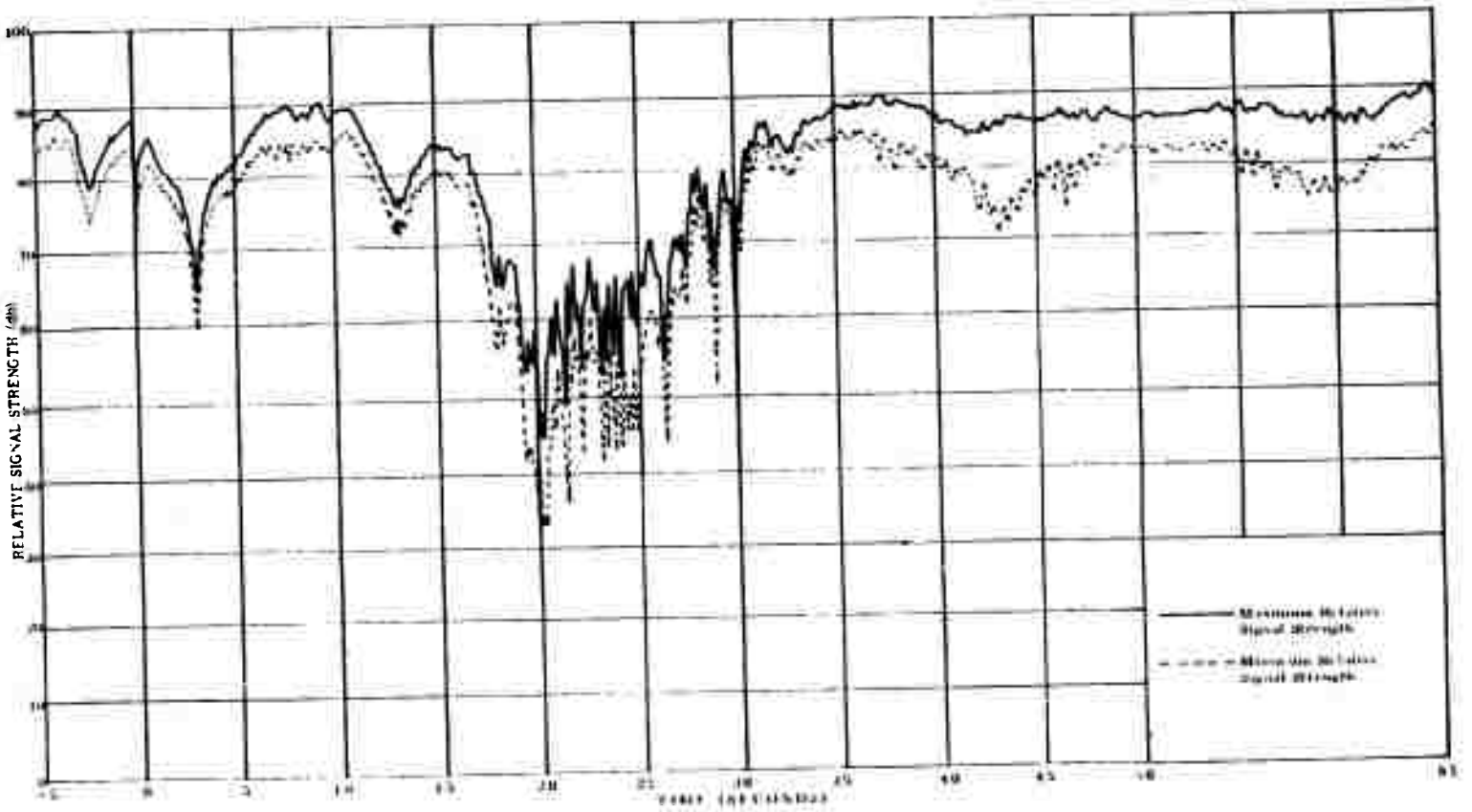

Figure 4.17 C-band relative signal strength envelopes, Tight Rope, Missile A, Ship 1.

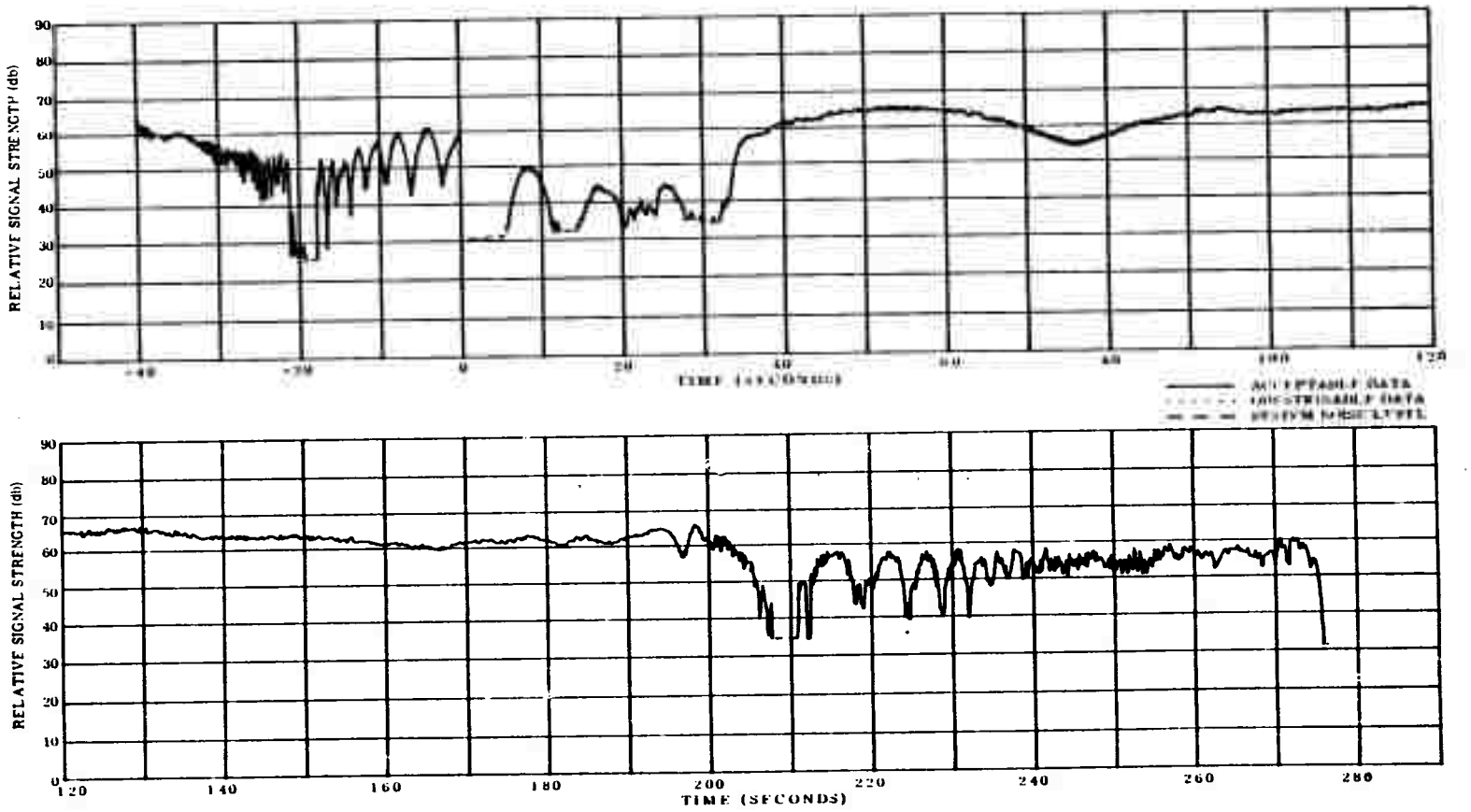

Figure 4.18 L Band relative signal strength, Tight Rope, Missile A, Ship 1.

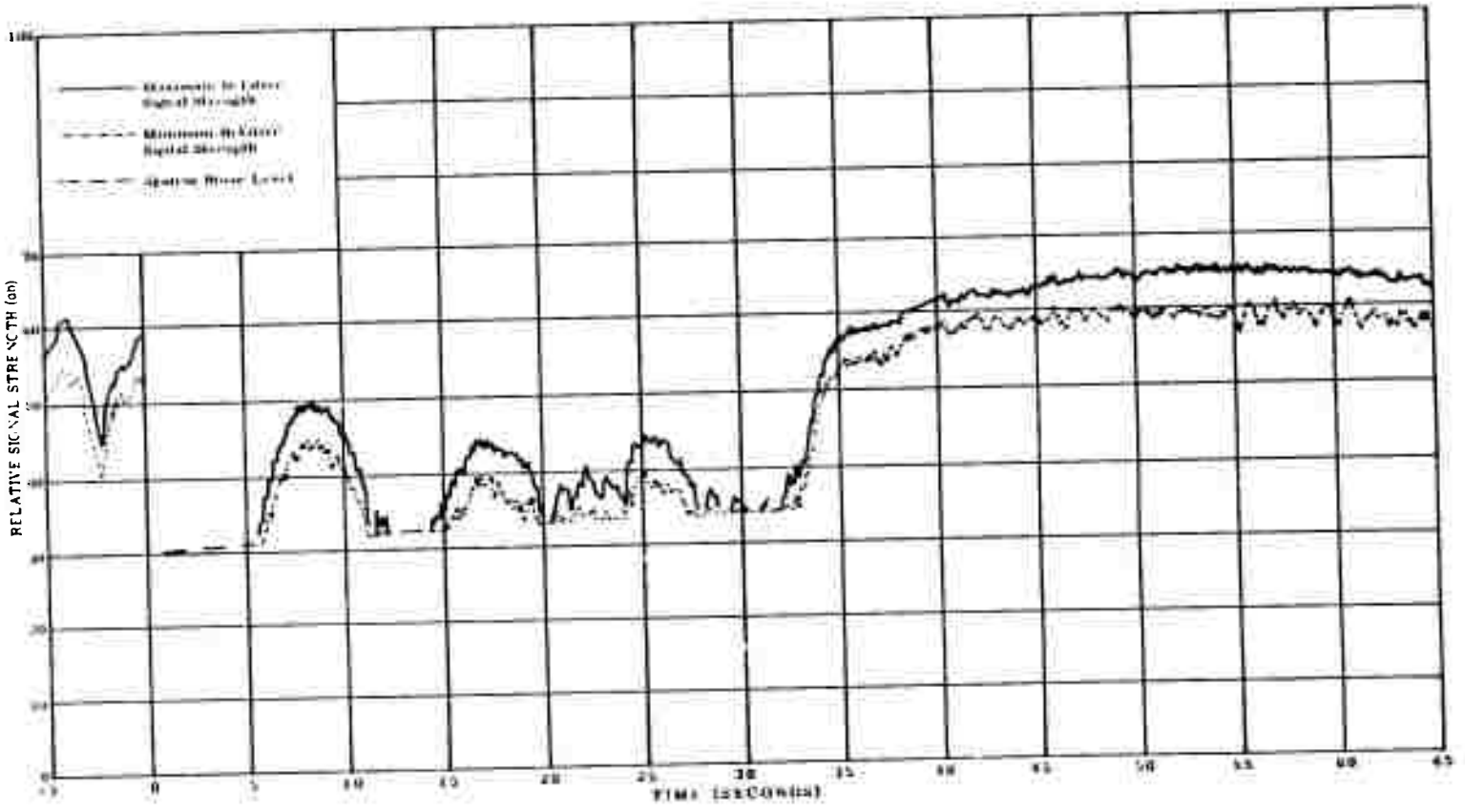

Figure 4.19 L-band relative signal strength envelopes, Tight Rope, Missile A, Ship 1

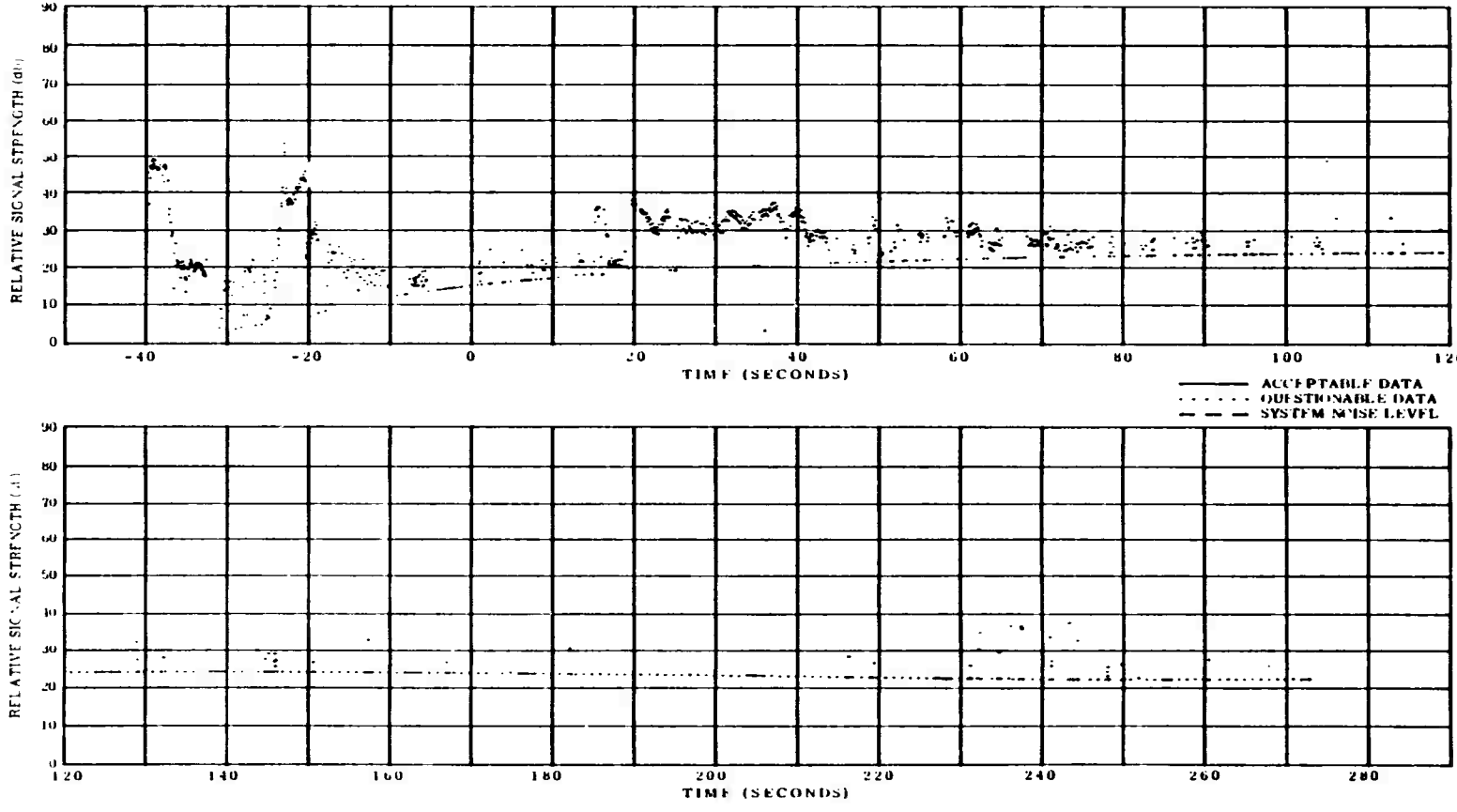

Figure 4.20 X-band relative signal strength, Tight Rope, Missile C, Ship 2.

Figure 4.21 C-band relative signal strength, Eight Bops, Missile C, Ship 2

Page 309 deleted.

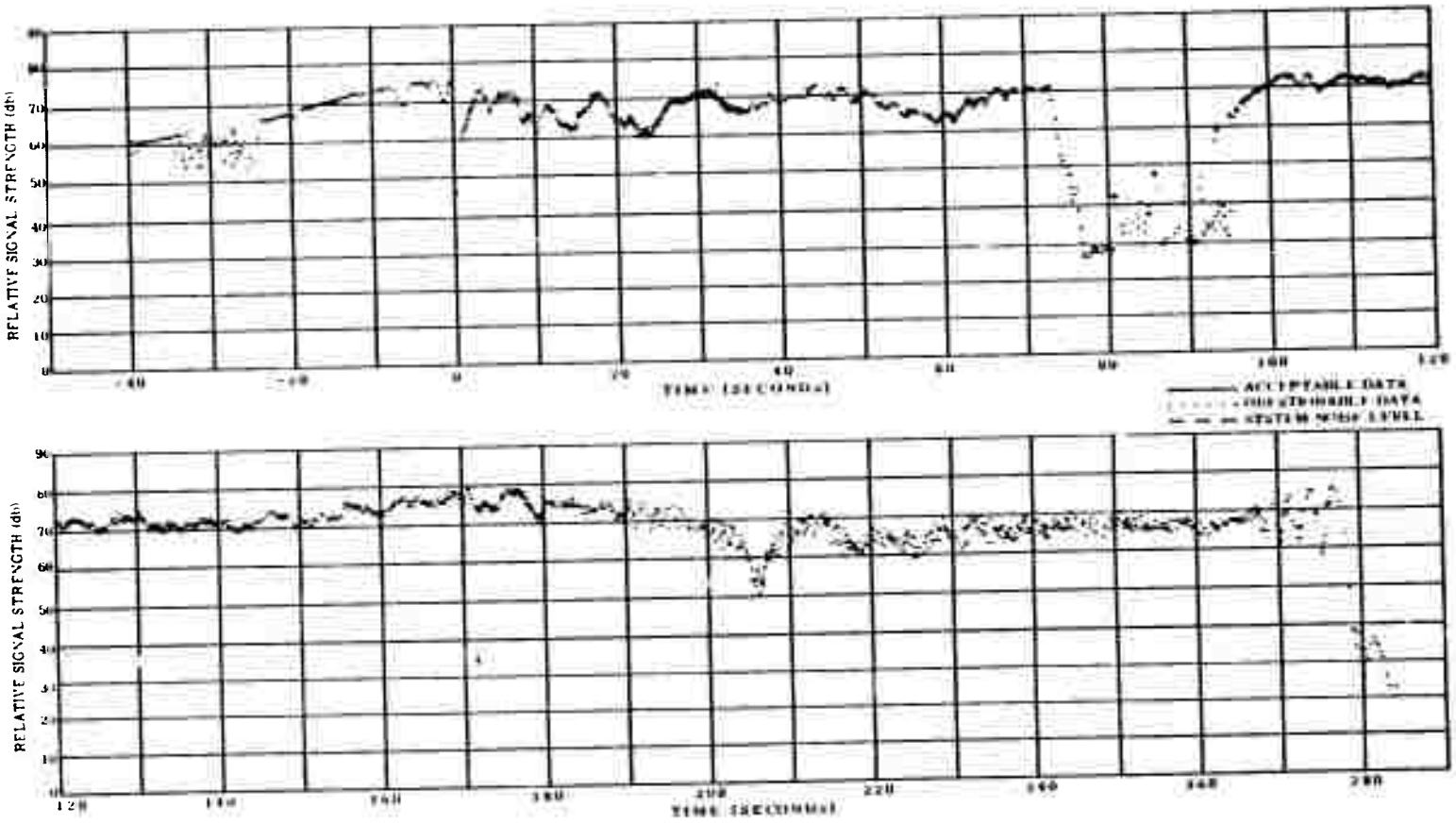

Figure 4-23 L band relative signal strength, Tight Rope, Missile C, Ship 2.

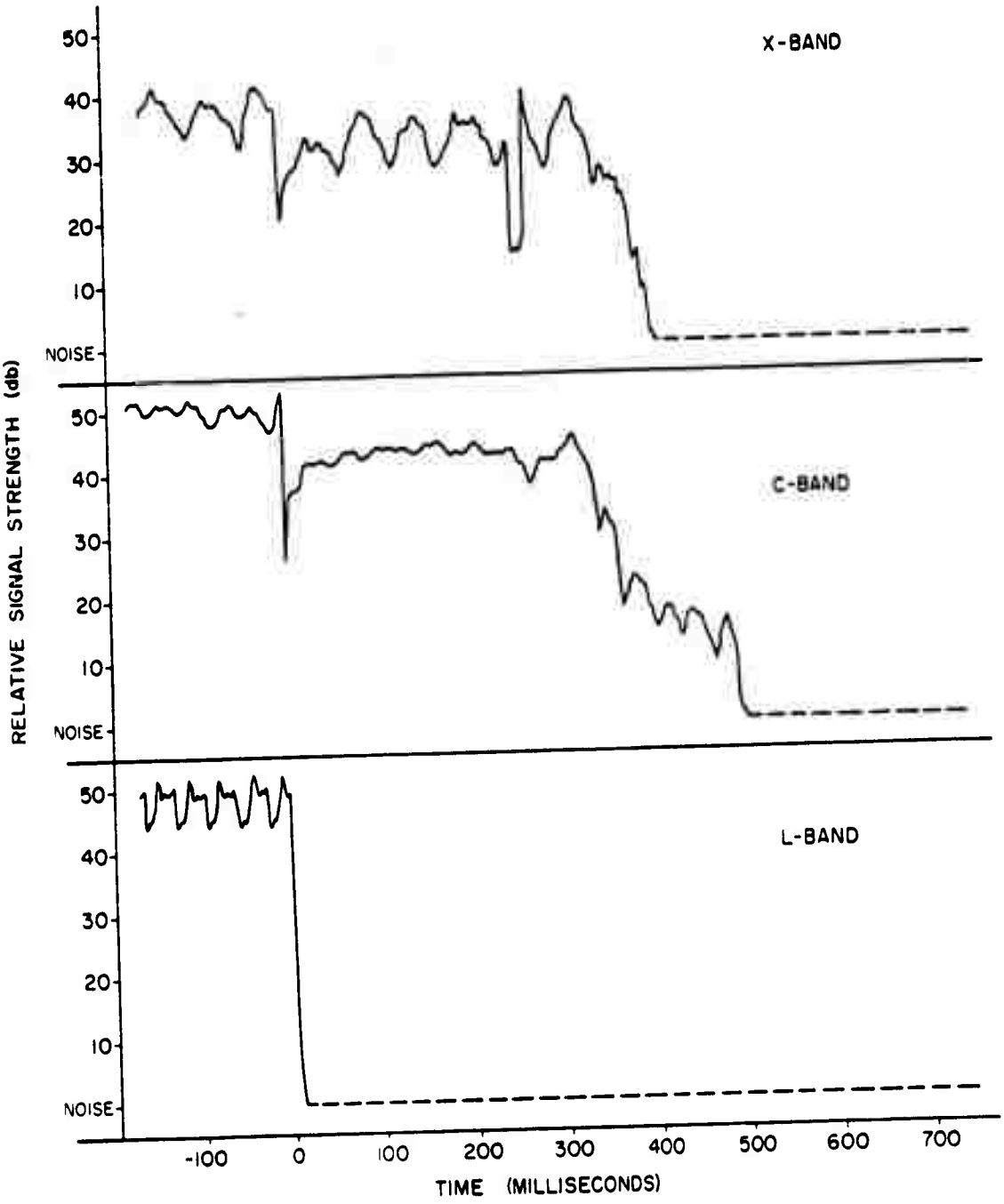

Figure 4.24 Relative signal strength, Tight Rope, Missile B, Ship 3.

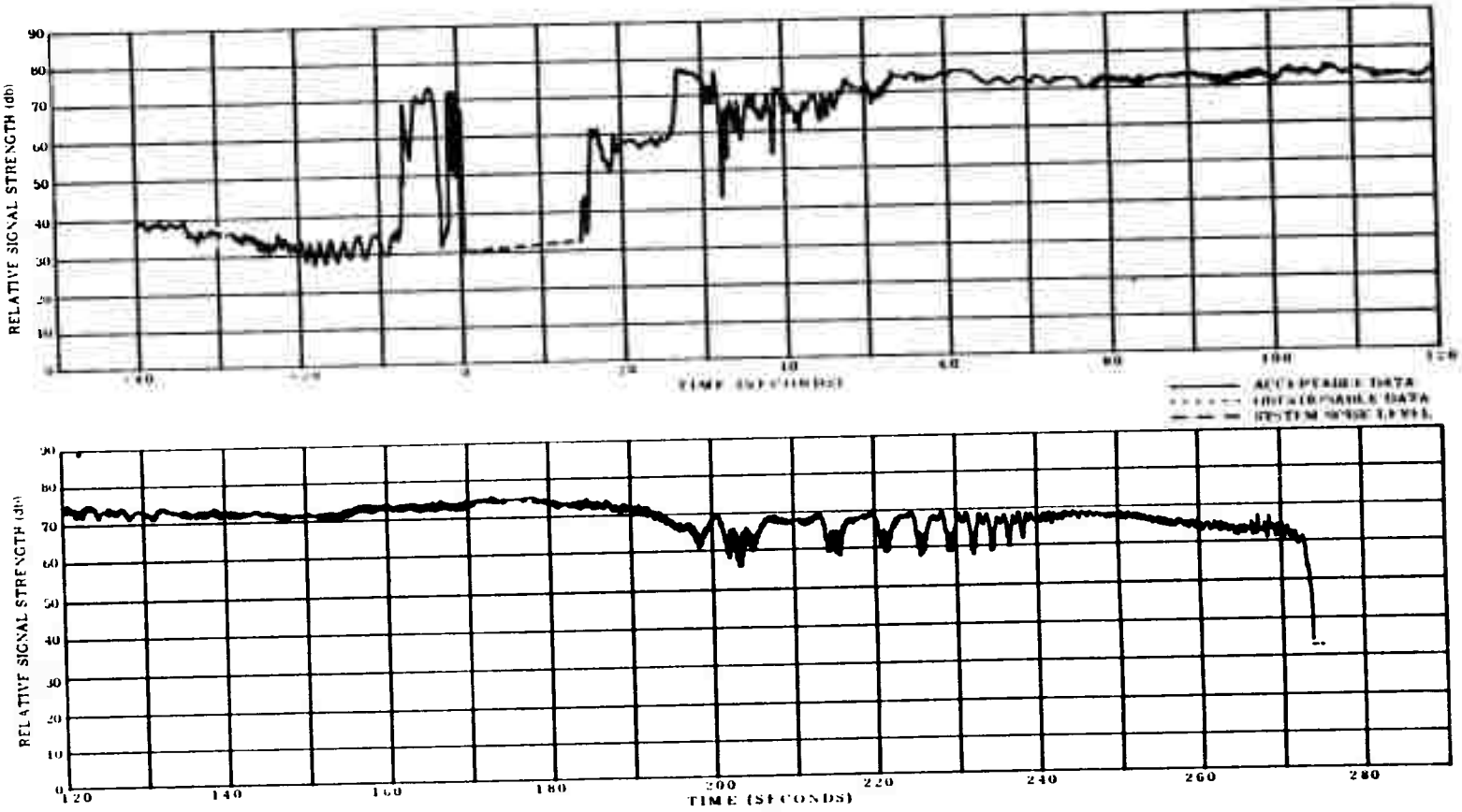

Figure 4.25 X band relative signal strength, Tight Rope, Missile B, Step 3

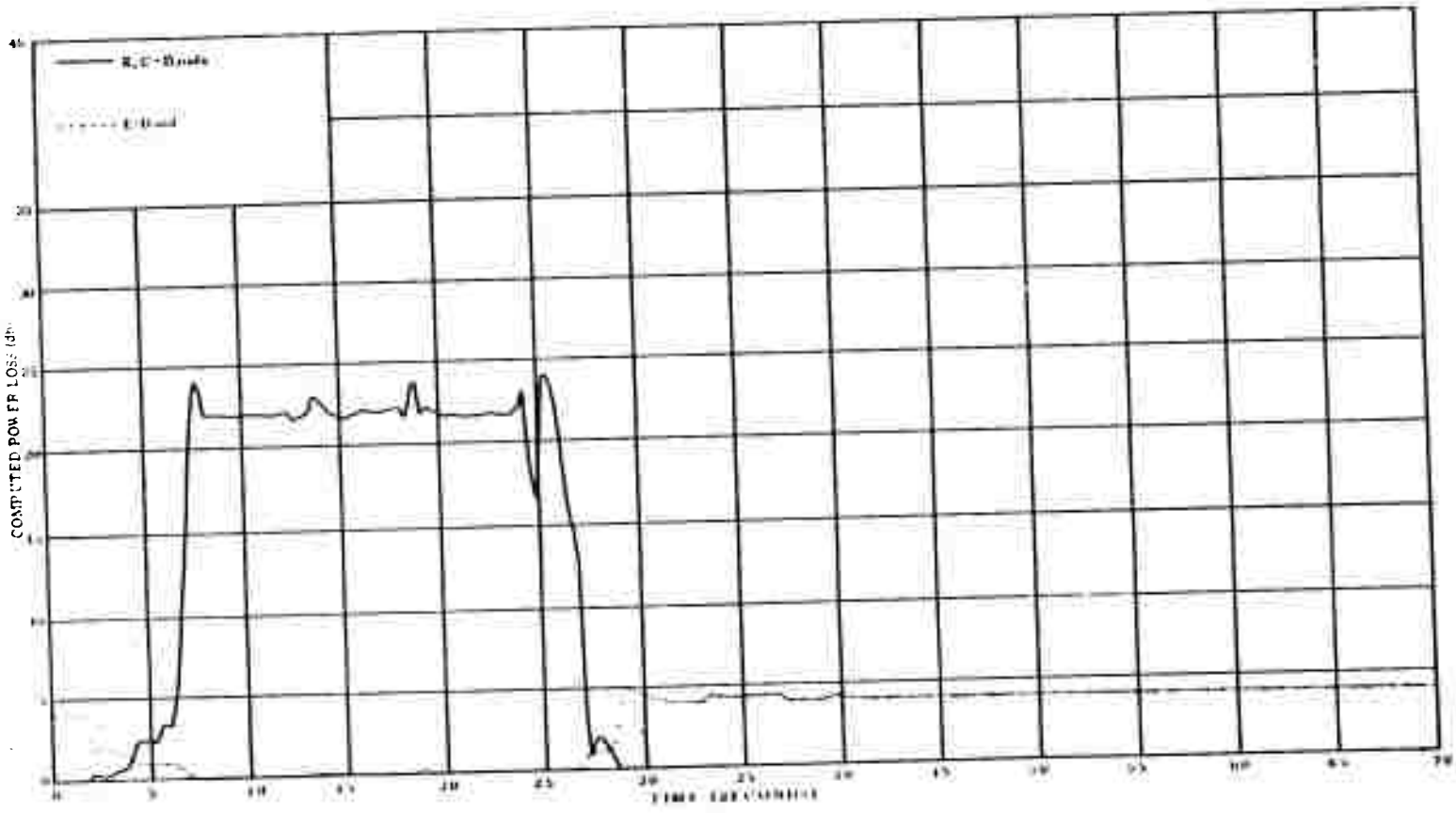

Figure 4.26 Computed power loss due to antenna pointing errors, Tight Rope, Missile B, Ship 3

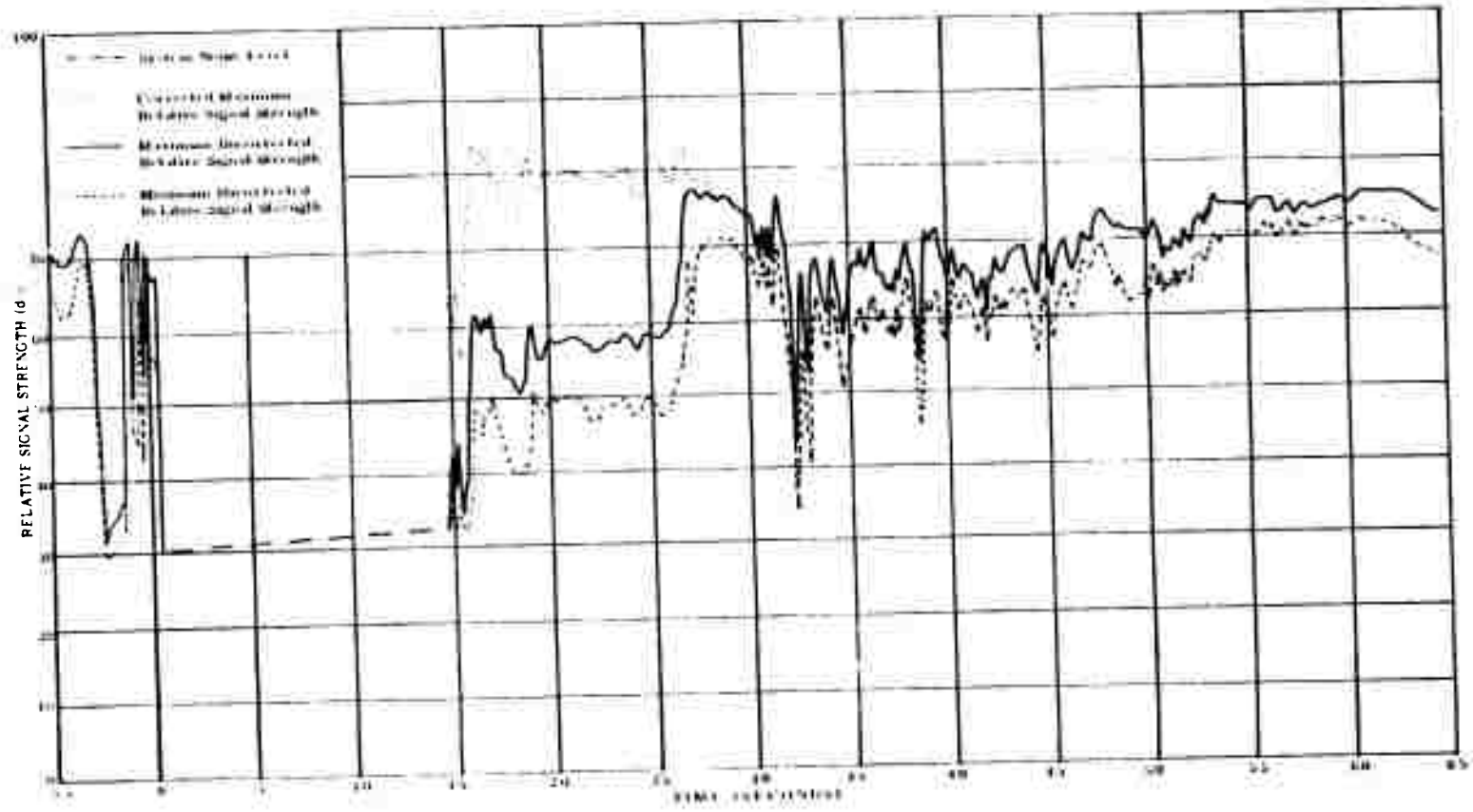

Figure 4-27 X-band relative signal strength with correction for antenna pointing errors, Tight Rope, Missile B, Ship 3.

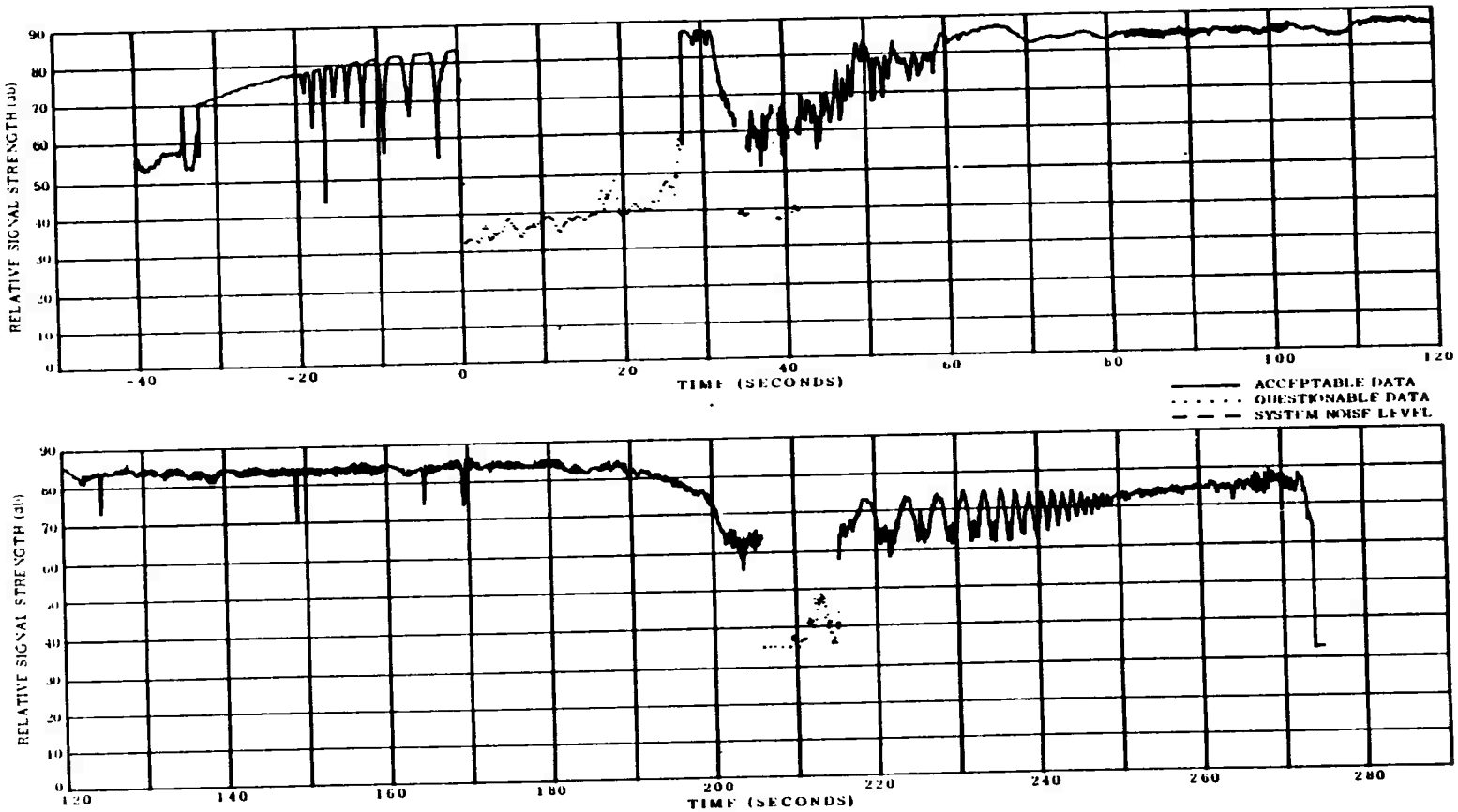

Figure 4-28 C-band relative signal strength, Tight Rope, Missile B, Ship 3.

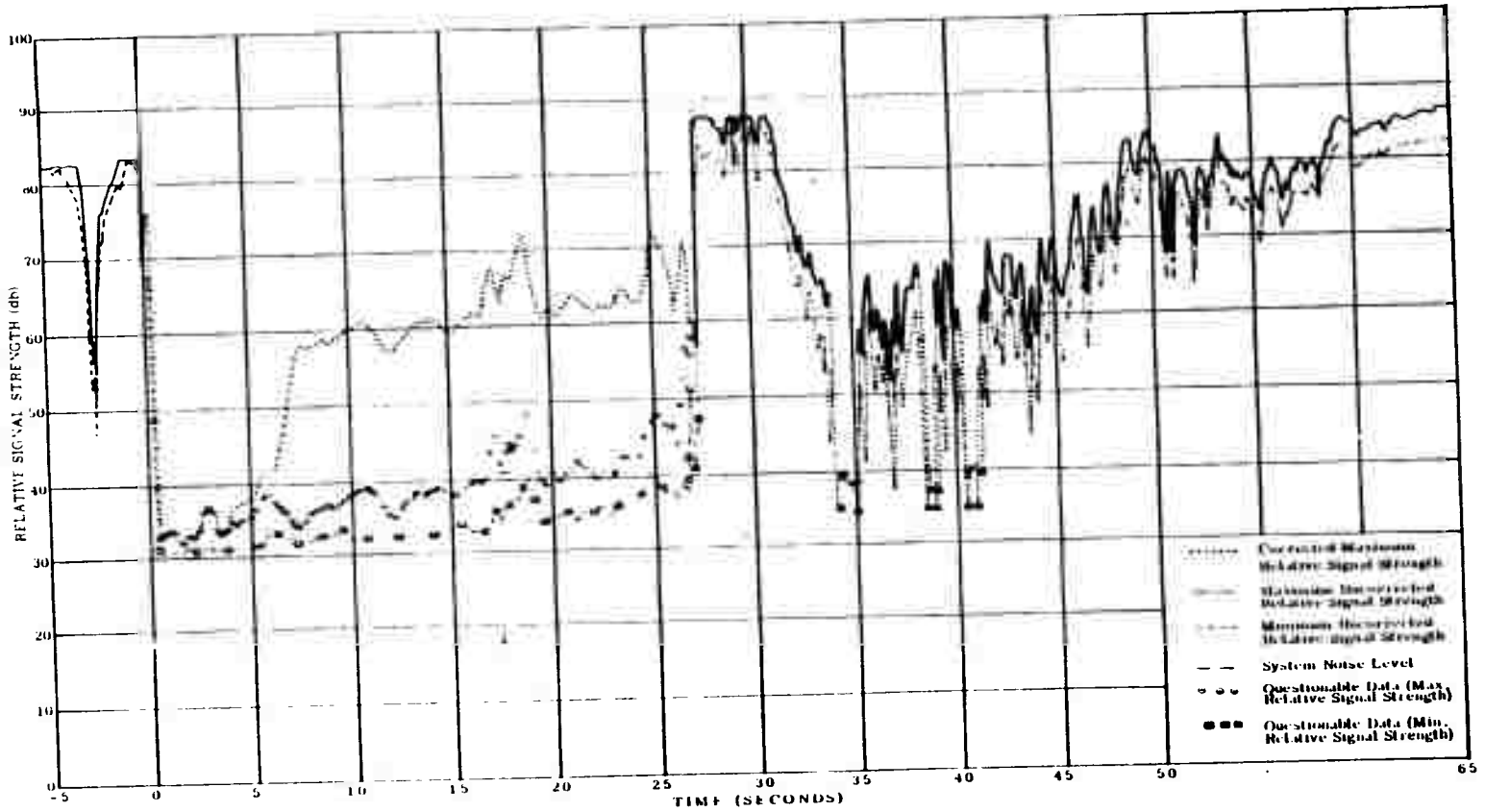

Figure 4.29 C band relative signal strength with correction for antenna pointing errors, Tight Rope, Missile B, Ship 3.

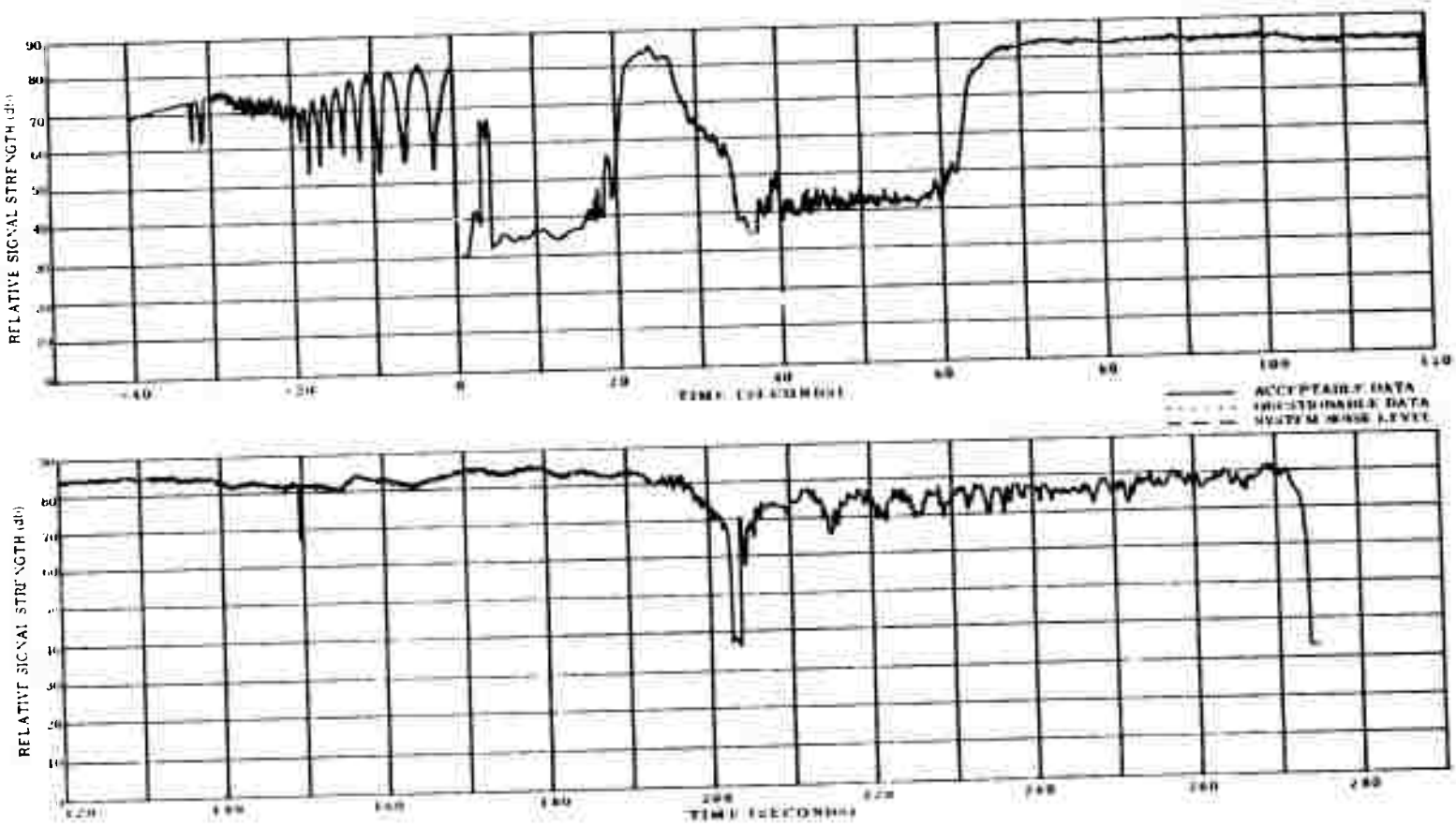

Figure 4.30 L band relative signal strength, Tight Rope, Missile B, Ship 3.

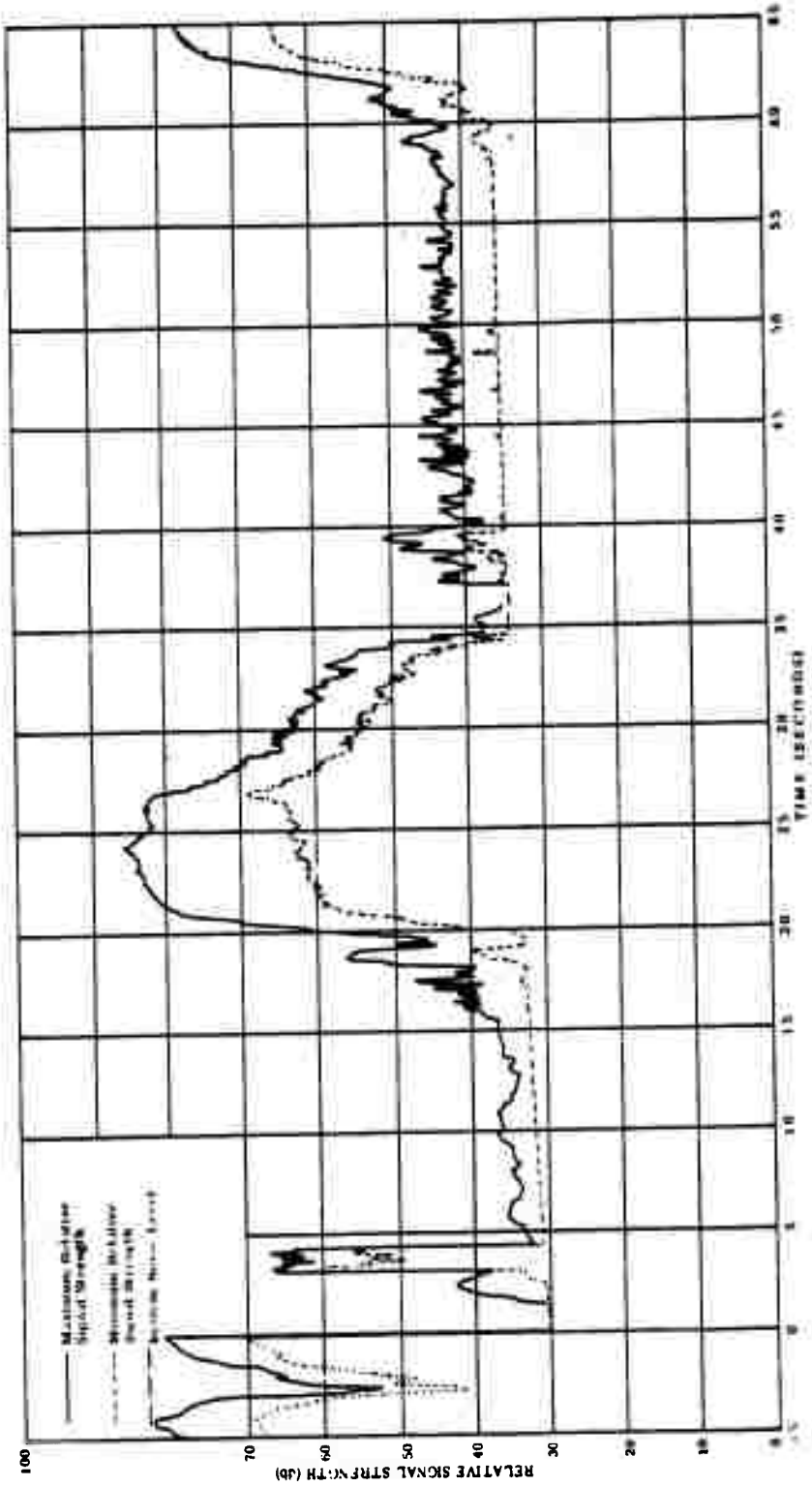

Figure 4.31 L-band relative signal strength envelopes, Tight Rope, Missile B, Ship 3.

Page 319 deleted.

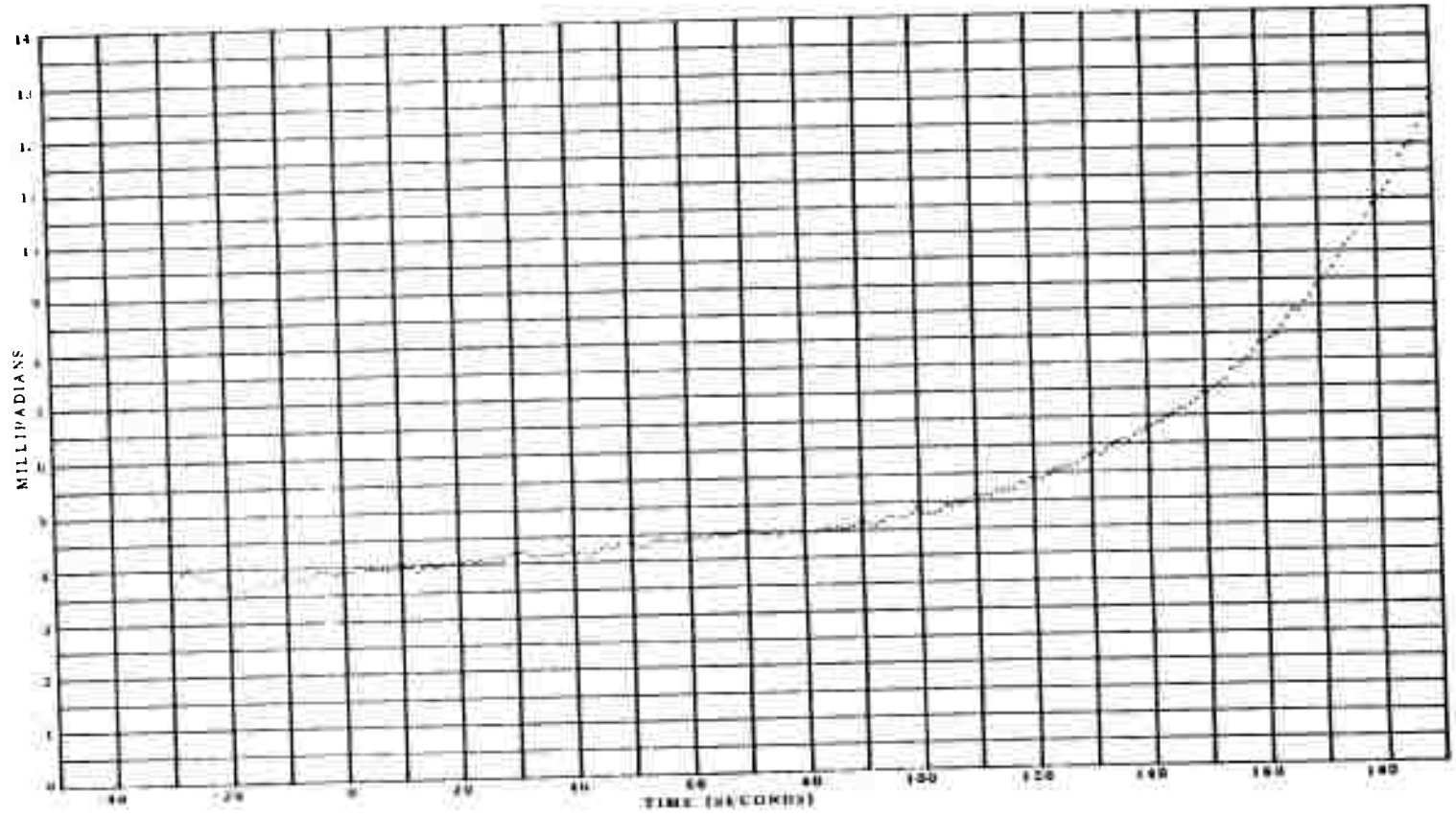

Figure 4.33 Interferometer and trajectory angular comparison, Tight Rope, Missile A, interferometer, least squares combination.

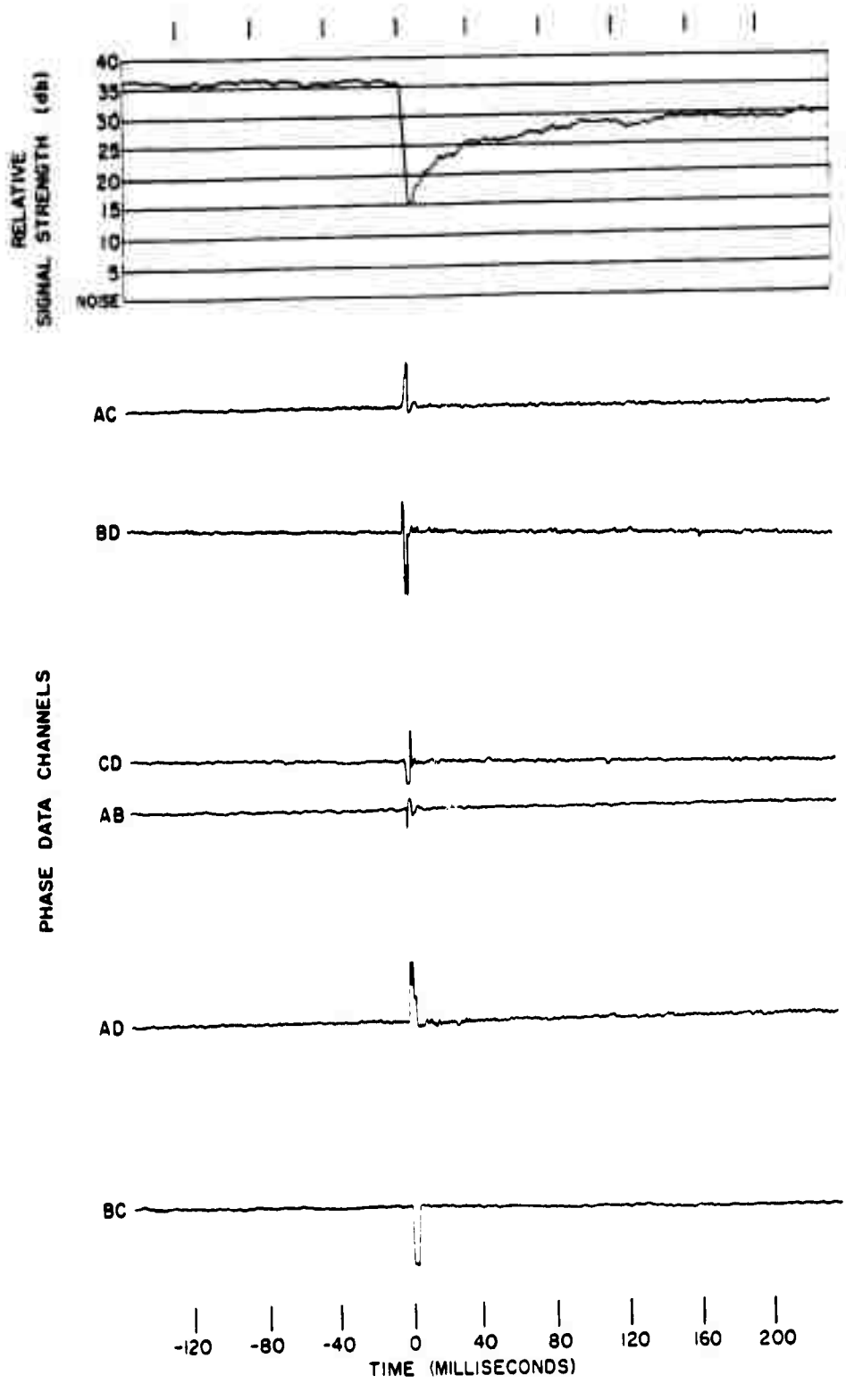

Figure 4.34 Raw phase data and relative signal strength at event, Tight Rope, Missile A, interferometer, C-band.

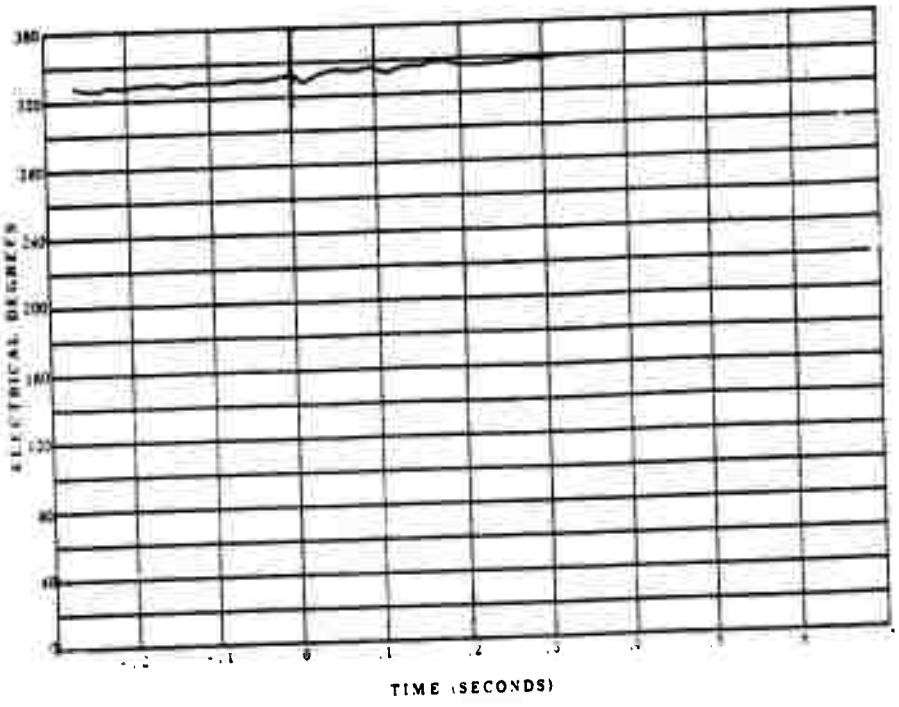

Figure 4.35 Phase perturbation at event: Tight Rope, Missile A, interferometer: Leg AB.

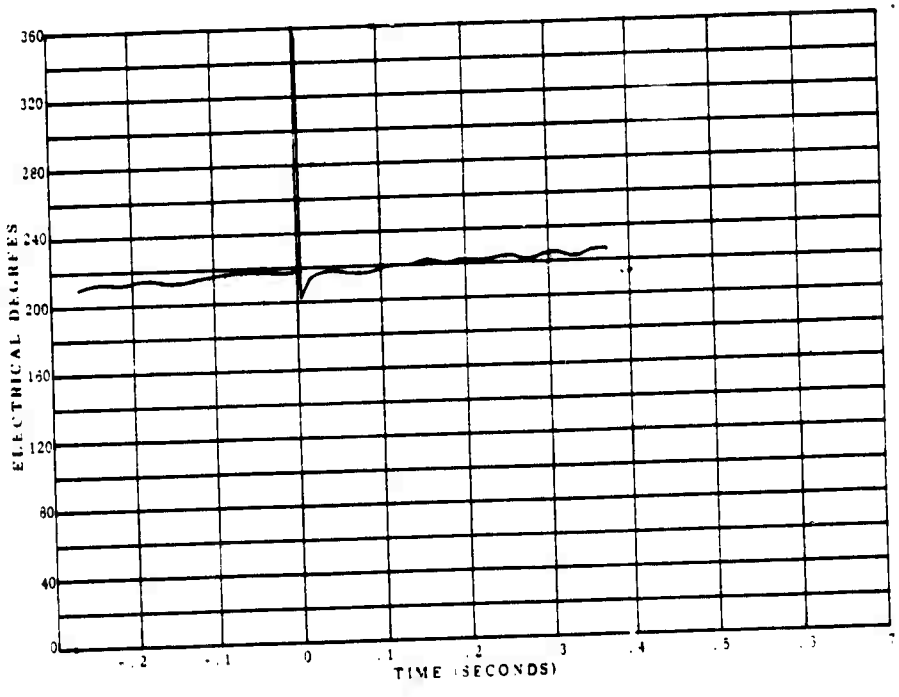

Figure 4.36 Phase perturbation at event: Tight Rope, Missile A, interferometer: Leg BC.

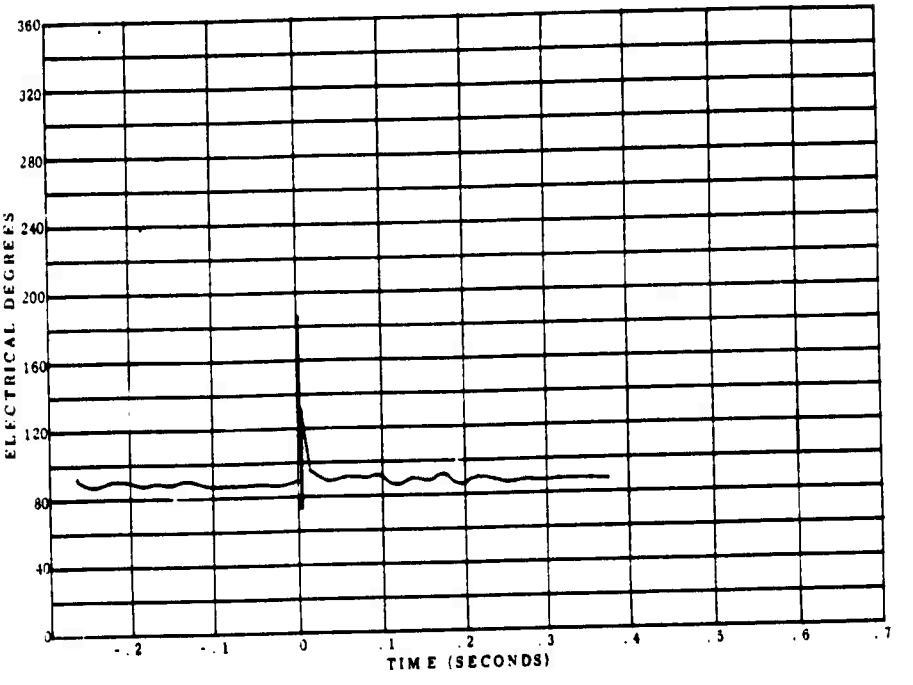

Figure 4.37 Phase perturbation at event, Tight Rope, Missile A, interferometer, Leg AC.

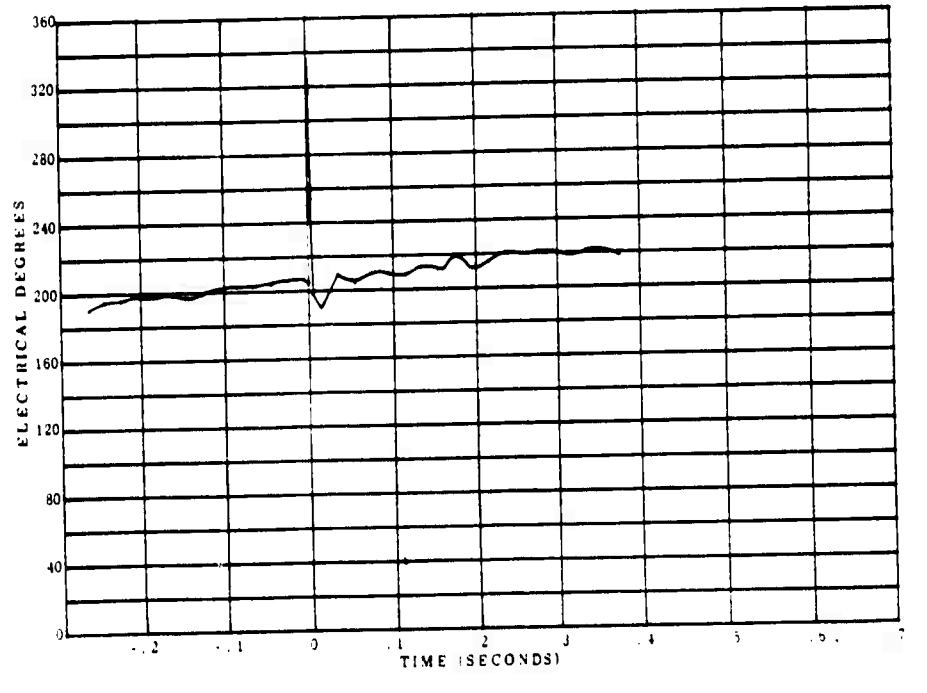

Figure 4.38 Phase perturbation at event, Tight Rope, Missile A, interferometer, Leg AD.

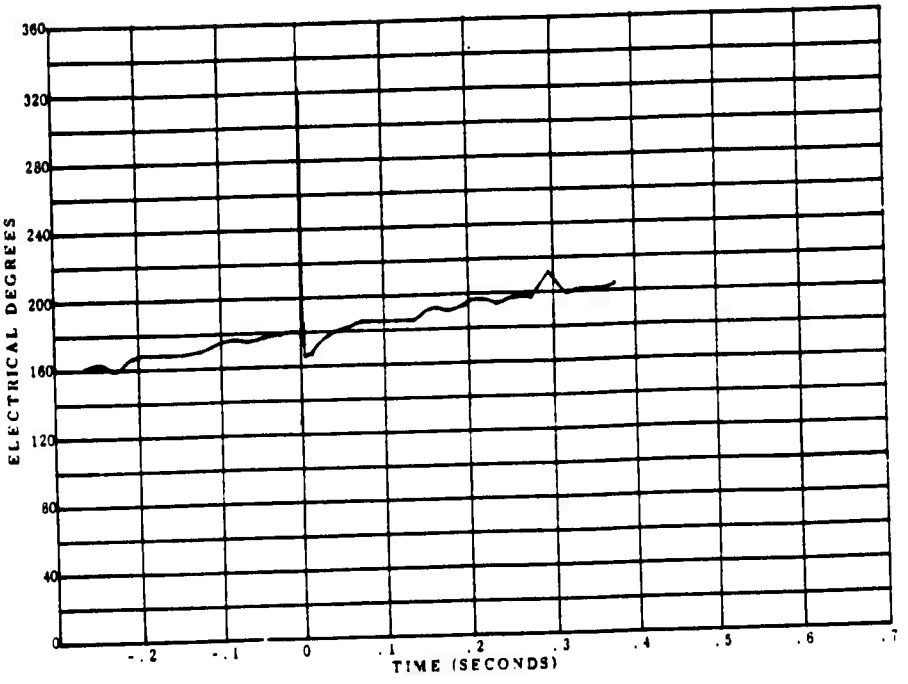

Figure 4 39 Phase perturbation at event, Tight Rope, Missile A, interferometer, Leg BD.

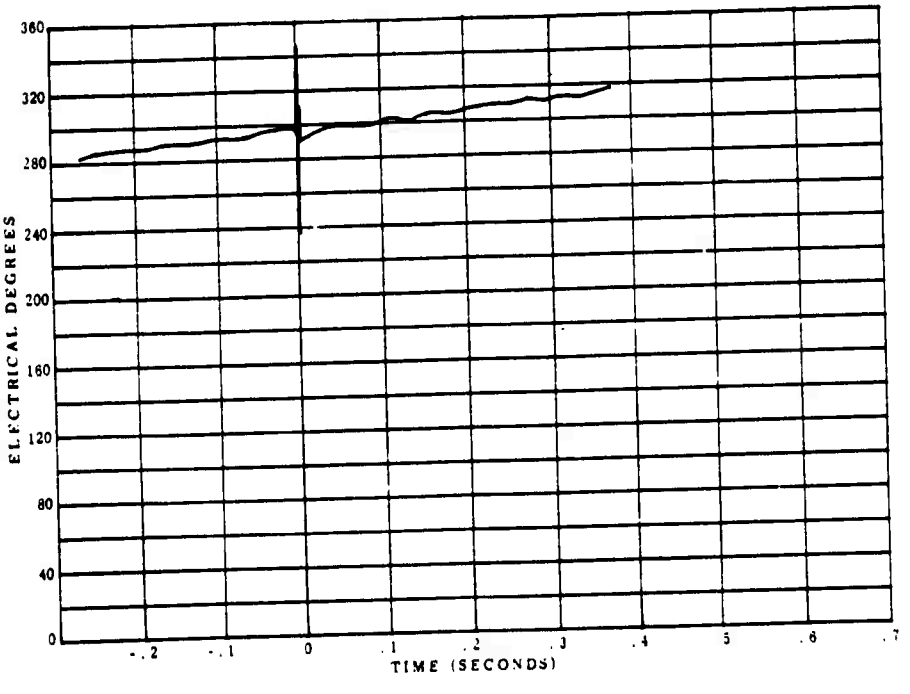

Figure 4 40 Phase perturbation at event, Tight Rope, Missile A, interferometer, Leg CD.

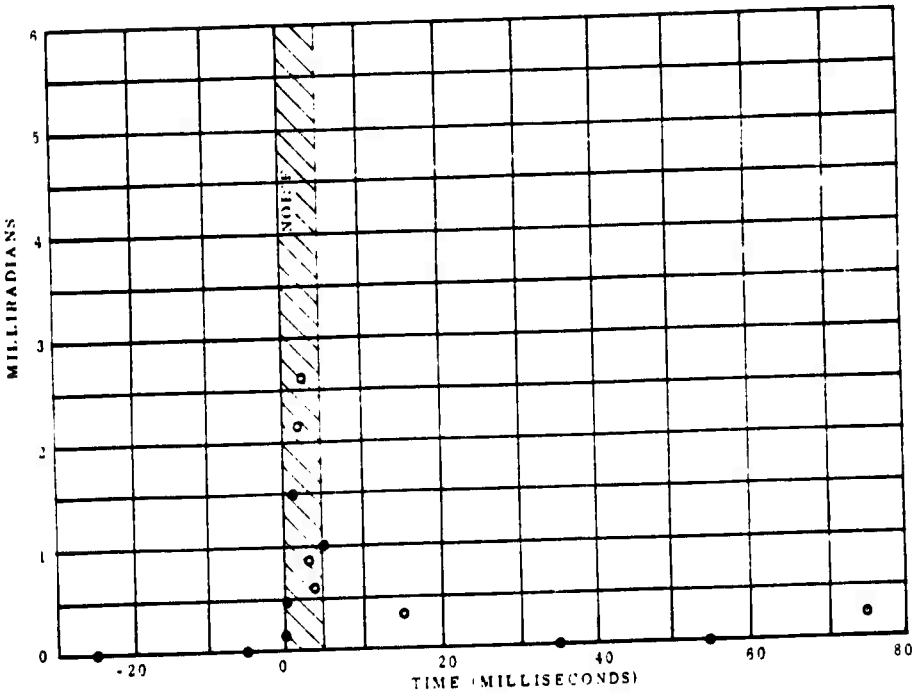

Figure 4.41 Refraction at event, Tight Rope, Interferometer Combination AC+BD.

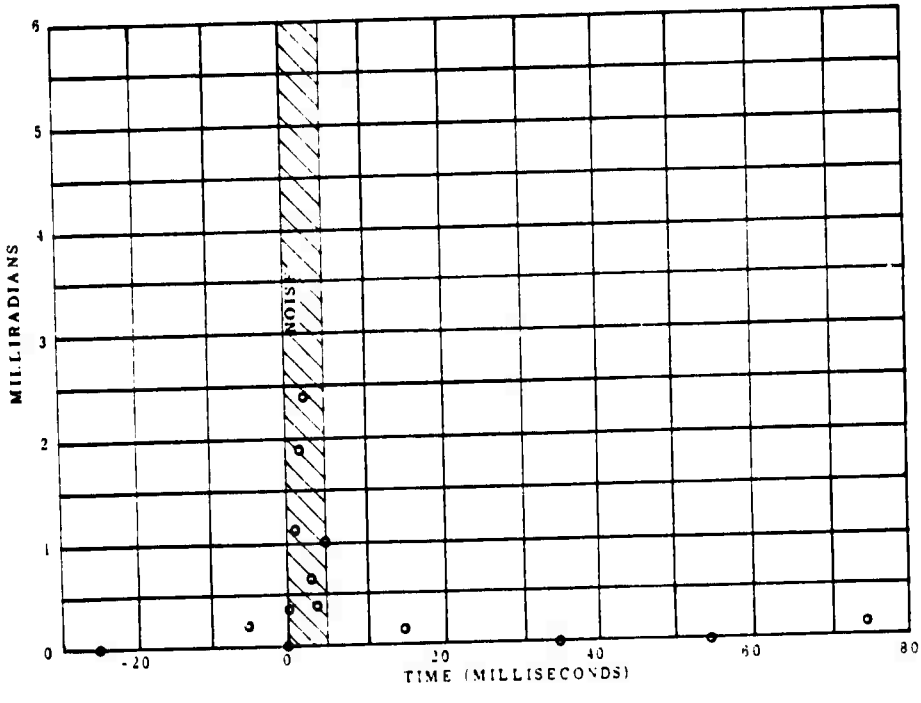

Figure 4.42 Refraction at event, Tight Rope, Interferometer Combination AC-BD.

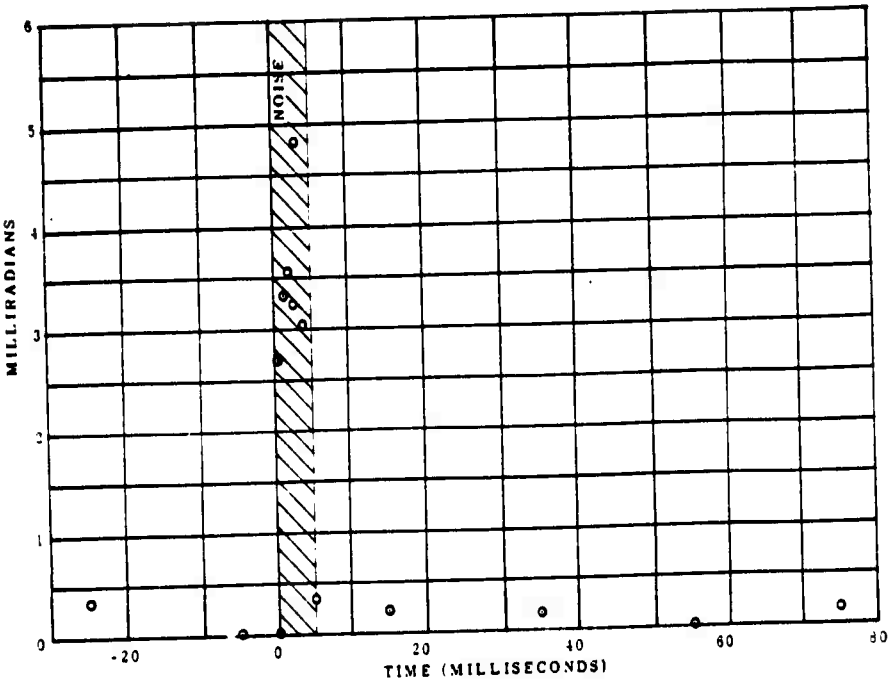

Figure 4.43 Refraction at event, Tight Rope, Interferometer Combination BC-BD.

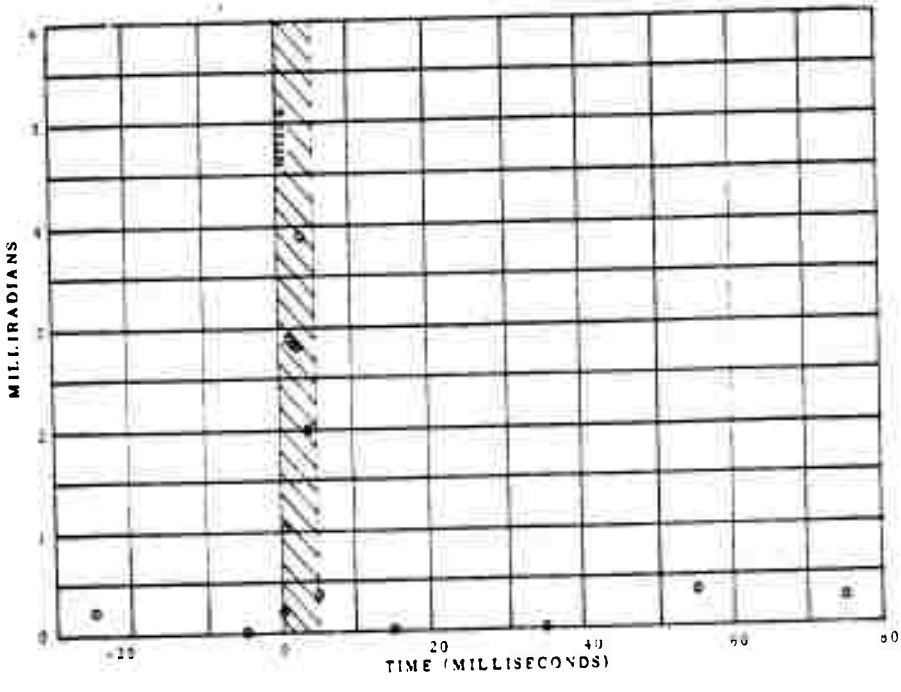

Figure 4.44 Refraction at event, Tight Rope, Interferometer Combination BC-CD.

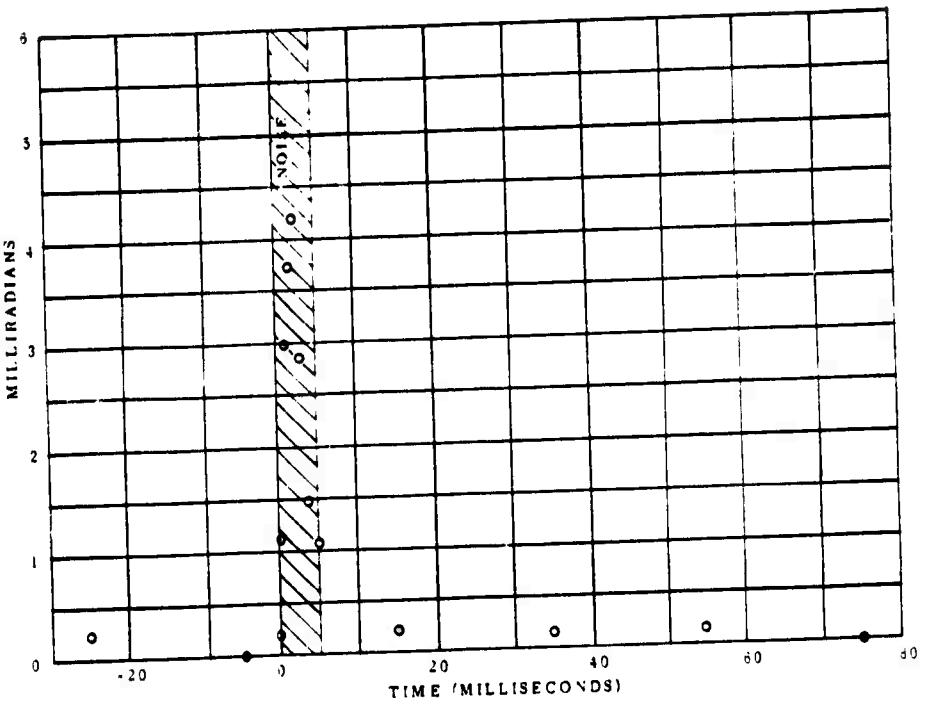

Figure 4.45 Refraction at event, Tight Rope, Interferometer Combination BC-AC.

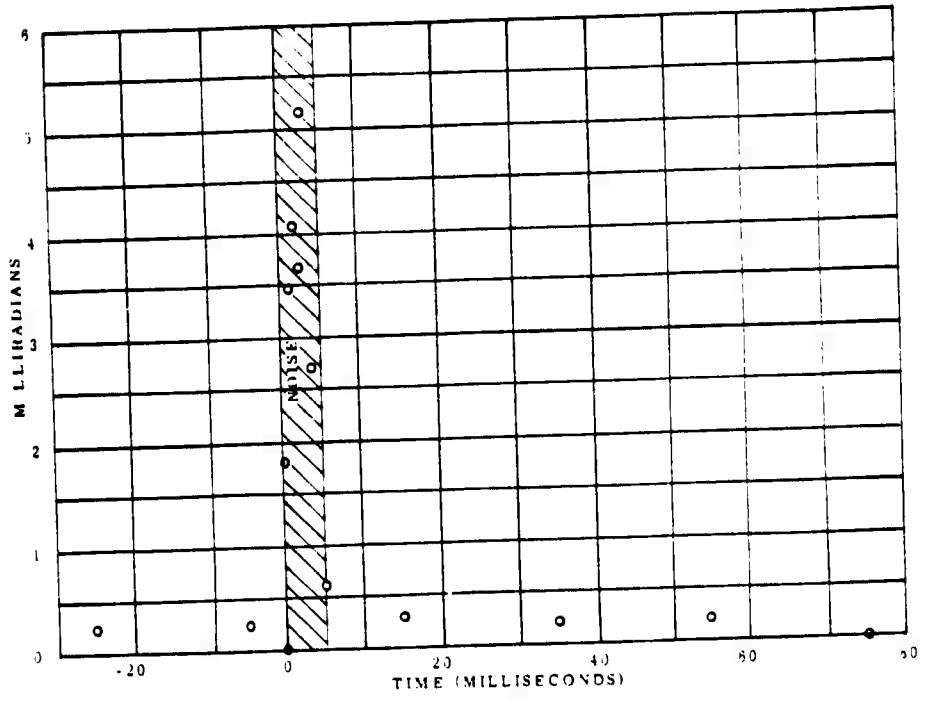

Figure 4.46 Refraction at event, Tight Rope, Interferometer Combination BC-AD.

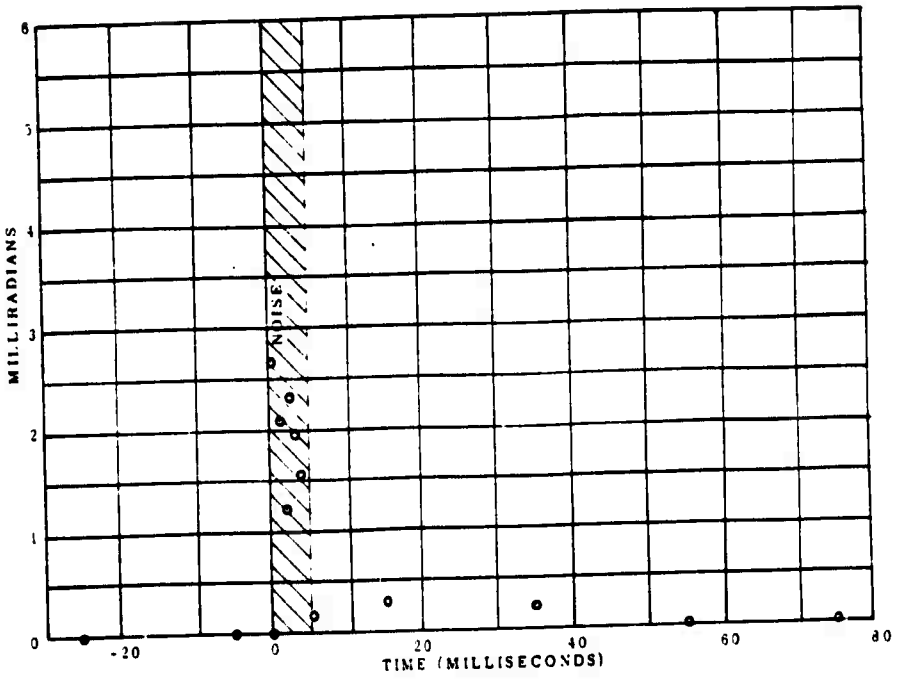

Figure 4.47 Refraction at event, Tight Rope, Interferometer Combination AB-AD.

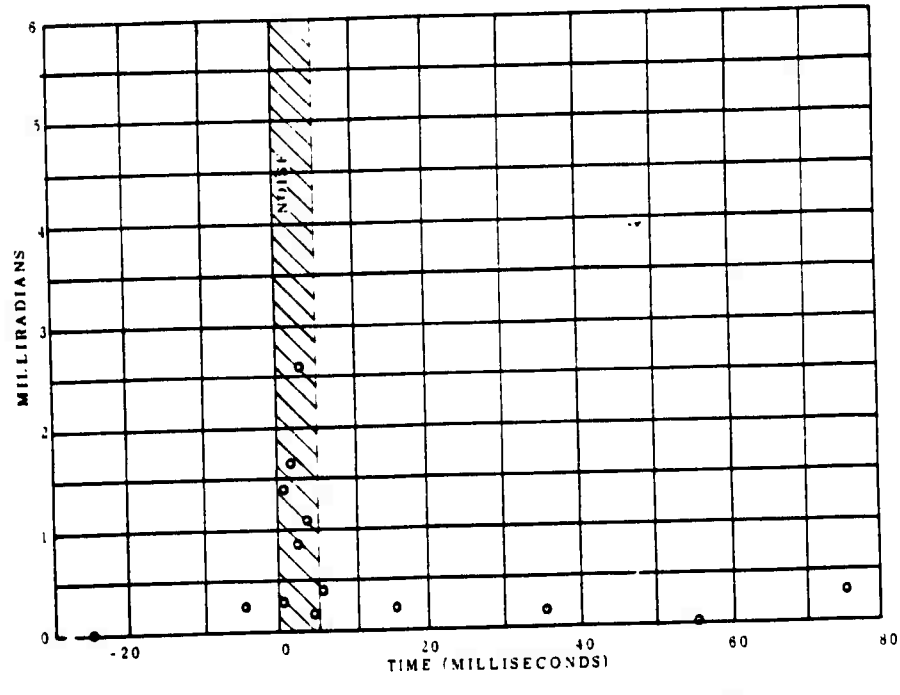

Figure 4.48 Refraction at event, Tight Rope, Interferometer Combination AB-BD.

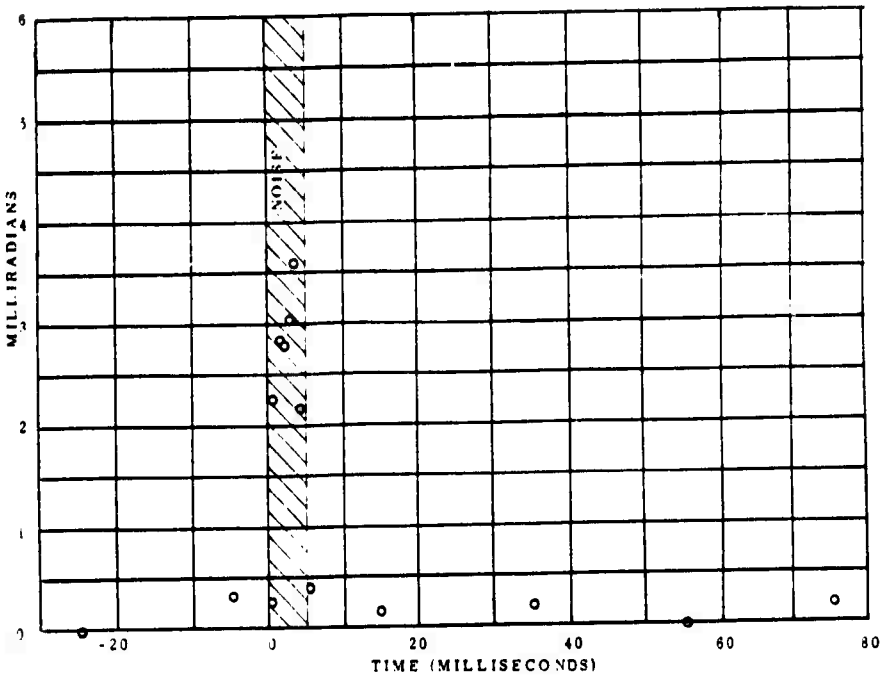

Figure 4.49 Refraction at event, Tight Rope, Interferometer Combination AB-BC.

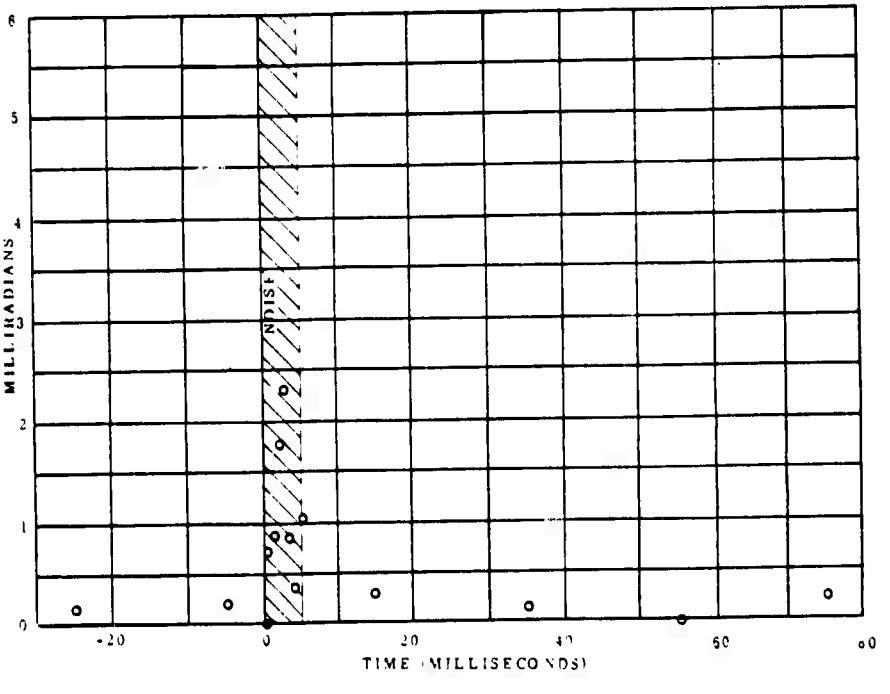

Figure 4.50 Refraction at event, Tight Rope, Interferometer Combination AB-AC

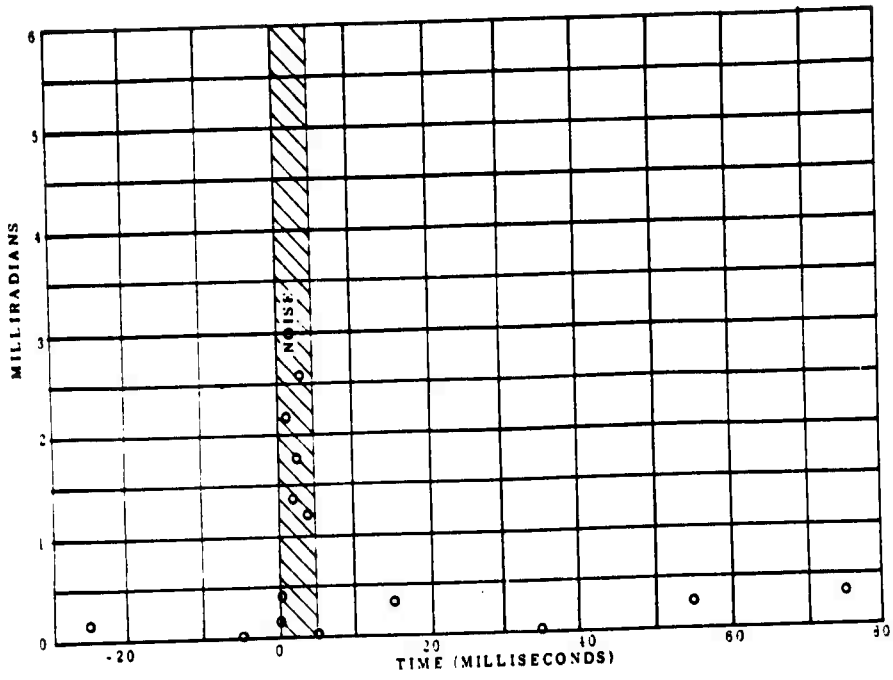

Figure 4.51 Refraction at event, Tight Rope, Interferometer Combination AD-CD.

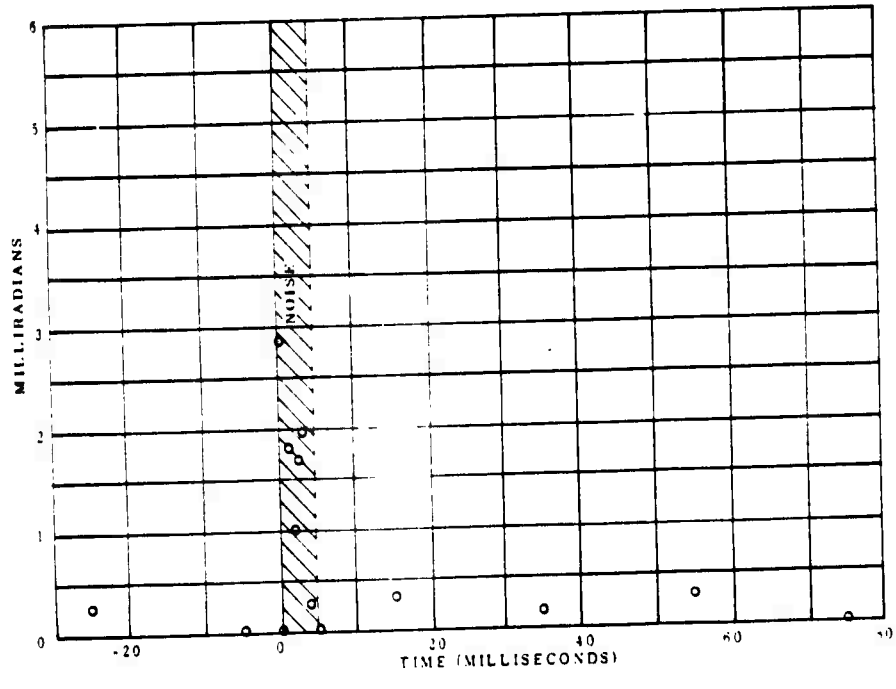

Figure 4.52 Refraction at event, Tight Rope, Interferometer Combination BD-CD.

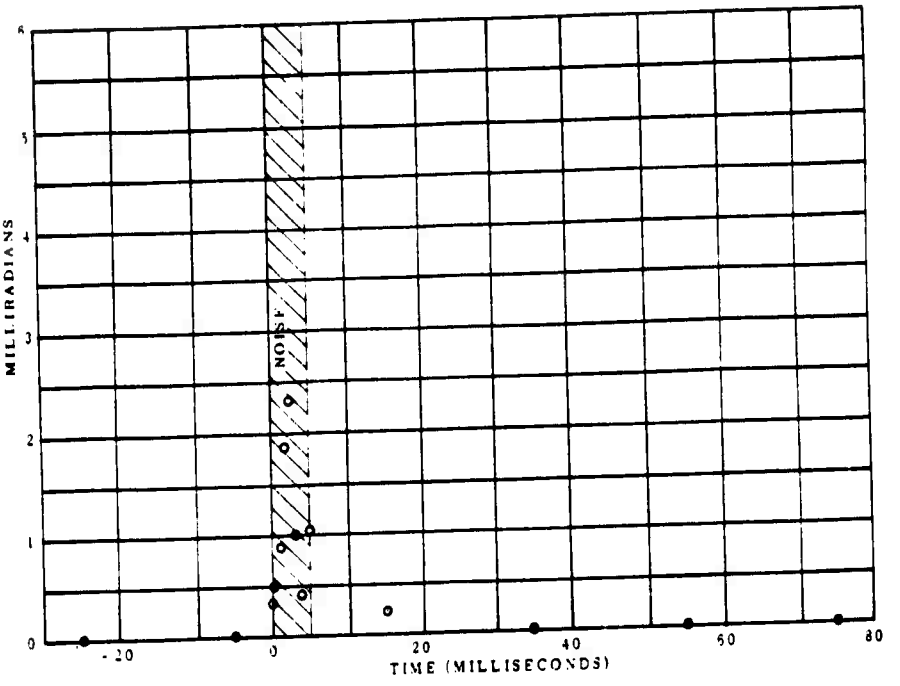

Figure 4.53 Refraction at event, Tight Rope, Interferometer Combination AC-CD.

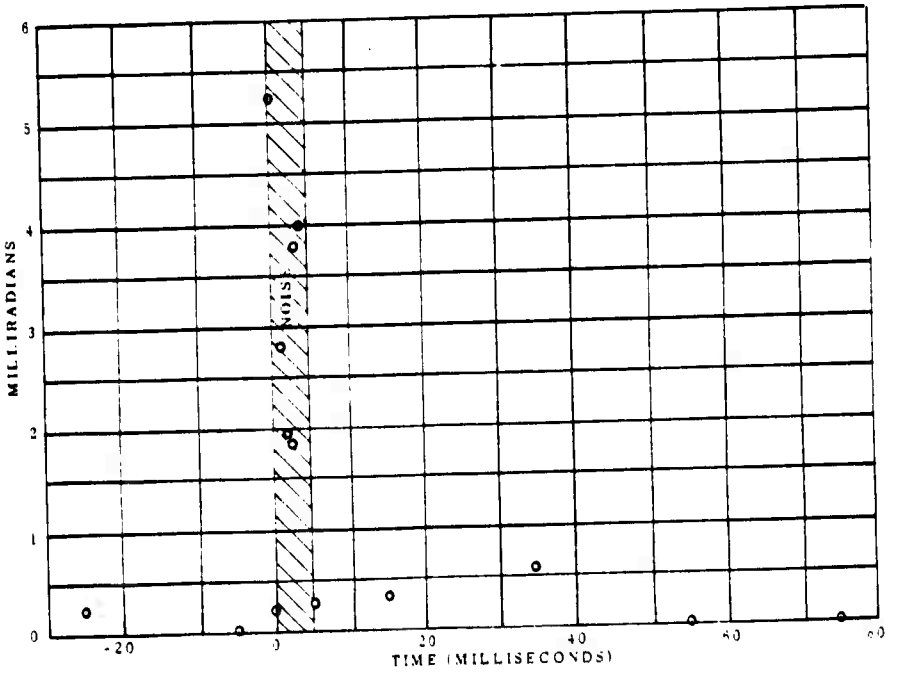

Figure 4.54 Refraction at event, Tight Rope, Interferometer Combination AD-BD.

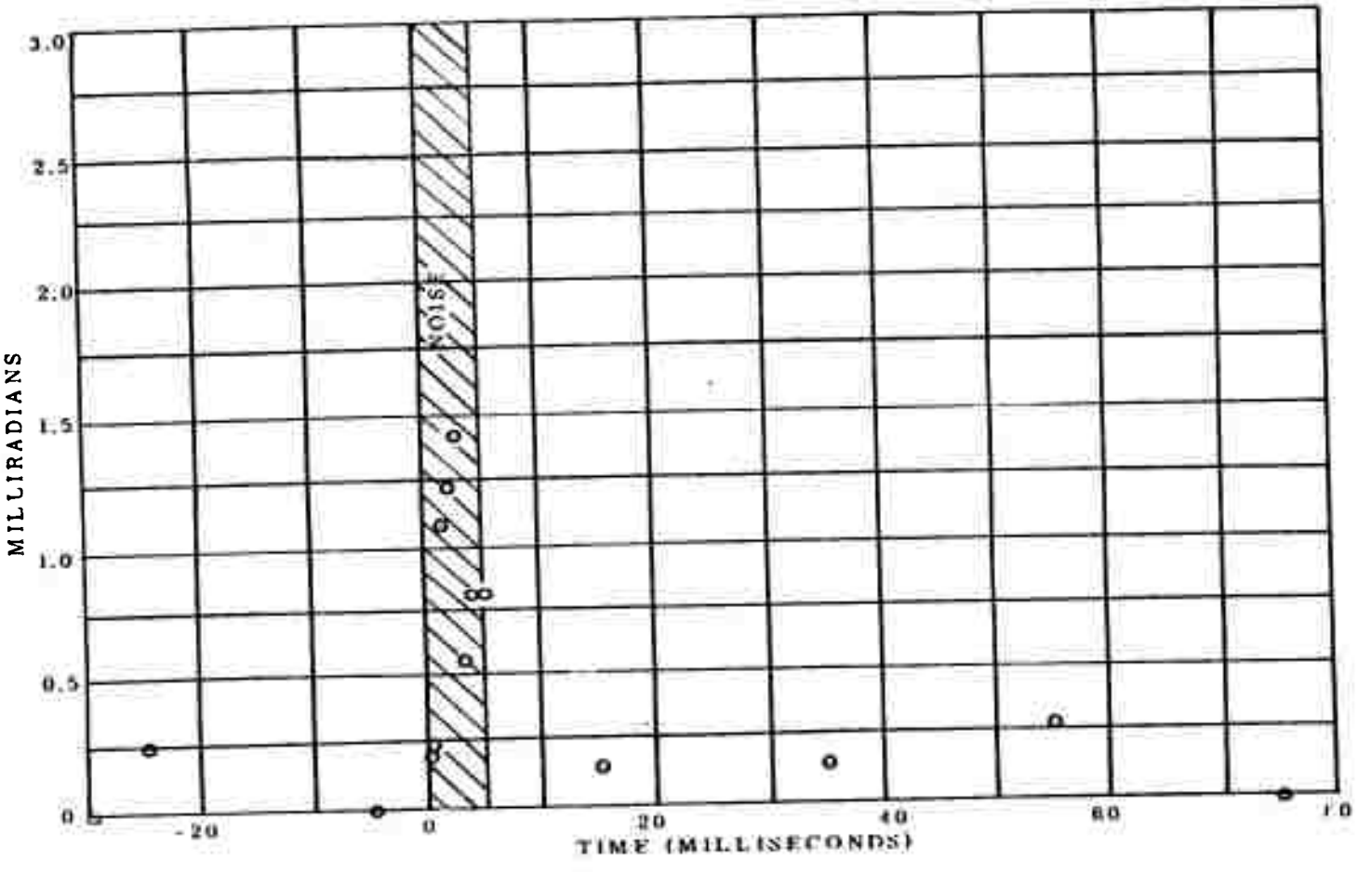

Figure 4.55 Refraction at event, Tight Rope, interferometer, least-squares combination.

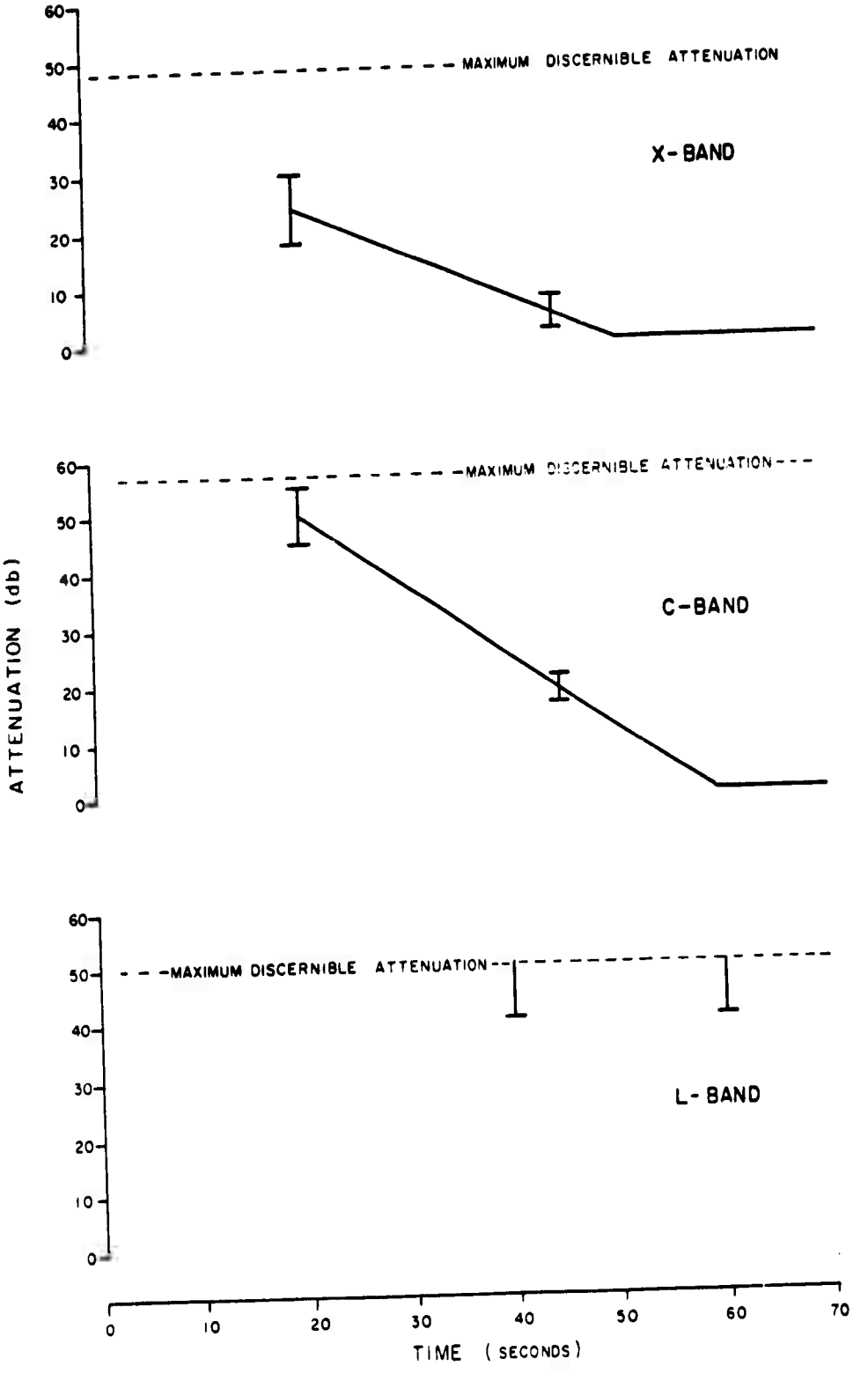

Figure 4.56 Characteristic attenuation through the Tight Rope fireball.

CHAPTER 5

CONCLUSIONS AND RECOMMENDATIONS

5.1 CONCLUSIONS

5.1.1 Attenuation. The major objective of measuring fireball attenuation was achieved. It has been observed that the fireball produced by event at km altitude will attenuate X-band frequencies ≥30 db for at least 35 seconds; C-band frequencies ≥45 db for at least 35 seconds; and L-band frequencies ≥45 db for at least 60 seconds. Amplitude scintillations during recovery periods are very severe, and a return to pre-event signal levels cannot be expected in less than 60 seconds at X- and C-bands and in less than 100 seconds at L-band. Less severe scintillations persist for some time following overall signal level recovery.

Although similar attenuation periods appear to result from a -km-altitude event, less attenuation is produced by the smaller device because of shorter penetration distances through the ionized region. For an event of this size and at this altitude, it is evident that the center of the torus is less opaque than the torus itself.

The beta patch formed by event at -km altitude will attenuate L-band transmissions ≥35 db for at least

15 seconds without causing significant deterioration of C-band signals for more than a few milliseconds. Amplitude scintillations produced through a beta patch are not as severe as those generated through a fireball.

The exact relationship of attenuation to frequency is difficult to assess from the available data other than that an inverse proportionality exists. It is not known to what degree the stated attenuation was caused by absorption or to what degree by refraction, reflection, or other multipath phenomena.

5.1.2 Refraction. Very little refraction data is available from this project. The only information of unquestioned value was elicited from short-term data recorded immediately after the King Fish detonation. The peak apparent refraction in C-band was ≤3 milliradians. With reference to the geometry of the experiment, the refraction in azimuth was 24 milliradians (west), in elevation 0.13 milliradians (down).

5.2 RECOMMENDATIONS

Although Project 6.1 succeeded in the original major design objective of measuring attenuation through a fireball, a study of ABM radar systems and the types of information required for fireball modeling revealed the need for further investigation.

Additional information is needed concerning the nature of debris regions produced by devices of other yields detonated at other altitudes and of attenuation-producing phenomena in near regions outside of the visible fireball. A further study of beta-induced ionized regions is necessary to augment existing data concerning their dimension, movement, and propensity to absorb radar frequencies. It is suggested that comprehensive measurements be made of these phenomena to permit the construction of coherent time histories.

It is recommended that wide-band data instrumentation be employed to enhance the measurement, in depth and resolution, of amplitude scintillations and to aid in the determination of phase-front distortion and its effect on ABM radar systems. The geometry of all such operations should be designed to provide cross-sectional data of fireball and beta-patch attenuation.

It is further recommended that existing instrumentation be redesigned to provide a more reasonable refraction measuring capability and that measures be taken to insure adequately defined locations of all transmitting and receiving elements employed in Project 6.1 systems.

Pages 337 and 338
deleted.